Real-Time Cognitive Sense-and-Notch Radar

By

Jonathan William Owen

Submitted to the graduate degree program in Electrical Engineering and Computer Science and the Graduate Faculty of the University of Kansas in partial fulfillment of the requirements for the degree of Doctor of Philosophy.

Dr. Shannon Blunt, Chairperson

Dr. Chris Allen

Dr. Jim Stiles

Dr. Carl Leuschen

Dr. Zsolt Talata

Date Defended: May 11, 2023

The dissertation committee for Jonathan William Owen certifies that this is the approved version of the following dissertation:

Real-Time Cognitive Sense-and-Notch Radar

_____

Dr. Shannon Blunt, Chairperson

Date Approved: May 11, 2023

Abstract

Spectrum sensing and transmit waveform frequency notching is a form of cognitive radar that seeks to reduce mutual interference with other spectrum users in a cohabitated band. With the reality of increasing radio frequency (RF) spectral congestion, radar systems capable of dynamic spectrum sharing are needed. The cognitive sense-and-notch (SAN) emission strategy is experimentally demonstrated as an effective way to reduce the interference that the spectrum sharing radar causes to other in-band users. The physical radar emission is based on a random FM waveform structure possessing attributes that are inherently robust to range-Doppler sidelobes. To contend with dynamic interference the transmit notch may be required to move during the coherent processing interval (CPI), which introduces a nonstationarity effect that results in increased residual clutter after cancellation. The nonstationarity effect, which otherwise distorts the range-Doppler estimation, is characterized and compensated for using computationally efficient processing methods. The steps from initial analysis of cognitive system performance to implementation of sense-and-notch radar spectrum sharing in real-time are discussed.

~ In loving memory of my mother ~

Acknowledgments

Foremost, I'd like to thank my advisor Dr. Shannon Blunt and the Radar Systems Laboratory (RSL) faculty including Dr. Chris Allen, Dr. Jim Stiles, and Dr. Patrick McCormick for their outstanding guidance. I offer thanks to my fellow graduate students, specifically Brandon Ravenscroft, Christian Jones, Daniel Herr, Charles Mohr, Lu Harnett, and Matthew Heintzelman, all of whom have entertained numerous crazy research ideas. Thank you to everyone at the Army Research Laboratory that supervised and assisted with the development of the cognitive spectrum sharing framework, especially Ben Kirk, Kelly Sherbondy, Anthony Martone, and Kyle Gallagher.

To my mother and father, your persistent love and encouragement made this journey possible and will be remembered always. To my siblings, I appreciate you being there for me. I am grateful to my friends and the Lawrence Tango community for keeping me sensible. Jennifer, thank you for being patient, caring, and kind during this undertaking.

This work was supported by the U.S. Army Research Office under grant # W911NF-15-2-0063 and by the Office of Naval Research under contract # N00014-16-C-2029

Journal Papers

1. R. J. Chang, C. C. Jones, **J. W. Owen** and S. D. Blunt, "Gradient-Based Optimization of Pseudo-Random PRI Staggering," IEEE Transactions on Radar Systems.
2. J. Quirk, R. Chang, **J. W. Owen**, S. D. Blunt, P. M. McCormick, "A Simple yet Effective Metric for Assessing Doppler Tolerance," IEEE Transactions on Radar Systems, vol. 1, pp 12-20, 2023.
3. A. F. Martone, K. Sherbondy, J. Kovarskiy, B. Kirk, R. Narayanan, C. Thornton, R. M. Buehrer, **J. W. Owen**, B. Ravenscroft, S. Blunt, A. Egbert, A. Goad, C. Baylis, "Closing the Loop on Cognitive Radar for Spectrum Sharing," IEEE Aerospace and Electronic Systems Magazine, vol. 36, no. 9, pp. 44-55, 1 Sept. 2021.
4. S. D. Blunt, J. Jakabosky, C. Mohr, P. McCormick, **J. W. Owen**, et al., "Principles and Applications of Random FM Radar Waveform Design," in IEEE Aerospace and Electronic Systems Magazine, vol. 35, no. 10, pp. 20-28, 1 Oct. 2020.
5. B. Ravenscroft, **J. W. Owen**, J. Jakabosky, S. D. Blunt, A. F. Martone, K. D. Sherbondy, "Experimental Demonstration and Analysis of Cognitive Spectrum Sensing & Notching for Radar," IET Radar, Sonar & Navigation, vol. 12, no. 12, pp. 1466-1475, December 2018.

Conference Papers

1. **J. W. Owen**, P. M. McCormick, C. Jones, S. Blunt, "On the Optimality of Spectrally Notched Radar Waveform & Filter Designs", 2023 IEEE Radar Conference, San Antonio, TX, 2023.
2. M. Heintzelman, **J. W. Owen**, S. Blunt, B. Maio, Eric Steinbach, "Practical Considerations for Optimal Mismatched Filtering of Nonrepeating Waveforms", 2023 IEEE Radar Conference, San Antonio, TX, 2023.
3. R. Chang, D. Herr, **J. W. Owen**, P. M. McCormick, S. Blunt, J. Stiles, "On the Relationship Between PRI Staggering and Sparse Arrays", 2023 IEEE Radar Conference, San Antonio, TX, 2023.
4. **J. W. Owen**, C. Mohr, B. Ravenscroft, S. Blunt, B. Kirk, A. Martone, "Real-Time Experimental Demonstration and Evaluation of Open-Air Sense-and-Notch Radar," IEEE Radar Conference, New York City, NY, March 2022.
5. C. Jones, Z. Gannon, D. DePardo, **J. W. Owen**, S.D. Blunt, C. Allen, B. Kirk, "Development & experimental assessment of robust direction finding and self-calibration," IEEE Radar Conference, New York City, NY, March 2022.
6. **J. W. Owen**, C. A. Mohr, B. H. Kirk, S. D. Blunt, A. F. Martone and K. D. Sherbondy, "Demonstration of Real-time Cognitive Radar using Spectrally-Notched Random FM Waveforms," 2020 IEEE International Radar Conference (RADAR), Washington, DC, USA, 2020.

7. C. A. Mohr, **J. W. Owen**, S. D. Blunt and C. T. Allen, "Zero-Order Reconstruction Optimization of Waveforms (ZOROW) for Modest DAC Rates," 2020 IEEE International Radar Conference (RADAR), Washington, DC, USA, 2020.
8. B. Ravenscroft, **J. W. Owen**, et al., "Experimental Assessment of Joint Range-Doppler Processing to Address Clutter Modulation from Dynamic Radar Spectrum Sharing," 2020 IEEE International Radar Conference (RADAR), Washington, DC, USA, 2020.
9. J. A. Kovarskiy, **J. W. Owen**, R. M. Narayanan, S. D. Blunt, A. F. Martone and K. D. Sherbondy, "Spectral Prediction and Notching of RF Emitters for Cognitive Radar Coexistence," 2020 IEEE International Radar Conference (RADAR), Washington, DC, USA, 2020.
10. A. F. Martone, K. Sherbondy, J. Kovarskiy, B. Kirk, C. Thornton, **J. W. Owen**, et al., "Metacognition for Radar Coexistence," 2020 IEEE International Radar Conference (RADAR), Washington, DC, USA, 2020.
11. A. F. Martone, K. Sherbondy, J. Kovariskiy, B. Kirk, **J. W. Owen**, et al., "Practical Aspects of Cognitive Radar," 2020 IEEE Radar Conference (RadarConf20), Florence, Italy, 2020.
12. **J. W. Owen**, B. Ravenscroft, S. D. Blunt, "Devoid Clutter Capture and Filling (DeCCaF) to Compensate for Intra-CPI Spectral Notch Variation," SEE International Radar Conference, Toulon, France, 23-27 Sep. 2019.
13. B. Ravenscroft, **J. W. Owen**, S. D. Blunt, A. F. Martone, K. D. Sherbondy, "Optimal Mismatched Filtering to Address Clutter Spread from Intra-CPI Variation of Spectral Notches," IEEE Radar Conference, Boston, MA, 22-26 Apr. 2019.
14. **J. W. Owen**, C. Mohr, S. D. Blunt, K. Gallagher, "Nonlinear Radar via Intermodulation of Jointly Optimized FM Noise Waveform Pairs," IEEE Radar Conference, Boston, MA, 22-26 Apr. 2019.
15. **J. W. Owen**, B. Ravenscroft, B. H. Kirk, S. D. Blunt, C. T. Allen, A. F. Martone, K. D. Sherbondy, R. M. Narayanan, "Experimental Demonstration of Cognitive Spectrum Sensing & Notching for Radar," IEEE Radar Conference, Oklahoma City, OK, 23-27 Apr. 2018.
16. B. H. Kirk, K. A. Gallagher, **J. W. Owen**, R. M. Narayanan, A. F. Martone and K. D. Sherbondy, "Cognitive software defined radar: A reactive approach to RFI avoidance," IEEE Radar Conference, Oklahoma City, OK, 23-27 Apr. 2018.
17. **J. W. Owen**, S. D. Blunt, K. Gallagher, P. McCormick, C. Allen and K. Sherbondy, "Nonlinear radar via intermodulation of FM noise waveform pairs," IEEE Radar Conference, Oklahoma City, OK, 23-27 Apr. 2018.

Honors and Awards

1. 1st Alternate in the Student Paper Competition (out of 84), First Author, for "On the Optimality of Spectrally Notched Radar Waveform & Filter Designs", 2023 IEEE Radar Conference
2. 1st Place in the Student Paper Competition (out of 71), First Author, for "Real-Time Experimental Demonstration and Evaluation of Open-Air Sense-and-Notch Radar", 2022 IEEE Radar Conference
3. 2nd Place in the Student Paper Competition (out of 71), Fourth Author, for "Development & experimental assessment of robust direction _nding and self-calibration", 2022 IEEE Radar Conference
4. The IET Radar, Sonar & Navigation Premium Award, Joint Author, for "Experimental demonstration and analysis of cognitive spectrum sensing and notching for radar", Volume 12, Issue 12, December 2018, p. 1466-1475
5. Army Research Laboratory Director's Commendation Award, 3rd place (out of 1000), 2019 CCDC-ARL Summer Student Symposium Competition
6. Army Research Laboratory SEDD Director's Commendation Award, 1st Place (out of 100), 2019 Sensors & Electron Devices Directorate (SEDD) Student Symposium Competition
7. 1st Alternative Top 5 Finalist in the Student Paper Competition, Second Author, for "Optimal Mismatched Filtering to Address Clutter Spread from Intra-CPI Variation of Spectral Notches", 2019 IEEE Radar Conference

Table of Contents

1. Chapter I: Fundamentals 1

1.1. Radar Objectives 1

1.2. Radar Transmission Modes 2

1.3. Radar Orientation 3

1.4. Radar Dimensions 4

1.4.1. Time-Frequency 5

1.4.1.1. Definitions 5

1.4.1.2. Review of Digital Signal Theory 6

1.4.1.3. Fast time versus Slow time 11

1.4.1.4. Definition of Baseband and Passband Frequency Representations 13

1.4.1.5. Amplifier Effects on Transmit Waveforms 16

1.4.1.6. Analog Upconversion 21

1.4.1.7. Digital Upsampling, Interpolation, & Upconversion 23

1.4.1.8. Digital Upsampling & Interpolation Methods 25

1.4.1.9. Analog Downconversion 29

1.4.1.10. Digital Hilbert Transform, Downconversion, & Downsampling 31

1.4.1.11. Sub-Nyquist Sampling 33

1.4.1.12. Phase Coherence 35

1.4.1.13. Review of Fourier Transformations 38

1.4.1.14. Parseval's Theorem and the L_p-norm 39

1.4.1.15. Additive White Gaussian Noise (AWGN) 40

1.4.2. Range 41
1.4.2.1. Electromagnetic Fundamentals 41
1.4.2.2. Received Scattering from a Stationary Scene 47
1.4.2.3. The Pulse Compression Matched Filter, Autocorrelation 50
1.4.2.4. The Least-Squares Mismatched Filter, Cross-correlation 59
1.4.2.5. Percent Bandwidth Definition (Narrowband, Wideband, Ultra-Wideband) 69
1.4.2.6. Waveform Types 69
1.4.2.6.1. Unmodulated Pulse (Sinusoidal Tones) 70
1.4.2.6.2. Chirp Waveforms 71
1.4.2.6.3. Phase Coded Waveforms & Angle Modulated Waveforms 73
1.4.2.6.4. Polyphase Coded Frequency Modulation (PCFM) 78
1.4.2.7. Range Ambiguities and Pulse Eclipsing 82
1.4.2.8. Signal-to-Noise Ratio, Pulse Compression Gain & Coherent Integration 83
1.4.2.9. Coherent Integration Range Sidelobe Reduction for Non-repeating Waveforms, Range Sidelobe Modulation (RSM) 85
1.4.3. Doppler Frequency 87
1.4.3.1. The Doppler Effect 87
1.4.3.2. The Ambiguity Function 89
1.4.3.3. Range-Doppler Processing, The Point Spread Function 91

2. Chapter II: Cognitive Radar and Spectrum Sharing 96

2.1. Spectrally Notched Radar Waveform Design 98
2.2. Experimental Emulation 101

2.2.1. Fast Spectrum Sensing (FSS) Algorithm 101
2.2.2. Cognitive Radar Emulation 103
2.2.3. Case 1: Stationary Interference 107
2.2.4. Case 2: Hopped Interference, No Latency 111
2.2.5. Case 3: Hopped Interference, 1 PRI Latency 113
2.2.6. Conclusions 115
2.3. Clutter Range Sidelobe Modulation Compensation 116
2.3.1. Devoid Clutter Capture and Filling 117
2.3.2. Case 4: Hopped Interference, No Latency, Clutter Filling by Temporally Adjacent Full-Band Waveforms 122
2.3.3. Case 5: Hopped Interference, No Latency, Clutter Filling by Temporally Adjacent Notched Waveforms 123
2.3.4. Conclusions 127
2.4. Notched Power Spectra for Optimal Sidelobe Reduction 128
2.4.1. Global Minimum Power Spectrum for Range Sidelobe Reduction 128
2.4.2. Global Minimum Power Spectrum for Range-Doppler Sidelobe Reduction 133
2.4.3. Application of Optimal Template for Spectral Shaping 141
2.4.4. Conclusions 146
2.5. Real Time Implementation of Sense-and-Notch Radar (Early Development) 147
2.5.1. Cognitive Spectral Notching on Software-Defined Radar 149
2.5.2. Implementation Considerations 153
2.5.3. Evaluation of Real-Time Operation 155
2.5.4. Conclusions 160

2.6. Real Time Implementation of Sense-and-Notch Radar (Late Development) 161

2.6.1. Reducing the Adaptation Latency..... 162

2.6.2. Real-Time Cognitive Sense-and-Notch Moving Target Indication..... 164

2.6.3. Conclusions..... 170

2.7. Final Remarks..... 170

3. References..... 171

4. Appendix..... 186

4.1. Table of Nonlinear FM waveforms 186

Table of Figures

Figure 1: Radar transmission modes 2

Figure 2: Illustration of radar orientations 4

Figure 3: Bandlimited sample rate frequency windows and temporal sinc basis functions 7

Figure 4: Discrete sampling of a continuous real signal with sinc reconstruction 8

Figure 5: Discrete sampling of a continuous complex signal with sinc reconstruction..... 10

Figure 6: Fast time versus slow time representation, with temporal duration definitions 12

Figure 7: Fast time-frequency representations of baseband signals versus passband signals. 13

Figure 8: Amplifier power operating curve 17

Figure 9: Nonlinear amplifier distortions simulated using the power series model and enforcing amplifier bandpass filtering effects 18

Figure 10: Analog upconversion RF chain 22

Figure 11: Analog upconversion stages 22

Figure 12: Digital upsampling, interpolation, and upconversion chain 24

Figure 13: Digital upsampling, interpolation and upconversion stages 24

Figure 14: Stages of temporal interpolation and phase interpolation 27

Figure 15: Temporal and phase interpolation methods 28

Figure 16: Analog downconversion RF chain 30

Figure 17: Analog downconversion stages 30

Figure 18: Digital Hilbert transform, downconversion, and downsampling chain..... 32

Figure 19: Digital Hilbert transformation, downconversion, & downsampling stages 32

Figure 20: Combined analog downconversion RF chain and sub-Nyquist sampling..... 34

Figure 21: Combined analog downconversion and sub-Nyquist sampling stages 34

Figure 22: Types of radar coherence errors 37

Figure 23: Summary of Fourier methods..... 38

Figure 24: Spherical coordinate system electromagnetic definitions 43

Figure 25: Generalized coordinate system electromagnetic definitions 45

Figure 26: Ideal superposition of multiple equidistant scatterer reflections..... 48

Figure 27: Relationship between autocorrelation and power spectrum, time-bandwidth product gain, and fast time pulse compressed resolution..... 55

Figure 28: Various autocorrelation responses and power spectrum shapes 56

Figure 29: The dangers of autocorrelation sidelobes..... 57

Figure 30: Nonideal versus ideal autocorrelation, and bandlimited versus band-unlimited power spectra, related by the Fourier transform. 58

Figure 31: Illustration of least squares regression optimization to achieve a desired cross-correlation response 64

Figure 32: Example correlation responses and power spectra, when the least squares filter is applied to the bandlimited signal to achieve super-resolution 66

Figure 33: Example correlation responses and power spectra, when the least squares filter formed with regularization is applied to the bandlimited signal to achieve super-resolution 67

Figure 34: Example correlation responses and power spectra, when the least squares filter formed with beamspoiling is applied to the bandlimited signal. Super-resolution is waived in trade to mitigate mismatch loss and improve the sidelobe level performance 68

Figure 35: Unmodulated sinusoidal waveform in fast time-frequency 70

Figure 36: Various nonlinear FM waveform power spectra, autocorrelations, and instantaneous frequencies 72

Figure 37: Amplitude envelopes and power spectra of phase coded waveforms having uniformly distributed phase chips applying either the rectangular or sinc temporal shaping filter 74

Figure 38: Power spectrum of a phase coded waveform and an angle modulated waveform, after applying the rectangular temporal shaping filter 75

Figure 39: Various randomly initialized PRO-FM waveforms power spectra, autocorrelations, and instantaneous frequencies 77

Figure 40: Relationship between the rectangular frequency shaping filter and the ramp phase shaping filter 79

Figure 41: Mean power spectrum of $P = 1000$ unoptimized PCFM waveforms for upsampling factors $\beta_\alpha = 2, 4, 8$ 80

Figure 42: Various unoptimized PCFM waveforms power spectra, autocorrelations, and instantaneous frequencies 81

Figure 43: Range Unambiguous, Ambiguous, and Eclipsed Returns. 82

Figure 44: Coherent integration across P pulse compressed, identical LFM chirp waveforms with AWGN present. 84

Figure 45: Sidelobe reduction from coherently integrating non-identical PROFM autocorrelations, with no AWGN present. 86

Figure 46: Ambiguity function of an up-chirped LFM waveform and a PROFM waveform 90

Figure 47: Point spread functions of LFM waveforms and PROFM waveforms for $P = 100$ pulse repetition intervals. 95

Figure 48: Perception-action cycle (PAC) concept for radar 96

Figure 49: Experimental measurements of PRO-FM waveforms, designed with or without a spectral null collocated with observed OFDM interference. 98

Figure 50: The coherently averaged waveform autocorrelations and mean waveform power spectra for 2500 full-band PROFM and 2500 spectrally notched PROFM waveforms, transmitted on an arbitrary waveform generator and received on a real-time spectrum analyzer 100

Figure 51: FSS-determined occupied and unoccupied sub-bands for two OFDM signals 102

Figure 52: Example power spectra of measured OFDM interference, spectrally notched PROFM (adapted using FSS), and full-band PROFM waveforms 104

Figure 53: Experimental timing diagram for the single contiguous RFI band scenario 105

Figure 54: Experimental timing diagram for the two disjoint contiguous RFI bands scanario .. 105

Figure 55: Open-air hardware setup 107

Figure 56: Range-Doppler plot of full-band PRO-FM with no injected RFI, intended as the baseline comparison, Case 1 107

Figure 57: Range-Doppler plot of notched PRO-FM with no injected RFI, possessing a stationary spectral notch, Case 1. 108

Figure 58: Range-Doppler plot of full-band PROFM with injected stationary RFI, Case 1. 109

Figure 59: Range-Doppler plot of notched PROFM with injected stationary RFI, Case 1. 109

Figure 60: Range-Doppler plot of full-band PRO-FM with no injected RFI, intended as the baseline comparison, Case 2 111

Figure 61: Range-Doppler plot of notched PRO-FM with no injected RFI, possessing a spectral notch hopped every four PRIs, Case 2. 111

Figure 62: Range-Doppler plot of notched PROFM with injected frequency hopping RFI, reacting with no adaptation latency, Case 2. 112

Figure 63: Range-Doppler plot of full-band PRO-FM with no injected RFI, intended as the baseline comparison, Case 3. 113

Figure 64: Range-Doppler plot of notched PRO-FM with no injected RFI, possessing a spectral notch hopped every four PRIs, Case 3. 113

Figure 65: Range-Doppler plot of full-band PROFM with injected frequency hopping RFI, reacting with adaptation latency T_{PRI}, Case 3. 114

Figure 66: Loopback measured spectra for a full-band waveform, a notched waveform, and a BPF version of the full-band waveform..... 119

Figure 67: Timing diagram of the waveform arrangement used for experimental evaluation of DeCCaF. Full-band and notched waveforms are interleaved, with the borrowed clutter taken from an adjacent full-band response..... 120

Figure 68: Range-Doppler plot of full-band PRO-FM with no injected RFI, intended as the baseline comparison, applying the matched filter to the single notch data collect..... 121

Figure 69: Measured range-Doppler response from 2500 PRO-FM waveforms with dynamic spectral notches, applying the matched filter and least squares mismatched filter, for the single notch data collect. 121

Figure 70: Measured range-Doppler response from 2500 PRO-FM waveforms with dynamic spectral notches, applying interleaved & spectrally-filtered full-band responses for clutter filling via the matched filter & DeCCaF or the mismatched filter & DeCCaF..... 122

Figure 71: Timing diagram of the waveform arrangement used to evaluate the operationally useful form of DeCCaF. The borrowed clutter is taken from temporally adjacent, spectrally non-overlapping notched responses..... 124

Figure 72: Measured range-Doppler response from 2500 PRO-FM waveforms with dynamic spectral notches, applying adjacent spectrally-filtered notched waveform responses for clutter filling via the matched filter & DeCCaF or the mismatched filter & DeCCaF..... 125

Figure 73: Mean power spectra of the matched filtered range profile estimate over the given CPI for Case 1 (full-band) and Case 2 (notched without clutter filling). The mean compensated range profile estimate after applying DeCCaF for Case 5 (notched, clutter filling with other notched responses) is quite similar the full-band response. 126

Figure 74: Power spectra of the matched filtered range profile estimate for the pth pulse before applying DeCCaf and the compensated range profile estimates after applying DeCCaF 127

Figure 75: Optimum desired power spectrum templates and autocorrelation responses with minimized autocorrelation ISL according to (6.13), for 40 dB spectral null and varied beamspoiling ratios of 1%, 2%, 4%, 6% relative to total window length 130

Figure 76: Optimum desired power spectrum templates and autocorrelation responses with minimized autocorrelation ISL according to (6.13), for 40 dB spectral nulls (at different locations) and beamspoiling ratio of 2% relative to total window length. 131

Figure 77: Optimum desired power spectrum templates and autocorrelation responses with minimized autocorrelation PSL $\mathscr{p} = 8$ according to (6.14), for 40 dB spectral null and varied beamspoiling ratios of 1%, 2%, 4%, 6% relative to total window. 132

Figure 78: Optimum desired power spectrum template set and point spread function responses with minimized point spread function ISL $\mathscr{p} = 2$ according to (6.18), for 40 dB spectral nulls and enforcing the 2% range beamspoiling ratio relative to the window length M_{d} and 4% Doppler beamspoiling ratio relative to the number of pulses P. The spectral notches are stationary across all pulses. 135

Figure 79: Desired power spectrum set and point spread function responses with minimized autocorrelation ISL $\mathscr{p} = 2$ determined on a per-pulse basis according to (6.14), for 40 dB spectral nulls and enforcing the 2% range beamspoiling ratio relative to the window length M_{d}. The spectral notches are stationary across all pulses. 136

Figure 80: Optimum desired power spectrum template set and point spread function responses with minimized point spread function ISL $\mathscr{p} = 2$ according to (6.18), for 40 dB spectral nulls and enforcing the 2% range beamspoiling ratio relative to the window length M_{d} and 4% Doppler beamspoiling ratio relative to the number of pulses P. The spectral notches drift slowly across pulses in a semi-deterministic pattern. 137

Figure 81: Desired power spectrum set and point spread function responses with minimized autocorrelation ISL $\mathscr{p} = 2$ determined on a per-pulse basis according to (6.14), for 40 dB spectral nulls and enforcing the 2% range beamspoiling ratio relative to the window length M_{d}. The spectral notches drift slowly across pulses in a semi-deterministic pattern. RSM appears in the zero-range cut due to slow time spectral deviations. 138

Figure 82: Optimum desired power spectrum template set and point spread function responses with minimized point spread function ISL $\mathscr{p} = 2$ according to (6.18), for 40 dB spectral nulls and enforcing the 2% range beamspoiling ratio relative to the window length M_{d} and 4% Doppler beamspoiling ratio relative to the number of pulses P. The spectral notch randomly hops within the radar operational band over the CPI 139

Figure 83: Desired power spectrum set and point spread function responses with minimized autocorrelation ISL $\mathscr{p} = 2$ determined on a per-pulse basis according to (6.14), for 40 dB spectral nulls and enforcing the 2% range beamspoiling ratio relative to the window length M_{d}. The spectral notch randomly hops within the radar operational band over the CPI. 140

Figure 84: Notched PRO-FM mean PSD and coherently averaged autocorrelation from applying an ad-hoc tapered spectral template determined via (6.2) and (6.3) 143

Figure 85: Notched PRO-FM mean PSD and coherently averaged autocorrelation from applying the least-squares optimal spectral template that minimizes autocorrelation ISL determined via (6.14). 144

Figure 86: Notched PRO-FM mean PSD and coherently averaged autocorrelation from applying an ad-hoc taperedspectral template determined via (6.2) and (6.3). The coherently averaged LS-MMF cross-correlations are shown along with their mean cross-power spectrum 145

Figure 87: Notched PRO-FM mean PSD and coherently averaged autocorrelation from applying the LS optimal spectral template determined via (6.14). The coherently averaged LS-MMF cross-correlations are shown along with their mean cross-power spectrum..... 146

Figure 88: Mean power spectra of PRO-FM / ZOROW waveform sets for a central notch location spanning 10% of the band after $K = 2$ PRO-FM iterations and $Q = 6 \text{ and } 1000$ ZOROW iterations 152

Figure 89: Comparison of cost-function (2.23) minimization for various gradient-descent methods 153

Figure 90: Cognitive radar architecture on the SDR during Early Development..... 153

Figure 91: Timing diagram of SAN cognitive radar adjusting a spectral notch location to coincide with dynamic RFI with adaptation latency..... 154

Figure 92: Spectrum capture showing three tonal interferers and the SAN radar spectrum with collocated notches, Case 1..... 156

Figure 93: Waterfall spectrogram versus time for RFI comprised of three stepped tones and the SAN radar spectrum with notches, where the RFI changes every 15 ms, Case 1a..... 157

Figure 94: Waterfall spectrogram versus PRI time for RFI comprised of three stepped tones and the SAN radar spectrum with notches, where the RFI changes every 5 ms, Case 1b..... 158

Figure 95: Waterfall spectrogram versus PRI time for RFI comprised of three 5 MHz bands of OFDM subcarriers and the SAN radar spectrum with notches, where the RFI changes every 15 ms, Case 2 159

Figure 96: Waterfall spectrogram versus PRI time for RFI comprised of one 40 MHz band of OFDM subcarriers and the SAN radar spectrum with notches, where the RFI changes every 15 ms, Case 3 160

Figure 97: Cognitive radar architecture on the SDRadar during Late Development 163

Figure 98: Test setup overview, with sense-and-notch radar and dynamic interferer 164

Figure 99: Open-air test setup: Ettus x310 SDRadar and illuminated traffic intersection 164

Figure 100: Open-air test setup: interference source 165

Figure 101: Range-Doppler plot of full-band PRO-FM without RFI, intended as the baseline comparison. All radar operations are performed in real-time via the SDRadar. 166

Figure 102: Range-Doppler plot of full-band PRO-FM with stationary RFI, intended as the baseline comparison. All radar operations are performed in real-time via the SDRadar. 167

Figure 103: Range-Doppler plot for sense-and-notch PRO-FM with stationary RFI. All radar operations are performed in real-time via the SDRadar. 167

Figure 104: Range-Doppler plot for sense-and-notch PRO-FM with RFI hopping every 50ms. All radar operations are performed in real-time via the SDRadar. 168

Figure 105: Range-Doppler plot for sense-and-notch PRO-FM with RFI hopping every 10ms. All radar operations are performed in real-time via the SDRadar. 169

Figure 106: Range-Doppler plot for sense-and-notch PRO-FM with RFI hopping every 0.6ms. All radar operations are performed in real-time via the SDRadar. 169

Introduction

The pace of increasing spectral congestion creates a major challenge for radar systems, with traditional spectrum allocations inadequately supporting the competing demands for greater bandwidth [1-5]. The position of the US DoD Chief Information Officer is "spectrum sharing is the way ahead to maintain economic dominance" [6]. Consequently, radar spectrum sharing techniques are necessary to preserve acceptable performance amidst other active RF users. Of course, depending on the particular manner of spectrum sharing, potential pitfalls may exist [7]. Growing RF congestion represents a transition from the era of noise-limited legacy radar to interference-limited operation. When in-band RF interference (RFI) is dynamically changing during the radar's coherent processing interval (CPI), one way this condition can be addressed is by enabling the radar to become similarly dynamic.

Cognitive radar, also known as fully adaptive radar, attempts to improve performance and efficiency by "learning" from a priori observations to supplement decision making from low-level (e.g., waveform selection/design) up to high-level tasks (e.g., mission-level command and control) [4]. The most common forms of cognitive radar in the literature include optimization/selection of transmit parameters, waveforms, or filters [8-11]). Due to increasing spectral congestion and competition [1], an important topic of research is the use of cognition in a spectrum sharing context [12] to modify the radar transmission according to sensed RF interference (RFI) in the band of interest. Essentially, these efforts are working to develop "good spectral neighbor" capabilities for the radar by mitigating the mutual interference to/from other spectrum users. The particular focus here is on the automated generation of physically realizable waveforms that possess spectral notches to avoid in-band interference. Such a condition is expected to become more problematic with the continued proliferation of 4G and 5G communication systems into radar bands.

The notion of spectrally notching radar waveforms as a means of radio frequency interference (RFI) avoidance has been considered by many, with a recent survey from an optimization theory perspective appearing in [13]. While the majority of such approaches involve spectral notching of a single waveform, or by extension the same waveform over the CPI, it was shown in [14] that doing so incurs a rather significant penalty in terms of increased radar range sidelobes. However, it was recently experimentally demonstrated that the spectral notching of random

FM waveforms partially avoids this limitation because the incoherent combining of range sidelobes across multiple unique pulsed waveforms in the coherent processing interval serves to reduce the resulting sidelobe level. Here, the random FM waveform spectral notching capability is incorporated into a cognitive radar framework that performs spectrum sensing on a per-pulse basis, estimates the spectral properties of any in-band interference, and then adjusts the notch locations and widths in an automated manner. For interference taking the form of frequency hopping OFDM communications, this overall cognitive strategy employs RFI sensing updates to inform the subsequent notching of random FM waveforms, with the ultimate goal of achieving real-time RFI avoidance.

The remainder of the document is parsed into two chapters. The former section discusses radar fundamentals that are key to understanding the behavior of spectrally notched waveform and filter design in the context of pulse-Doppler radar processing. Topics include hardware considerations for waveform design and experimental evaluation, the basics of radar electromagnetic modeling, waveform design theory in the context of correlation-based range processing, and slow time-Doppler processing considerations. From these fundamentals, important insights about the anticipated behaviors of the sense-and-notch cognitive radar performance are drawn.

The latter chapter regards multiple aspects of the cognitive sense-and-notch frameworks, wherein random FM waveforms are spectrally notched in reaction to the observed interference. In Section 2.1, relevant waveform design methods with incorporated spectral nulls are described. In Section 2.2, the spectrum sharing approach is evaluated via emulation in a semi-controlled environment for experimental evaluation. Section 2.3 evaluates an ad hoc post-processing technique to compensate for the clutter modulation distortion effect that occurs when dynamic spectral notches are present during the radar coherent processing interval. The fundamental dynamic range limitations while performing range correlation processing or joint range correlation processing and slow time-Doppler processing with spectrally notched waveform/filter designs are examined in Section 2.4. Finally, both Sections 2.5 and 2.6 examine design tradeoffs and considerations for real-time implementation of cognitive sense-and-notch radar for moving target indication (MTI) during different stages of development. The topics covered here extend from initial experimentation and fundamental theory, through to real-time implementation and development of cognitive sense-and-notch radar performance.

1. CHAPTER I: FUNDAMENTALS

Radar technology is used for weather forecasting, autonomous vehicle operation, space observation, defense surveillance, medical imaging, and more. Radar systems consist of transmitters that emit electromagnetic waves and receivers that capture the waves scattered from a given physical environment. Attributes of scatterers are then determined based on the received wave characteristics. Four fundamental perspectives are considered here, including the radar 1) objective, 2) transmission mode, 3) orientation, and 4) dimensions. The fundamental background provides necessary radar systems and digital signal processing groundwork. Upon these fundamentals, aspects of radar spectrum sharing are explored.

1.1. RADAR OBJECTIVES

The objective defines the intended output measurements of the radar. Standard radar objectives include target detection, indication (or localization), tracking, classification (or identification), and imaging. Subtle differences exist between each objective:

A) Detection determines whether a target is present but does not necessarily resolve target attributes of range, velocity, and spatial angle.

B) Indication (or localization) determines whether a target is present, and additionally resolves target attributes of range, velocity, and spatial angle.

C) Tracking determines whether a target is present, resolves target attributes of range, velocity, and spatial angle, and predicts the target's future location based on prior observations. Parameters of the antennae or platform motion adjust to maintain target observation.

D) Classification (or identification) determines the type of target present (e.g. drone versus bird) based on target-specific scattering signatures.

E) Imaging forms a picture of the target for visual interpretation by a human or machine.

Application-specific objectives include nonlinear target detection [15], moving target indication (MTI) [16], monopulse tracking [17, 18], micro-Doppler (MD) motion classification [19], synthetic aperture radar (SAR) imaging [20, 21] or single-pulse imaging (SPI) [22]. Applications are constrained by implicit platform/target motion, scene-specific clutter/interference, and the degree of resolution required in various dimensions. Through-the-wall (TTW) radar [23, 24], sea-observation radar [25, 26], over-the-horizon (OTH) radar [27], and foliage/ground penetration (FOPEN/GPR) radar [28] contend with scene-specific clutter.

1.2. RADAR TRANSMISSION MODES

The transmission mode describes how the environment is illuminated electromagnetically for observation of subsequent scattering. Active radar systems may transmit continuous wave (CW) or pulsed wave emissions in a desired direction. Reflections from pulsed emissions can be processed on a single-pulse (e.g. SPI) or multi-pulse (e.g. SAR) basis, depending on the radar objective. The user may wish to remain silent and instead operate in a passive radar mode, utilizing emissions from other radio frequency (RF) users in the environment that then scatter from targets of interest towards the radar receiver.

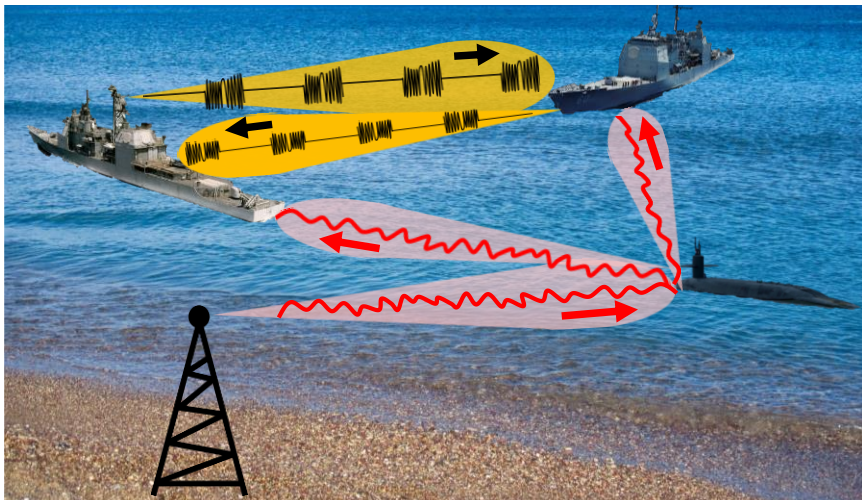

Figure 1: Radar transmission modes: The leftmost ship transmits active, multi-pulse emissions (yellow) towards other ships, which reflect and are captured for localization. The communications radio tower (which is agnostic of the ships) transmits CW waves (red), which reflect off a nearby surfaced submarine. Both ships passively receive the reflected waves and process them to detect the submarine.

1.3. RADAR ORIENTATION

The orientation describes the positions of transmitters and receivers relative to one another. Various potential radar orientations are illustrated in Figure 2. Monostatic radar describes an orientation where a single transmitter and receiver are collocated and may (but need not) share the same antennae for electromagnetic transconductance via a microwave switch or circulator [29]. Monostatic radar processing is the least demanding with regards to scene geometry modeling and system synchronization, relying on electromagnetic wave backscattering phenomenology for target observation. Bistatic radar describes an orientation where a single transmitter and receiver are physically separated by a considerable distance. Bistatic orientation implies complex scene geometry, relying on electromagnetic wave backward and forward scattering phenomenology. Location, motion, and oscillator frequency of the transmitter and receiver must be jointly considered during radar processing to achieve phase coherence. Multistatic radar is an extension of bistatic radar, wherein multiple transmitters and receivers are distributed throughout the environment. Bistatic and multistatic radar are often referred to as distributed radar.

Multiple-input multiple-output (MIMO) radar characteristically has spatially diverse emissions that provide an enhanced spatial resolution capability [30, 31]. MIMO radar encompasses any radar orientation that applies spatial beamforming with multiple antenna elements to provide a spatial resolution enhancement [30]. MIMO radar encompasses both distributed radar techniques [31] and non-distributed transmit/receive array processing methods [32]. In contrast, simultaneous multifunction radars utilize emissions comprised of multiple antenna elements to execute multiple functions *without* necessarily achieving a spatial resolution improvement [30]. Other forms of simultaneous multifunction radar do not take advantage of antenna spatial orientation to achieve multiple objectives, but instead splice the “multifunction” aspect into radar dimensions such as the fast time-frequency spectrum [33-35].

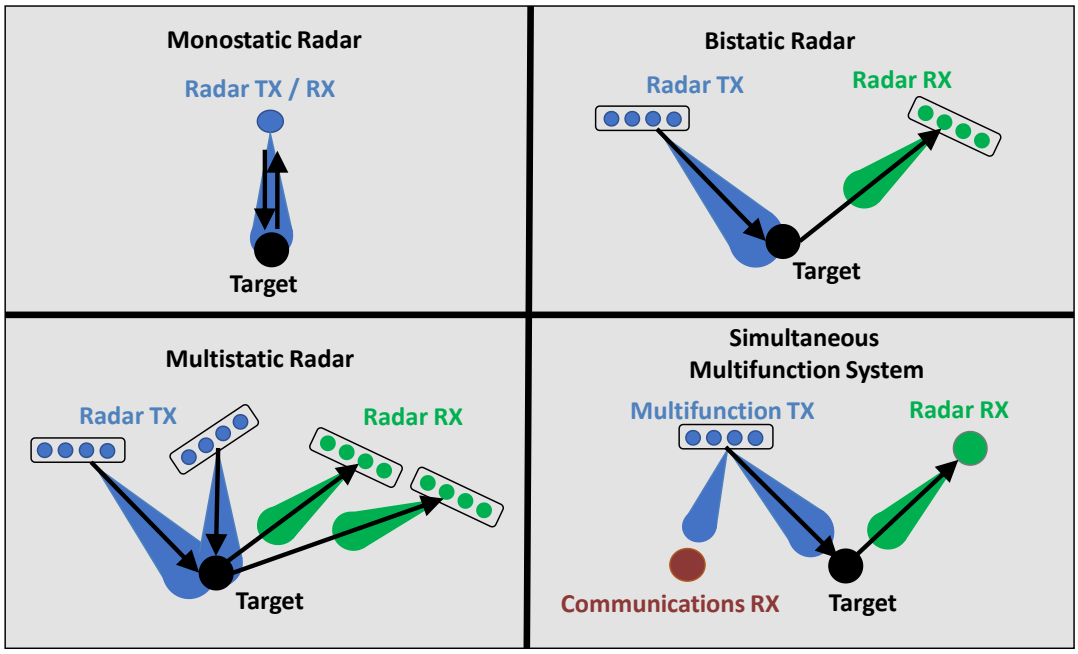

Figure 2: Illustration of radar orientations. Circles represent antennas, blocks of circles represent beamforming antenna arrays.

1.4. RADAR DIMENSIONS

The dimensions of the radar system describe which mathematically modeled phenomena are exploited to achieve the desired objective. Standard dimensions in radar systems include fast time-frequency, range, slow time-frequency (Doppler), polarization, and space. Distinctions are made between each dimension for system modeling and optimization purposes. Model representation is critical to successfully optimize a desired objective [36]. Non-traditional dimensions have likewise been examined (see [37-39]).

Radar phenomenology is described by continuous or discrete models. Continuous dimensions are modeled around reality-driven physical behaviors, which are sampled to obtain discrete dimensions. For example, the continuous time signal $s(t)$ sampled every T_s seconds for N samples forms the discrete time signal $s(nT_s)$ for $n \in [0 \cdots N-1]$, described by the discrete vector $\mathbf{s} = [s_1 \cdots s_N]^T$. Continuous and discrete models are described hereafter for standard radar dimensions.

1.4.1. TIME-FREQUENCY

1.4.1.1. DEFINITIONS

The time dimension is defined in terms of how modulated electromagnetic waves are A) received, recorded, & processed or B) designed, stored, & transmitted.

A) To observe the electromagnetic environment on receive, variations of the environment over time are captured by an antenna at a probe point in space. The microwave system intended to record and process the signals over time operates with either analog or digital procedures. An analog receive chain will process the captured waves in the continuous dimension; the waves are physically processed near the speed of light using filters, mixers, lenses, slits, and other analog transforms to yield pertinent material information for the given objective. Some legacy radar systems exclusively used analog receive processing for objectives such as SAR imaging, but such systems are expensive, lack reconfigurability, and lie prone to machine miscalibration [16]. Digital receive chains use analog-to-digital converters (ADCs) to sample continuous waves at set time intervals and record the measured samples for subsequent digital processing. Due to the limitations of ADC precision and sample rates relative to higher costs, modern radar systems use a hybrid of analog signal conditioning and digital processing to capture a signal of interest from the electromagnetic spectrum.

B) Transmit electromagnetic waves are designed within an analog or digital transmit chain for controlled antenna emission into the RF environment. While transmit waveform characteristics can be modulated using analog devices such as surface acoustic wave (SAW) structures [40], modern systems typically design in a discrete dimension that subsequently translates to the continuous dimension using a digital-to-analog converter (DAC) to achieve more precise modulation and dynamic waveform generation capability [41]. The DAC analog output is then additionally modulated using analog components such as mixers, filters, and amplifiers to create an electromagnetic wave at the desired frequency, bandwidth, and transmit power in the band of system operation.

1.4.1.2. REVIEW OF DIGITAL SIGNAL THEORY

A brief review of digital signal theory is presented for subsequent relation to the transmit and receive design considerations for radar operation. If a continuous signal has a given maximum frequency $f_{\max}$ dictated by the distance between sinusoidal component peaks, the Nyquist sampling theorem in (1.1) states that the uniform sample rate capturing measurements must be at least twice the maximum frequency of the continuous *bandlimited* signal being captured for subsequent perfect signal reconstruction.

$$f_s \geq 2f_{\max} \tag{1.1}$$

Upon capturing an electromagnetic wave impinged on an antenna and temporally sampling at uniform intervals of nT_s for a given sample frequency $f_s = \frac{1}{T_s}$ where $n \in \{0, 1, \dots, N-1\}$, the time sampling process imposes rectangular bounds in the frequency dimension in the set $f \in \left[-\frac{f_s}{2}, \frac{f_s}{2}\right)$. The rectangular frequency window restricted by the sampling process implies an assumption by Fourier definition that the continuous time dimension signal is composed of time-shifted sinc basis functions (as is only completely true for perfectly frequency bandlimited signals [42]). The sinc function is defined as $\mathrm{sinc}(t) = \frac{\sin(\pi t)}{\pi t}$. The relationship between normalized frequency sample rate bounds and their corresponding implied sinc basis functions is illustrated in Figure 3. The critical Nyquist sampling rate is defined as $f_s^{\text{Nyquist}} = 2f_{\max}$.

The Nyquist theorem can be understood intuitively from a time-dimension perspective by illustrating the attempted sinc reconstruction of a real continuous signal when sampled below, meeting, or exceeding the Nyquist sample rate, shown in the left column of Figure 4. Note that the signal being reconstructed is not truly bandlimited, but the Nyquist rate is chosen to be twice the maximum frequency 3-dB power of the signal. Reconstruction is performed using the Whittaker-Shannon interpolation theorem shown in (1.2). The sinc interpolation theorem describes the method by which Fourier sinc basis functions are used to reconstruct the continuous signal structure from a sampled bandlimited signal via discrete convolution.

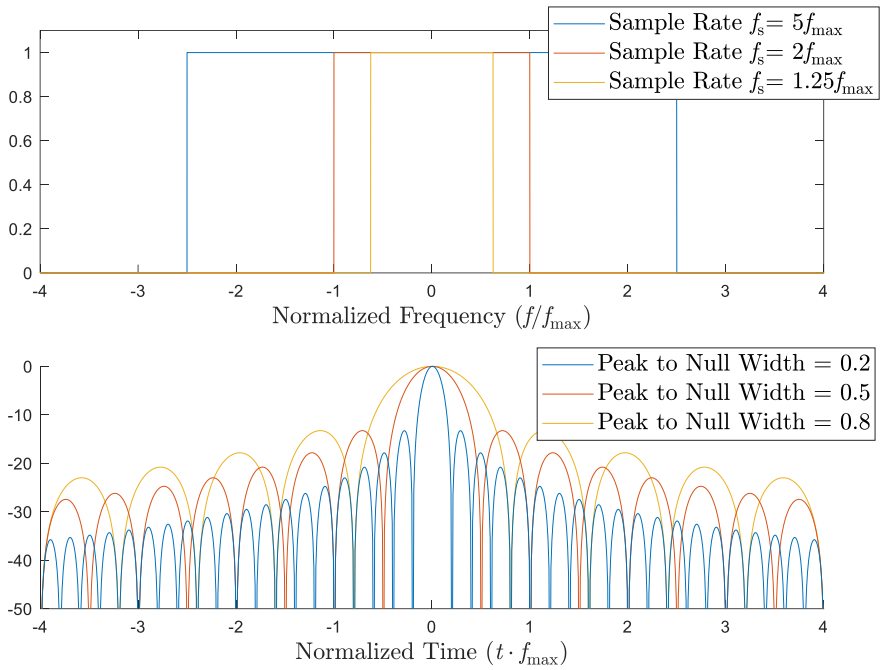

Figure 3: Varied bandlimited sample rate windows in the frequency dimension (top) and the implied time dimension sinc basis functions assumed to compose any continuous signal within the bandlimited frequency window (bottom).

$$s(t) = \sum_{n=-\infty}^{\infty} s(nT_s)\,\mathrm{sinc}\left(\frac{t - nT_s}{T_s}\right) \tag{1.2}$$

The frequency dimension of each reconstructed signal is shown in the right column of Figure 4. When a continuous signal is not sampled at sufficiently frequent time intervals according to the Nyquist sample rate, the continuous signal structure cannot be reconstructed without error. Here, f_{max} is selected as the highest frequency indicating a 3-dB power drop-off. The error introduced by sampling a bandlimited signal below the Nyquist rate $f_s < 2f_{max}$ is referred to as aliasing and is shown in the bottom plots of Figure 4. When sampling below the Nyquist rate, the signal is improperly reconstructed. Even when the Nyquist rate is roughly met by $f_s = 2f_{max}$ the signal is not perfectly reconstructed because the original signal is not perfectly bandlimited in the frequency dimension. The reconstruction error is minimized, but not completely eliminated, only when the signal is oversampled $f_s \gg 2f_{max}$.

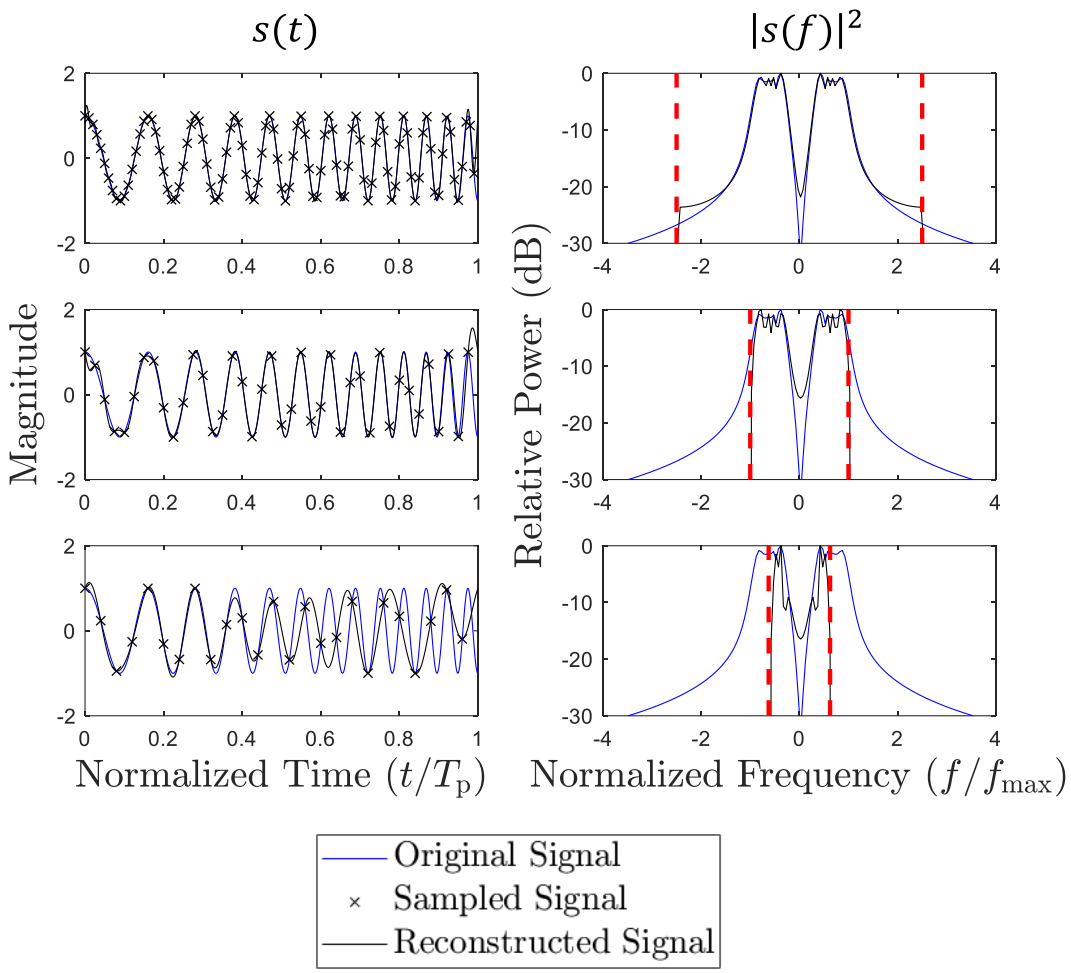

Figure 4: Discrete sampling of a continuous real signal of duration T_p with sinc reconstruction (left column) and the frequency dimension of the continuous and reconstructed signals (right column). Here $f_\mathrm{s} = 5f_\mathrm{max} \gg f_\mathrm{s}^{\mathrm{Nyquist}}$ (top row), $f_\mathrm{s} = 2f_\mathrm{max} = f_\mathrm{s}^{\mathrm{Nyquist}}$ (middle row), $f_\mathrm{s} = 1.25f_\mathrm{max} < f_\mathrm{s}^{\mathrm{Nyquist}}$ (bottom row).

The fundamental relationship between real and complex signal notation is often overlooked. Only real signals exist in the physical world. Rather, complex notation captures two orthogonal basis components of a real modulated signal. Each basis component represents entirely unique information due to the orthogonality of the cosine and sine functions over all time t. Any physical signal can be represented as

$$A(t)\cos\big(\omega_\mathrm{c}t + \phi(t)\big) = A(t)\cos\big(\phi(t)\big)\cos(\omega_\mathrm{c}t) - A(t)\sin\big(\phi(t)\big)\sin(\omega_\mathrm{c}t)$$
$$= s_\mathrm{I}(t)\cos(\omega_\mathrm{c}t) - s_\mathrm{Q}(t)\sin(\omega_\mathrm{c}t)\,, \tag{1.3}$$

and can therefore be represented by the summation of two scaled basis components corresponding to the unique information captured in $\cos(\omega_c t)$ and $\sin(\omega_c t)$, where $\omega_c = 2\pi f_c$. Euler's identity maps the orthogonal basis functions cosine and sine to an in-phase & quadrature (I/Q) representation, commonly illustrated by the complex unit circle. That is

$$A(t)e^{j\phi(t)} = A(t)\cos\big(\phi(t)\big) + jA(t)\sin\big(\phi(t)\big) = s_I(t) + j\, s_Q(t)\,. \tag{1.4}$$

The I/Q representation can demonstrate relationships including $A(t) = \sqrt{s_I^2(t) + s_Q^2(t)}$ and $\phi(t) = \operatorname{atan}\left(\frac{s_Q(t)}{s_I(t)}\right)$. When $s_I(t)$ and $s_Q(t)$ arbitrarily scale their respective basis components $\cos(\omega_c t)$ and $\sin(\omega_c t)$ as in (1.3), the amplitude and phase of the constructed signal $A(t)\cos\big(\omega_c t + \phi(t)\big)$ are determinable from $s_I(t)$ and $s_Q(t)$. To enforce a signal to have constant amplitude $(A(t) = A_0\ \forall\ t)$, the basis components $s_I(t)$ and $s_Q(t)$ must be orthogonal $s_I(t) = A_0^2\cos\big(\phi(t)\big)$ and $s_Q(t) = A_0^2\sin\big(\phi(t)\big)$ such that $A(t) = A_0\sqrt{\cos^2\big(\phi(t)\big) + \sin^2\big(\phi(t)\big)} = A_0$.

The imaginary number j is not truly "imaginary", but rather is a mathematical definition that allows tracking the degree to which a modulated signal is composed of either the orthogonal basis functions cosine or sine. Carl Friedrich Gauss said "That this subject [imaginary numbers] has hitherto been surrounded by mysterious obscurity, is to be attributed largely to an ill adapted notation. If, for example, +1, -1, and $\sqrt{-1}$ had been called direct, inverse and lateral units, instead of positive, negative and imaginary, such an obscurity would have been out of the question." Note that for purely real signals as shown in Figure 4, the frequency information is double-sided (symmetric about zero) because information pertaining to the cosine basis function is considered and information pertaining to the sine basis function is not considered (i.e. half the information has been disregarded by not capturing the unique information mapped from the orthogonal sine component of the signal). When a complex signal that captures both the sine and cosine phase basis function information is reconstructed in Figure 5 with temporal sinc basis functions according to (1.2), the real and imaginary portions of the signal experience similar error as that shown in Figure 4.

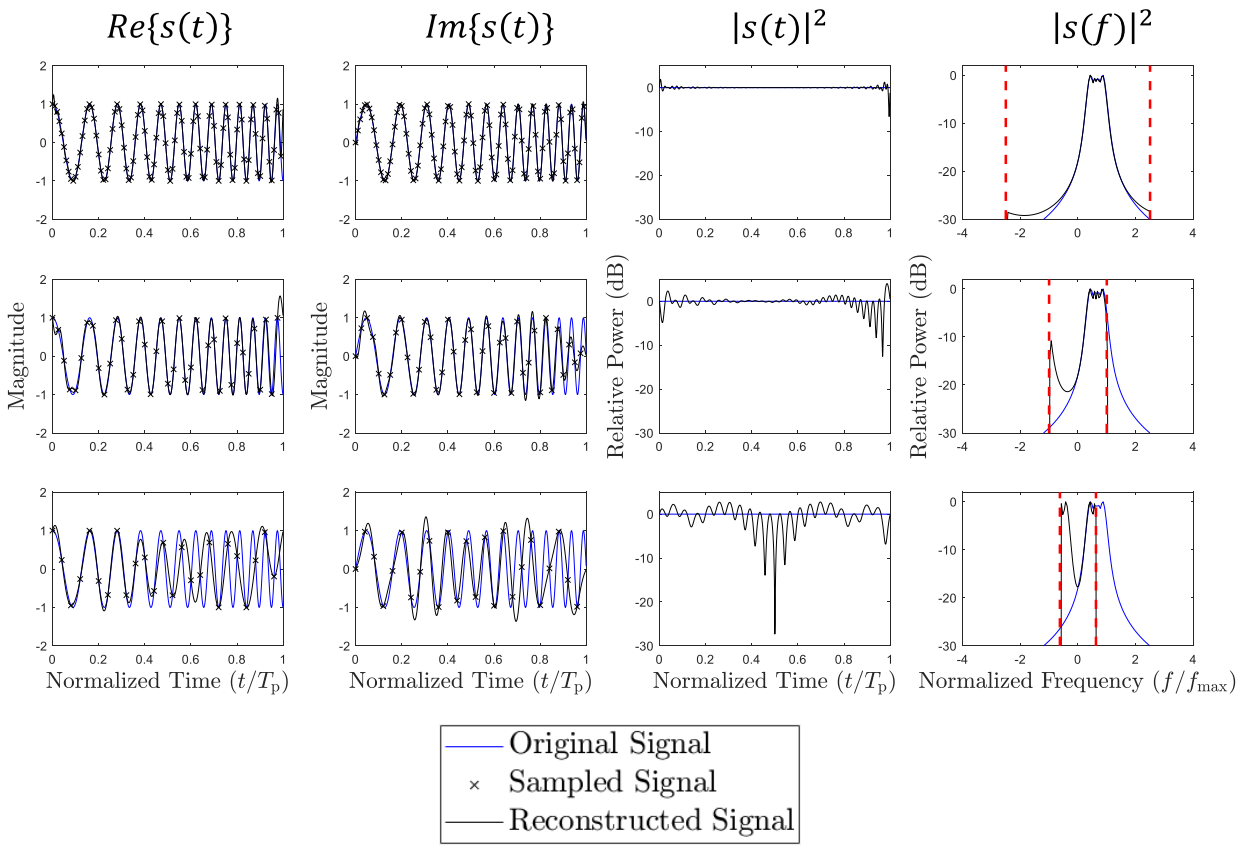

Figure 5: Discrete sampling of a continuous complex signal with sinc reconstruction (first & second column), the amplitude envelope of complex signals before and after sinc reconstruction (third column), and the frequency dimension of the original and reconstructed signals (fourth column); Here $f_s > 2f_{max}$ (top row), $f_s = 2f_{max}$ (middle row), $f_s < 2f_{max}$ (bottom row).

Note in Figure 5 that the frequency dimension representation of the complex signal now occupies unique spectral information in the entire frequency band ("negative" frequencies are decoupled from the "positive" frequencies after discrete Fourier transformation), while still being sampled according to the original Nyquist rates. The available signal information is fully captured by sampling both cosine and sine basis components, in comparison to the information captured solely by the cosine basis component. This is mathematically represented by plugging the Fourier identities

$$\cos(2\pi f_0 t) = \frac{1}{2}[e^{j2\pi f_0 t} + e^{-j2\pi f_0 t}] \overset{\mathcal{F}}{\leftrightarrow} \frac{1}{2}[\delta(f + f_0) + \delta(f - f_0)]$$

$$\sin(2\pi f_0 t) = \frac{-j}{2}[e^{j2\pi f_0 t} - e^{-j2\pi f_0 t}] \overset{\mathcal{F}}{\leftrightarrow} \frac{-j}{2}[-\delta(f + f_0) + \delta(f - f_0)]$$

(1.5)

into (1.4) to show the negative frequency components cancelling in (1.6).

$$\begin{aligned} e^{-j2\pi f_0 t} = \cos(2\pi f_0 t) - j\sin(2\pi f_0 t) &= \frac{1}{2}[e^{j2\pi f_0 t} + e^{-j2\pi f_0 t}] - j\left(\frac{-j}{2}\right)[e^{j2\pi f_0 t} - e^{-j2\pi f_0 t}] \\ &= \frac{1}{2}[e^{j2\pi f_0 t} + e^{-j2\pi f_0 t}] - \frac{1}{2}[e^{j2\pi f_0 t} - e^{-j2\pi f_0 t}] \end{aligned}$$

$$\begin{aligned} e^{-j2\pi f_0 t} \overset{\mathcal{F}}{\leftrightarrow} & \frac{1}{2}[\delta(f + f(t)) + \delta(f - f(t))] - j\left(\frac{-j}{2}\right)[\delta(f + f(t)) - \delta(f - f(t))] \\ &= \frac{1}{2}[\delta(f + f(t)) + \delta(f - f(t))] - \frac{1}{2}[-\delta(f + f(t)) + \delta(f - f(t))] \\ &= \delta(f + f(t)) \end{aligned}$$

(1.6)

Negative frequency representations result from mathematical definitions, indicating the degree that a signal maps to the cosine or sine basis function for a given frequency.

1.4.1.3. FAST TIME VERSUS SLOW TIME

Consider an active pulsed radar transmission emitted into free space. Time samples are coherently captured at a sampling interval T_s and sampling frequency $f_s = 1/T_s$ over a given duration. The received signature is illustrated in Figure 6. The transmission consists of P pulses, each emitted for duration T_p. Sampling over the duration T_p yields $N_p = f_s \cdot T_p$ samples. The time duration between consecutive pulses is the pulse repetition interval (PRI) T_{PRI}, which recurs with a pulse repetition frequency (PRF) $f_{PRF} = 1/T_{PRI}$. Sampling over the duration T_{PRI} yields $N_{PRI} = f_s \cdot T_{PRI}$ samples. The time windowed duration of the receive signature is the coherent processing interval (CPI) $T_{CPI} = P \cdot T_{PRI}$. Sampling over the duration T_{CPI} yields $N_{CPI} = f_s \cdot T_{CPI} = P \cdot N_{PRI}$ samples. It is generally true that $T_s \ll T_p \leq T_{PRI} \ll T_{CPI}$ and $f_{PRF} \ll f_s$.

The data set is segmented into P pulse repetition intervals, each containing N_{PRI} discrete samples. The fast time dimension refers to the samples within a given PRI segment collected at sample intervals $n \cdot T_{\mathrm{s}}$ for $n \in \{0, 1, \ldots, N_{\mathrm{PRI}} - 1\}$. The slow time dimension refers to the samples between PRI segments separated by pulse repetition intervals $p \cdot T_{\mathrm{PRI}}$ for $p \in \{0, 1, \ldots, P - 1\}$. Note that uniform PRI segmentation of samples is not always used in practice [16]. Recent work has explored the use of random non-uniform (staggered) PRIs to glean additional information from the RF environment [43].

The fast time-frequency dimension examines the frequency content across multiple contiguous fast time samples using the discrete Fourier transform. The instantaneous time-frequency dimension examines the sample-to-sample frequency deviation occurring between two contiguous fast time samples (via differencing) and is a subset of the fast time-frequency dimension. The slow time-frequency dimension examines the frequency content across multiple contiguous slow time samples using the discrete Fourier transform.

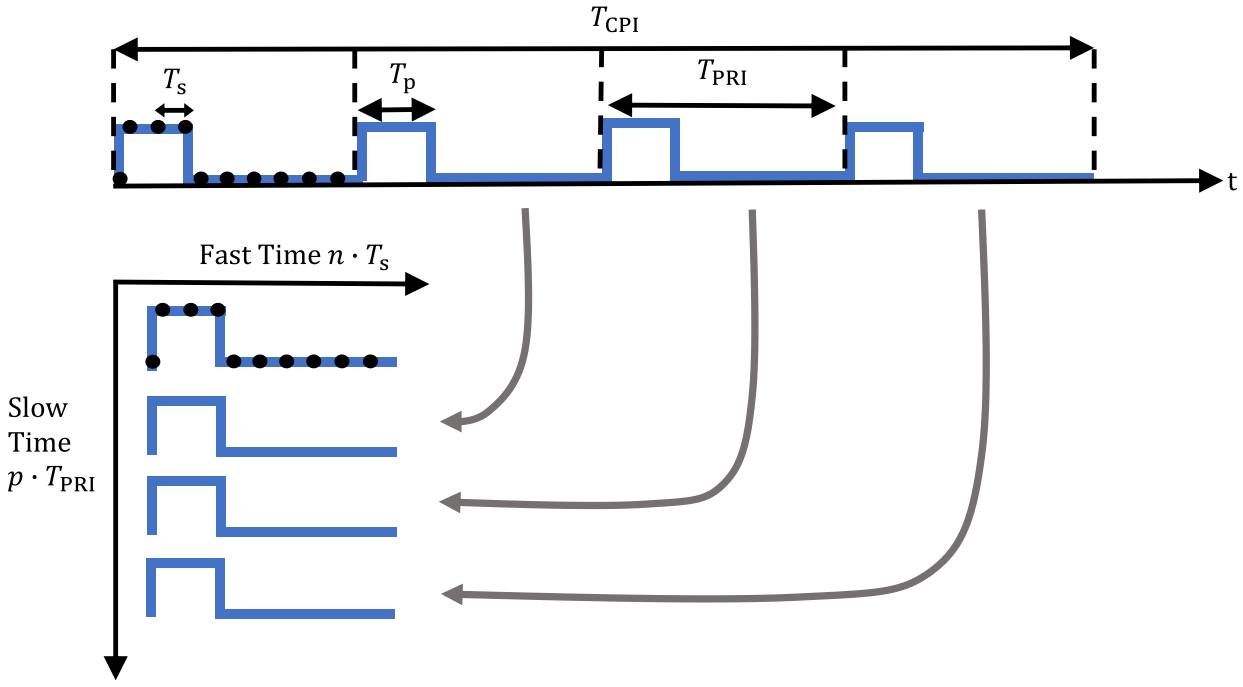

Figure 6: Fast time versus slow time representation, with temporal duration definitions.

1.4.1.4. DEFINITION OF BASEBAND AND PASSBAND FREQUENCY REPRESENTATIONS

Two common signal models are referred to as baseband and passband representation. The fast time-frequency representations of a baseband versus passband representation are shown in Figure 7.

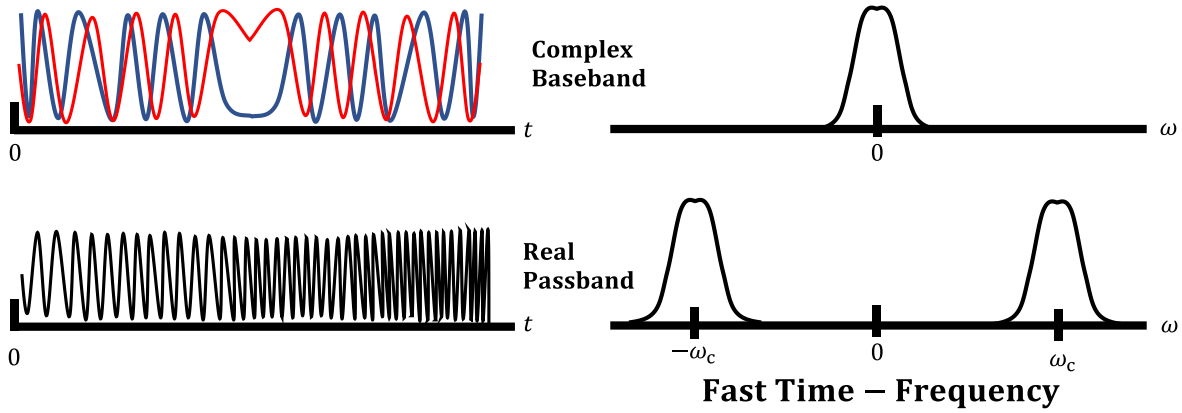

Figure 7: Fast time-frequency representations of baseband signals versus passband signals.

A passband representation refers to a real signal with center frequency $\omega_c = 2\pi f_c$, written as

$$s_{pb}(t) = A(t)\cos\big(\omega_c t + \phi(t)\big) = s_I(t)\cos(\omega_c t) - s_Q(t)\sin(\omega_c t)$$

(1.7)

One may recognize this form as being equivalent to (1.3). All physically realizable electromagnetic waveforms that exist in reality have positive frequency content, which can be considered a mapping of $s_I(t)$ and $s_Q(t)$ when mixed with orthogonal basis components $\cos(\omega_c t)$ and $\sin(\omega_c t)$ to generate the purely real signal $A(t)\cos\big(\omega_c t + \phi(t)\big)$. Conveniently, (1.7) can be written as

$$\begin{aligned} s_{pb}(t) = A(t)\cos\big(\omega_c t + \phi(t)\big) &= s_I(t)\cos(\omega_c t) - s_Q(t)\sin(\omega_c t) \\ &= Re\left\{\Big(s_I(t) + j\, s_Q(t)\Big)\big(\cos(\omega_c t) + j\sin(\omega_c t)\big)\right\} \\ &= Re\big\{\big(s_{bb}(t)\big)\big(\cos(\omega_c t) + j\sin(\omega_c t)\big)\big\} \end{aligned}$$

(1.8)

Generation of a passband signal may be achieved either using analog or digital signal representations of $s_I(t)$ and $s_Q(t)$, each with their own pitfalls.

Baseband representation refers to the complex signal representation shown in (1.9), which only considers the portion of the passband signal that provides its amplitude and phase characteristics. One may recognize this form as being equivalent to (1.4).

$$s_{\mathrm{bb}}(t) = A(t)\, e^{j\phi(t)} = A(t)\cos\big(\phi(t)\big) + jA(t)\sin\big(\phi(t)\big) = s_{\mathrm{I}}(t) + j\, s_{\mathrm{Q}}(t)$$

(1.9)

Frequency modulated (FM) signals have constant amplitude envelopes ($A(t) = A_0\ \forall\ t$) and non-constant phase ($\phi(t) \neq \phi_0\ \forall\ t$) over their duration. Amplitude modulated (AM) signals have non-constant amplitude envelopes ($A(t) \neq A_0\ \forall\ t$) and constant phase ($\phi(t) = \phi_0\ \forall\ t$) for their entire duration. Signals having both non-constant amplitude and phase characteristics ($A(t) \neq A_0\ \forall\ t,\ \phi(t) \neq \phi_0\ \forall\ t$) are often also referred to as amplitude modulated (AM) signals to emphasize non-constant amplitude envelopes.

For FM signals, only a single instantaneous frequency exists at a given time instant defined by $f_{\mathrm{i}}(t) = \frac{1}{2\pi}\left(\frac{d\phi(t)}{dt}\right)$ [44]. For AM signals, two or more instantaneous frequencies exist simultaneously, as the amplitude term $A(t)$ itself introduces a time varying frequency component. Instantaneous frequency definitions are explored for specific signal types in [44].

A received passband signal can be demodulated to obtain its baseband signal representation (assuming adequate out-of-band interference rejection) by the process outlined hereafter. Consider the passband signal representation from (1.7) transmitted at a reference time t_{ref}.

$$\begin{aligned} s_{\mathrm{pb}}(t - t_{\mathrm{ref}}) &= A(t - t_{\mathrm{ref}})\cos\big(\omega_{\mathrm{c}} \cdot (t - t_{\mathrm{ref}}) + \phi(t - t_{\mathrm{ref}})\big) \\ &= s_{\mathrm{I}}(t - t_{\mathrm{ref}})\cos\big(\omega_{\mathrm{c}} \cdot (t - t_{\mathrm{ref}})\big) - s_{\mathrm{Q}}(t - t_{\mathrm{ref}})\sin\big(\omega_{\mathrm{c}} \cdot (t - t_{\mathrm{ref}})\big) \end{aligned}$$

(1.10)

In physical reality, the receive signal $y(t)$ will be a delayed copy of the transmitted signal due to the near speed of light (non-instantaneous) propagation delay t_{delay}.

$$\begin{aligned} y(t) &= s_{\mathrm{pb}}\left(t - t_{\mathrm{ref}} - t_{\mathrm{delay}}\right) \\ &= A\left(t - t_{\mathrm{ref}} - t_{\mathrm{delay}}\right)\cos\left(\omega_{\mathrm{c}} \cdot \left(t - t_{\mathrm{ref}} - t_{\mathrm{delay}}\right) + \phi\left(t - t_{\mathrm{ref}} - t_{\mathrm{delay}}\right)\right) \\ &= s_{\mathrm{I}}\left(t - t_{\mathrm{ref}} - t_{\mathrm{delay}}\right)\cos\left(\omega_{\mathrm{c}} \cdot \left(t - t_{\mathrm{ref}} - t_{\mathrm{delay}}\right)\right) - s_{\mathrm{Q}}\left(t - t_{\mathrm{ref}} - t_{\mathrm{delay}}\right)\sin\left(\omega_{\mathrm{c}} \cdot \left(t - t_{\mathrm{ref}} - t_{\mathrm{delay}}\right)\right) \end{aligned}$$

(1.11)

For convenience, assume no propagation delay $t_{\mathrm{delay}} = 0$ and transmit reference time $t_{\mathrm{ref}} = 0$ such that $y(t) = s_{\mathrm{pb}}(t)$. The received signal can be mixed with a single oscillator $\cos(\omega_{\mathrm{c}}t)$, or two independent orthogonal oscillator signals $\cos(\omega_{\mathrm{c}}t)$ and $\sin(\omega_{\mathrm{c}}t)$ (see 1.4.1.9). The latter configuration recovers the complex baseband signal without loss of information as in (1.12). Note that the imaginary component *j* distinguishes the independent radio frequency channels of the cosine component $\cos(\omega_{\mathrm{c}}t)$ and the sine component $\sin(\omega_{\mathrm{c}}t)$.

$$\begin{aligned} y_{\mathrm{mix}}(t) &= y(t) \cdot (\cos(\omega_{\mathrm{c}}t) - j\sin(\omega_{\mathrm{c}}t)) \\ &= s_{\mathrm{pb}}(t) \cdot (\cos(\omega_{\mathrm{c}}t) - j\sin(\omega_{\mathrm{c}}t)) \\ &= A(t)\cos\left(\omega_{\mathrm{c}}t + \phi(t)\right) \cdot (\cos(\omega_{\mathrm{c}}t) - j\sin(\omega_{\mathrm{c}}t)) \\ &= \frac{1}{2}A(t)\{\left[\cos\left(2\omega_{\mathrm{c}}t + \phi(t)\right) + \cos\left(\phi(t)\right)\right] + j\left[-\sin\left(2\omega_{\mathrm{c}}t + \phi(t)\right) + \sin\left(\phi(t)\right)\right]\} \end{aligned}$$

(1.12)

Bandstop filtering the components at $2\omega_{\mathrm{c}}t$ in both channels yields the complex baseband signal

$$s_{\mathrm{bb}}(t) = A(t)\{\cos\left(\phi(t)\right) + j\ \sin\left(\phi(t)\right)\} = A(t)\ e^{j\phi(t)}\,.$$

(1.13)

The same derivation can be equivalently shown using the inphase and quadrature signal representation as

$$\begin{aligned} y_{\mathrm{mix}}(t)\ &= \left(s_{\mathrm{I}}(t)\cos(\omega_{\mathrm{c}}t) - s_{\mathrm{Q}}(t)\sin(\omega_{\mathrm{c}}t)\right) \cdot \cos(\omega_{\mathrm{c}}t) \\ &\quad + \left(s_{\mathrm{I}}(t)\cos(\omega_{\mathrm{c}}t) - s_{\mathrm{Q}}(t)\sin(\omega_{\mathrm{c}}t)\right) \cdot (-j\sin(\omega_{\mathrm{c}}t)) \\ &= \left(s_{\mathrm{I}}(t)\cos(\omega_{\mathrm{c}}t)\cos(\omega_{\mathrm{c}}t) - s_{\mathrm{Q}}(t)\sin(\omega_{\mathrm{c}}t)\cos(\omega_{\mathrm{c}}t)\right) \\ &\quad + j\left(-s_{\mathrm{I}}(t)\cos(\omega_{\mathrm{c}}t)\sin(\omega_{\mathrm{c}}t) + s_{\mathrm{Q}}(t)\sin(\omega_{\mathrm{c}}t)\sin(\omega_{\mathrm{c}}t)\right) \end{aligned}$$

(1.14)

Expanding via trigonometric identities

$$
\begin{aligned}
y_{\mathrm{mix}}(t) &= \left(s_{\mathrm{I}}(t)\cos(\omega_{\mathrm{c}}t)\cos(\omega_{\mathrm{c}}t) - s_{\mathrm{Q}}(t)\sin(\omega_{\mathrm{c}}t)\cos(\omega_{\mathrm{c}}t)\right) \\
&\quad + j\left(-s_{\mathrm{I}}(t)\cos(\omega_{\mathrm{c}}t)\sin(\omega_{\mathrm{c}}t) + s_{\mathrm{Q}}(t)\sin(\omega_{\mathrm{c}}t)\sin(\omega_{\mathrm{c}}t)\right) \\
&= \left(\frac{s_{\mathrm{I}}(t)}{2}\cos(2\omega_{\mathrm{c}}t) + \frac{s_{\mathrm{I}}(t)}{2}\cos(0) - \frac{s_{\mathrm{Q}}(t)}{2}\sin(2\omega_{\mathrm{c}}t) - \frac{s_{\mathrm{Q}}(t)}{2}\sin(0)\right) \\
&\quad + j\left(-\frac{s_{\mathrm{I}}(t)}{2}\sin(2\omega_{\mathrm{c}}t) - \frac{s_{\mathrm{I}}(t)}{2}\sin(0) - \frac{s_{\mathrm{Q}}(t)}{2}\cos(2\omega_{\mathrm{c}}t) + \frac{s_{\mathrm{Q}}(t)}{2}\cos(0)\right)
\end{aligned}
$$

(1.15)

and bandstop filtering the higher frequency component at $2\omega_{\mathrm{c}}t$ in both channels yields the baseband signal

$$s_{\mathrm{bb}}(t) = s_{\mathrm{I}}(t) + j\, s_{\mathrm{Q}}(t)\,.$$

(1.16)

1.4.1.5. AMPLIFIER EFFECTS ON TRANSMIT WAVEFORMS

A typical amplifier power characteristic curve is shown in Figure 8, here divided into linear and saturated regions. Class A amplifiers operate at relatively low power (in the linear region) and have low power efficiency. Class AB, B, and C amplifiers operate at relatively moderate-to-high power (in the saturated region) with high power efficiency, at the cost of inducing signal distortions [45].

High-power amplifiers are often used for radar signal transmission. The input signal power to an HPA is driven far into the saturated region to maximize power efficiency and minimize heat dissipation. Hypothetical input ($\bar{\mathcal{P}}_{\mathrm{in}}$) and output ($\bar{\mathcal{P}}_{\mathrm{out}}$) power operating points for optimal high-power amplifier efficiency are indicated in Figure 8. Because HPAs often are biased to remain far in the saturated region, input AM waveforms would be afflicted by significant distortion as the input amplitude $A(t)$ and corresponding instantaneous power $\mathcal{P}_{\mathrm{in}}(t)$ traverses the nonlinear amplifier power curve. Moreso, HPAs are not designed to operate below the saturated region and power efficiency becomes poor in the linear region. Because the average input power of an AM waveform may be significantly less than that of an FM waveform, the amplifier may operate in an inefficient region and dissipate additional heat into the amplifier heat sink (which becomes significant when >1 kW output power is needed).

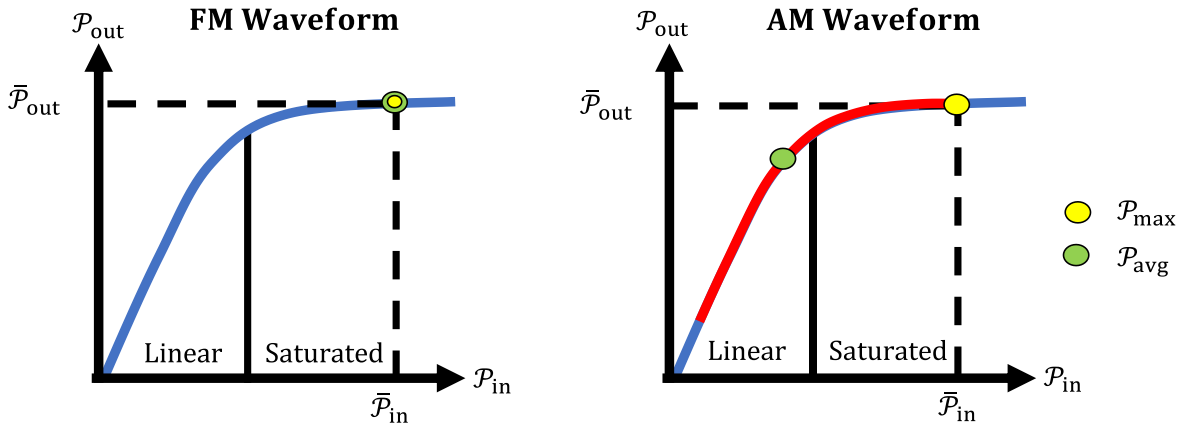

Figure 8: Amplifier power operating curve. $\bar{\mathcal{P}}_{\text{in}}$ and $\bar{\mathcal{P}}_{\text{out}}$ indicate hypothetical optimal power efficiency operating points for a high-power amplifier. For AM waveforms, the instantaneous power (red line) and peak power (yellow dot) deviate significantly from the average power (green dot). For FM waveforms, minimum deviation occurs and the amplifier is always saturated. Peak power must not exceed the maximum input power limitations of an amplifier.

Noting the significant deviation between peak and average power delivered for an AM waveform shown in Figure 8, the peak-to-average power ratio (PAPR) is a common metric gauging how efficiently an input signal can be amplified. PAPR is defined in (1.17) after normalization. Physical signals of non-zero frequency always experience a deviation between the peak and average power ratio of at least 2. For example, an FM signal with constant amplitude A_0 exhibits $\mathcal{P}_{\text{max}}^{\text{pb}} = A_0^2$ and $\mathcal{P}_{\text{avg}}^{\text{pb}} = A_0^2/2$. Baseband signals aren't always perfectly recreated at passband, such that the baseband PAPR is approximately equal to the passband PAPR at the amplifier input (see 1.4.1.6). FM waveforms maintain an ideal $(= 1)$ PAPR and meet the necessary signal input conditions for efficient amplifier operation, while AM waveforms have non-ideal (> 1) PAPR that causes heat dissipation and signal distortion.

$$\text{PAPR} = \frac{1}{2}\frac{\mathcal{P}_{\text{max}}^{\text{pb}}}{\mathcal{P}_{\text{avg}}^{\text{pb}}} = \frac{1}{2}\left(\frac{\max\left\{\left|s_{\text{pb}}(t)\right|^2\right\}}{\frac{1}{T_{\text{p}}}\int_0^{T_{\text{p}}}\left|s_{\text{pb}}(t)\right|^2 dt}\right) \approx \frac{\mathcal{P}_{\text{max}}^{\text{bb}}}{\mathcal{P}_{\text{avg}}^{\text{bb}}} = \left(\frac{\max\{|s_{\text{bb}}(t)|^2\}}{\frac{1}{T_{\text{p}}}\int_0^{T_{\text{p}}}|s_{\text{bb}}(t)|^2 dt}\right) \tag{1.17}$$

Spectral regrowth refers to undesired signal spectral characteristics that result from RF amplifier distortion. Spectral regrowth contaminates optimal waveform characteristics and impairs the transmission waveform spectral containment required to mitigate interference with other RF users. Amplifier nonlinear distortions are labeled in terms of specific components including harmonics, intermodulations (or cross-modulations), and memory effects [46-50]. Common models for nonlinear distortions include power series, memory polynomials, Volterra series, and Wiener-Hammerstein models [46-50]. The Matlab system identification toolbox provides functions and documentation to model a wide variety of nonlinear models [51]. Real-time hardware implementations for amplifier nonlinearity approximation have been implemented [52, 53].

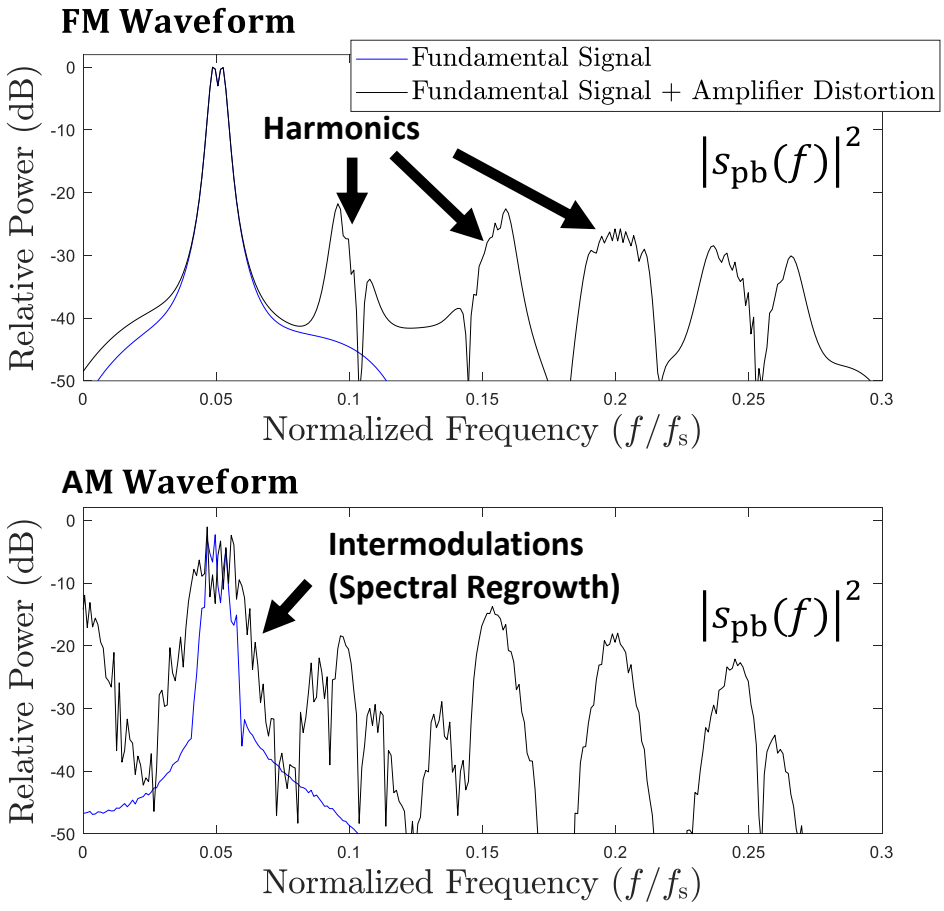

Figure 9: Nonlinear amplifier distortions simulated using the power series model and enforcing amplifier bandpass filtering effects. The simulated distortions to an FM waveform (top) create harmonics only. The simulated distortions to an AM waveform (bottom) create harmonics and intermodulations, referred to as spectral regrowth.

The HPA nonlinearities are easily modeled via power series when limited to consideration of harmonics and intermodulations [30]. The fundamental signal represented in (1.3) is $A(t)\cos\big(\omega_c t+\phi(t)\big)$. The power series model represents a summation of memory-less polynomials of integer order ξ forming the distorted signal $s_{\text{power}}(t)$.

$$s_{\text{power}}(t)=\sum_{\xi=1}^{\infty}A^{\xi}(t)\cos^{\xi}\big(\omega_c t+\phi(t)\big)$$

(1.18)

Even order polynomials exclusively produce harmonics at frequency multiples of the fundamental signal, e.g. $A^2(t)\cos^2\big(\omega_c t+\phi(t)\big)=A^2(t)\big(2+2\cos\big(2\omega_c t+2\phi(t)\big)\big)$. Odd order polynomials produce harmonics at the fundamental frequency and multiples thereof, e.g. $A^3(t)\cos^3\big(\omega_c t+\phi(t)\big)=A^3(t)\left(\frac{3}{4}\cos\big(\omega_c t+\phi(t)\big)+\frac{1}{4}\cos\big(3\omega_c t+3\phi(t)\big)\right)$. Examining the odd order polynomials, any amplitude modulation produced by the amplifier at the fundamental center frequency $A^{\xi}(t)\cos\big(\omega_c t+\phi(t)\big)$ will superimpose with the transmit signal and cause distortion [30]. FM waveforms mitigate amplifier distortion since $A(t)=A_0\ \forall\ t$, yielding the fundamental signal.

The source of spectral regrowth outside of the fundamental signal bandwidth becomes apparent after decomposing an AM waveform into instantaneous frequency components. The time-varying amplitude $A(t)$ and frequency $\cos(\omega_c t)$ components imply that multiple instantaneous frequencies exist simultaneously [44]. Here, consider the AM waveform generated by the superposition of two or more FM waveforms.

$$A(t)\cos\big(\omega_c t+\phi(t)\big)=\sum_{\forall i}A_i\cos(\omega_c t+\phi_i(t))$$

(1.19)

The simple case where two FM waveforms with different phases are superimposed [54] can be expressed as

$$A_1\cos(\omega_c t+\phi_1(t))+A_2\cos(\omega_c t+\phi_2(t))$$
$$=\sqrt{[A_1\cos(\phi_1(t))+A_2\cos(\phi_2(t))]^2+[A_1\sin(\phi_1(t))+A_2\sin(\phi_2(t))]^2}$$
$$\cdot\cos\left(\omega_c t+\tan^{-1}\left[\frac{A_1\sin(\phi_1(t))+A_2\sin(\phi_2(t))}{A_1\cos(\phi_1(t))+A_2\cos(\phi_2(t))}\right]\right)$$

(1.20)

By examination, the resulting amplitude and phase components when summing two FM waveforms are

$$A(t)=\sqrt{[A_1\cos(\phi_1(t))+A_2\cos(\phi_2(t))]^2+[A_1\sin(\phi_1(t))+A_2\sin(\phi_2(t))]^2}$$

$$\phi(t)=\tan^{-1}\left[\frac{A_1\sin(\phi_1(t))+A_2\sin(\phi_2(t))}{A_1\cos(\phi_1(t))+A_2\cos(\phi_2(t))}\right]$$

(1.21)

The superimposed signal will exhibit amplitude modulation (and therefore spectral regrowth) unless the comprising phases are equivalent $\phi_1(t)=\phi_2(t)$. Furthermore, applying the power series model reveals the root source of spectral regrowth. Plugging (1.20) when $A_1=A_2=0.5$ and $\phi_1(t)\neq\phi_2(t)$ into (1.18) where $\xi=3$ yields harmonic terms (e.g. $\cos(3\omega_c t+3\phi_1(t))$ & $\cos(3\omega_c t+3\phi_2(t))$), in addition to intermodulation terms (e.g. $\cos(\omega_c t+2\phi_1(t)-\phi_2(t))$ & $\cos(\omega_c t-\phi_1(t)+2\phi_2(t))$) located near the fundamental frequency. The intermodulation terms indicate frequency expansion beyond the initial signal bandwidth.

$$\left(0.5\cos\left(\omega_c t+\phi_1(t)\right)+0.5\cos\left(\omega_c t+\phi_2(t)\right)\right)^3$$
$$=0.219\cos\left(\omega_c t+\phi_1(t)\right)+0.219\cos\left(\omega_c t+\phi_2(t)\right)+0.031\cos\left(3\omega_c t+3\phi_1(t)\right)+0.031\cos\left(3\omega_c t+3\phi_2(t)\right)$$
$$+0.062\cos\left(\phi_1(t)\right)+0.062\cos\left(\phi_2(t)\right)+0.093\cos\left(\omega_c t+2\phi_1(t)-\phi_2(t)\right)$$
$$+0.093\cos\left(\omega_c t-\phi_1(t)+2\phi_2(t)\right)+0.062\cos\left(2\omega_c t+\phi_1(t)+2\phi_2(t)\right)$$
$$+0.062\cos\left(2\omega_c t+2\phi_1(t)+\phi_2(t)\right)+0.031\cos\left(3\omega_c t+\phi_1(t)+2\phi_2(t)\right)$$
$$+0.031\cos\left(3\omega_c t+2\phi_1(t)+\phi_2(t)\right)$$

(1.22)

1.4.1.6. ANALOG UPCONVERSION

Two common methods exist to form a passband signal for subsequent transmission, which are analog upconversion and digital upsampling, interpolation & upconversion. The choice of analog or digital passband signal generation often amounts to which equipment is commercially available and sufficient for an engineering application given hardware costs. For instance, software-defined radios (SDR) often have built-in analog upconversion, while arbitrary waveform generators (AWG) often require digital passband signal generation.

Analog upconversion is illustrated in Figure 10 and Figure 11, where ω, f denotes analog frequency and $f_{\mathrm{s}}^{\mathrm{DAC}}$ is the digital-to-analog converter sample rate. To form the passband signal: A) the analog baseband components $s_{\mathrm{I}}(t)$ and $s_{\mathrm{Q}}(t)$ are generated by separate DACs and lowpass filtered to remove Nyquist spectral images, B) the filtered baseband components are respectively mixed with $\cos(\omega_{\mathrm{c}}t)$ and $-\sin(\omega_{\mathrm{c}}t)$ local oscillators for upconversion and summed using an analog combiner, C) the passband signal is bandpass filtered to enforce spectral containment. The basis component $-\sin(\omega_{\mathrm{c}}t) = \cos\left(\omega_{\mathrm{c}}t - \frac{\pi}{2}\right)$ is created by pushing the $\cos(\omega_{\mathrm{c}}t)$ oscillator through an analog 90° phase shifter to maintain phase coherence between channels.

I/Q imbalance exists when the upconverted inphase and quadrature channels have inequal scaling $\left(c_{\mathrm{I}}(t)\ \&\ c_{\mathrm{Q}}(t)\right)$ due to RF fabrication variations, local oscillator (LO) amplitude variations, or crosstalk between the baseband and LO channels [55]. Crosstalk from the LO to the passband channels in the transmit chain, called transmit LO leakage, can be mathematically represented as a DC offset $\left(d_{\mathrm{I}}(t)\ \&\ d_{\mathrm{Q}}(t)\right)$ of the baseband components $s_{\mathrm{I}}(t)$ and $s_{\mathrm{Q}}(t)$ [56]. If the I/Q imbalance or LO leakage is significant and uncompensated, the passband waveform may exhibit undesired amplitude and phase distortion. I/Q imbalance and LO leakage may drift over time with environmental factors. Mixers introduce errors due to frequency push-pull effects and intermodulations [57]. The passband signal when incorporating non-ideal I/Q imbalance and LO leakage effects is represented as

$$\begin{aligned} s_{\mathrm{pb}}(t) = A(t)\cos\big(\omega_{\mathrm{c}}t + \phi(t)\big) &\cong c_{\mathrm{I}}(t)s_{\mathrm{I}}(t)\cos(\omega_{\mathrm{c}}t) - c_{\mathrm{Q}}(t)s_{\mathrm{Q}}(t)\sin(\omega_{\mathrm{c}}t) + d_{\mathrm{I}}(t)\cos(\omega_{\mathrm{c}}t) - d_{\mathrm{Q}}(t)\sin(\omega_{\mathrm{c}}t) \\ &= c_{\mathrm{I}}(t)\big(s_{\mathrm{I}}(t) + d_{\mathrm{I}}(t)\big)\cos(\omega_{\mathrm{c}}t) - c_{\mathrm{Q}}(t)\left(s_{\mathrm{Q}}(t) + d_{\mathrm{Q}}(t)\right)\sin(\omega_{\mathrm{c}}t) \end{aligned} \tag{1.23}$$

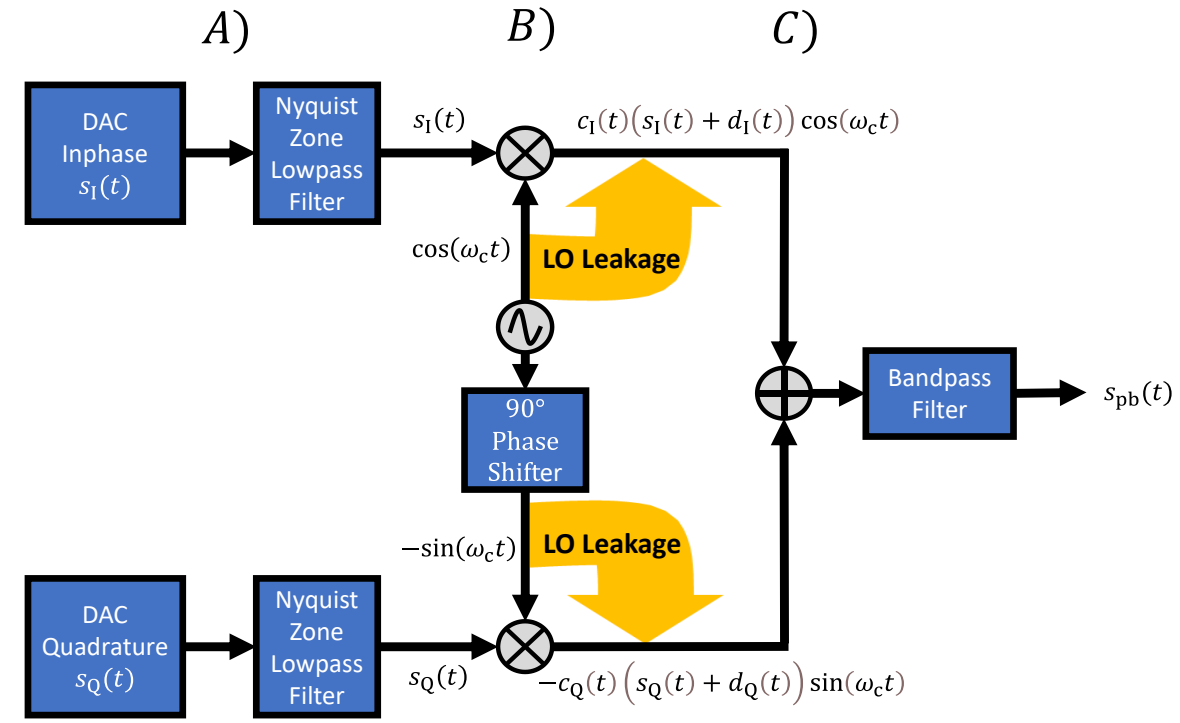

Figure 10: Analog upconversion RF chain.

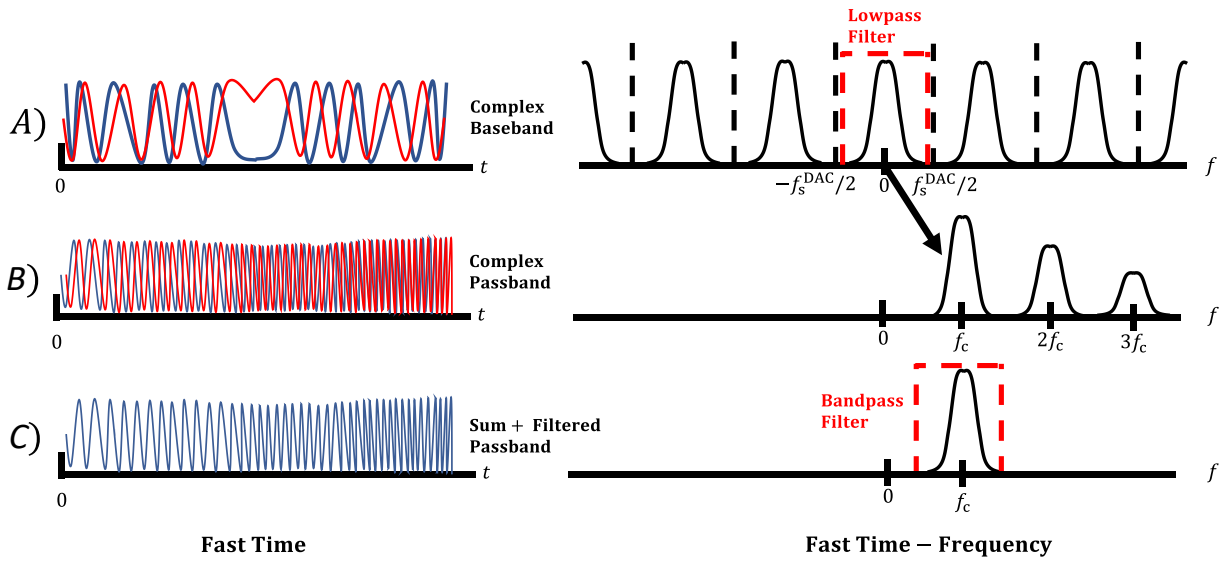

Figure 11: Analog upconversion stages: A) Form the I/Q baseband signal components on separate DACs and lowpass filter to remove the Nyquist spectral images, B) Mix the analog complex baseband waveform by either $\cos(\omega_c t)$ or $-\sin(\omega_c t)$, C) Sum the components using an analog combiner to form the passband signal and bandpass filter the signal to enforce spectral containment.

1.4.1.7. DIGITAL UPSAMPLING, INTERPOLATION, & UPCONVERSION

Digital upsampling, interpolation, and upconversion are illustrated in Figure 12 and Figure 13, where ω, f denotes analog frequency, Ω denotes digital frequency, f_s^{TX} is the initial baseband waveform transmit sample rate, and f_s^{DAC} is the digital-to-analog converter sample rate. To form the passband signal: A) the digital baseband signal is formed, B) the number of complex baseband waveform samples is increased via upsampling & interpolation, C) the interpolated baseband waveform is digitally mixed with a complex carrier for upconversion, D) the real component of the upconverted waveform is extracted, E) the analog passband signal is formed with a high sample rate DAC and bandpass filtered to enforce spectral containment.

Consider a baseband signal designed with initial baseband transmit sample rate f_s^{TX}, pulse duration T_p, and $N_p^{\mathrm{TX}} = f_s^{\mathrm{TX}} \cdot T_p$ samples. Digital upsampling and interpolation is necessary when the DAC sample rate is greater than the initial baseband transmit sample rate, $f_s^{\mathrm{DAC}} = \beta \cdot f_s^{\mathrm{TX}} > f_s^{\mathrm{TX}}$, where β is an integer upsampling factor. To maintain the desired pulse duration T_p at the DAC sample rate f_s^{DAC}, the number of waveform samples must be increased to $N_p^{\mathrm{DAC}} = f_s^{\mathrm{DAC}} \cdot T_p = \beta \cdot f_s^{\mathrm{TX}} \cdot T_p$. Upsampling and interpolation increases the number of waveform samples while attempting to preserve amplitude and phase characteristics. The interpolation stage introduces non-ideal distortions to $s_I(n)$ and $s_Q(n)$ (see 1.4.1.8), where the distorted baseband components are distinguished as $\tilde{s}_I(n)$ and $\tilde{s}_Q(n)$. After analog conversion and bandpass filtering, the distorted baseband components are represented as $\tilde{s}_I(t)$ and $\tilde{s}_Q(t)$. The passband signal when incorporating non-ideal digital interpolation effects is represented as

$$\begin{aligned} s_{\mathrm{pb}}(t) = A(t)\cos\big(\omega_c t + \phi(t)\big) &\cong Re\left\{\left(\tilde{s}_I(t) + j\,\tilde{s}_Q(t)\right)(\cos(\omega_c t) + j\sin(\omega_c t))\right\} \\ &= Re\left\{\left(\tilde{s}_{\mathrm{bb}}(t)\right)(\cos(\omega_c t) + j\sin(\omega_c t))\right\} \\ &= \tilde{s}_I(t)\cos(\omega_c t) - \tilde{s}_Q(t)\sin(\omega_c t) \end{aligned} \tag{1.24}$$

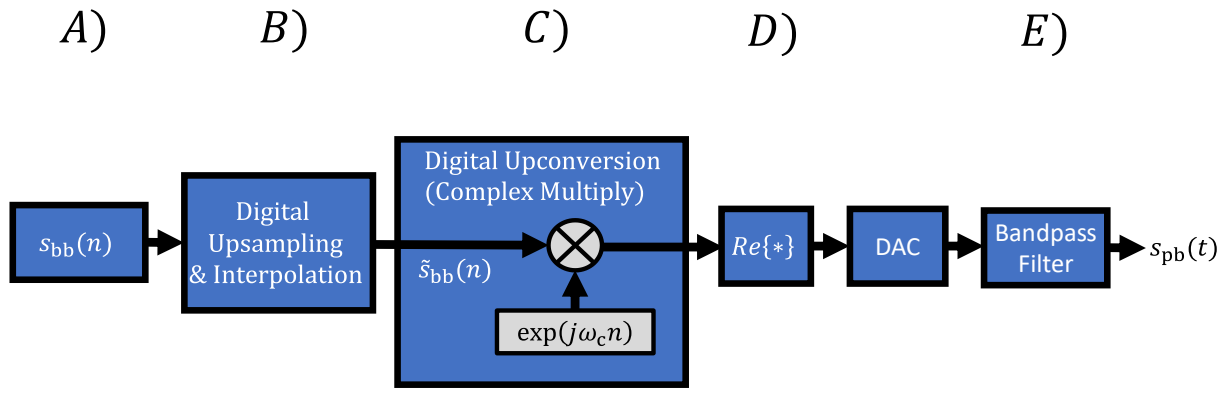

Figure 12: Digital upsampling, interpolation, and upconversion chain.

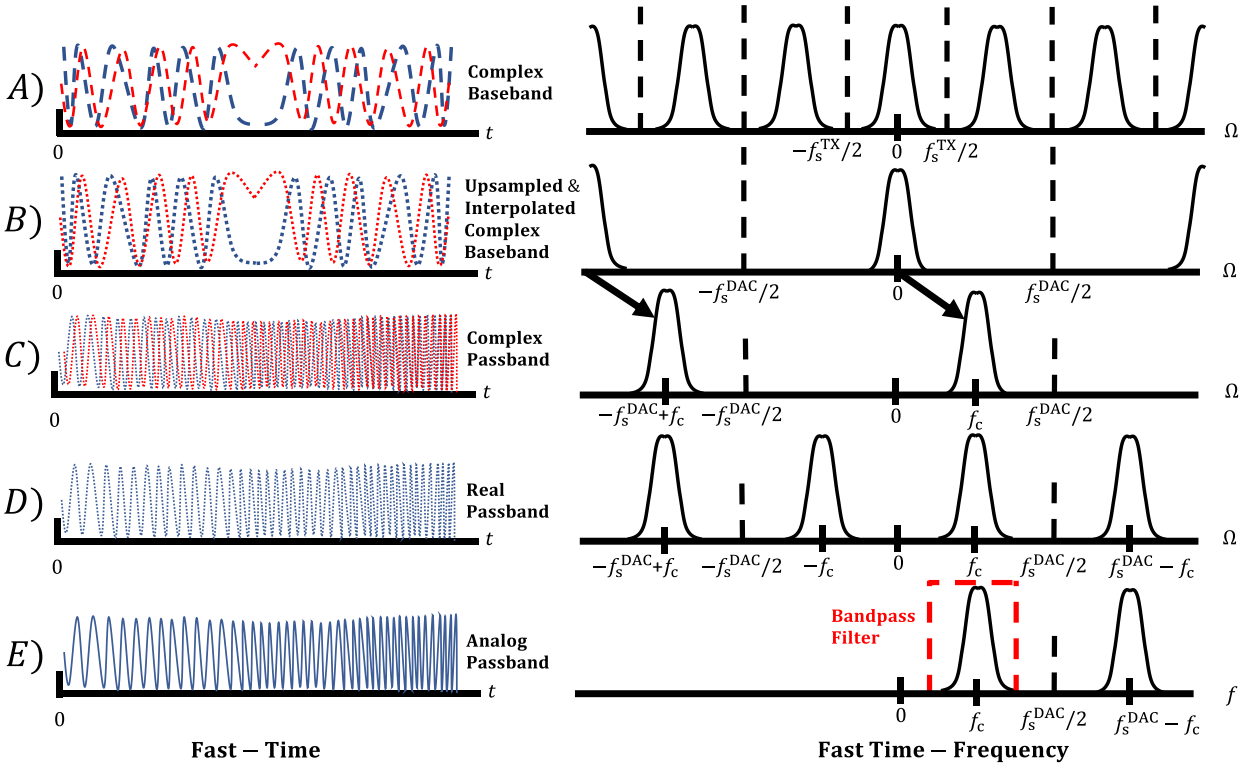

Figure 13: Digital upsampling, interpolation and upconversion stages: A) Form a complex baseband waveform, B) Upsample and interpolate the complex baseband waveform to expand the digital frequency space, C) Mix the digital complex baseband waveform with a complex sinusoid at frequency f_c, D) Extract the real portion of the passband waveform E) Construct the analog passband signal using a DAC and bandpass filter the signal to enforce spectral containment.

1.4.1.8. DIGITAL UPSAMPLING & INTERPOLATION METHODS

Digital upsampling & interpolation increases the number of samples in the vectorized signal $\mathbf{s}$ while attempting to preserve amplitude and phase characteristics. Digital upsampling refers to the insertion of zero-padding between existing signal samples to increase sample spacing. Digital interpolation refers to filtering an upsampled signal to form non-zero interior samples where zero-padding previously existed. Here, interpolation is considered in the fast time dimension or the phase angle dimension.

Digitally upsampling is defined mathematically in (1.25), where $\otimes$ is the Kronecker product and β is an integer upsampling factor.

$$\mathbf{s} \otimes \begin{bmatrix} 1 \\ 0 \\ \vdots \\ 0 \end{bmatrix}_{\beta \times 1} \tag{1.25}$$

Uniform temporal interpolation is defined mathematically in (1.26), where $\tilde{\mathbf{s}}$ is the interpolated signal, $\mathbf{H}$ is a filter bank, and $\mathbf{s}$ is the signal-to-be-upsampled.

$$\tilde{\mathbf{s}} = \mathbf{H}\left(\mathbf{s} \otimes \begin{bmatrix} 1 \\ 0 \\ \vdots \\ 0 \end{bmatrix}_{\beta \times 1} \right) \tag{1.26}$$

Here, the upsampling factor β represents the frequency space expansion ratio between the initial baseband transmit sample rate $f_{\mathrm{s}}^{\mathrm{TX}}$ and the digital-to-analog converter sample rate $f_{\mathrm{s}}^{\mathrm{DAC}}$, such that $f_{\mathrm{s}}^{\mathrm{DAC}} = \beta \cdot f_{\mathrm{s}}^{\mathrm{TX}}$. Equivalently stated from a temporal perspective, $T_{\mathrm{s}}^{\mathrm{TX}} = \beta \cdot T_{\mathrm{s}}^{\mathrm{DAC}}$.

Whittaker-Shannon sinc reconstruction and associated bandlimited spectral assumptions are described in Section 1.4.1.2. Sinc reconstruction is a specific form of temporal interpolation derived from fundamental signal theory. The Whittaker-Shannon sinc reconstruction formula is restated in (1.27) for comparison to (1.26), though here specific time instances are evaluated and the signal $s(t)$ is not assumed perfectly bandlimited.

$$\tilde{s}(t)|_{t=n'T_s^{\mathrm{DAC}}} = \sum_{n=-\infty}^{\infty} s(nT_s^{\mathrm{TX}})\ \mathrm{sinc}\left(\frac{n'T_s^{\mathrm{DAC}} - nT_s^{\mathrm{TX}}}{T_s^{\mathrm{TX}}}\right)$$

(1.27)

By observation, (1.27) can be represented in the form of (1.26) for sinc reconstruction between uniform samples (i.e. when t is evaluated at $t = n'T_s^{\mathrm{DAC}}$). The columns of $\mathbf{H}$ consist of sinc functions with peaks incrementally offset by β and sinc nulls every β samples from the peak. Imperfect reconstruction via sinc interpolation of a constant amplitude signal when critically sampled creates significant amplitude dips (see Figure 5), implying that the resulting physical signal would not deliver constant average power to an amplifier and thus cause distortion (see Section 1.4.1.5). While temporal interpolation via sinc reconstruction is common, other interpolation filters are applicable [59]. Piecewise spline interpolation adaptively forms ζ^{th} integer order polynomial interpolation estimates based on piecewise segments of $\mathbf{s}$. Cubic spline interpolation ($\zeta = 3$) minimizes mean squared error during reconstruction of imperfectly bandlimited signals (i.e. signals with spectral roll-off) [60]. Cubic spline interpolation is effective for temporal interpolation schemes.

For high power radar applications, it is desirable to transmit constant amplitude waveforms (see Section 1.4.1.5) which are written of the form $\mathbf{s} = \cos(\boldsymbol{\phi}) + j\sin(\boldsymbol{\phi})$. A complex constant amplitude envelope can be enforced by applying Euler's identity $\exp(j\boldsymbol{\phi}) = \cos(\boldsymbol{\phi}) + j\sin(\boldsymbol{\phi})$, where $\boldsymbol{\phi}$ is an arbitrary phase angle function. The angle of the signal-to-be-upsampled $\mathbf{s}$ is extracted via the angle argument operator $\angle(\cdot)$, which calculates the phase as $\boldsymbol{\phi} = \mathrm{atan}\left(\frac{Im\{\mathbf{s}\}}{Re\{\mathbf{s}\}}\right)$. Interpolation is then performed on the phase angle of the baseband signal. After performing phase interpolation, the temporal signal is formed by complex exponentiation $\exp(j\cdot)$ to reconstruct a constant amplitude waveform. Phase interpolation is an inherently nonlinear operation. While the original samples of $\mathbf{s}$ are preserved, the upsampled signal $\tilde{\mathbf{s}}$ will have mildly distorted fast time-frequency characteristics with the benefit of having a constant complex amplitude envelope. Effective interpolation methods in the phase dimension include piecewise linear ($\zeta = 1$) and piecewise cubic ($\zeta = 3$) spline interpolation.

Uniform phase interpolation is defined mathematically in (1.28).

$$\tilde{\mathbf{s}} = \exp\left[j\,\mathbf{H}\left((\angle \mathbf{s}) \otimes \begin{bmatrix} 1 \\ 0 \\ \vdots \\ 0 \end{bmatrix}_{\beta \times 1} \right) \right] \tag{1.28}$$

The stages of temporal interpolation and phase interpolation are shown in Figure 14. A comparison between temporal interpolation and phase interpolation for a given transmit signal is shown in Figure 15 displaying corresponding effects on fast time-frequency and the amplitude envelope when $\beta = 10$. Temporal interpolation distorts both amplitude and frequency characteristics (especially when extrapolating), though cubic spline interpolation introduces less amplitude distortion than sinc interpolation. Phase interpolation preserves a constant amplitude envelope with only minor frequency distortion. The distortions induced by each method are emphasized in the zoomed plots of Figure 15. Note that spline methods are not designed to extrapolate, potentially causing error at temporal edges.

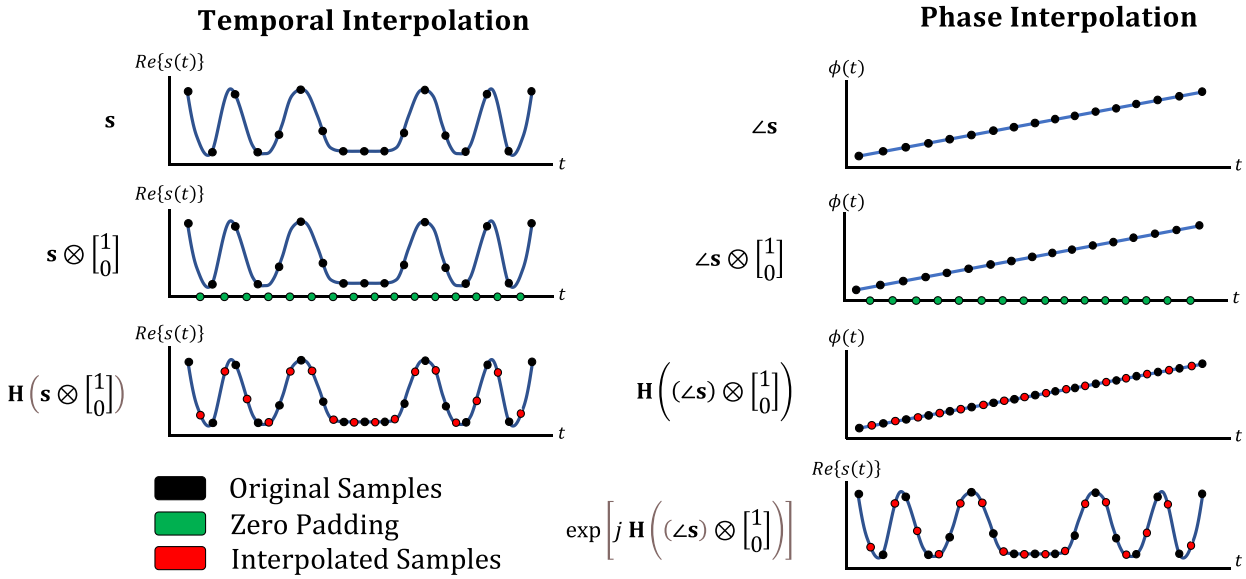

Figure 14: Stages of temporal interpolation and phase interpolation

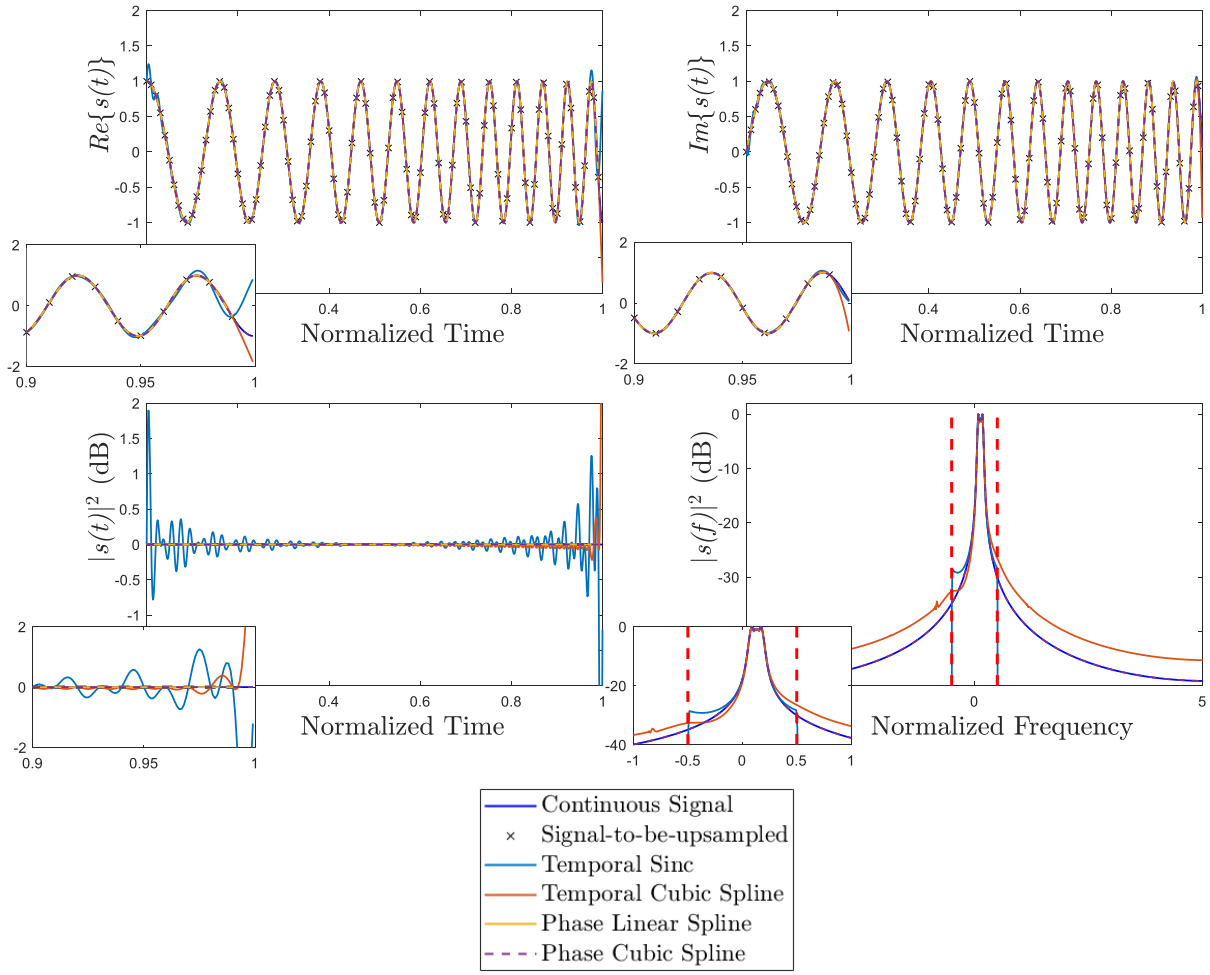

Figure 15: Temporal and phase interpolation methods. Phase interpolation methods overlap the continuous signal with minimal error.

1.4.1.9. ANALOG DOWNCONVERSION

Two common methods exist to form a complex baseband signal from an electromagnetic wave captured at passband, which are analog downconversion and digital downconversion & decimation. The choice of analog or digital downconversion often amounts to which equipment is commercially available and sufficient for an engineering application given hardware costs. For instance, real-time spectrum analayzers (RSA) often have built-in analog downconversion, while high-speed oscilloscopes often require digital downconversion.

Analog downconversion is illustrated in Figure 16 and Figure 17, where ω, f denotes analog frequency and $f_{\mathrm{s}}^{\mathrm{ADC}}$ is the analog-to-digital converter sample rate. To capture the baseband signal: A) the received passband signal is bandpass filtered to remove out-of-band interference, B) the filtered passband signal is mixed with either $\cos(\omega_c t)$ or $-\sin(\omega_{\mathrm{c}} t)$ on separate channels, C) the analog baseband signals are lowpass filtered to remove mixer output higher order products and sampled on ADCs. The basis component $-\sin(\omega_{\mathrm{c}} t) = \cos\left(\omega_{\mathrm{c}} t - \frac{\pi}{2}\right)$ is created by pushing the $\cos(\omega_{\mathrm{c}} t)$ oscillator through a 90° phase shifter analog component to maintain phase coherence between channels. The ADC sample rate can be increased to mitigate the effects of aliasing due to imperfect signal spectral containment (with diminishing returns when $f_{\mathrm{s}}^{\mathrm{ADC}} \gg 2f_{\max}$).

I/Q imbalance exists when the downconverted inphase and quadrature channels have inequal scaling $\left(c_{\mathrm{I}}(t)\ \&\ c_{\mathrm{Q}}(t)\right)$ due to RF fabrication variations, local oscillator (LO) amplitude variations, or crosstalk from the passband channel to the LO channel [55]. Crosstalk from the LO to the passband channels in the receive chain, called receive LO leakage, can be mathematically represented as a DC offset $\left(d_{\mathrm{I}}(t)\ \&\ d_{\mathrm{Q}}(t)\right)$ of the baseband components $s_{\mathrm{I}}(t)$ and $s_{\mathrm{Q}}(t)$ [56]. If the I/Q imbalance or LO leakage is significant and uncompensated, the baseband waveform may exhibit undesired amplitude and phase distortion. I/Q imbalance and LO leakage may drift over time with environmental factors. Mixers introduce errors due to frequency push-pull effects and intermodulations [57]. The baseband signal when incorporating non-ideal I/Q imbalance and LO leakage effects is represented as

$$s_{\mathrm{bb}}(t) = c_{\mathrm{I}}(t)\left(s_{\mathrm{I}}(t) + d_{\mathrm{I}}(t)\right) + j\, c_{\mathrm{Q}}(t)\left(s_{\mathrm{Q}}(t) + d_{\mathrm{Q}}(t)\right) \tag{1.29}$$

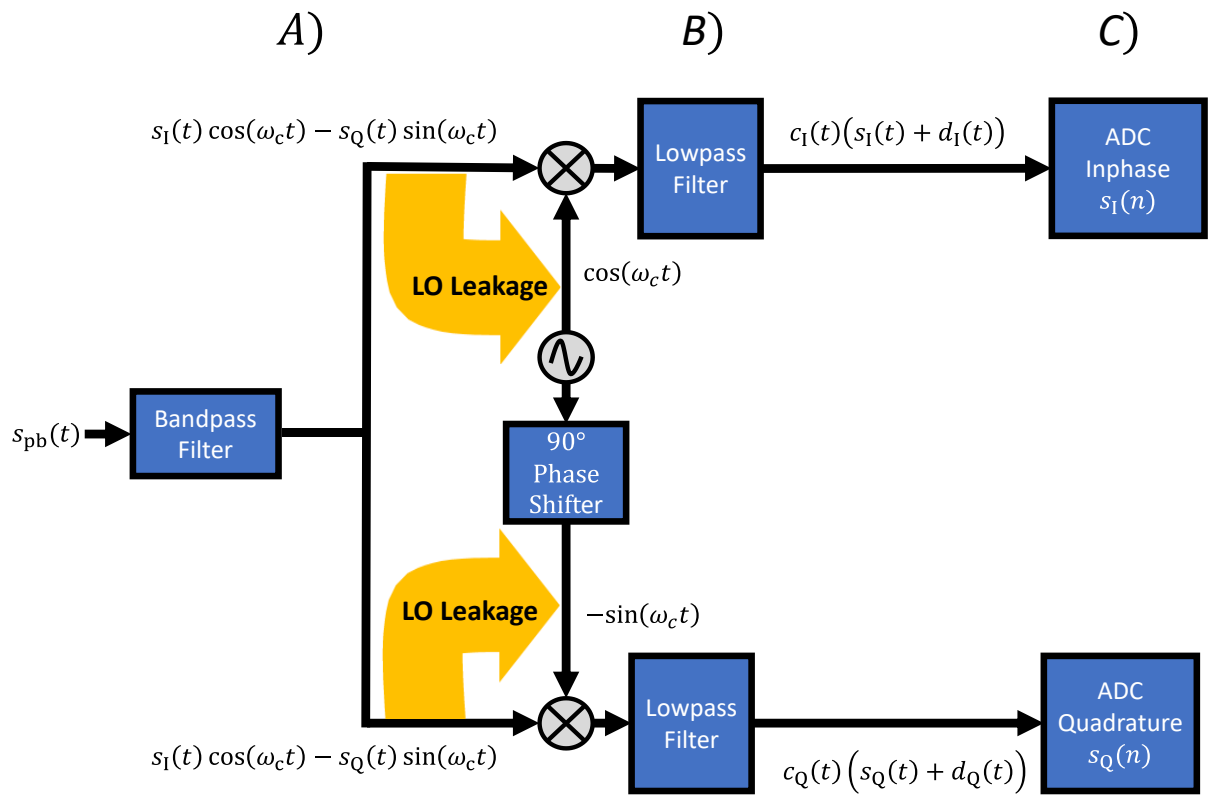

Figure 16: Analog downconversion RF chain.

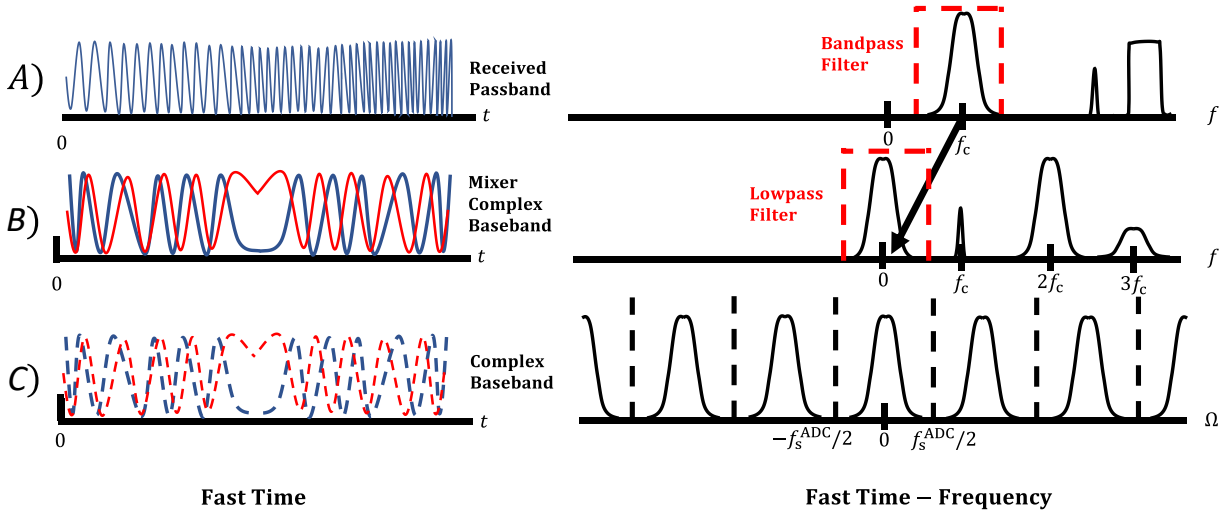

Figure 17: Analog downconversion stages: A) Capture the passband signal and bandpass filter to remove out-of-band interference, B) Mix the filtered passband waveform by either $\cos(\omega_c t)$ or $-\sin(\omega_c t)$, C) Lowpass filter the baseband signals to remove undesired mixing products and sample using separate ADCs.

1.4.1.10. DIGITAL HILBERT TRANSFORM, DOWNCONVERSION, & DOWNSAMPLING

Digital Hilbert transformation, downconversion, & downsampling is illustrated in Figure 18 and Figure 19, where ω, f denotes analog frequency, Ω denotes digital frequency, f_s^{ADC} is the analog-to-digital converter sample rate, and f_s^{RX} is the desired baseband waveform sample rate (i.e. after downsampling). The baseband components are minimally distorted from digital processing, albeit the method is computationally expensive compared to analog downconversion. To capture the baseband signal: A) the received passband signal is bandpass filtered to remove out-of-band interference, B) the filtered passband signal is sampled with an ADC, C) the Hilbert transform is performed on the real passband samples to convert to complex notation, D) the complex passband signal is digitally mixed with a complex carrier for downconversion, E) the complex baseband signal is lowpass filtered to enforce band-limiting and then downsampled (keep every $\tilde{\beta}^{\mathrm{th}}$ time sample) to reduce the sample rate while sufficiently exceeding the Nyquist sample rate.

The real passband signal captured by an ADC must be sampled according to the Nyquist rate $f_s^{\mathrm{ADC}} \geq 2f_{\max}$. Upon bandpass filtering and sampling the real passband signal (having a symmetric frequency spectrum), the Hilbert transform is applied to cancel redundant negative frequencies, thereby converting samples to complex notation. The Hilbert transformed signal $s_{\mathrm{H}}(t)$ is defined as

$$
\begin{aligned}
s_{\mathrm{H}}(t) &= s_{\mathrm{pb}}(t) + j\,\mathcal{H}\left(s_{\mathrm{pb}}(t)\right) = s_{\mathrm{pb}}(t) + j\left(s_{\mathrm{pb}}(t) * \frac{-1}{\pi t}\right) \\
s_{\mathrm{H}}(f) &= s_{\mathrm{pb}}(f) + j\,\mathcal{H}\left(s_{\mathrm{pb}}(f)\right) = s_{\mathrm{pb}}(f) + j\left(s_{\mathrm{pb}}(f) \cdot -j\,\mathrm{sgn}(f)\right) \\
&= \left(s_{\mathrm{pb}}^{+}(f) + s_{\mathrm{pb}}^{-}(f)\right) + \left(\left(s_{\mathrm{pb}}^{+}(f) + s_{\mathrm{pb}}^{-}(f)\right) \cdot \mathrm{sgn}(f)\right) \\
&= \left(s_{\mathrm{pb}}^{+}(f) + s_{\mathrm{pb}}^{-}(f)\right) + \left(s_{\mathrm{pb}}^{+}(f) - s_{\mathrm{pb}}^{-}(f)\right) \\
&= 2\,s_{\mathrm{pb}}^{+}(f)
\end{aligned}
$$

(1.30)

where $s_{\mathrm{pb}}^{+}(f)$ indicates positive frequencies and $s_{\mathrm{pb}}^{-}(f)$ indicates negative frequencies of the passband signal. The signum function $\mathrm{sgn}(f)$ is equal to +1 for positive frequencies, -1 for negative frequencies, and 0 at $f = 0$. For FM signals, $\mathcal{H}\left(A\cos\left(\omega_{\mathrm{c}}t + \phi(t)\right)\right) = A\sin\left(\omega_{\mathrm{c}}t + \phi(t)\right)$ and simplifies as in (1.6). Applying the Hilbert transform mitigates frequency aliasing in subsequent steps.

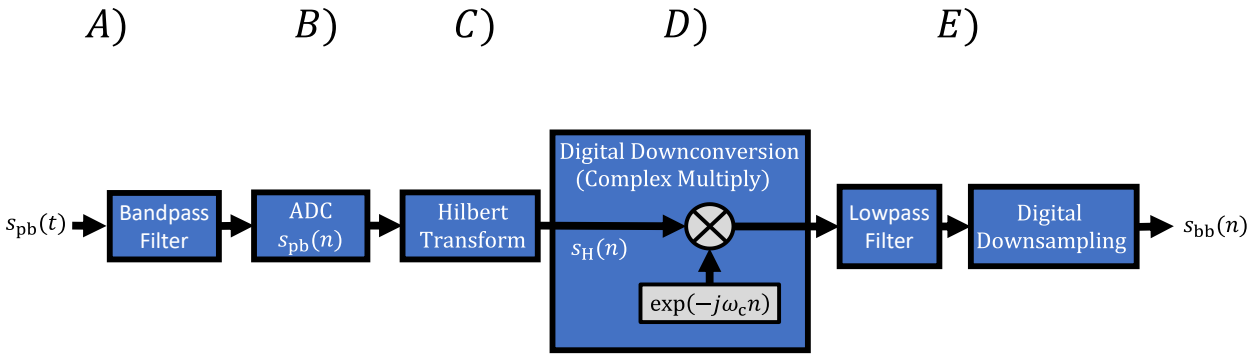

Figure 18: Digital Hilbert transform, downconversion, and downsampling chain.

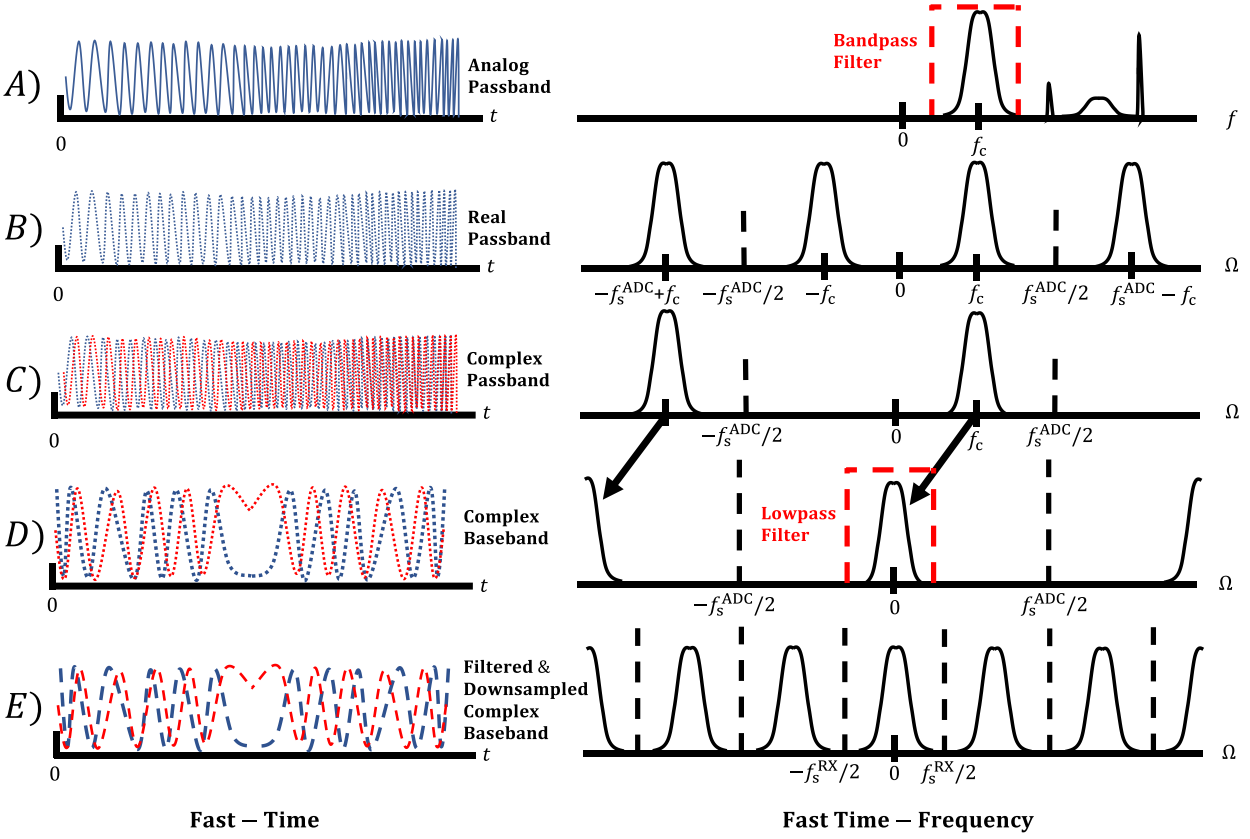

Figure 19: Digital Hilbert transformation, downconversion, & downsampling stages: A) Capture the passband signal and analog bandpass filter to remove out-of-band interference, B) Sample the filtered passband signal with an ADC, C) Apply the Hilbert transform to the real passband samples to convert to complex data representation D) Mix the digital complex baseband waveform with a complex sinusoid at frequency f_c for downconversion, E) Downsample the data for compression while still exceeding the Nyquist sample rate.

Consider a passband signal captured with initial ADC sample rate f_s^{ADC}. Digital downconversion converts the passband signal from center frequency f_c to baseband representation. The resulting baseband signal is often oversampled relative to the Nyquist sample rate. Digital downsampling is beneficial when the ADC sample rate is unnecessarily greater than the desired baseband waveform sample rate, $f_s^{\mathrm{ADC}} = \tilde{\beta} \cdot f_s^{\mathrm{RX}} > f_s^{\mathrm{RX}}$, where $\tilde{\beta}$ is an integer downsampling factor. Digital downsampling requires lowpass filtering to ensure the baseband signal is sufficiently bandlimited), then preserving every $\tilde{\beta}$ samples to reduce the incoming data rate. Cascaded integrator comb (CIC) filters and polyphase filter banks (PFBs) are computationally efficient implementations for digital downsampling [58].

1.4.1.11. SUB-NYQUIST SAMPLING

When the available ADC sample rate is less than the frequency of interest, sub-Nyquist sampling is suitable to capture the information. The sub-Nyquist sampling method exploits discrete frequency periodicity, wherein sampling a bandlimited signal produces spectral duplicates spaced at frequency integer multiples $\varsigma\, f_s^{\mathrm{ADC}}$. Sub-Nyquist sampling is often paired with analog frequency conversion, implemented in certain SDRs.

For example, consider the analog downconversion stages described in Section 1.4.1.9, though now with local oscillators tuned to an arbitrary frequency $\omega_0 = 2\pi f_0$. When $\omega_0 = \omega_c$, direct analog downconversion occurs as aforementioned. However, ω_0 may be tuned to convert the passband signal to an intermediate center frequency $\omega_{\mathrm{IF}} = 2\pi f_{\mathrm{IF}}$, where $\omega_{\mathrm{IF}} = \omega_c - \omega_0$. The duplicate image of the discretized intermediate frequency signal spectrum is then captured at baseband center frequency $\omega_{\mathrm{IF}} - \varsigma\, f_s^{\mathrm{ADC}}$, where $-f_s^{\mathrm{ADC}}/2 < \omega_{\mathrm{IF}} - \varsigma\, f_s^{\mathrm{ADC}} < f_s^{\mathrm{ADC}}/2$ determines the integer ς. The combined analog downconversion and sub-Nyquist sampling method is illustrated in Figure 20 and Figure 21, where ω, f denotes analog frequency and f_s^{ADC} is the analog-to-digital converter sample rate. To capture the baseband signal: A) the received passband signal is bandpass filtered to remove out-of-band interference, B) the filtered passband signal is mixed with either $\cos(\omega_0 t)$ or $-\sin(\omega_0 t)$ on separate channels, C) the analog intermediate frequency signals are bandpass filtered to remove mixer products and enforce bandlimiting, then sub-Nyquist sampled on separate ADCs.

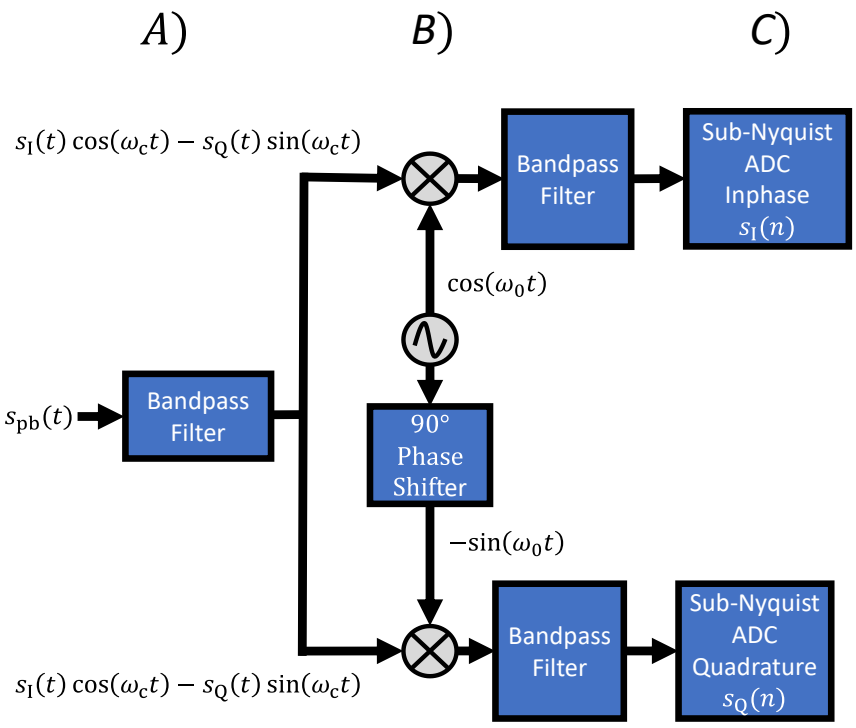

Figure 20: Combined analog downconversion RF chain and sub-Nyquist sampling.

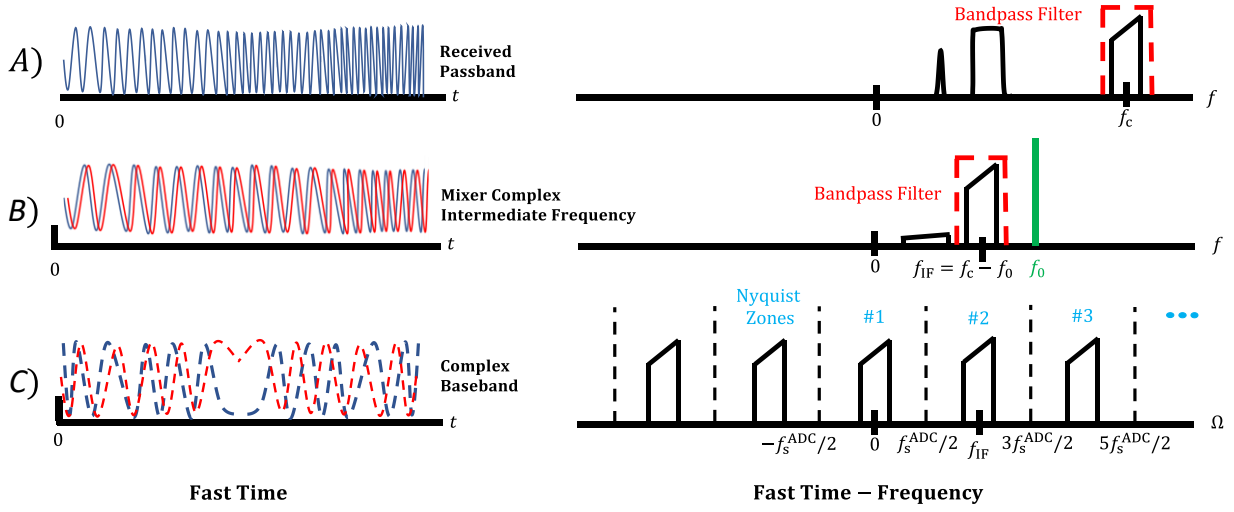

Figure 21: Combined analog downconversion and sub-Nyquist sampling stages: A) Capture the passband signal and bandpass filter to remove out-of-band interference, B) Mix the filtered passband waveform by either $\cos(\omega_0 t)$ or $-\sin(\omega_0 t)$, C) Bandpass filter the intermediate frequency signals to remove undesired mixing products and enforce bandlimiting, then sub-Nyquist sample using separate ADCs.

1.4.1.12. PHASE COHERENCE

Phase coherence refers to the degree of accuracy between the true phase and estimated phase of a given sinusoidal wave, relative to a given time-frequency reference point. The phase of a sinusoid $\cos\big(\omega_{\text{ref}} \cdot (t - t_{\text{ref}})\big)$ depends on the true reference center frequency ω_{ref} and reference time t_{ref}. Multiple RF systems are mutually phase coherent when synchronized to the same time-frequency reference point within an acceptable uncertainty. For example, an analog downconverter (see 1.4.1.9) forms orthogonal inphase and quadrature baseband channels by mixing the passband signal with phase coherent oscillators $\cos\big(\omega_{\text{ref}} \cdot (t - t_{\text{ref}})\big)$ and $-\sin\big(\omega_{\text{ref}} \cdot (t - t_{\text{ref}})\big)$. If the oscillators are not phase coherent $\big(\text{e.g. } \cos\big(\omega_1 \cdot (t - t_1)\big) \text{ and } -\sin\big(\omega_2 \cdot (t - t_2)\big),\ t_1 \neq t_2,\ \omega_1 \neq \omega_2\big)$, then the baseband channels are no longer orthogonal and the generated baseband signal does not accurately represent the passband signal information.

Consider the phase coherence between a transmitter and receiver. A coherent radar system minimizes the uncertainty of the propagation delay t_{delay} between the transmitter and receiver, thus allowing for accurate radar localization. For convenience, the time-frequency reference t_{ref} and ω_{ref} is set relative to the radar transmitter. The transmit signal $s_{\text{pb}}(t)$ is emitted in a vacuum with center frequency ω_{ref} beginning at a time reference t_{ref}

$$s_{\text{pb}}(t - t_{\text{ref}}) = A(t - t_{\text{ref}}) \cos\big(\omega_{\text{ref}} \cdot (t - t_{\text{ref}}) + \phi(t - t_{\text{ref}})\big) \tag{1.31}$$

After a given time delay t_{delay} traversed at the speed of light, the transmit signal is recorded by the receiver as

$$y(t) = A\big(t - t_{\text{ref}} - t_{\text{delay}}\big) \cos\Big(\omega_{\text{ref}} \cdot \big(t - t_{\text{ref}} - t_{\text{delay}}\big) + \phi\big(t - t_{\text{ref}} - t_{\text{delay}}\big)\Big) \tag{1.32}$$

To determine the propagation delay t_{delay}, the receive signal $y(t)$ is mixed with oscillators to yield the receive signal $y_{\text{mix}}(t, \omega'_{\text{ref}}, t'_{\text{ref}})$, where ω'_{ref} and t'_{ref} are the assumed (but potentially incorrect) time-frequency references.

$$
\begin{aligned}
y_{\text{mix}}(t, \omega'_{\text{ref}}, t'_{\text{ref}}) &= y(t) \cdot \left(\cos\left(\omega'_{\text{ref}} \cdot (t - t'_{\text{ref}})\right) - j \sin\left(\omega'_{\text{ref}} \cdot (t - t'_{\text{ref}})\right)\right) \\
&= A\left(t - t_{\text{ref}} - t_{\text{delay}}\right) \cos\left(\omega_{\text{ref}} \cdot \left(t - t_{\text{ref}} - t_{\text{delay}}\right) + \phi\left(t - t_{\text{ref}} - t_{\text{delay}}\right)\right) \\
&\qquad \cdot \left(\cos\left(\omega'_{\text{ref}} \cdot (t - t'_{\text{ref}})\right) - j \sin\left(\omega'_{\text{ref}} \cdot (t - t'_{\text{ref}})\right)\right) \\
&= \frac{1}{2} A\left(t - t_{\text{ref}} - t_{\text{delay}}\right) \\
&\quad \cdot \left\{ \begin{array}{l} \left[\begin{array}{l} \cos\left(\omega_{\text{ref}} \cdot \left(t - t_{\text{ref}} - t_{\text{delay}}\right) + \omega'_{\text{ref}} \cdot (t - t'_{\text{ref}}) + \phi\left(t - t_{\text{ref}} - t_{\text{delay}}\right)\right) \\ + \cos\left(\omega_{\text{ref}} \cdot \left(t - t_{\text{ref}} - t_{\text{delay}}\right) - \omega'_{\text{ref}} \cdot (t - t'_{\text{ref}}) + \phi\left(t - t_{\text{ref}} - t_{\text{delay}}\right)\right) \end{array} \right] \\ -j \left[\begin{array}{l} \sin\left(\omega_{\text{ref}} \cdot \left(t - t_{\text{ref}} - t_{\text{delay}}\right) + \omega'_{\text{ref}} \cdot (t - t'_{\text{ref}}) + \phi\left(t - t_{\text{ref}} - t_{\text{delay}}\right)\right) \\ + \sin\left(\omega_{\text{ref}} \cdot \left(t - t_{\text{ref}} - t_{\text{delay}}\right) - \omega'_{\text{ref}} \cdot (t - t'_{\text{ref}}) + \phi\left(t - t_{\text{ref}} - t_{\text{delay}}\right)\right) \end{array} \right] \end{array} \right\}
\end{aligned}
$$

(1.33)

After mixing, the additive frequency component of $y_{\text{mix}}(t, \omega'_{\text{ref}}, t'_{\text{ref}})$ is removed by filtering to yield

$$
\begin{aligned}
y_{\text{error}}(t, \omega'_{\text{ref}}, t'_{\text{ref}}) &= \frac{1}{2} A\left(t - t_{\text{ref}} - t_{\text{delay}}\right) \\
&\quad \cdot \left\{ \begin{array}{l} \cos\left(\omega_{\text{ref}} \cdot \left(t - t_{\text{ref}} - t_{\text{delay}}\right) - \omega'_{\text{ref}} \cdot (t - t'_{\text{ref}}) + \phi\left(t - t_{\text{ref}} - t_{\text{delay}}\right)\right) \\ -j \sin\left(\omega_{\text{ref}} \cdot \left(t - t_{\text{ref}} - t_{\text{delay}}\right) - \omega'_{\text{ref}} \cdot (t - t'_{\text{ref}}) + \phi\left(t - t_{\text{ref}} - t_{\text{delay}}\right)\right) \end{array} \right\}
\end{aligned}
$$

(1.34)

A perfectly coherent radar transmitter and receiver will allow for determination of the transmitted signal at a given delay in a vacuum, where $\omega_{\text{ref}} = \omega'_{\text{ref}}$ and $t_{\text{ref}} = t'_{\text{ref}}$, shown in (1.35). Note that a phase shift $\omega_{\text{ref}}\left(-t_{\text{delay}}\right)$ is imposed on the resulting receive signal based on the frequency of operation (relative to wavelength) and the delay of the received signal t_{delay}.

$$
y_{\text{coherent}}(t) = \frac{1}{2} A\left(t - t_{\text{ref}} - t_{\text{delay}}\right) \cdot \left\{ \begin{array}{l} \cos\left(\omega_{\text{ref}}\left(-t_{\text{delay}}\right) + \phi\left(t - t_{\text{ref}} - t_{\text{delay}}\right)\right) \\ -j \sin\left(\omega_{\text{ref}}\left(-t_{\text{delay}}\right) + \phi\left(t - t_{\text{ref}} - t_{\text{delay}}\right)\right) \end{array} \right\}
$$

(1.35)

A radar system is non-coherent if the transmitter and receiver oscillator are not time/phase synchronous within a degree of acceptable uncertainty, where $\omega_{\text{ref}} \neq \omega'_{\text{ref}}$ and/or $t_{\text{ref}} \neq t'_{\text{ref}}$. The time-frequency reference may drift over time due to oscillator phase noise and frequency drift from environmental factors. Frequency coherence error, where $\omega_{\text{ref}} \neq \omega'_{\text{ref}}$ and $t_{\text{ref}} = t'_{\text{ref}}$, leads to drift in temporal and phase estimates over time such that processing over slow time intervals is challenging without compensation.

$$y_{\text{noncoherent}}(t, \omega'_{\text{ref}}) = A(t - t_{\text{delay}}) \left[\cos\left((\omega_{\text{ref}} - \omega'_{\text{ref}}) \cdot (t - t_{\text{delay}}) + \phi(t - t_{\text{delay}})\right)\right]$$

(1.36)

Temporal coherence errors, where $\omega_{\text{ref}} = \omega'_{\text{ref}}$ and $t_{\text{ref}} \neq t'_{\text{ref}}$, leads to incorrect estimation of t_{delay}. Defining $\Delta t_{\text{ref}} = t_{\text{ref}} - t'_{\text{ref}}$, the additional phase term $\omega_{\text{ref}}\left(-\Delta t_{\text{ref}} - t_{\text{delay}}\right)$ imposes additional uncertainty in determining t_{delay}. Here, fine phase coherence errors occur when $\omega_{\text{ref}}\left(-\Delta t_{\text{ref}}\right) < 2\pi$ and coarse phase coherence errors occur when $\omega_{\text{ref}}\left(-\Delta t_{\text{ref}}\right) > 2\pi$. Practically, temporal coherence errors can be calibrated for by GPS or observance of strong scene reflections at known locations [20].

$$y_{\text{noncoherent}}(t, t'_{\text{ref}}) = A(t - \Delta t_{\text{ref}} - t_{\text{delay}}) \left[\cos\left(\omega_{\text{ref}} \cdot (-\Delta t_{\text{ref}} - t_{\text{delay}}) + \phi(t - \Delta t_{\text{ref}} - t_{\text{delay}})\right)\right]$$

(1.37)

Illustrations of each coherence error are shown in Figure 22. All radar systems considered henceforth are assumed to be phase coherent systems, such that non-ideal range uncertainties are assumed negligible.

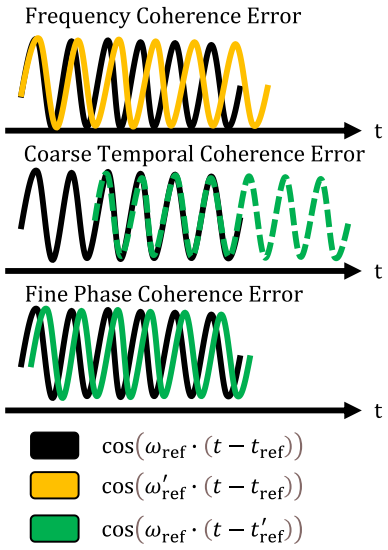

Figure 22: Types of radar coherence errors, resulting in inaccuracies for target range/Doppler estimation and radar processing. Phase coherence between channels is dependent on the assumed center frequency, temporal synchronization (coarse tuning between fast time samples), and phase synchronization (fine tuning of phase relative to the center frequency).

1.4.1.13. REVIEW OF FOURIER TRANSFORMATIONS

Four flavors of Fourier notation include the Fourier Transform (FT), Fourier Series (FS), Discrete Time Fourier Transform (DTFT), and Discrete Fourier Transform (DFT). Each transform represents a transference between a discrete/continuous time dimension to a discrete/continuous frequency dimension for signals of periodic/aperiodic nature as summarized in Figure 23 [42]. While each Fourier representation has purpose, modern radar systems often implement discrete time processing. Consequently, the DFT and DTFT are of interest as transformations from discrete time to discrete/continuous frequency. The DFT assumes input signal periodicity, though the DFT is often applied to aperiodic input signals and the error is assumed negligible.

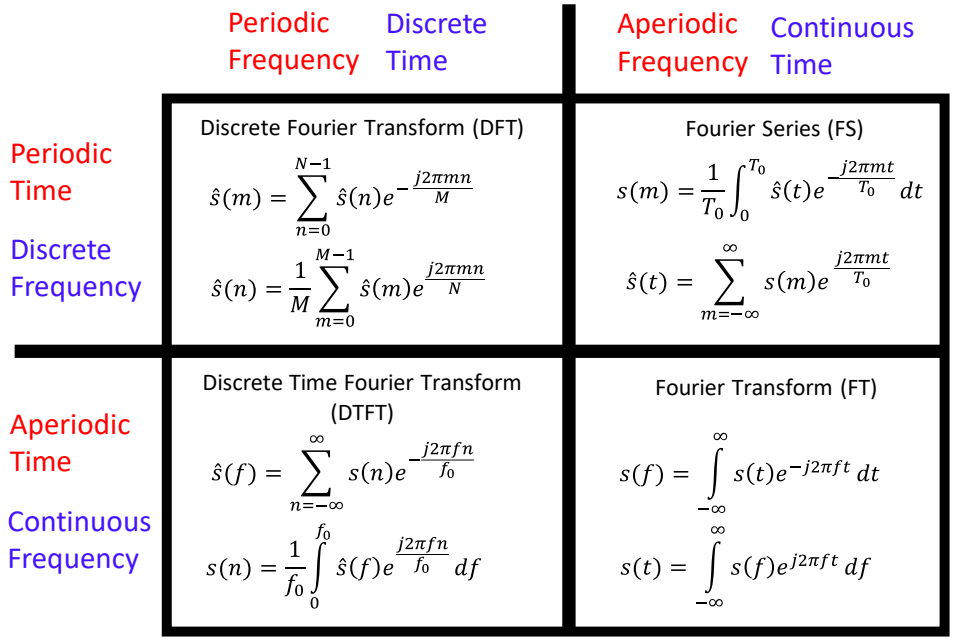

Figure 23: Summary of Fourier methods. Periodicity is indicated by the $\hat{\cdot}$ accent.

The formal definition of the discrete Fourier transform (DFT) and inverse discrete Fourier transform (IDFT) is

$$s(m) = \sum_{n=0}^{N-1} s(n) e^{-\frac{j2\pi mn}{M}}$$
$$s(n) = \frac{1}{M} \sum_{m=0}^{M-1} s(m) e^{\frac{j2\pi mn}{N}} \quad (1.38)$$

The DFT and IDFT are defined over discrete time $\mathbf{n} = [0 \quad \cdots \quad N-1]^T$ and frequency $\mathbf{m} = [0 \quad \cdots \quad M-1]^T$. The square DFT matrix $\mathbf{A}$ and IDFT matrix $\mathbf{A}^H$ are defined with equal dimensions ($N = M$).

$$\begin{aligned}\mathbf{A} &= e^{-j2\pi(\mathbf{m}\,\mathbf{n}^T)/N} \\ \mathbf{s}_\mathrm{f} &= \mathbf{A}\mathbf{s} \\ \mathbf{s} &= \left(\frac{1}{N}\right)\mathbf{A}^H\mathbf{s}_\mathrm{f} \\ \mathbf{s} &= \left(\frac{\mathbf{A}^H\mathbf{A}}{N}\right)\mathbf{s} = (\mathbf{I})\mathbf{s}\end{aligned}$$

(1.39)

The square transformation matrix $\mathbf{T}$ applies a DFT circular shift vector rearrangement. The operation $\mathbf{T}\mathbf{s}_\mathrm{f}$ swaps the former length $\lceil N/2 \rceil$ and latter length $\lfloor N/2 \rfloor$ halves of the vector $\mathbf{s}_\mathrm{f}$, where $\lceil \cdot \rceil$ is the ceil operator and $\lfloor \cdot \rfloor$ is the floor operator. The transformation matrix $\mathbf{T}^T$ applies an IDFT circular shift vector rearrangement. The operation $\mathbf{T}^T\mathbf{s}_\mathrm{f}$ swaps the former length $\lfloor N/2 \rfloor$ and latter length $\lceil N/2 \rceil$ halves of the vector $\mathbf{s}_\mathrm{f}$, undoing the DFT shift. For convenience, the matrices $\bar{\mathbf{A}} = \mathbf{A}\mathbf{T}^T$ and $\bar{\mathbf{A}}^H = \mathbf{T}\mathbf{A}^H$ are defined.

1.4.1.14. PARSEVAL'S THEOREM AND THE L_p-NORM

Parseval's theorem formally states the unitary transformation property of the Fourier transform, which defines that the time and frequency representations have equal energy. Here, $\|\cdot\|_2$ is the L_2-norm operation.

$$\int_{-\infty}^{\infty} |s(t)|^2 dt = \|s(t)\|_2^2 = \int_{-\infty}^{\infty} |s(f)|^2 dt = \|s(f)\|_2^2$$

(1.40)

Parseval's theorem is valid for the discrete Fourier transform, though the frequency vector "energy" must be scaled by the number of DFT samples in accordance with (1.38).

$$\sum_{n=0}^{N-1} |s(n)|^2 = \mathbf{s}^H\mathbf{s} = \|\mathbf{s}\|_2^2 = \frac{1}{M}\sum_{m=0}^{M-1} |s(m)|^2 = \frac{\mathbf{s}_\mathrm{f}^H\mathbf{s}_\mathrm{f}}{N} = \frac{\|\mathbf{s}_\mathrm{f}\|_2^2}{N}$$

(1.41)

The L_p -norm of the continuous signal $s(t)$ or the discrete vector $\mathbf{s}$ is formally defined as

$$\|s(t)\|_p = \left(\int_{-\infty}^{\infty} |s(t)|^p \, dt \right)^{1/p}$$
$$\|\mathbf{s}\|_p = \left(\sum_{n=0}^{N-1} |s(n)|^p \right)^{1/p}$$

(1.42)

As $p \to \infty$, the norm determines the signal maximum magnitude (where $p = 8$ is a sufficient approximation). Additionally, $p = 2$ determines the signal root-mean squared magnitude (called the Euclidean norm) and $p = 1$ determines the signal mean magnitude.

1.4.1.15. ADDITIVE WHITE GAUSSIAN NOISE (AWGN)

Additive white Gaussian noise (AWGN) refers to the background radiation of the universe, which temporally exhibits zero-mean Gaussian distribution due to the statistical central limit theorem amidst extraterrestrial sources [61]. Noise perturbations are frequency indiscriminate, exhibiting a uniform power spectrum as the observation interval increases. The ratio of the average signal power $\mathcal{P}_\mathrm{s}$ to the expected noise power $\mathcal{P}_\mathrm{v}$ over the interval T_p is called the unprocessed signal-to-noise ratio (SNR). The additive noise $v(t)$ has an expected power $\mathrm{E}\{|v(t)|^2\}$ equal to the variance σ_v^2 for the mean-ergodic, zero-mean Gaussian process [61].

$$\mathrm{SNR}_\mathrm{init} = \frac{\mathcal{P}_\mathrm{s}}{\mathcal{P}_\mathrm{v}} = \frac{\mathcal{P}_\mathrm{s}}{\mathrm{E}_\mathrm{v}\{|v(t)|^2\}} = \frac{\mathcal{P}_\mathrm{s}}{\sigma_\mathrm{v}^2} = \frac{\frac{1}{T_\mathrm{p}} \int_0^{T_\mathrm{p}} |s(t)|^2 dt}{\lim\limits_{T \to \infty} \left\{ \frac{1}{T} \int_0^{T} |v(t)|^2 dt \right\}}$$

(1.43)

Upon sampling the random process $v(t)$, the sample values are determined. The discrete initial SNR is expressed as

$$\mathrm{SNR}_\mathrm{init} = \frac{\mathcal{P}_\mathrm{s}}{\mathcal{P}_\mathrm{v}} = \frac{\mathcal{P}_\mathrm{s}}{\mathrm{E}_\mathrm{v}\{|v(n)|^2\}} = \frac{\mathcal{P}_\mathrm{s}}{\sigma_\mathrm{v}^2} = \frac{\frac{1}{N_\mathrm{p}} \sum_{\forall n} |s(n)|^2}{\lim\limits_{N \to \infty} \left\{ \frac{1}{N} \sum_{\forall n} |v(n)|^2 \right\}} \approx \frac{\|\mathbf{s}\|_2^2}{\|\mathbf{v}\|_2^2} \, .$$

(1.44)

1.4.2. RANGE

The fast time dimension refers to unprocessed data collected over the radar CPI, whereas the range dimension refers to processed data that provides ranging information about the illuminated scene. Here, a simple RF scattering environment is considered to define fundamental phenomenology. The transmit signal is assumed to be frequency modulated, in consideration of amplifier power efficiency and distortions, such that the waveform instantaneous frequency is $f_{\mathrm{i}}(t) = \frac{1}{2\pi}\left(\frac{d\phi(t)}{dt}\right)$.

1.4.2.1. ELECTROMAGNETIC FUNDAMENTALS

The fundamentals of electromagnetic scattering are briefly discussed here to establish a physical context for range dimension modeling. The reader is referred to [62] for additional details on electromagnetic theory and antenna considerations. First, electromagnetic equations are defined to describe radiation from a source located at the coordinate origin. Second, electromagnetic equations are defined to describe radiation from a source located at an arbitrary position. Third, Maxwell's wave equation and the Green's function are defined. The Green's function substantiates that electromagnetic scattering can be modeled as convolution between the transmit signal and point scatterers in the environment. Fourth, the Borne approximation is defined to establish the assumptions involved when modeling electromagnetic scattering as a linear process.

Consider a time-harmonic signal traveling in a free space vacuum. An ideal antenna located at position $\bar{r}$ receives the electromagnetic fields emitted from a source located at the origin. The electric field strength $\vec{\mathbf{E}}(\bar{r},t)$ $[\mathrm{V/m}]$ and magnetic field strength $\vec{\mathbf{H}}(\bar{r},t)$ $[\mathrm{A/m}]$ form the magnitude power density as $\overrightarrow{\mathbf{W}}(\bar{r})$ $[\mathrm{W/m^2}]$. The wave intensity $U(\theta,\varphi)$ $[\mathrm{W/steradian}]$ describes the power density normalized relative to a 4π steradian spherical spreading loss, which characteristically drops off with range between two points as $1/r^2$. Note that the Poynting vector $\overrightarrow{\mathbf{W}}(\bar{r})$ is not a function of time, as the fields $\vec{\mathbf{E}}(\bar{r},t)$ and $\vec{\mathbf{H}}(\bar{r},t)$ are spatially orthogonal fields for all time and thus deliver constant power at a given spatial position (consider the analogous time dimension description from Section 1.4.1.4). The electromagnetic definitions from (1.45)-(1.49) are written with respect to a transmission source located at the origin to provide the simplest basis coordinates, which are then generalized.

$$\begin{aligned}\vec{\mathbf{E}}(\bar{r},t) &= \frac{1}{r}\left(E_\theta\left(\hat{\boldsymbol{r}}(\theta,\varphi)\right)\widehat{\boldsymbol{\theta}} + E_\varphi\left(\hat{\boldsymbol{r}}(\theta,\varphi)\right)\widehat{\boldsymbol{\varphi}}\right)e^{-jk_0(t)r}e^{j(\omega_c t+\phi(t))} && \text{(Extended Notation)}\\ &= \frac{1}{r}\vec{\mathbf{e}}\left(\hat{\boldsymbol{r}}(\theta,\varphi)\right)e^{-jk_0(t)r}e^{j(\omega_c t+\phi(t))} && \text{(Vector Notation)}\\ &= \frac{1}{r}\left|\vec{\mathbf{e}}\left(\hat{\boldsymbol{r}}(\theta,\varphi)\right)\right|\,\hat{\mathbf{e}}\left(\hat{\boldsymbol{r}}(\theta,\varphi)\right)e^{-jk_0(t)r}e^{j(\omega_c t+\phi(t))} && \text{(Magnitude/Polarization Notation)}\end{aligned}$$

(1.45)

$$\vec{\mathbf{H}}(\bar{r},t) = \frac{1}{-j\omega\mu_0}\left(\nabla\times\vec{\mathbf{E}}(\bar{r},t)\right)$$

(1.46)

$$\begin{aligned}\overrightarrow{\mathbf{W}}(\bar{r}) &= \frac{1}{2}Re\left\{\vec{\mathbf{E}}(\bar{r},t)\ \times\ \vec{\mathbf{H}}(\bar{r},t)\right\}\\ &= \frac{\left(\left|E_\theta\left(\hat{\boldsymbol{r}}(\theta,\varphi)\right)\right|^2 + \left|E_\varphi\left(\hat{\boldsymbol{r}}(\theta,\varphi)\right)\right|^2\right)}{2\eta_0}\frac{\hat{\mathbf{r}}(\theta,\varphi)}{r^2} && \text{(Extended Notation)}\\ &= \frac{\left|\vec{\mathbf{e}}\left(\hat{\boldsymbol{r}}(\theta,\varphi)\right)\right|^2}{2\eta_0}\frac{\hat{\mathbf{r}}(\theta,\varphi)}{r^2} && \text{(Vector Notation)}\\ &= U\left(\hat{\boldsymbol{r}}(\theta,\varphi)\right)\frac{\hat{\mathbf{r}}(\theta,\varphi)}{r^2} && \text{(Intensity Notation)}\end{aligned}$$

(1.47)

$$\bar{r} = r\sin(\theta)\,cos(\varphi)\hat{\mathbf{x}} + r\sin(\theta)\,sin(\varphi)\hat{\mathbf{y}} + rcos(\theta)\hat{\mathbf{z}} \qquad \text{(Spherical to Cartesian Mapping)}$$

(1.48)

$$\hat{\boldsymbol{r}}(\theta,\varphi) = \frac{\bar{r}(\theta,\varphi)}{|\bar{r}(\theta,\varphi)|} = \frac{\bar{r}(\theta,\varphi)}{r} \qquad \text{(Normalized Direction Unit Vector)}$$

(1.49)

The value μ_0 is the magnetic permeability of free-space, η_0 is the intrinsic impedance of free-space, and $k_0(t) = \frac{2\pi(f_c+f_{\mathrm{i}}(t))}{c} = \frac{\left(\omega_c+\frac{d\phi(t)}{dt}\right)}{c} = \frac{2\pi}{\lambda(t)}$ is the wavenumber in the direction of propagation.

The wavenumber $k_0(t)$ is often assumed constant (i.e. $k_0(t) = k_0$ and $\lambda(t) = \lambda_c$) to decouple the space-time dimensions (implying that the waveform has narrow bandwidth). Coupling exists when the instantaneous frequency $f_{\mathrm{i}}(t)$ significantly deviates from the center frequency f_c (implying that the waveform has wide bandwidth).

E_θ and E_φ are components of the electric field vector $\vec{\mathbf{e}}$ defined in the $\widehat{\boldsymbol{\theta}}$ and $\widehat{\boldsymbol{\varphi}}$ spherical unit vector directions. The electric field vector $\vec{\mathbf{e}}$ is decomposed into magnitude $\left|\vec{\mathbf{e}}\left(\hat{\boldsymbol{r}}(\theta,\varphi)\right)\right|$ and polarization $\hat{\mathbf{e}}\left(\hat{\boldsymbol{r}}(\theta,\varphi)\right)$ components.

The term $e^{-jk_0(t)r}$ describes the wavefront phase with respect to spatial position. The term $e^{j(\omega_c t+\phi(t))}$ describes the phase with respect to time, independent of spatial position r.

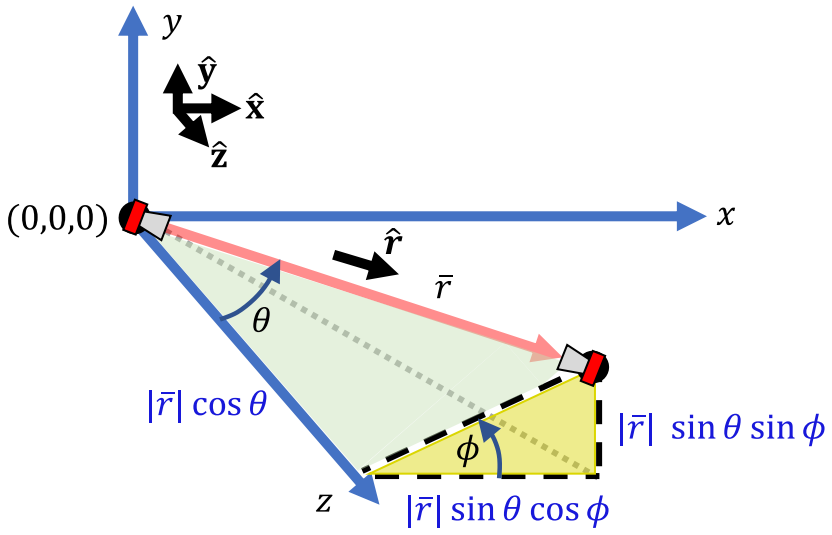

Figure 24: Spherical coordinate system electromagnetic definitions.

The equations outlined in (1.50)-(1.55) are a generalization of (1.45)-(1.49). Two ideal antennas located at arbitrary locations $\bar{r}$ and $\bar{r}'$ receive and transmit electromagnetic fields, respectively. The electric field strength $\vec{\mathbf{E}}(\bar{k},t)$ [V/m] and magnetic field strength $\vec{\mathbf{H}}(\bar{k},t)$ [A/m] form a magnitude power density $\overrightarrow{\mathbf{W}}(\bar{k})$ [W/m^2]. The wave intensity $U(\theta,\varphi)$ [W/steradian] describes the power density normalized relative to a 4π steradian spherical spreading loss, which characteristically drops off with range between two points as $1/R^2$, where $R = r - r'$. Notice that $\hat{\boldsymbol{k}}$ is defined between two arbitrary positions $\bar{r}$ and $\bar{r}'$. Because $\hat{\boldsymbol{k}}$ is dependent on two arbitrary positions, the electric field is now defined in terms of vector components that are orthogonal to $\hat{\boldsymbol{k}}$, namely the horizontal $\hat{\boldsymbol{h}}$ and vertical $\hat{\boldsymbol{v}}$ vector components. The polarization components in $\hat{\mathbf{e}}(\hat{\boldsymbol{k}})$ are likewise defined by the horizontal $\hat{\boldsymbol{h}}$ and vertical $\hat{\boldsymbol{v}}$ vector components.

$$\vec{\mathbf{E}}(\bar{r},t)=\frac{1}{|R|}\left(E_H(\hat{\boldsymbol{k}})\hat{\boldsymbol{h}}+E_V(\hat{\boldsymbol{k}})\hat{\boldsymbol{v}}\right)e^{-jk_0(t)|R|}e^{j(\omega_c t+\phi(t))}=\frac{1}{|R|}\left(E_H(\hat{\boldsymbol{k}})\hat{\boldsymbol{h}}+E_V(\hat{\boldsymbol{k}})\hat{\boldsymbol{v}}\right)e^{-jk_0(t)\,\hat{\mathbf{k}}\cdot(\bar{r}-\bar{r}')}e^{j(\omega_c t+\phi(t))}$$

$$=\frac{1}{|R|}\left(E_H(\hat{\boldsymbol{k}})e^{+j\bar{k}(t)\cdot\bar{r}'}\,\hat{\boldsymbol{h}}+E_V(\hat{\boldsymbol{k}})e^{+j\bar{k}(t)\cdot\bar{r}'}\,\hat{\boldsymbol{v}}\right)e^{-j\bar{k}(t)\cdot\bar{r}}e^{j(\omega_c t+\phi(t))}\qquad\text{(Extended Notation)}$$

$$=\frac{1}{|R|}\vec{\mathbf{e}}(\hat{\boldsymbol{k}},t)e^{-j\bar{k}(t)\cdot\bar{r}}e^{j(\omega_c t+\phi(t))}\qquad\text{(Vector Notation)}$$

$$=\frac{1}{|R|}\left|\vec{\mathbf{e}}(\hat{\boldsymbol{k}})\right|\hat{\mathbf{e}}(\hat{\boldsymbol{k}},t)e^{-j\bar{k}(t)\cdot\bar{r}}e^{j(\omega_c t+\phi(t))}\qquad\text{(Magnitude/Polarization Notation)}$$

(1.50)

$$\vec{\mathbf{H}}(\bar{r},t)=\frac{1}{-j\omega\mu_0}\left(\nabla\times\vec{\mathbf{E}}(\bar{r},t)\right)$$

(1.51)

$$\overrightarrow{\mathbf{W}}(\bar{r})=\frac{1}{2}Re\{\vec{\mathbf{E}}(\bar{r},t)\times\vec{\mathbf{H}}(\bar{r},t)\}$$

$$=\frac{\left(\left|E_H(\hat{\boldsymbol{k}})\right|^2+\left|E_V(\hat{\boldsymbol{k}})\right|^2\right)}{2\eta_0}\frac{\hat{\mathbf{k}}}{|R|^2}\qquad\text{(Extended Notation)}$$

$$=\frac{\left|\vec{\mathbf{e}}(\hat{\boldsymbol{k}})\right|^2}{2\eta_0}\frac{\hat{\mathbf{k}}}{|R|^2}\qquad\text{(Vector Notation)}$$

$$=U(\hat{\boldsymbol{k}})\frac{\hat{\mathbf{k}}}{|R|^2}\qquad\text{(Intensity Notation)}$$

(1.52)

$$\bar{r}=r\sin(\theta)\,cos(\varphi)\hat{\mathbf{x}}+r\sin(\theta)\,sin(\varphi)\hat{\mathbf{y}}+rcos(\theta)\hat{\mathbf{z}}$$

$$\bar{r}'=r'\sin(\theta')\,cos(\varphi')\hat{\mathbf{x}}+r'\sin(\theta')\,sin(\varphi')\hat{\mathbf{y}}+r'cos(\theta')\hat{\mathbf{z}}$$

(1.53)

$$\hat{\boldsymbol{k}}(\theta,\varphi)=\frac{\bar{r}(\theta,\varphi)-\bar{r}'(\theta,\varphi)}{|\bar{r}(\theta,\varphi)-\bar{r}'(\theta,\varphi)|}$$

$$\bar{k}(t)=k_0(t)\hat{\boldsymbol{k}}$$

(1.54)

$\hat{\boldsymbol{h}}=\dfrac{\hat{\boldsymbol{z}}\times\hat{\boldsymbol{k}}}{|\hat{\boldsymbol{z}}\times\hat{\boldsymbol{k}}|}$ (Orthogonal to $\hat{\boldsymbol{k}}$ *and* $\hat{\boldsymbol{z}}$, horizontal polarization cross $\hat{\boldsymbol{z}}$ direction)

$\hat{\boldsymbol{v}}=\hat{\boldsymbol{k}}\times\hat{\boldsymbol{h}}$ (Orthogonal to $\hat{\boldsymbol{k}}$ *and* $\hat{\boldsymbol{h}}$, vertical polarization in $\hat{\boldsymbol{z}}$ direction)

(1.55)

E_H and E_V are components of the electric field vector $\vec{\mathbf{e}}$ defined in the horizontal $\hat{\boldsymbol{h}}$ and vertical $\hat{\boldsymbol{v}}$ unit vector directions. The electric field vector $\vec{\mathbf{e}}$ is decomposed into magnitude $\left|\vec{\mathbf{e}}(\hat{\boldsymbol{k}})\right|$ and polarization $\hat{\mathbf{e}}(\hat{\boldsymbol{k}},t)$ components.

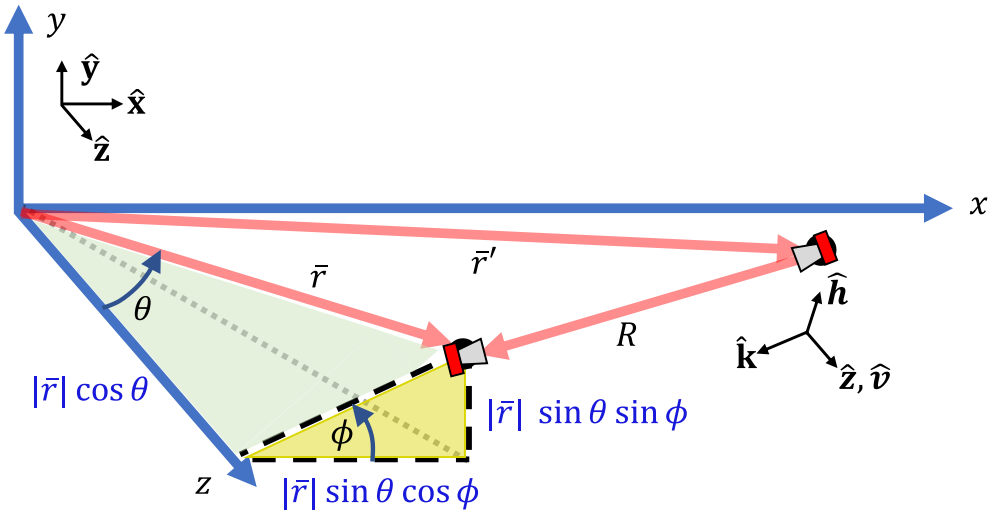

Figure 25: Generalized coordinate system electromagnetic definitions.

Electromagnetic propagation in a vacuum is constituted from Maxwell's electromagnetic wave equation. It can be shown [63] that the electric field $\vec{\mathbf{G}}(\bar{r} - \bar{r}', t)$ originating from an arbitrary source $\vec{\mathbf{S}}(\bar{r}', t)$ transmitting at location $\bar{r}'$ is determined by solving Maxwell's electromagnetic wave equation shown in (1.56).

$$-\nabla \cdot \nabla \vec{\mathbf{G}}(\bar{r} - \bar{r}', t) + \frac{1}{c^2} \frac{\partial^2 \vec{\mathbf{G}}(\bar{r} - \bar{r}', t)}{\partial t^2} = \vec{\mathbf{S}}(\bar{r}', t) \tag{1.56}$$

Assuming $\vec{\mathbf{S}}(\bar{r}', t)$ takes the form of an impulse $\left(\text{i.e. } \vec{\mathbf{S}}_\delta(\bar{r}', t) = \delta(\bar{r}')\delta(t)\right)$, then the transfer function response of the differential equation in (1.56) can be determined, and is referred to as the Green's function in (1.57).

$$\vec{\mathbf{G}}_\delta(\bar{r} - \bar{r}', t) = \frac{\delta\left(t - \frac{|\bar{r} - \bar{r}'|}{c}\right)}{4\pi|\bar{r} - \bar{r}'|} \tag{1.57}$$

Importantly, the wave equation in (1.56) is a linear differential equation. From the impulse transfer function listed in (1.57), the general expression for $\vec{\mathbf{G}}(\bar{r}-\bar{r}',t)$ is written as a convolution between the arbitrary electric field and the impulse response of the system [64]. Conveniently, because the transfer function is simply an impulse response in delayed time and range, the convolution $(*)$ results in an attenuated and delayed copy of the source $\vec{\mathbf{S}}(\bar{r}',t)$.

$$\vec{\mathbf{G}}(\bar{r}-\bar{r}',t)=\vec{\mathbf{S}}(\bar{r}',t)*\vec{\mathbf{G}}_{\delta}(\bar{r}-\bar{r}',t)=\vec{\mathbf{S}}(\bar{r}',t)*\frac{\delta\left(t-\frac{|\bar{r}-\bar{r}'|}{c}\right)}{4\pi|\bar{r}-\bar{r}'|}$$
$$=\frac{\vec{\mathbf{S}}\left(\bar{r}',t-\frac{|\bar{r}-\bar{r}'|}{c}\right)}{4\pi|\bar{r}-\bar{r}'|}$$

(1.58)

The impinging electromagnetic field $\vec{\mathbf{G}}(\bar{r}-\bar{r}',t)$ reflects on a composite scatterer located at $\bar{r}=\bar{r}''$. The Borne approximation [63] asserts that the incident electromagnetic field is the single driving field at each point in the composite scatterer (signifying a collection of point scatterers). The Borne approximation enforces that the waveform is linearly scattered from the environment, where each reflection is deemed independent. The reflected wave $\vec{\mathbf{G}}_{\mathrm{ref}}$ is modeled as a reemission of the incident wave $\vec{\mathbf{G}}_{\mathrm{inc}}$ scaled by the scattering term γ.

$$\vec{\mathbf{G}}_{\mathrm{ref}}(\bar{r}''-\bar{r}',t)=\gamma\vec{\mathbf{G}}_{\mathrm{inc}}(\bar{r}''-\bar{r}',t)$$

(1.59)

Significant error results when extended scatterers or excessive multipath (wave bounces between scatterers before reflecting towards the receiver) are present, as scatterer reflections are no longer independent. The approximation is effective when the scattered field has significantly less power density than the incident field, so multipath becomes sufficiently attenuated.

1.4.2.2. RECEIVED SCATTERING FROM A STATIONARY SCENE

Consider a monostatic radar emitting the passband signal $s_{\mathrm{pb}}(t)$ with narrow bandwidth assumed. The transmit signal propagates towards scatterers, reflects from the scene, then propagates back to the radar receiver for downconversion to baseband. Consider a scene model containing a single stationary point scatterer located at a distance R from the radar. From the Green's function and the Borne approximation, the received backscatter signal from a single point scatterer $y_{\mathrm{pb}}^{\mathrm{single}}(t)$ is a scaled and delayed copy of the transmit signal $s_{\mathrm{pb}}(t)$. The electromagnetic wave has a two-way propagation delay $\tau = 2R/c$ when traveling at the speed of light c. Assume that additive white Gaussian noise (AWGN) is captured at passband, represented by $v_{\mathrm{pb}}(t)$.

$$y_{\mathrm{pb}}^{\mathrm{single}}(t) = s_{\mathrm{pb}}(t) * \big(\gamma\, \delta(t-\tau)\big) + v_{\mathrm{pb}}(t) = \gamma s_{\mathrm{pb}}(t-\tau) + v_{\mathrm{pb}}(t)$$

(1.60)

Attenuation from spherical spreading loss is subsumed into the complex scattering term γ. An implicit assumption is that the scattering term γ is independent of transmit frequency, however, atmospheric effects [65] and frequency dependent scattering [16, 23-28] must be considered in scene specific radar design. The passband signal $y_{\mathrm{pb}}^{\mathrm{single}}(t)$ is demodulated to form the baseband signal $y_{\mathrm{bb}}^{\mathrm{single}}(t)$, where $s_{\mathrm{pb}}(t) = s_{\mathrm{bb}}(t)e^{j2\pi f_{\mathrm{c}}t}$ and $v_{\mathrm{pb}}(t) = v_{\mathrm{bb}}(t)e^{j2\pi f_{\mathrm{c}}t}$.

$$\begin{aligned}
y_{\mathrm{bb}}^{\mathrm{single}}(t) &= \gamma\big[s_{\mathrm{pb}}(t-\tau) + v_{\mathrm{pb}}(t)\big]e^{-j2\pi f_{\mathrm{c}}t} \\
&= \gamma\big[s_{\mathrm{bb}}(t-\tau)e^{j2\pi f_{\mathrm{c}}(t-\tau)} + v_{\mathrm{bb}}(t)e^{j2\pi f_{\mathrm{c}}t}\big]e^{-j2\pi f_{\mathrm{c}}t} \\
&= \gamma\, s_{\mathrm{bb}}(t-\tau)e^{-j2\pi f_{\mathrm{c}}\tau} + v_{\mathrm{bb}}(t) = \gamma\, s_{\mathrm{bb}}\left(t-\frac{2R}{c}\right)e^{-j\left(\frac{4\pi R}{\lambda_{\mathrm{c}}}\right)} + v_{\mathrm{bb}}(t) \\
&= s_{\mathrm{bb}}(t) * (\gamma\, \delta(t-\tau)e^{-j2\pi f_{\mathrm{c}}\tau}) + v_{\mathrm{bb}}(t) = s_{\mathrm{bb}}(t) * \left(\gamma\, \delta\left(t-\frac{2R}{c}\right)e^{-j\left(\frac{4\pi R}{\lambda_{\mathrm{c}}}\right)}\right) + v_{\mathrm{bb}}(t)
\end{aligned}$$

(1.61)

Consider multiple scatterers present in the scene. Due to the linearity of Maxwell's wave equation, the reflected electromagnetic waves are superimposed to form the passband receive signal $y_{\mathrm{pb}}^{\mathrm{multi}}(t)$ or demodulated baseband receive signal $y_{\mathrm{bb}}^{\mathrm{multi}}(t)$. The ideal superposition of multiple scatterer echoes is shown in Figure 26.

$$y_{\mathrm{pb}}^{\mathrm{multi}}(t) = \sum_{\forall i} \gamma_i \, s_{\mathrm{pb}}(t-\tau_i) + v_{\mathrm{pb}}(t)$$

$$= s_{\mathrm{pb}}(t) * \left(\sum_{\forall i} \gamma_i \, \delta(t-\tau_i) \right) + v_{\mathrm{pb}}(t)$$

$$y_{\mathrm{bb}}^{\mathrm{multi}}(t) = \sum_{\forall i} \gamma_i \, s_{\mathrm{bb}}(t-\tau_i) e^{-j2\pi f_c \tau_i} + v_{\mathrm{bb}}(t) = \sum_{\forall i} \gamma_i \, s_{\mathrm{bb}}\left(t - \frac{2R_i}{c}\right) e^{-j\left(\frac{4\pi R_i}{\lambda_c}\right)} + v_{\mathrm{bb}}(t)$$

$$= s_{\mathrm{bb}}(t) * \left(\sum_{\forall i} \gamma_i \, \delta(t-\tau_i) e^{-j2\pi f_c \tau_i} \right) + v_{\mathrm{bb}}(t) = s_{\mathrm{bb}}(t) * \left(\sum_{\forall i} \gamma_i \, \delta\left(t - \frac{2R_i}{c}\right) e^{-j\left(\frac{4\pi R_i}{\lambda_c}\right)} \right) + v_{\mathrm{bb}}(t)$$

(1.62)

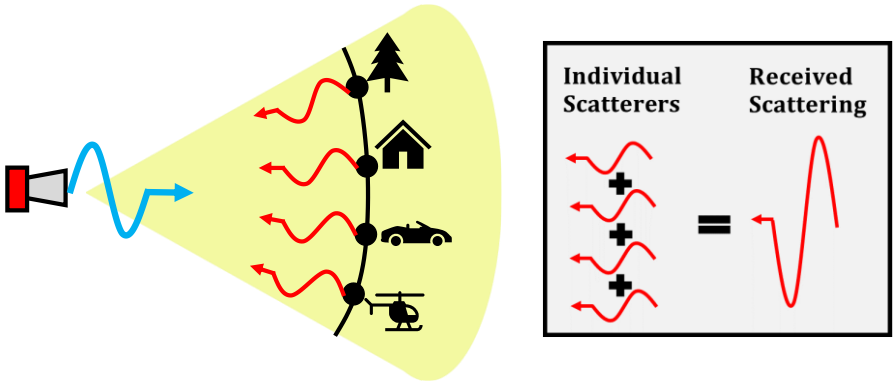

Figure 26: Ideal superposition of multiple equidistant scatterer reflections

The continuum of point scatterers $\sum_{\forall i \to \infty} \left(\gamma_i \, \delta(t - \tau_i) \right)$ forms the range profile $\gamma(t)$. The passband receive signal $y_{\mathrm{pb}}^{\mathrm{cont}}(t)$ is modeled as a convolution of the transmission $s_{\mathrm{pb}}(t)$ and the range profile $\gamma(t)$. The passband signal $y_{\mathrm{pb}}^{\mathrm{cont}}(t)$ is then demodulated to form the baseband signal $y_{\mathrm{bb}}^{\mathrm{cont}}(t)$.

$$y_{\mathrm{pb}}^{\mathrm{cont}}(t) = \int \gamma(\tau) \, s_{\mathrm{pb}}(t-\tau) \, d\tau + v_{\mathrm{pb}}(t)$$

$$= s_{\mathrm{pb}}(t) * \gamma(t) + v_{\mathrm{pb}}(t)$$

$$y_{\mathrm{bb}}^{\mathrm{cont}}(t) = \int \gamma(\tau) \, s_{\mathrm{bb}}(t-\tau) e^{-j2\pi f_c \tau} \, d\tau + v_{\mathrm{bb}}(t) = \int \gamma(\tau) \, s_{\mathrm{bb}}\left(t - \frac{2R(\tau)}{c}\right) e^{-j\left(\frac{4\pi R(\tau)}{\lambda_c}\right)} \, d\tau + v_{\mathrm{bb}}(t)$$

$$= s_{\mathrm{bb}}(t) * (\gamma(t) e^{-j2\pi f_c t}) + v_{\mathrm{bb}}(t) = s_{\mathrm{bb}}(t) * \bar{\gamma}(t) + v_{\mathrm{bb}}(t)$$

(1.63)

Assume that a single point scatterer is present in the scene, such that $\gamma(t)e^{-j2\pi f_c t} = \gamma\delta(t-\tau)$. The ideal radar return is described as a scaled and delayed copy of the transmit signal, with no AWGN present. Note that the characteristics of the transmit signal $s(t)$ significantly impact the received radar response.

$$y^{\text{ideal}}(t) = s(t) * \gamma\delta(t-\tau) = \gamma\, s(t-\tau)$$

(1.64)

Consequently, observations can be made about desirable radar waveform traits. Radar processing is applied to the baseband receive signal for subsequent detections of scatterers in the scene.

The continuous scattering model from (1.63) is discretized, where $\mathbf{s}$ is the length $(N_\text{p} \times 1)$ waveform representing $s_{\text{bb}}(t)$, $\boldsymbol{\gamma}$ is the length $(N_\gamma \times 1)$ scatterer range profile representing $\bar{\gamma}(t)$.

$$\mathbf{y} = \mathbf{s} * \boldsymbol{\gamma} + \mathbf{v} = \mathbf{S}\boldsymbol{\gamma} + \mathbf{v}$$

(1.65)

Convolution may also be expressed through the convolution matrix $\mathbf{S}$ of size $(N_\text{p} + N_\gamma - 1 \times N_\gamma)$, which contains time-shifted versions of the vector $\mathbf{s}$.

$$\mathbf{S} = \begin{bmatrix} s_1 & & \mathbf{0} \\ \vdots & s_1 & \\ s_{N_\text{p}} & \vdots & \\ & s_{N_\text{p}} & \ddots \quad s_1 \\ & & \vdots \\ \mathbf{0} & & s_{N_\text{p}} \end{bmatrix}$$

(1.66)

1.4.2.3. THE PULSE COMPRESSION MATCHED FILTER, AUTOCORRELATION

A standard radar processing technique in the range dimension is pulse compression. Pulse compression involves filtering the received signal containing scattered echoes $y(t)$ with a selected filter $w(t)$ that compresses signal power to better estimate the illuminated scene characteristics $\hat{\gamma}(t)$. The continuous representation of pulse compression is written as a cross-correlation ($\star$) between the received signal and the pulse compression filter.

$$\hat{\gamma}(t) = w(t) \star y(t) = \int_{-\infty}^{\infty} w^*(\tau)\, y(t+\tau)\, d\tau = \int_{-\infty}^{\infty} w^*(\tau - t)\, y(\tau)\, d\tau$$

(1.67)

Recall the similar definition for linear convolution ($*$) is

$$\hat{\gamma}(t) = w(t) * y(t) = \int_{-\infty}^{\infty} w(\tau)\, y(t-\tau)\, d\tau = \int_{-\infty}^{\infty} w(t-\tau)\, y(\tau)\, d\tau\,.$$

(1.68)

Pulse compression via correlation ($\star$) can be equivalently expressed as a convolution ($*$) between the received signal $y(t)$ and the time reversed, conjugated pulse compression filter $w^*(-t)$, shown by applying substitutions where $\tau' = -\tau, \quad d\tau' = -d\tau, \quad \tau' = \tau'' - t, \quad d\tau' = d\tau''$.

$$\begin{aligned}\hat{\gamma}(t) = w^*(-t) * y(t) &= \int_{-\infty}^{\infty} w^*(-\tau)\, y(t-\tau)\, d\tau = \int_{\infty}^{-\infty} w^*(\tau')\, y(t+\tau')\, (-d\tau') = \int_{-\infty}^{\infty} w^*(\tau')\, y(t+\tau')\, d\tau' \\ &= \int_{-\infty}^{\infty} w^*(\tau'' - t)\, y(t+\tau''-t)\, d\tau'' = \int_{-\infty}^{\infty} w^*(\tau'' - t)\, y(\tau'')\, d\tau'' \\ &= w(t) \star y(t)\end{aligned}$$

(1.69)

The most broadly applied pulse compression filter is the matched filter, which has been proven to maximize the signal-to-noise ratio (SNR) of a receive signal in the presence of additive white Gaussian noise (AWGN) [66, 67]. The continuous representation of the normalized pulse compression matched filter is

$$w_{\mathrm{mf}}(t) = \frac{s(t)}{\int_{-\infty}^{\infty} |s(t)|^2 \, dt} = \frac{s(t)}{\|s(t)\|_2^2} \ ,$$

(1.70)

where the denominator power normalizes the matched filtered estimate $\hat{y}_{\mathrm{mf}}(t)$. Application of the normalized pulse compression matched filter via cross-correlation is expressed as

$$\hat{y}_{\mathrm{mf}}(t) = w_{\mathrm{mf}}(t) \star y(t) = \frac{s(t)}{\|s(t)\|_2^2} \star y(t) = \frac{1}{\|s(t)\|_2^2} \int_{-\infty}^{\infty} s^*(\tau - t) \, y(\tau) \, d\tau \ \ .$$

(1.71)

The matched filtered estimate is related to the autocorrelation function for deterministic signals. Recall the ideal receive signal model from (1.64), expressed as a scaled and delayed copy of the transmit signal. For demonstrative purposes, assume that the transmit signal is not attenuated ($\gamma = 1$) and ignore the wave propagation delay ($\delta(t - \tau) = \delta(t)$) so the ideal receive signal model becomes $y^{\mathrm{ideal}}(t) = s(t)$. Consequently, the normalized matched filtered estimate of (1.71) yields

$$\hat{y}_{\mathrm{mf}}^{\mathrm{ideal}}(t) = w_{\mathrm{mf}}(t) \star y^{\mathrm{ideal}}(t) = \frac{s(t)}{\|s(t)\|_2^2} \star s(t) = \frac{1}{\|s(t)\|_2^2} \int_{-\infty}^{\infty} s^*(\tau - t) \, s(\tau) \, d\tau \ .$$

(1.72)

The autocorrelation function $r(t)$ of the deterministic signal $s(t)$ is defined as

$$r(t) = s(t) \star s(t) = \int_{-\infty}^{\infty} s^*(\tau - t) \, s(\tau) \, d\tau \ .$$

(1.73)

The ideal normalized matched filtered estimate from (1.72) is equivalent to the normalized autocorrelation function of the deterministic signal $s(t)$. The normalized autocorrelation function $\check{r}(t)$ is defined as

$$\check{r}(t) = \frac{s(t) \star s(t)}{\|s(t)\|_2^2} = \frac{1}{\|s(t)\|_2^2} \int_{-\infty}^{\infty} s^*(\tau - t)\, s(\tau)\, d\tau \ .$$

(1.74)

The Wiener-Khinchin autocorrelation theorem states that the signal autocorrelation $r(t)$ is related via the Fourier transform to the signal absolute power spectrum $r(f)$, as expressed in (1.75) [61]. Recalling the relationship between correlation and convolution from (1.69), the Weiner-Khinchin theorem is directly related to the Fourier transform pair between temporal convolution and frequency multiplication.

$$r(t) = s(t) \star s(t) \ = s^*(-t) * s(t) \quad \underset{\mathcal{F}}{\leftrightarrow} \quad r(f) = s^*(f)s(f) = |s(f)|^2$$

(1.75)

Pulse compression may likewise be expressed in discrete dimensions. Recall the discrete radar receive signal model expressed in (1.65). The $(N_{\mathrm{w}} \times 1)$ pulse compression filter $\mathbf{w}$ is correlated with the $(N_{\mathrm{p}} + N_{\gamma} - 1 \times 1)$ receive vector $\mathbf{y}$, which determines the $\left(N_{\mathrm{w}} + N_{\mathrm{p}} + N_{\gamma} - 2 \times 1\right)$ range profile estimate $\hat{\boldsymbol{\gamma}}$ with convolutional tails. The convolutional tails of the range profile estimate $\hat{\boldsymbol{\gamma}}$, consisting of the leading and trailing $(N_{\mathrm{w}} + N_{\mathrm{p}})/2$ samples, are removed to examine the relevant $\left(N_{\gamma} \times 1\right)$ scene for comparison to the true range profile $\boldsymbol{\gamma}$. The convolution matrix $\mathbf{W}$ of size $(N_{\mathrm{p}} + N_{\gamma} - 1) \times (N_{\mathrm{w}} + N_{\mathrm{p}} + N_{\gamma} - 2)$ contains time-shifted versions of the pulse compression filter $\mathbf{w}$. The Hermitian transposed matrix $\mathbf{W}^H$ exhibits conjugation and vector reversal of the filter $\mathbf{w}$, consequently applying the cross-correlation operator.

$$\hat{\boldsymbol{\gamma}} = \mathbf{w} \star \mathbf{y} = \mathbf{W}^H\mathbf{y} = \mathbf{W}^H(\mathbf{S}\boldsymbol{\gamma} + \mathbf{v}) = \mathbf{W}^H\mathbf{S}\boldsymbol{\gamma} + \mathbf{W}^H\mathbf{v}$$

(1.76)

The convolution matrix $\mathbf{W}$ is expressed in (1.77).

$$\mathbf{W} = \begin{bmatrix} w_{N_\mathrm{w}} & \cdots & w_1 & & \mathbf{0} \\ & w_{N_\mathrm{w}} & \cdots & w_1 & \\ & & \ddots & & \\ \mathbf{0} & & & w_{N_\mathrm{w}} & \cdots & w_1 \end{bmatrix}, \quad \mathbf{W}^H = \begin{bmatrix} w_{N_\mathrm{w}}^* & & & \mathbf{0} \\ \vdots & w_{N_\mathrm{w}}^* & & \\ w_1^* & \vdots & & \\ & w_1^* & \ddots & w_{N_\mathrm{w}}^* \\ & & & \vdots \\ \mathbf{0} & & & w_1^* \end{bmatrix}$$

(1.77)

While analog matched filtering may be performed using SAW filters for repeating pulsed waveforms [40], matched filtering is typically performed after analog-to-digital conversion using the baseband model. The discrete normalized pulse compression matched filter $\mathbf{w}_\mathrm{mf}$ is expressed in (1.78), where the denominator power normalizes the matched filtered estimate $\hat{\boldsymbol{\gamma}}_\mathrm{mf}$.

$$\mathbf{w}_\mathrm{mf} = \frac{\mathbf{s}}{(\mathbf{s}^H\mathbf{s})} = \frac{\mathbf{s}}{\|\mathbf{s}\|_2^2}$$

(1.78)

The normalized matched filter estimation is written in terms of the linear model expressed by (1.76). The matched filter vector $\mathbf{w}_\mathrm{mf}$ forms the convolution matrix $\mathbf{W}_\mathrm{mf}$. The matched filter convolution matrix is often expressed instead as an extended, normalized signal convolution matrix $\mathbf{W}_\mathrm{mf} = \frac{1}{\|\mathbf{s}\|_2^2}\tilde{\mathbf{S}}$.

$$\hat{\boldsymbol{\gamma}}_\mathrm{mf} = \mathbf{w}_\mathrm{mf} \star \mathbf{y} = \frac{\mathbf{s} \star \mathbf{y}}{\mathbf{s}^H\mathbf{s}} = \mathbf{W}_\mathrm{mf}^H\mathbf{S}\boldsymbol{\gamma} + \mathbf{W}_\mathrm{mf}^H\mathbf{v} = \frac{\mathbf{1}}{\|\mathbf{s}\|_2^2}\left(\tilde{\mathbf{S}}^H\mathbf{S}\boldsymbol{\gamma} + \tilde{\mathbf{S}}^H\mathbf{v}\right)$$

(1.79)

The ideal normalized matched filter estimate is expressed from (1.79), where the ideal range profile $\boldsymbol{\gamma}^\mathrm{ideal} = [1]$ is a unit scalar. The ideal received signal $\mathbf{y}^\mathrm{ideal}$ is the transmit signal $\mathbf{s}$ with no propagation delay and no noise present.

$$\hat{\boldsymbol{\gamma}}_\mathrm{mf}^\mathrm{ideal} = \mathbf{w}_\mathrm{mf} \star \mathbf{y}^\mathrm{ideal} = \frac{\mathbf{s}}{\|\mathbf{s}\|_2^2} \star \mathbf{y}^\mathrm{ideal} = \frac{\mathbf{s}}{\|\mathbf{s}\|_2^2} \star \mathbf{s} = \mathbf{W}_\mathrm{mf}^H\mathbf{S}\boldsymbol{\gamma}^\mathrm{ideal} = \mathbf{W}_\mathrm{mf}^H\mathbf{s} = \frac{1}{\|\mathbf{s}\|_2^2}\tilde{\mathbf{S}}^H\mathbf{s}$$

(1.80)

The autocorrelation function $\mathbf{r}$ of the deterministic signal $\mathbf{s}$ is defined as

$$\mathbf{r} = \mathbf{s} \star \mathbf{s} = \tilde{\mathbf{S}}^H \mathbf{s} \ .$$

(1.81)

The ideal normalized match filtered estimate from (1.80) is equivalent to the normalized autocorrelation function of the deterministic signal $\mathbf{s}$. The normalized autocorrelation function $\check{\mathbf{r}}$ of the deterministic signal $\mathbf{s}$ is defined as

$$\check{\mathbf{r}} = \frac{\mathbf{s} \star \mathbf{s}}{\|\mathbf{s}\|_2^2} = \frac{1}{\|\mathbf{s}\|_2^2} \tilde{\mathbf{S}}^H \mathbf{s} \, .$$

(1.82)

The discrete Wiener-Khinchin autocorrelation theorem is defined in (1.83), demonstrating the relationship between the deterministic signal $\mathbf{s}$, the signal frequency $\bar{\mathbf{s}}_{\mathrm{f}}$, the autocorrelation $\mathbf{r}$, and the absolute power spectrum $\mathbf{r}_{\mathrm{f}}$. The DFT matrix $\mathbf{A}$ and shifted DFT matrix $\overline{\mathbf{A}}$ are defined in Section 1.4.1.13. By discrete definition, the correlation expressed in (1.82) between two vectors $\mathbf{s}$ of equal length N_{p} results in the vector $\mathbf{r}$ of length $N_{\mathrm{r}} = 2N_{\mathrm{p}} - 1$. To achieve the defined autocorrelation vector length, $\mathbf{s}$ is zero-padded to length N_{r} forming $\bar{\mathbf{s}}$ prior to Fourier transformation. The operator $\odot$ is the elementwise multiply Hadamard product.

$$\bar{\mathbf{s}} = \begin{bmatrix} \mathbf{s} \\ \mathbf{0}_{N_{\mathrm{p}}-1 \times 1} \end{bmatrix}$$

$$\mathbf{r}_{\mathrm{f}} = |\bar{\mathbf{s}}_{\mathrm{f}}|^2 = |\mathbf{A}\bar{\mathbf{s}}|^2 = \mathbf{A}\bar{\mathbf{s}} \odot (\mathbf{A}\bar{\mathbf{s}})^* = \overline{\mathbf{A}}\mathbf{r}$$

$$\mathbf{r} = \mathbf{s} \star \mathbf{s} = \left(\frac{1}{N_{\mathrm{r}}}\right) \overline{\mathbf{A}}^H (\mathbf{A}\bar{\mathbf{s}} \odot (\mathbf{A}\bar{\mathbf{s}})^*) = \left(\frac{1}{N_{\mathrm{r}}}\right) \overline{\mathbf{A}}^H \mathbf{r}_{\mathrm{f}}$$

(1.83)

Standard Fourier relations hold based on the Weiner-Khinchine autocorrelation theorem. For instance, broadening of the rectangular signal power spectrum (wider 3-dB bandwidth $B_{3\mathrm{dB}}$) results in narrowing of the autocorrelation response (finer fast time resolution $\Delta t_{\mathrm{res}} = 1/B_{3\mathrm{dB}}$). Assuming a single scatterer is present, the peak-to-null range resolution achieved by matched filtering is $\Delta r = \frac{c\Delta t_{\mathrm{res}}}{2} = \frac{c}{2B_{3\mathrm{dB}}}$. The total amount of gain achieved by pulse compression for scatterer localization (assuming the signal is FM to deliver constant power) is determined as $G_{\mathrm{pc}} \approx B_{3\mathrm{dB}} T_{\mathrm{p}}$, referred to as the time-bandwidth product or pulse compression gain ratio. The relationships between power spectrum and autocorrelation, fast time resolution, and time-bandwidth product are summarized in Figure 27. The relationship between the signal power spectrum bandwidth and the corresponding range resolution achieved is often described as $\Delta r \approx \frac{c}{2B_{3\mathrm{dB}}}$. The range resolution estimate $\Delta r \approx \frac{c}{2B_{3\mathrm{dB}}}$ holds for waveforms that have a clearly defined (near rectangular) 3-dB bandwidth [41].

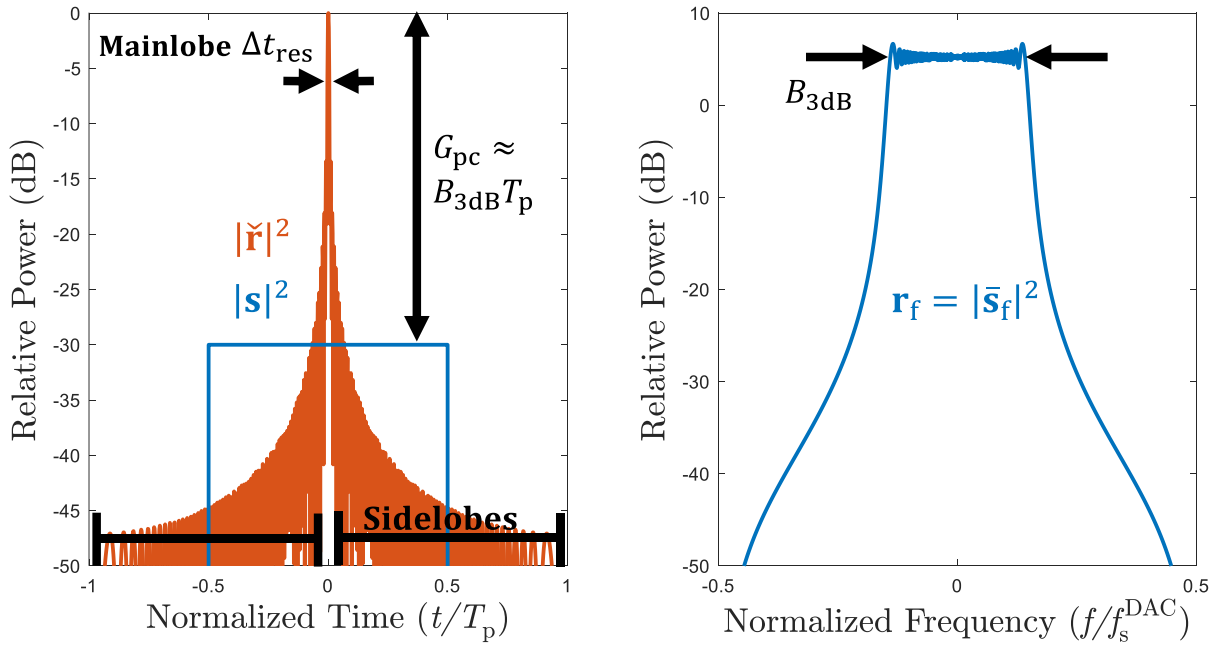

Figure 27: Relationship between autocorrelation and power spectrum, time-bandwidth product gain, and fast time pulse compressed resolution (for $B_{3\mathrm{dB}} T_{\mathrm{p}} = 1000$ or 30 dB).

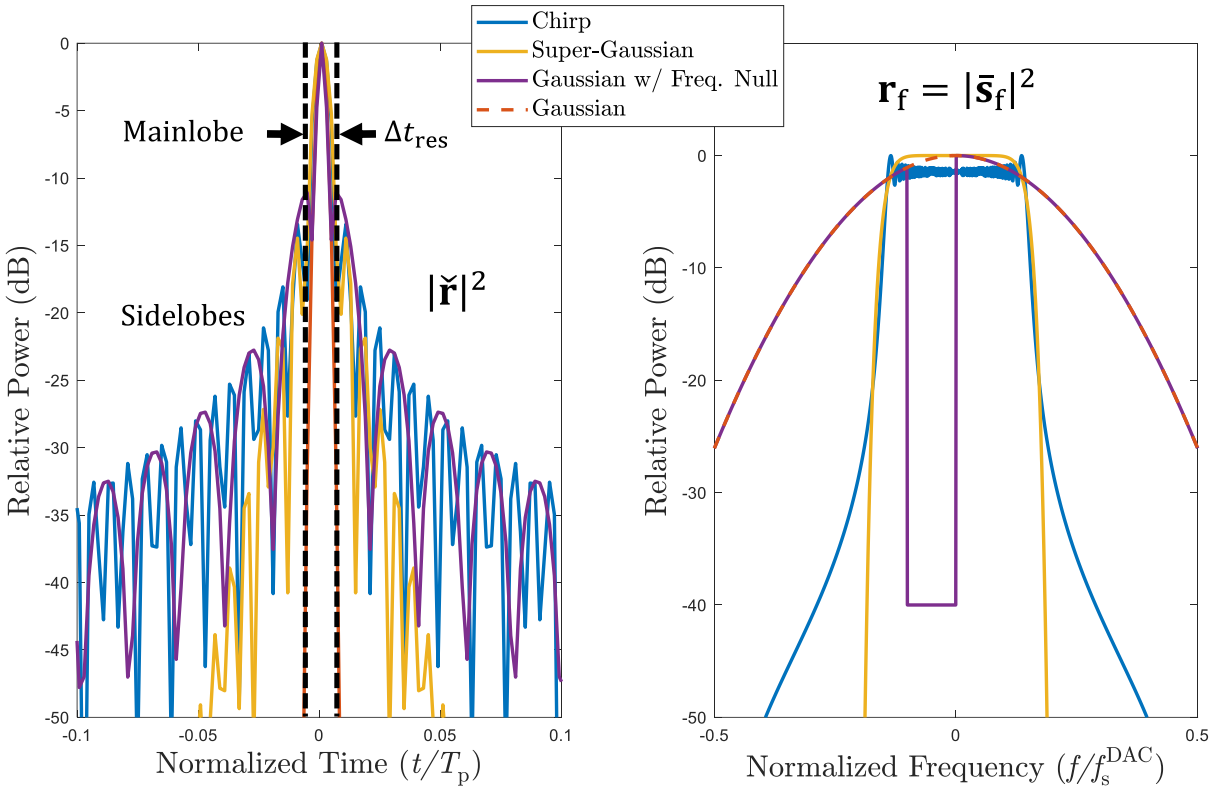

Figure 28: Various autocorrelation responses and power spectrum shapes, related by the Fourier transform.

The range sidelobe level must be considered for waveforms having a non-contiguous power spectrum such as the Gaussian with frequency null shown in Figure 28, which demonstrates significant sidelobes below the -13 dB marker. The pulse compression gain ratio metric alone does not describe the power in the autocorrelation sidelobes. Consider the matched filtered output when a large scatterer reflection is temporally overlapping a small scatterer reflection. The matched filtered sidelobes of the large scatterer estimate may mask the small scatterer estimate, depending on the signal power spectrum shape, as shown in Figure 29.

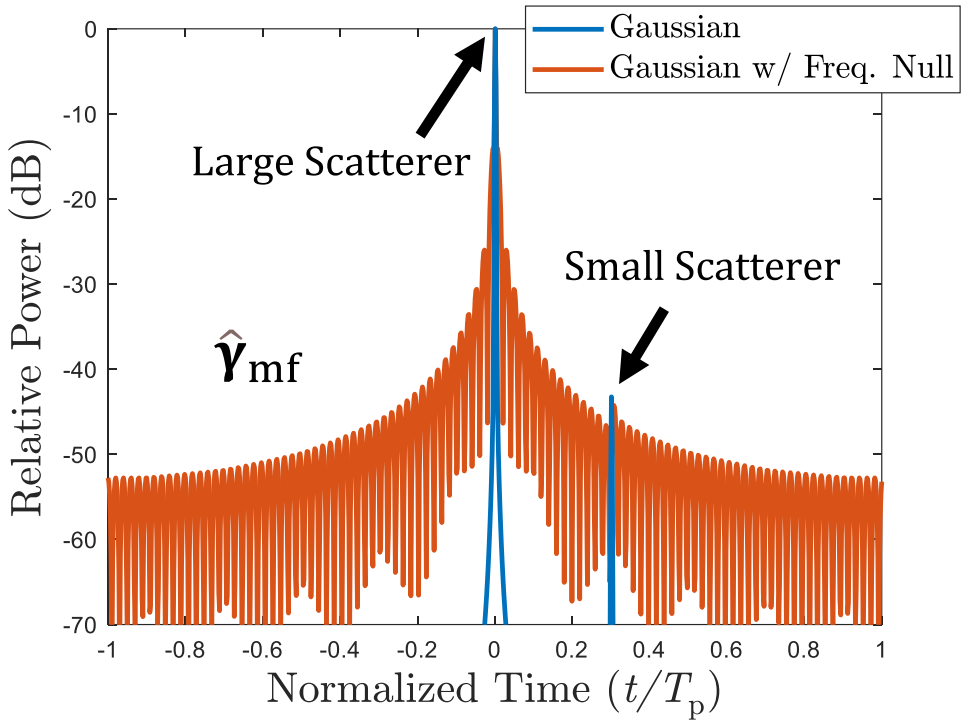

Figure 29: The dangers of autocorrelation sidelobes - The matched filtered output of a Gaussian spectrally shaped signal can distinguish the small scatterer. However, the matched filtered output of a Gaussian with frequency null spectrally shaped signal cannot distinguish the small scatterer due to sidelobe masking.

The pulse compression gain ratio does not capture the degree of waveform out-of-band spectral energy. Waveform spectral containment is needed to avoid interfering with other users (and thus meet FCC regulations). The ideal autocorrelation response is often considered to be an impulse response, having a mainlobe peak and no sidelobes, $\mathbf{e} = [0 \quad \cdots \quad 0 \quad 1 \quad 0 \quad \cdots \quad 0]^T$. To achieve the ideal autocorrelation response, many phase coded waveform sequences (see Section 1.4.2.6.3) have been formulated to achieve theoretically zero sidelobes. Based on the Fourier relationship between the autocorrelation and power spectrum, any waveform achieving an impulse response autocorrelation $\mathbf{e}$ must exhibit the power spectrum $\mathbf{e}_f$ having theoretically infinite bandwidth, as shown in Figure 30. If the transmit waveform is not bandlimited (i.e. attempts to achieve a perfect autocorrelation response), then the transmission will likely interfere with other radio frequency users occupying nearby frequency bands. Other RF user transmissions would mutually interfere with the radar receive echoes, degrading scatterer detection capability.

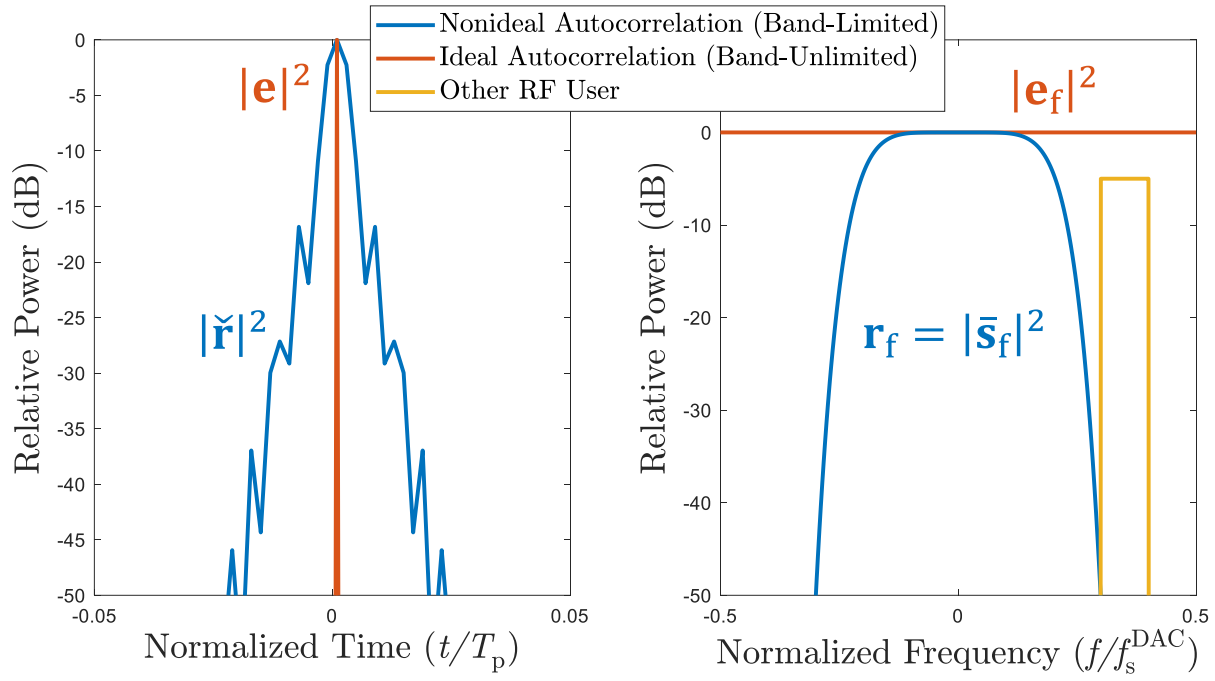

Figure 30: Nonideal versus ideal autocorrelation (left) and bandlimited versus band-unlimited power spectra (right), related by the Fourier transform.

Transmission spectral containment to a bandwidth $B_{3\mathrm{dB}}$ is necessary to avoid interfering with other users. The range resolution achieved is dependent on the utilized bandwidth $\Delta t_\mathrm{res} = 1/B_{3\mathrm{dB}}$. Correlation sidelobes that lie outside of the expected resolution cell width Δt_res are commonly characterized by two metrics, known as the integrated sidelobe level (ISL) and peak sidelobe level (PSL). The modified generalized integrated sidelobe level (GISL) metric may determine both the ISL and PSL metrics as

$$\mathrm{GISL} = \|\mathbf{w}_\mathrm{sl} \odot \check{\mathbf{r}}\|_p \tag{1.84}$$

where $\mathbf{w}_\mathrm{sl}$ is the sidelobe selector mask with value 1 in the sidelobe region and value 0 in the mainlobe region. When the GISL metric is tuned for $p = 2$, the sidelobe root-mean-squared absolute value determines the ISL, whereas tuning for $p = 8$ well-approximates the sidelobe maximum absolute value determines the PSL. The GISL metric extends to the normalized cross-correlation metric for pulse compression mismatched filters.

1.4.2.4. THE LEAST-SQUARES MISMATCHED FILTER, CROSS-CORRELATION

A pulse compression mismatched filter is any pulse compression filter that is not the matched filter. Pulse compression mismatched filters invoke the tradeoff between reduced range sidelobes and degraded signal-to-noise ratio (relative to the matched filter). The continuous representation of pulse compression is written as a cross-correlation ($\star$) between the received signal $y(t)$ and the pulse compression filter $w(t)$ to compress the signal power for better estimation of the illuminated scene characteristics $\hat{\gamma}(t)$.

$$\hat{\gamma}(t) = w(t) \star y(t) = \int_{-\infty}^{\infty} w^*(\tau)\, y(t+\tau)\, d\tau = \int_{-\infty}^{\infty} w^*(\tau - t)\, y(\tau)\, d\tau$$

(1.85)

When $y^{\text{ideal}}(t) = s(t)$ to represent an ideal scatterer reflection, the pulse compressed estimate from (1.85) yields

$$\hat{\gamma}^{\text{ideal}}(t) = w(t) \star y^{\text{ideal}}(t) = w(t) \star s(t) = \int_{-\infty}^{\infty} w^*(\tau - t)\, s(\tau)\, d\tau \quad .$$

(1.86)

Note that the representation in (1.86) is equivalent to the cross-correlation function $c(t)$ between the deterministic signal $s(t)$ and pulse compression filter $w(t)$. Generally, the pulse compression filters $w(t)$ are designed to provide accurate range profile estimates $\hat{\gamma}(t)$ without additional normalization required.

$$c(t) = w(t) \star s(t) = \int_{-\infty}^{\infty} w^*(\tau - t)\, s(\tau)\, d\tau$$

(1.87)

Pulse compression mismatched filters invoke the tradeoff between range sidelobe levels and degraded signal-to-noise ratio (relative to the matched filter, which maximizes SNR). The estimation power loss is caused by decorrelation between $w(t)$ and $s(t)$. The degree of SNR degradation, called mismatch loss, is characterized by the Cauchy-Schwarz inequality [68] in (1.88).

$$\frac{\left|\int_{-\infty}^{\infty} w^*(\tau)\, s(\tau)\, d\tau\right|^2}{\left(\int_{-\infty}^{\infty} w^*(\tau)\, w(\tau)\, d\tau\right)\left(\int_{-\infty}^{\infty} s^*(\tau)\, s(\tau)\, d\tau\right)} = \frac{\left|\int_{-\infty}^{\infty} w^*(\tau)\, s(\tau)\, d\tau\right|^2}{\|w(t)\|_2^2\, \|s(t)\|_2^2} \leq 1$$

(1.88)

The pulse compression mismatch loss is written generally as

$$\sigma_{\mathrm{mml}} = \frac{\left|\int_{-\infty}^{\infty} w^*(\tau)\, s(\tau)\, d\tau\right|^2}{\|w(t)\|_2^2\, \|s(t)\|_2^2} = \frac{\max\{|c(t)|^2\}}{\|w(t)\|_2^2\, \|s(t)\|_2^2}, \quad 0 \leq \sigma_{\mathrm{mml}} \leq 1 \ .$$

(1.89)

The mismatch loss σ_{mml} determines the degree of estimation power loss when the filter $w(t)$ and signal $s(t)$ centrally overlap to form a pulse compression peak. The matched filter $w_{\mathrm{mf}}(t)$ yields no mismatch loss ($\sigma_{\mathrm{mml}} = 1$), whereas all other mismatched filters yield mismatch loss ($0 \leq \sigma_{\mathrm{mml}} < 1$). Incorporating mismatch loss into the cross-correlation definition, the normalized cross-correlation function $\check{c}(t)$ is useful for comparison of pulse compression filters $w(t)$ with respect to a given signal $s(t)$. When $w(t)$ is selected as the matched filter $w_{\mathrm{mf}}(t)$, the normalized cross-correlation $\check{c}(t)$ simplifies to the normalized autocorrelation $\check{r}(t)$.

$$\check{c}(t) = \frac{\int_{-\infty}^{\infty} w^*(\tau - t)\, s(\tau)\, d\tau}{\|w(t)\|_2\, \|s(t)\|_2}$$

(1.90)

The Wiener-Khinchin cross-correlation theorem states that the cross-correlation $c(t)$ is related via the Fourier transform to the cross-power spectrum $c(f)$, as expressed in (1.91) [61]. Recalling the relationship between correlation and convolution from (1.69), the Weiner-Khinchin theorem is directly related to the Fourier transform pair between temporal convolution and frequency multiplication.

$$c(t) = w(t) \star s(t) = w^*(-t) * s(t) \underset{\mathcal{F}}{\leftrightarrow} c(f) = w^*(f) s(f)$$

(1.91)

Recall that pulse compression may also be expressed in discrete dimensions. The discrete pulse compression model described in (1.76) is restated here, for reference. The pulse compression filter $\mathbf{w}$ is correlated with the receive vector $\mathbf{y}$, which determines the range profile estimate $\hat{\boldsymbol{\gamma}}$ with convolutional tails.

$$\hat{\boldsymbol{\gamma}} = \mathbf{w} \star \mathbf{y} = \mathbf{W}^H \mathbf{y} = \mathbf{W}^H (\mathbf{S}\boldsymbol{\gamma} + \mathbf{v}) = \mathbf{W}^H \mathbf{S}\boldsymbol{\gamma} + \mathbf{W}^H \mathbf{v}$$

(1.92)

When the ideal range profile $\boldsymbol{\gamma}^{\text{ideal}} = [1]$ is a unit impulse scalar with no propagation delay, the ideal pulse compression output $\hat{\boldsymbol{\gamma}}^{\text{ideal}}$ is expressed as the cross-correlation function between the transmit signal $\mathbf{s}$ and the mismatched filter $\mathbf{w}$. The ideal received signal $\mathbf{y}^{\text{ideal}}$ is the transmit signal $\mathbf{s}$ with no propagation delay or noise present.

$$\hat{\boldsymbol{\gamma}}^{\text{ideal}} = \mathbf{w} \star \mathbf{y}^{\text{ideal}} = \mathbf{w} \star \mathbf{s} = \mathbf{W}^H \mathbf{S}\boldsymbol{\gamma}^{\text{ideal}} = \mathbf{W}^H \mathbf{s}$$

(1.93)

The cross-correlation function $\mathbf{c}$ is similarly expressed as

$$\mathbf{c} = \mathbf{w} \star \mathbf{s} = \mathbf{W}^H \mathbf{s} \ .$$

(1.94)

The degree of SNR degradation is characterized by the Cauchy-Schwarz inequality [68] in (1.95).

$$\frac{|\mathbf{w}^H \mathbf{s}|^2}{\|\mathbf{w}\|_2^2 \, \|\mathbf{s}\|_2^2} \leq 1$$

(1.95)

The pulse compression mismatch loss (SNR degradation relative to matched filtering) is written generally as

$$\sigma_{\text{mml}} = \frac{|\mathbf{w}^H \mathbf{s}|^2}{\|\mathbf{w}\|_2^2 \, \|\mathbf{s}\|_2^2} = \frac{\max\{|\mathbf{c}|^2\}}{\|\mathbf{w}\|_2^2 \, \|\mathbf{s}\|_2^2}, \qquad 0 \leq \sigma_{\text{mml}} \leq 1 \ .$$

(1.96)

The mismatch loss σ_{mml} determines the degree of estimation power loss when the filter $\mathbf{w}$ and signal $\mathbf{s}$ centrally overlap to form a pulse compression peak. Incorporating mismatch loss into the cross-correlation definition, the normalized cross-correlation function $\check{\mathbf{c}}$ is useful for comparison of pulse compression filters $\mathbf{w}$ with respect to a given signal $\mathbf{s}$. When $\mathbf{w}$ is selected as the matched filter $\mathbf{w}_{\mathrm{mf}}$, the normalized cross-correlation $\check{\mathbf{c}}$ simplifies to the normalized autocorrelation $\check{\mathbf{r}}$.

$$\check{\mathbf{c}} = \frac{\mathbf{W}^H \mathbf{s}}{\|\mathbf{w}\|_2 \, \|\mathbf{s}\|_2}$$

(1.97)

The discrete Wiener-Khinchin cross-correlation theorem is defined in (1.98), demonstrating the relationship between the signal $\mathbf{s}$ and filter $\mathbf{w}$, the signal frequency $\bar{\mathbf{s}}_{\mathrm{f}}$ and filter frequency $\bar{\mathbf{w}}_{\mathrm{f}}$, the cross-correlation $\mathbf{c}$, and the complex cross-power spectral density $\mathbf{c}_{\mathrm{f}}$. The DFT matrix $\mathbf{A}$ and shifted DFT matrix $\bar{\mathbf{A}}$ are defined in Section 1.4.1.13. By discrete definition, the correlation expressed in (1.94) between vectors $\mathbf{s}$ and $\mathbf{w}$ of lengths N_{p} and N_{w} results in the vector $\mathbf{c}$ of length $N_{\mathrm{c}} = N_{\mathrm{p}} + N_{\mathrm{w}} - 1$. To achieve the defined cross-correlation vector length, $\mathbf{s}$ and $\mathbf{w}$ are each symmetrically zero-padded to length N_{c} prior to Fourier transformation. Because the vectors $\mathbf{s}$ and $\mathbf{w}$ aren't necessarily equal length, symmetric zero padding enforces a pulse compression mainlobe peak located at their central overlap. The zero padded symmetry is dependent on whether N_{p} and N_{w} are odd or even valued, requiring the symmetry term $\mathcal{N} = \big(N_{\mathrm{p}} \bmod 2\big)\big(1 - (N_{\mathrm{w}} \bmod 2)\big)$. The operator $\odot$ is the elementwise multiply Hadamard product, $\lfloor \cdot \rfloor$ applies the floor operator, and mod applies the modulo operator.

$$\bar{\mathbf{s}} = \begin{bmatrix} \mathbf{0}_{\lfloor N_{\mathrm{w}}/2 \rfloor - \mathcal{N} \times 1} \\ \mathbf{s} \\ \mathbf{0}_{N_{\mathrm{w}} - \lfloor N_{\mathrm{w}}/2 \rfloor - 1 + \mathcal{N} \times 1} \end{bmatrix}, \quad \bar{\mathbf{w}} = \begin{bmatrix} \mathbf{0}_{\lfloor N_{\mathrm{p}}/2 \rfloor \times 1} \\ \mathbf{w} \\ \mathbf{0}_{N_{\mathrm{p}} - \lfloor N_{\mathrm{p}}/2 \rfloor - 1 \times 1} \end{bmatrix}$$

$$\mathbf{c}_{\mathrm{f}} = \bar{\mathbf{w}}_{\mathrm{f}}^{*} \odot \bar{\mathbf{s}}_{\mathrm{f}} = (\mathbf{A}\bar{\mathbf{w}})^{*} \odot (\mathbf{A}\bar{\mathbf{s}}) = \bar{\mathbf{A}}\mathbf{c}$$

$$\mathbf{c} = \mathbf{w} \star \mathbf{s} = \left(\frac{1}{N_{\mathrm{c}}}\right) \bar{\mathbf{A}}^H (\bar{\mathbf{w}}_{\mathrm{f}}^{*} \odot \bar{\mathbf{s}}_{\mathrm{f}}) = \left(\frac{1}{N_{\mathrm{c}}}\right) \bar{\mathbf{A}}^H \big((\mathbf{A}\bar{\mathbf{w}})^{*} \odot (\mathbf{A}\bar{\mathbf{s}})\big)$$

(1.98)

Linear algebra expressions can be formed and optimized to achieve a desired pulse compression response. One such optimization problem is least squares regression. The objective function for least squares regression takes the general form of (1.99) where $\mathbf{Y}$ is the desired complex output, $\mathbf{X}$ is the given complex input, and $\mathbf{B}$ is optimized to minimize the difference between $\mathbf{Y}$ and $\mathbf{X}$. The operation $\|\cdot\|_2$ denotes the Euclidean 2-norm.

$$\min_{\mathbf{B}} \|\mathbf{Y} - \mathbf{X}\mathbf{B}\|_2^2 \tag{1.99}$$

Expanding the least squares regression objective function, taking the gradient, and setting the gradient equal to zero (to determine objective function inflection points) allows for calculation of a closed form solution. Here, complex valued $\mathbf{Y}$, $\mathbf{X}$, and $\mathbf{B}$ are considered. The gradient can be calculated using matrix derivatives [69] and Wirtinger calculus [70] as in (1.100). For Wirtinger calculus, complex $\mathbf{B}$ and $\mathbf{B}^*$ are treated as independent variables (orthogonal by definition), such that $\frac{\partial}{\partial \mathbf{B}^*}(\mathbf{B}) = 0$ and $\frac{\partial}{\partial \mathbf{B}}(\mathbf{B}^*) = 0$.

$$\begin{aligned}
\|\mathbf{Y} - \mathbf{X}\mathbf{B}\|_2^2 &= (\mathbf{Y} - \mathbf{X}\mathbf{B})^H(\mathbf{Y} - \mathbf{X}\mathbf{B}) = \mathbf{Y}^H\mathbf{Y} - \mathbf{Y}^H\mathbf{X}\mathbf{B} - \mathbf{B}^H\mathbf{X}^H\mathbf{Y} + \mathbf{B}^H\mathbf{X}^H\mathbf{X}\mathbf{B} \\
\frac{\partial}{\partial \mathbf{B}^*}\|\mathbf{Y} - \mathbf{X}\mathbf{B}\|_2^2 &= -\mathbf{X}^H\mathbf{Y} + \mathbf{X}^H\mathbf{X}\mathbf{B} \\
\frac{\partial}{\partial \mathbf{B}^*}\|\mathbf{Y} - \mathbf{X}\mathbf{B}\|_2^2 &= -\mathbf{X}^H\mathbf{Y} + \mathbf{X}^H\mathbf{X}\mathbf{B} = 0 \rightarrow \mathbf{X}^H\mathbf{X}\mathbf{B} = \mathbf{X}^H\mathbf{Y} \\
\mathbf{B} &= (\mathbf{X}^H\mathbf{X})^{-1}\mathbf{X}^H\mathbf{Y}
\end{aligned} \tag{1.100}$$

Using least squares regression, it is feasible to determine the pulse compression filter $\mathbf{w}$ that correlates with the signal $\mathbf{s}$ to achieve a desired cross-correlation response $\mathbf{d}$. Recall that correlation and convolution are related via $w(t) \star s(t) = w^*(-t) * s(t)$. The discrete relationship between correlation and convolution is expressed as $\mathbf{w} \star \mathbf{s} = (\mathbf{T}_\mathrm{R}\mathbf{w})^* * \mathbf{s} = \breve{\mathbf{w}} * \mathbf{s}$, where the transformation matrix $\mathbf{T}_\mathrm{R}$ reverses the elements of $\mathbf{w}$. In matrix notation, $\mathbf{w} \star \mathbf{s} = \mathbf{W}^H\mathbf{s} = \breve{\mathbf{w}} * \mathbf{s} = \mathbf{S}\breve{\mathbf{w}}$, where here the signal convolution matrix $\mathbf{S}$ has dimensions $(N_\mathrm{w} + N_\mathrm{p} - 1) \times (N_\mathrm{w})$. The filter $\breve{\mathbf{w}}$ is optimized via least squares regression using the convolutional model $(\mathbf{S}\breve{\mathbf{w}})$. The filter $\breve{\mathbf{w}}$ is transformed via $\mathbf{w} = (\mathbf{T}_\mathrm{R}\breve{\mathbf{w}})^*$ to instead apply the correlational model $(\mathbf{W}^H\mathbf{s})$.

The least squares regression objective function is revised to achieve a desired pulse compression response. The least squares optimal filter $\breve{\mathbf{w}}_{\text{ls}}$ that minimizes the difference between the cross-correlation $\mathbf{c} = \mathbf{S}\breve{\mathbf{w}}_{\text{ls}}$ and the desired pulse compression response $\mathbf{d}$ is determined by minimizing the objective function

$$\min_{\breve{\mathbf{w}}_{\text{ls}}} \|\mathbf{d} - \mathbf{S}\breve{\mathbf{w}}_{\text{ls}}\|_2^2$$

(1.101)

where the solution to the pulse compression problem [71] is written as

$$\breve{\mathbf{w}}_{\text{ls}} = (\mathbf{S}^H\mathbf{S} + \Delta\mathbf{I})^{-1}\mathbf{S}^H\mathbf{d} \ .$$

(1.102)

Note that the addition of the term $\Delta\mathbf{I}$ within the matrix inverse, referred to as a regularization term, enforces that the matrix-to-be-inverted is full rank and thus invertible. Figure 31 depicts the least squares optimization, where $\mathbf{d}$ is the desired response (the impulse response $\mathbf{e} = [0 \quad \cdots \quad 0 \quad 1 \quad 0 \quad \cdots \quad 0]^T$ is selected here), $\mathbf{c} = \mathbf{S}\breve{\mathbf{w}}_{\text{ls}}$ is the least squares filter cross-correlation function, and $\breve{\mathbf{r}} = \mathbf{S}\breve{\mathbf{w}}_{\text{mf}}$ is the normalized matched filter autocorrelation function listed for comparison.

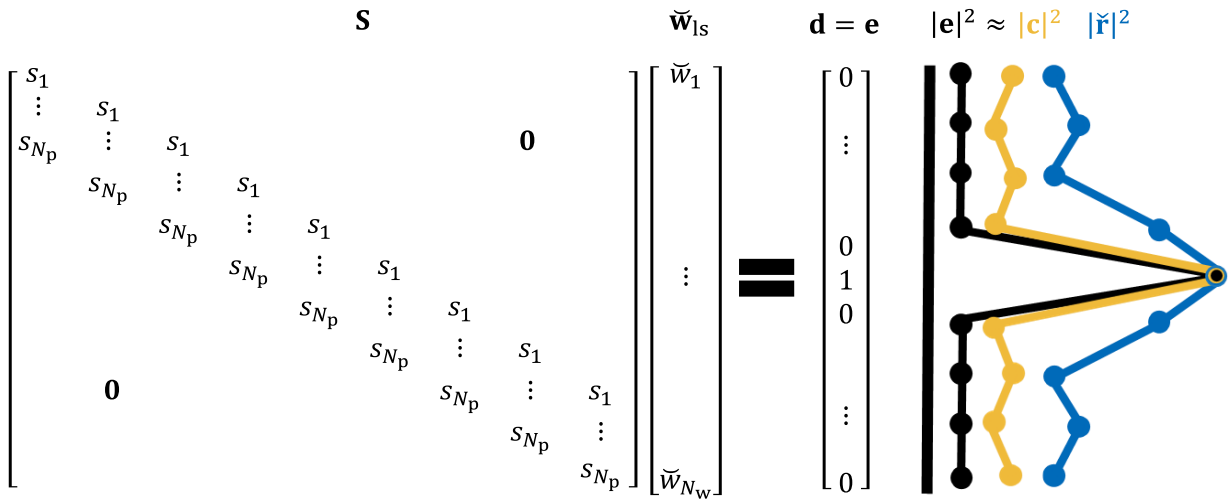

Figure 31: Illustration of least squares regression optimization to achieve a desired cross-correlation response.

Super-resolution occurs when the pulse compressed range resolution is finer than the signal 3-dB bandwidth resolution, i.e. $\Delta t_{\mathrm{res}} < 1/B_{3\mathrm{dB}}$. Achieving super-resolution via mismatched filtering invokes the additional tradeoff between range resolution, range sidelobes, and mismatch loss. Enforcing a finer resolution $\Delta t_{\mathrm{res}} < 1/B_{3\mathrm{dB}}$ implies that the cross-power spectrum ($\mathbf{c}_{\mathrm{f}} = \bar{\mathbf{w}}_{\mathrm{f}}^{*} \odot \bar{\mathbf{s}}_{\mathrm{f}}$) bandwidth is broadened relative to the signal power spectrum ($\mathbf{r}_{\mathrm{f}} = \bar{\mathbf{s}}_{\mathrm{f}}^{*} \odot \bar{\mathbf{s}}_{\mathrm{f}}$) bandwidth. With this intent, the mismatched filter spectrum $\bar{\mathbf{w}}_{\mathrm{f}}^{*}$ effectively "amplifies" portions of the signal spectrum $\bar{\mathbf{s}}_{\mathrm{f}}$. As the mismatched filter spectrum $\bar{\mathbf{w}}_{\mathrm{f}}^{*}$ becomes more dissimilar from signal spectrum $\bar{\mathbf{s}}_{\mathrm{f}}$, the mismatch loss degrades ($\sigma_{\mathrm{mml}} \to 0$) due to declining correlation between $\mathbf{w}$ and $\mathbf{s}$. Recall that the transmit signal $\mathbf{s}$ must be bandlimited to avoid interfering with other users upon transmission, as illustrated in Figure 30.

Applying the least squares optimal filter $\mathbf{w}_{\mathrm{ls}}$ to the bandlimited signal $\mathbf{s}$ could potentially impose considerable mismatch loss (without regularization Δ or further modification) if the desired response is the band-unlimited impulse $\mathbf{d} = \mathbf{e}$, as illustrated in Figure 32. In this example, the signal $\mathbf{s}$ has a bandlimited Gaussian power spectrum $|\bar{\mathbf{s}}_{\mathrm{f}}|^2$ and normalized autocorrelation $\check{\mathbf{r}}$. To achieve the impulse desired response $\mathbf{d} = \mathbf{e}$, then theoretically infinite spectrum is required by Fourier definition. When no regularization is applied ($\Delta = 0$), the mismatched filter spectrum $\bar{\mathbf{w}}_{\mathrm{f}}^{*}$ inverts the signal spectrum $\bar{\mathbf{s}}_{\mathrm{f}}$ to enforce a flat cross-power spectrum $\mathbf{c}_{\mathrm{f}} = \bar{\mathbf{w}}_{\mathrm{f}}^{*} \odot \bar{\mathbf{s}}_{\mathrm{f}}$. However, the degree of mismatch loss significantly degrades due to declining correlation between $\mathbf{w}$ and $\mathbf{s}$ (for example, $\sigma_{\mathrm{mml}} = 0.12$ corresponds to $-9\,\mathrm{dB}$ mismatch loss). The example mismatched filter minimizes the objective function, but limited degrees of freedom are available to here achieve super-resolution and minimize sidelobes. Remnant error exists and the resulting cross-correlation response may be less than desirable. Super-resolution achieved by linear filtering may be less desirable in scenarios where high SNR is necessary.

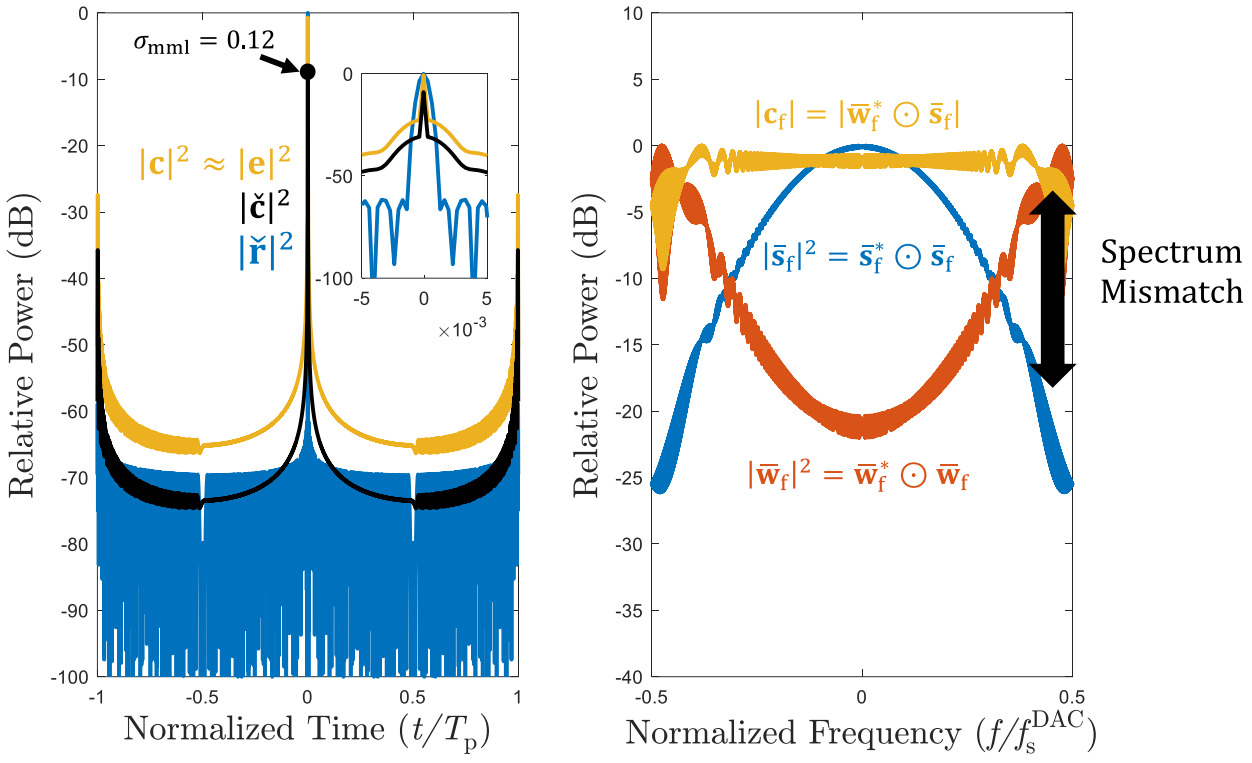

Figure 32: Example correlation responses (left) and power spectra (right). If the least squares filter $\mathbf{w}_{\mathrm{ls}}$ is applied to the bandlimited signal $\mathbf{s}$ to achieve super-resolution, significant mismatch loss occurs (for example, $\sigma_{\mathrm{mml}} = 0.12$). The filter spectrum $\bar{\mathbf{w}}_{\mathrm{f}}$ is mismatched from the signal spectrum $\bar{\mathbf{s}}_{\mathrm{f}}$ to form the cross-power spectrum $\mathbf{c}_{\mathrm{f}}$. Sidelobe level and mismatch loss performance are degraded in trade to achieve significant super-resolution.

Formulations to robustly determine the least squares filter exist. Consider the least squares filter solution. For large Δ, the matrix-to-be-inverted is approximately $(\mathbf{S}^H\mathbf{S} + \Delta\mathbf{I}) \approx \Delta\mathbf{I}$, so the mismatched filter simplifies to $\check{\mathbf{w}}_{\mathrm{ls}} = (\Delta\mathbf{I})^{-1}\mathbf{S}^H\mathbf{d} = (1/\Delta)\mathbf{I}\mathbf{S}^H\mathbf{d} = (1/\Delta)\mathbf{S}^H\mathbf{d}$. The desired response $\mathbf{d}$ may be selected as the impulse response $\mathbf{e}$. For large Δ values, when $\mathbf{d} \approx \mathbf{e}$ and $N_{\mathrm{w}} = N_{\mathrm{p}}$, the least squares optimal filter simplifies to the matched filter as $\check{\mathbf{w}}_{\mathrm{ls}} = (1/\Delta)(\mathbf{S}^H\mathbf{e}) = (1/\Delta)\check{\mathbf{s}} = \check{\mathbf{w}}_{\mathrm{mf}}$. By observation, the variable Δ allows for tuning between the least squares filter and matched filter when $\mathbf{d} \approx \mathbf{e}$. Consequently, increasing the regularization Δ minimizes the mismatch loss σ_{mml} inflicted by tuning closer to the matched filter solution, in exchange for degraded resolution or range sidelobe performance as illustrated in Figure 33.

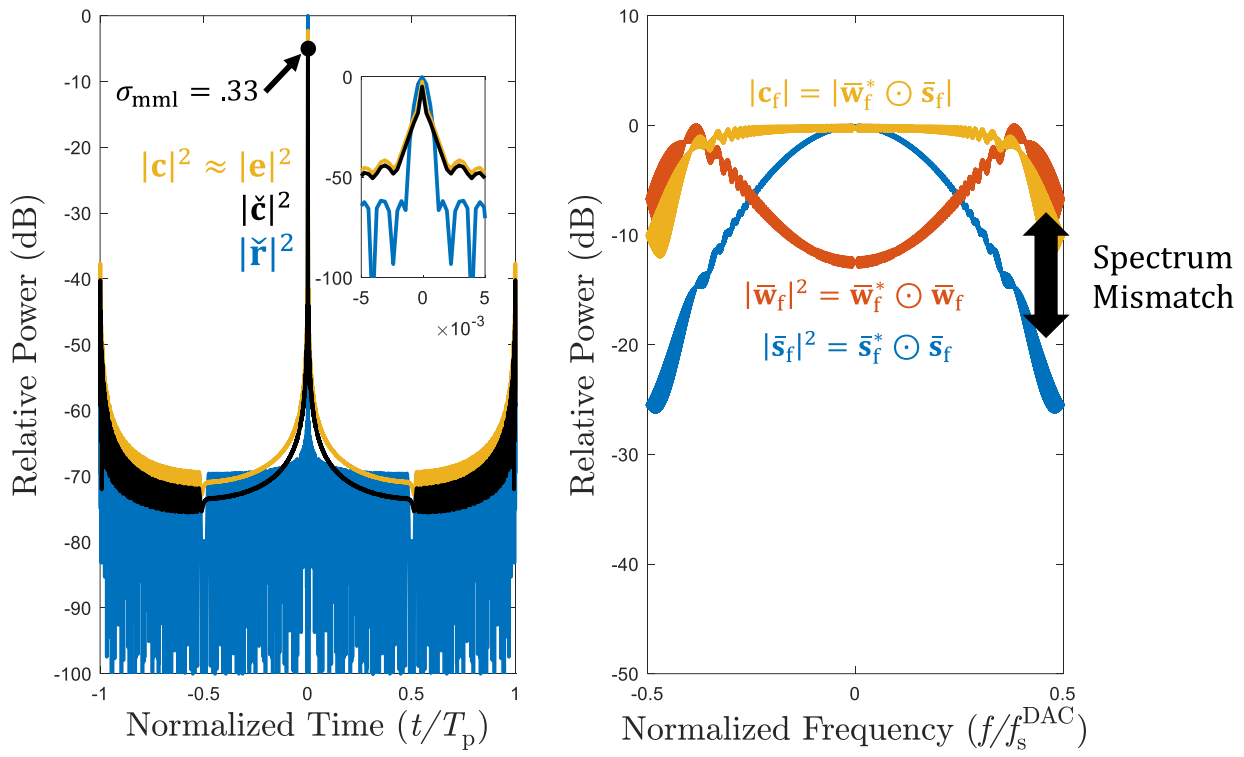

Figure 33: Example correlation responses (left) and power spectra (right). If the regularization Δ is increased to form the least squares filter $\mathbf{w}_{\text{ls}}$, which is then applied to the bandlimited signal $\mathbf{s}$ to achieve super-resolution, moderate mismatch loss occurs (for example, $\sigma_{\text{mml}} = 0.33$). Range resolution is degraded in trade to mitigate mismatch loss and improve the sidelobe level performance, though moderate super-resolution is still achieved.

Another method to counteract super-resolution effects is to simply reduce constraints around the correlation mainlobe within the least squares formulation. Consider the impulse $\mathbf{e}_\ell = [0 \quad \cdots \quad 0 \quad 1 \quad 0 \quad \cdots \quad 0]^T$, having a mainlobe peak (located at the ℓ^{th} sample) and no sidelobes. When the desired response is selected $\mathbf{d} = \mathbf{e}_\ell$, the cross-correlation $\mathbf{S}\check{\mathbf{w}}_{\text{ls}}$ aims to achieve the ideal impulse response. The $\bar{L}$ rows above and below the ℓ^{th} row in $\mathbf{S}$ (corresponding to the mainlobe resolution) may be zeroed, effectively removing constraints on the cross-correlation mainlobe resolution. The method of reducing resolution to compensate for other performance metrics is known as beamspoiling. Consequently, range resolution beamspoiling minimizes the mismatch loss σ_{mml} inflicted and improves range sidelobe performance as illustrated in Figure 34.

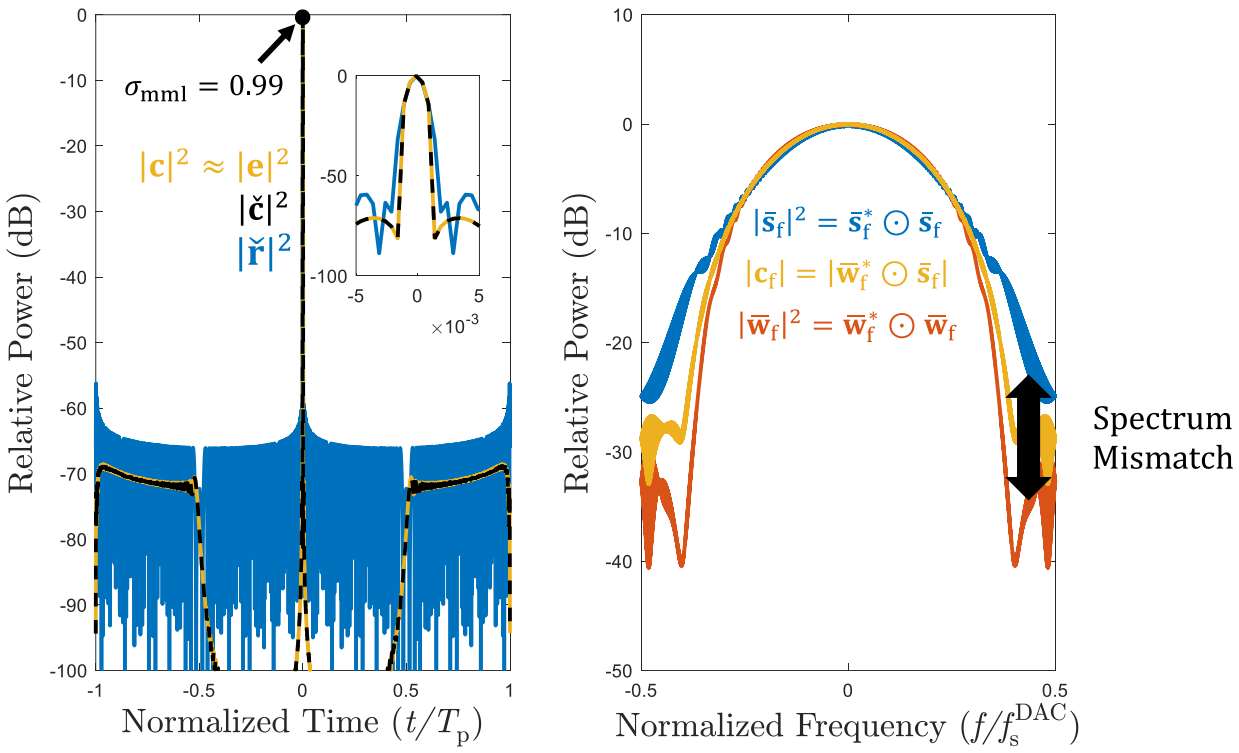

Figure 34: Example correlation responses (left) and power spectra (right). If range resolution beamspoiling is incorporated to form the least squares filter $\mathbf{w}_{\mathrm{ls}}$, which is then applied to the bandlimited signal $\mathbf{s}$, then slight mismatch loss occurs (for example, $\sigma_{\mathrm{mml}} = 0.99$). Super-resolution is waived in trade to mitigate mismatch loss and improve the sidelobe level performance.

In summary, the least squares optimal filter formulation may be adjusted to control the degree of mismatch loss, super-resolution, and sidelobe levels achieved. For the least squares formulations described thus far, the desired response $\mathbf{d}$ is selected as the impulse response $\mathbf{e}$ to provide insight regarding the algorithm behavior. However, a variety of templates may be selected for the desired response $\mathbf{d}$ [72,73]. Importantly, the degree of mismatch loss is minimized when the waveform spectrum $\bar{\mathbf{s}}_{\mathrm{f}}$ minimally deviates from the filter spectrum $\bar{\mathbf{w}}_{\mathrm{f}}^*$ [73]. By extension, the degree of mismatch loss is minimized when the signal power spectrum minimally deviates from the cross-power spectrum $\mathbf{r}_{\mathrm{f}} \approx \mathbf{c}_{\mathrm{f}}$ [73]. The desired correlation $\mathbf{d}$ and desired power spectrum $\mathbf{d}_{\mathrm{f}}$ are a Fourier transform pair according to the Wiener-Khinchin theorem, expressed as $\mathbf{d}_{\mathrm{f}} = \bar{\mathbf{A}}\mathbf{d}$. When the signal spectrum $\mathbf{r}_{\mathrm{f}}$ and cross-power spectrum $\mathbf{c}_{\mathrm{f}}$ are each designed to exhibit the same desired spectrum $\mathbf{d}_{\mathrm{f}}$, the mismatch loss is minimized.

Correlation-based pulse compression via matched or mismatched filtering relies on linear time invariant (LTI) processing to achieve the desired radar performance. Data-driven nonlinear processing techniques exist that likewise achieve super resolution in various radar dimensions [74-76]. For instance, adaptive pulse compression (APC) [74] forms multiple range-dependent filters (called a filter bank) that update based on the observed data statistics. For adaptive algorithms, sensitivity to imprecise model estimation may potentially cause false alarms, though incorporating robustness into adaptive algorithms mitigates undesirable effects [76].

1.4.2.5. PERCENT BANDWIDTH DEFINITION (NARROWBAND, WIDEBAND, ULTRA-WIDEBAND)

A definition for the size of bandwidth utilized relative to a wavelength is listed in (1.103). The bandwidth size used is important, as many assumptions are made depending on the bandwidth size relative to a wavelength. The narrowband assumption is often invoked to simplify processing. Definitions of narrowband, wideband, and ultra-wideband are defined in [77] based on the percent bandwidth utilized relative to the transmit center frequency.

$$\%\mathrm{BW} = \frac{B_{3\mathrm{dB}}}{f_{\mathrm{c}}} \tag{1.103}$$

Table 1: Narrowband, Wideband, Ultra-Wideband Definitions.

Narrowband $\%\mathrm{BW}$	Wideband $\%\mathrm{BW}$	Ultra-Wideband $\%\mathrm{BW}$
<1%	1% - 25%	>25%

1.4.2.6. WAVEFORM TYPES

The waveform types discussed here include unmodulated tones, linear frequency modulated (LFM) & nonlinear frequency modulated (NLFM) waveforms, phase coded & angle modulated waveforms, and polyphase coded frequency modulated (PCFM) waveforms. For further waveform analysis, the reader is directed to [41, 78, 79]. Keep in mind, the waveform power spectral density (PSD) $r(f)$ impacts the waveform autocorrelation function $r(t)$.

1.4.2.6.1. UNMODULATED PULSE (SINUSOIDAL TONES)

Sinusoidal tones have no modulated bandwidth and the range resolution achieved depends entirely on the duration T_p of the pulse. The 3-dB bandwidth of a tone having duration T_p is observed as $B_\mathrm{tone} \approx 1/T_\mathrm{p}$, due to the Fourier transform pair between the temporal rectangular function and frequency sinc function. The duration of the temporal rectangular window determines the sinc 3-dB bandwidth in frequency. The bandwidth B_tone determines the achievable range resolution $\Delta r_\mathrm{tone} = \frac{c}{2B_\mathrm{tone}} = \frac{cT_\mathrm{p}}{2}$. The range resolution Δr_tone of an unmodulated pulse is called the Rayleigh resolution [77]. Stepped frequency radar involves sequential transmission of tones with incrementing frequency to form bandwidth across slow time, which is used for ultra-wideband radar [80, 81].

$$s_\mathrm{tone}(t) = e^{j2\pi f_\mathrm{c} t} \tag{1.104}$$

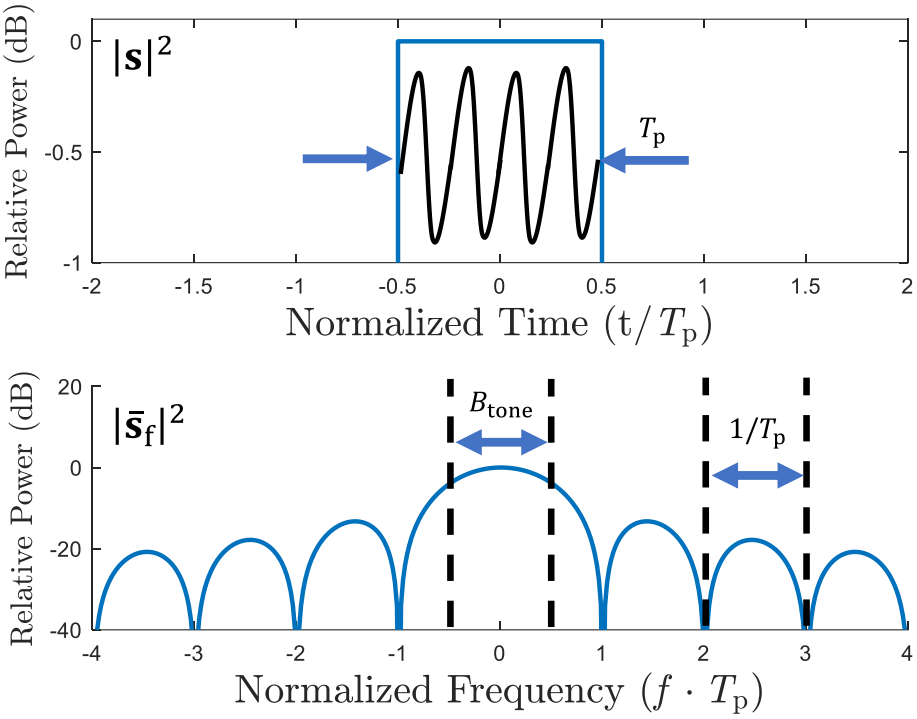

Figure 35: Unmodulated sinusoidal waveform in fast time-frequency

1.4.2.6.2. CHIRP WAVEFORMS

Most legacy radar systems transmit linear frequency modulated (LFM) or nonlinear frequency modulated (NLFM) chirp waveforms due to their simplicity in design by chirp rate modulation to shape the spectrum [67, 82]. Transmission of chirp waveforms generally implies pulse or CW segment repetition and a predictable instantaneous frequency modulation $f_{\mathrm{i}}(t)$. Linear FM waveforms have a linear instantaneous frequency function, which corresponds to a quadratic instantaneous phase function. The mathematical description of an LFM waveform is

$$s_{\mathrm{LFM}}(t) = e^{j2\pi\left(f_1 t + 0.5\left(\frac{B}{T_{\mathrm{p}}}\right)t^2\right)} \qquad t \in \left(0, T_{\mathrm{p}}\right) \ . \tag{1.105}$$

Nonlinear FM waveforms are often designed using the principle of stationary phase (POSP) to determine the instantaneous frequency function $f_{\mathrm{i}}(t)$ to achieve a desired PSD shape $r(f)$, originally detailed in [67].

The closed-form instantaneous frequency functions $f_{\mathrm{i}}(t)$ of numerous NLFM waveforms [79, 83-100] are listed in Section 4.1. The power spectra $r(f)$ and autocorrelations $r(t)$ of [79, 83-96] are shown in Figure 36. Other NLFM waveform optimizations do not have closed-form solutions [101-111]. The instantaneous frequency functions $f_{\mathrm{i}}(t)$ may be numerically determined to achieve a desired PSD shape $r(f)$, detailed in [112]. Methods for wideband synthesis of nonlinear FM waveforms are outlined in [113, 114]. NLFM waveforms has been applied in airborne SAR [108-111], and recent work used neural networks to select the NLFM instantaneous frequency functions based on the estimated scene [115]. Note that NLFM waveforms may be designed to arbitrary spectrum shapes [112], including those having spectral nulls [116].

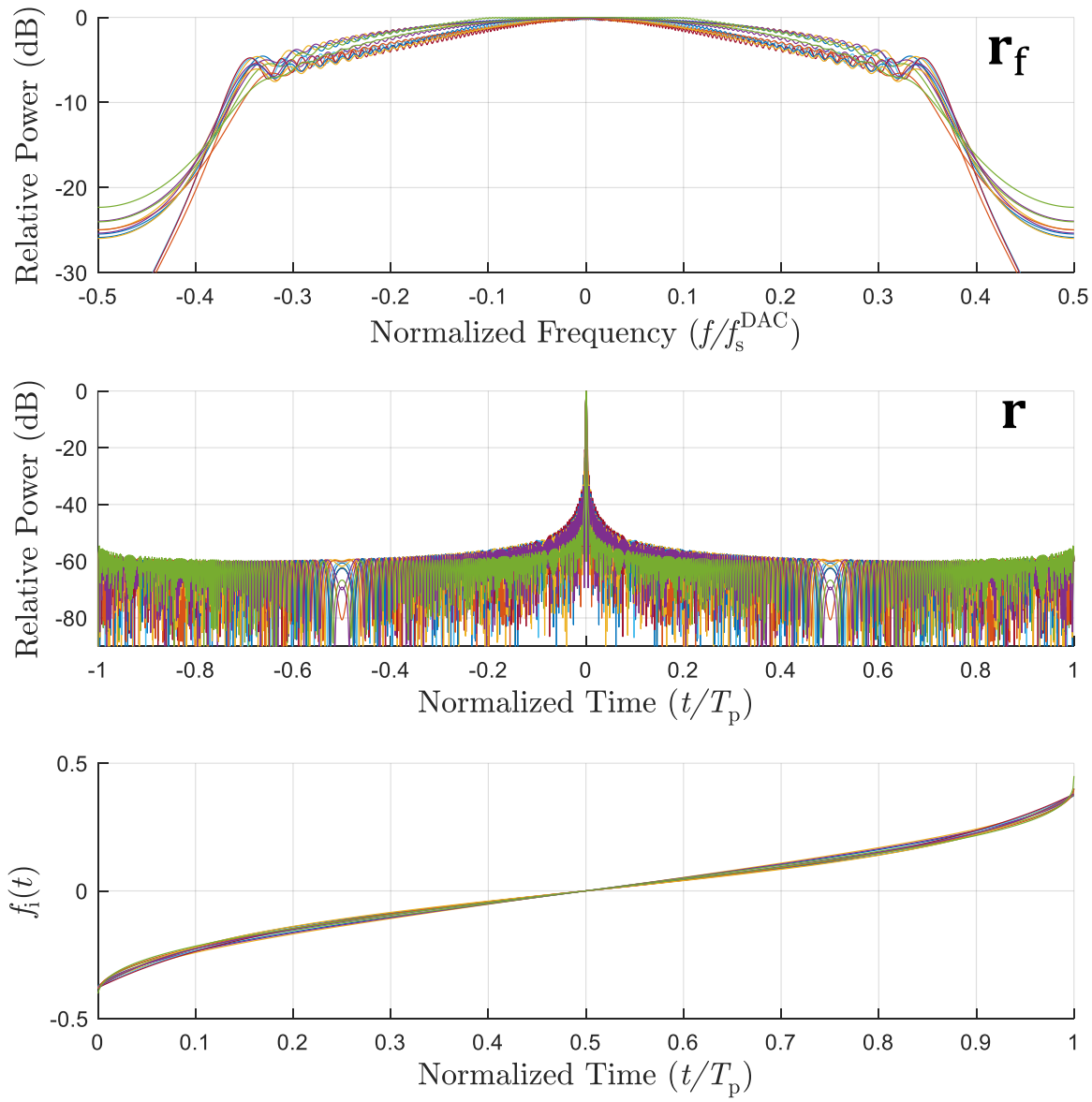

Figure 36: Various nonlinear FM waveform (top) power spectra, (middle) autocorrelations, and (bottom) instantaneous frequencies over time [79, 83-96] for $B_{3\mathrm{dB}}T_\mathrm{p} \approx 500$. When tuned appropriately, the performances achieved are quite similar.

1.4.2.6.3. PHASE CODED WAVEFORMS & ANGLE MODULATED WAVEFORMS

Phase coded waveforms [79] and angle modulated waveforms [117] have equivalent continuous representations $s_{\phi}(t)$, despite maintaining important distinctions. Here ϕ_n indicates the n^{th} of N_{ϕ} phase chips, T_{ϕ} is the time interval between adjacent phase chips, and $h_{\phi}(t)$ is a selected temporal shaping filter.

$$s_{\phi}(t) = h_{\phi}(t) * \left[\sum_{n=1}^{N_{\phi}} \delta\left(t - (n-1)T_{\phi}\right) e^{j\phi_n}\right] \tag{1.106}$$

The resulting waveform spectrum $s_{\phi}(f)$ is represented by the multiplication between the shaping filter spectrum $h_{\phi}(f)$ and the frequency representation of the phase chip impulse train.

$$s_{\phi}(f) = h_{\phi}(f) \cdot \left[\sum_{n=1}^{N_{\phi}} e^{-j2\pi f\left((n-1)T_{\phi}\right)} e^{j\phi_n}\right] \tag{1.107}$$

The temporal shaping filter $h_{\phi}(t)$ imposes the frequency spectrum shape $h_{\phi}(f)$, but may also introduce amplitude modulation to the waveform $s_{\phi}(t)$ depending on the selected shaping filter.

The rectangular temporal shaping filter $h_{\phi}(t) = \text{rect}(\frac{t - T_{\phi}/2}{T_{\phi}})$ is often examined because the resulting waveform $s_{\phi}(t)$ maintains constant amplitude, but forms the frequency mask $h_{\phi}(f) = T_{\phi}\,\text{sinc}\left(fT_{\phi}\right) e^{-j2\pi f(T_{\phi}/2)}$. In contrast, the sinc temporal shaping filter $h_{\phi}(t) = \text{sinc}(\frac{t}{T_{\phi}})$ imposes amplitude modulation upon the waveform $s_{\phi}(t)$, while forming the rectangular frequency mask $h_{\phi}(f) = T_{\phi}\,\text{rect}\left(fT_{\phi}\right)$. The rectangular and sinc temporal shaping filters are applied to generate waveforms $s_{\phi}(t)$ having uniformly distributed phase chips $\phi_n \in [-\pi, \pi]$, and the resulting waveform characteristics are shown in Figure 37.

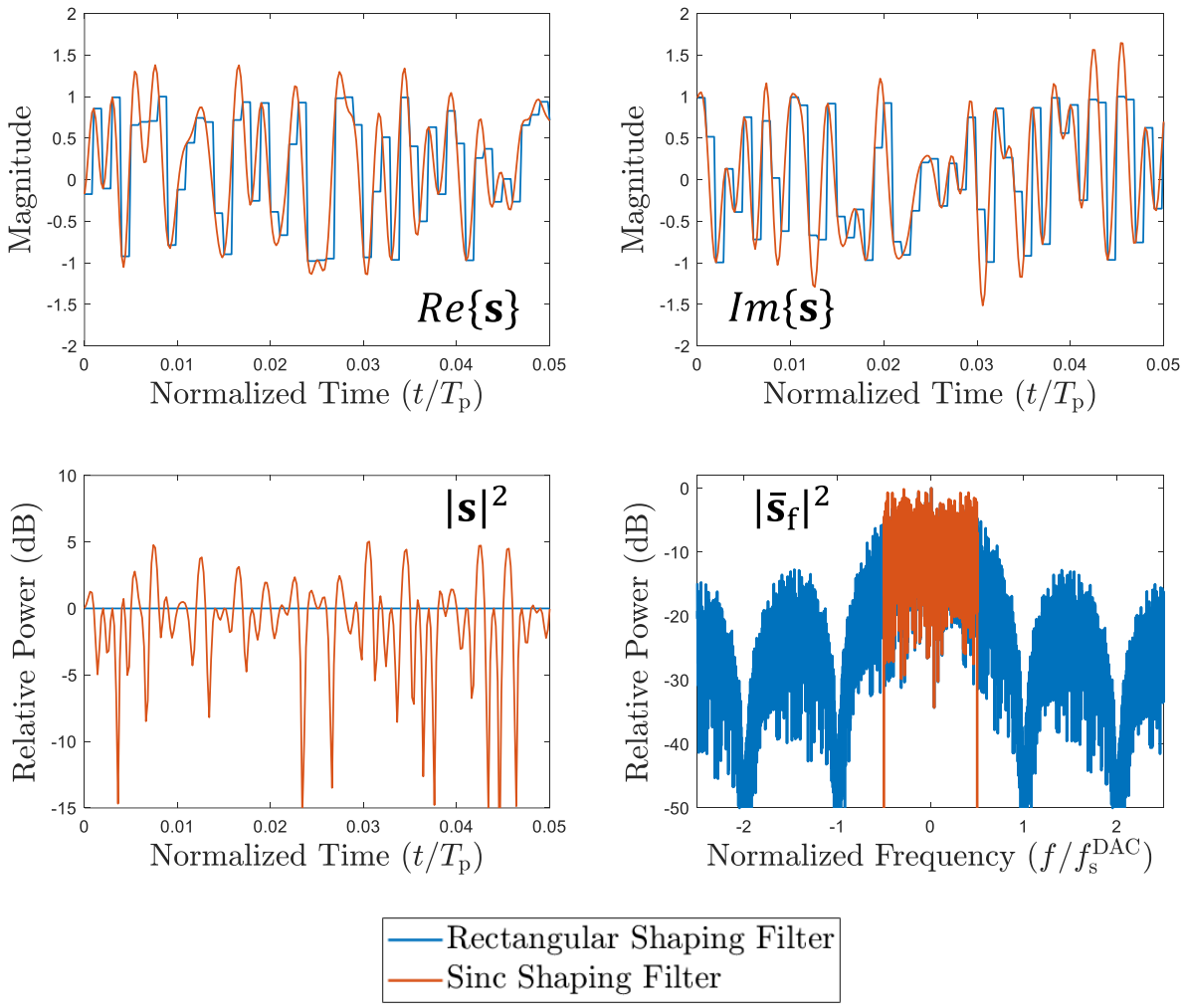

Figure 37: Amplitude envelopes $\left|s_{\phi}(t)\right|^2$ and power spectra $\left|s_{\phi}(f)\right|^2$ of phase coded waveforms having uniformly distributed phase chips $\phi_n \in [-\pi, \pi]$, applying either the shaping filter $h_{\phi}(t) = \text{rect}(\frac{t-T_{\phi}/2}{T_{\phi}})$ or $h_{\phi}(t) = \text{sinc}(\frac{t}{T_{\phi}})$.

The distinction between "phase coded" and "angle modulated" waveforms is subtle, but significant. Both are designed with a phase chip structure to modulate $s_{\phi}(t)$ – with the caveat that, when applying the rectangular shaping filter $h_{\phi}(t) = \text{rect}(\frac{t-T_{\phi}/2}{T_{\phi}})$, angle modulated waveforms exhibit spectral containment and phase coded waveforms do not exhibit spectral containment. Rather, phase coded waveforms require non-rectangular shaping filters $h_{\phi}(t) \neq \text{rect}(\frac{t-T_{\phi}/2}{T_{\phi}})$ to enforce spectral containment (as illustrated in Figure 37). In short, angle modulated waveforms simultaneously preserve an FM structure and spectral containment, whereas phase coded waveforms must trade between the degree of amplitude modulation and spectral containment.

The rectangular shaping filter $h_\phi(t) = \text{rect}(\frac{t-T_\phi/2}{T_\phi})$ models the sample-and-hold configuration utilized for DAC signal reconstruction to generate analog waveforms in RF transmit chains [42]. Applying the rectangular shaping filter to emulate DAC signal reconstruction, phase coded waveforms exhibit poor spectral containment due to unconstrained instantaneous frequency. Angle modulated waveforms exhibit adequate spectral containment due to frequency restrictions imposed during optimization.

Figure 38 illustrates the spectral containment of phase coded waveforms and angle modulated waveforms when the rectangular shaping filter is applied. By definition of the DTFT, an aperiodic discrete temporal signal results in a periodic continuous frequency spectrum (with spectral repetitions centered at $f/f_s^{\text{DAC}} = \pm 1, \pm 2, \ldots$). Due to the rectangular shaping filter, the spectral images of the angle modulated waveform become attenuated by the arising sinc spectral mask nulls. By observation, bandlimited waveforms are produced with greater accuracy by sample-and-hold DACs. The 3-dB oversampling ratio $\kappa_{3\text{dB}} = f_s^{\text{DAC}}/B_{3\text{dB}}$ is one indicator of spectral containment.

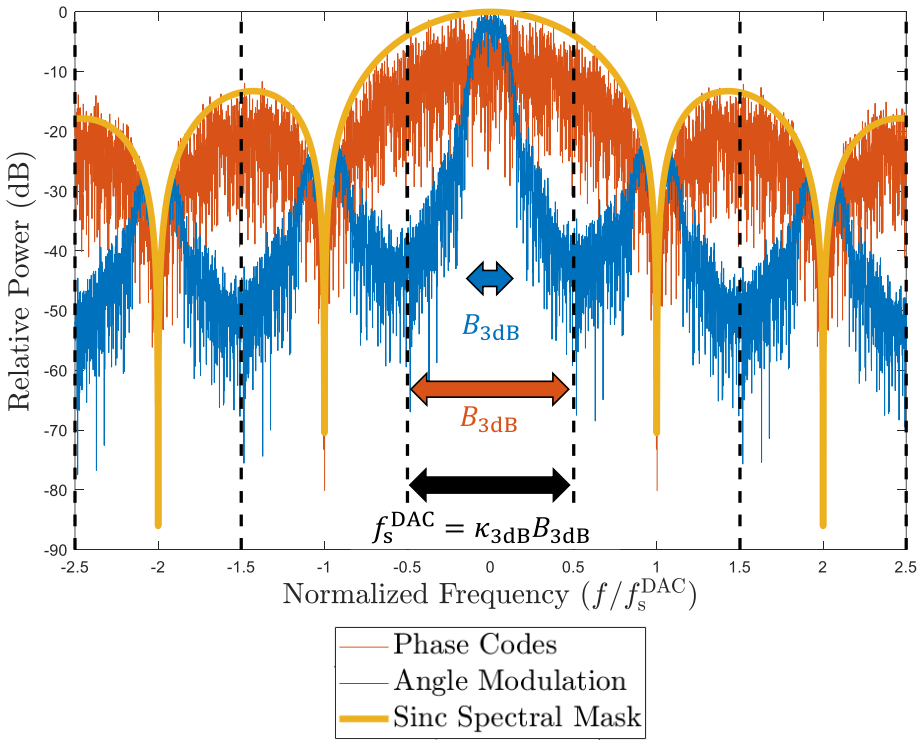

Figure 38: Power spectrum $|s_\phi(f)|^2$ of a phase coded waveform and an angle modulated waveform, after applying the temporal shaping filter $h_\phi(t) = \text{rect}(\frac{t-T_\phi/2}{T_\phi})$ that imposes the mask $h_\phi(f) = T_\phi \,\text{sinc}(fT_\phi)\, e^{-j2\pi f(T_\phi/2)}$.

When the baseband waveform $s_\phi(t)$ is uniformly sampled at intervals $t = (n/\beta_\phi)T_\phi$, the waveform model is defined by (1.108). The truncated convolution matrix $\mathbf{H}_\phi$ of size $N_\mathrm{p} \times \beta_\phi N_\phi$ contains time-shifted versions of the shaping filter $\mathbf{h}_\phi$. The phase chips in $\boldsymbol{\phi} = \begin{bmatrix}\phi_1 & \phi_2 & \cdots & \phi_{N_\phi}\end{bmatrix}^T$ of size $N_\phi \times 1$ determine the waveform properties. The upsampling factor β_ϕ describes the factor of interpolated samples $N_\mathrm{p} = \beta_\phi N_\phi$ imprinted by the temporal shaping filter $\mathbf{h}_\phi$ between sample intervals nT_ϕ.

$$\mathbf{s}_\phi = \mathbf{H}_\phi \left(e^{j\boldsymbol{\Phi}} \otimes \begin{bmatrix}1\\0\\\vdots\\0\end{bmatrix}_{\beta_\phi \times 1} \right)$$

(1.108)

However, the waveform model is typically simplified. Assume each phase chip is sampled only once $(\text{e.g. } \beta_\phi = 1)$. Consequently, the shaping filter $\mathbf{H}_\phi$ reduces to the identity matrix $\mathbf{I}$. The discrete waveform model then becomes

$$\mathbf{s}_\phi = e^{j\boldsymbol{\Phi}}\,.$$

(1.109)

Various forms of angle modulated waveforms exist [117-121]. Pseudo-random optimized frequency modulated (PRO-FM) waveforms are constructed with an alternating projection optimization, which leverages the waveform model $\mathbf{s} = e^{j\boldsymbol{\Phi}}$ [120-121]. The p^{th} of P waveforms is initialized with phase chips drawn from the uniform distribution $\phi_n \in [-\pi, \pi]$ to form the signal $\mathbf{s}_{0,p}$. The PRO-FM algorithm performs the k^{th} of K alternating iterations

$$\dot{\mathbf{s}}_p^{(k+1)} = \widetilde{\mathbf{A}}^H \left\{ \mathbf{d}_\mathrm{f}^{1/2} \odot \exp\left(j \angle \widetilde{\mathbf{A}} \mathbf{s}_p^{(k)} \right) \right\}$$

$$\mathbf{s}_p^{(k+1)} = \mathbf{u} \odot \exp\left(j \angle \dot{\mathbf{s}}_p^{(k+1)} \right)$$

(1.110)

where $\widetilde{\mathbf{A}}$ is the $M \times N$ truncated DFT matrix with $M \geq 2N-1$, $\widetilde{\mathbf{A}}^H$ is the $N \times M$ truncated IDFT matrix, $\mathbf{d}_\mathrm{f}$ is the $M \times 1$ desired PSD, $\mathbf{u}$ is the $N \times 1$ desired amplitude envelope, and $\angle(\cdot)$ extracts the argument phase.

Figure 39 illustrates the PRO-FM waveform characteristics, for $P = 10$ randomly initialized waveforms and $K = 200$ alternating projection iterations. The desired PSD $\mathbf{d}_{\mathrm{f}}$ is selected to have a super-Gaussian spectral shape [121] and $\mathbf{u}$ is constant amplitude. Due to random initializations, each PRO-FM waveform has an entirely unique instantaneous frequency structure. While the PRO-FM waveforms exhibit moderate instantaneous frequency compactness, notable deviations occur about the spectral band edges [122].

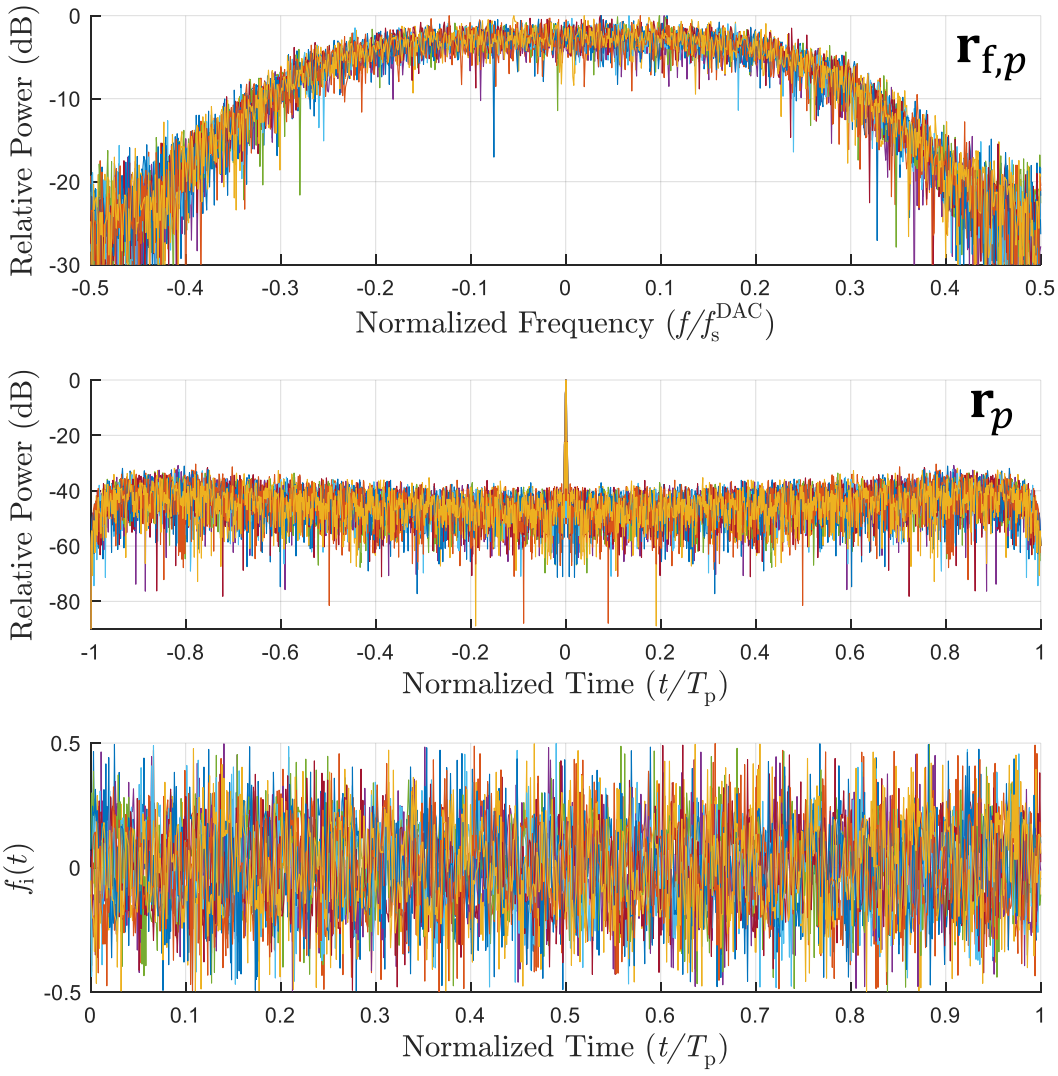

Figure 39: Various randomly initialized PRO-FM waveforms (top) power spectra, (middle) autocorrelations, and (bottom) instantaneous frequencies over time for $B_{3\mathrm{dB}}T_{\mathrm{p}} \approx 500$, for $P = 10$ waveforms and $K = 200$ iterations.

1.4.2.6.4. POLYPHASE CODED FREQUENCY MODULATION (PCFM)

Polyphase coded frequency modulated (PCFM) waveforms [123, 124] are mathematically defined to explicitly restrict the phase transition size between adjacent samples, which imparts innate spectral containment. PCFM waveforms are constructed by N_α instantaneous frequency values α_n, which are interpolated via the frequency shaping filter $h_\alpha(t)$ and then integrated to form a continuous phase term. PCFM waveforms are intrinsically constant modulus, and therefore amenable to high-power amplification. The PCFM waveform structure has been optimized to achieve a variety of objectives [123-132]

$$\begin{aligned} s_\alpha(t) &= \exp\left\{ j\left(\int_0^t h_\alpha(\tau) * \left[\sum_{n=1}^{N_\alpha} \alpha_n \delta(\tau - (n-1)T_\alpha) \right] d\tau \right) \right\} \\ &= \exp\left\{ j\left(\int_0^t \left[\sum_{n=1}^{N_\alpha} \alpha_n h_\alpha(\tau - (n-1)T_\alpha) \right] d\tau \right) \right\} \\ &= \exp\left\{ j\left(\sum_{n=1}^{N_\alpha} \alpha_n \int_0^t h_\alpha(\tau - (n-1)T_\alpha)\, d\tau \right) \right\} \end{aligned}$$

(1.111)

When the frequency shaping filter $h_\alpha(t)$ is defined only for positive time, such that $h_\alpha(t<0)=0$, then the integral is shift-invariant [133] and may be expressed instead by the phase shaping filter $b_\alpha(t) = \int_0^t h_\alpha(\tau)\, d\tau$. The relationship between $h_\alpha(t)$ and $b_\alpha(t)$ is illustrated in Figure 40, when $h_\alpha(t) = \frac{1}{T_\alpha}\mathrm{rect}(\frac{t-T_\alpha/2}{T_\alpha})$.

$$\begin{aligned} s_\alpha(t) &= \exp\left\{ j\left(\sum_{n=1}^{N_\alpha} \alpha_n \int_0^t h_\alpha(\tau - (n-1)T_\alpha)\, d\tau \right) \right\} = \exp\left\{ j\left(\sum_{n=1}^{N_\alpha} \alpha_n b_\alpha(t - (n-1)T_\alpha) \right) \right\} \\ &= \exp\left\{ j\left(b_\alpha(t) * \left[\sum_{n=1}^{N_\alpha} \alpha_n \delta(t - (n-1)T_\alpha) \right] \right) \right\} \end{aligned}$$

(1.112)

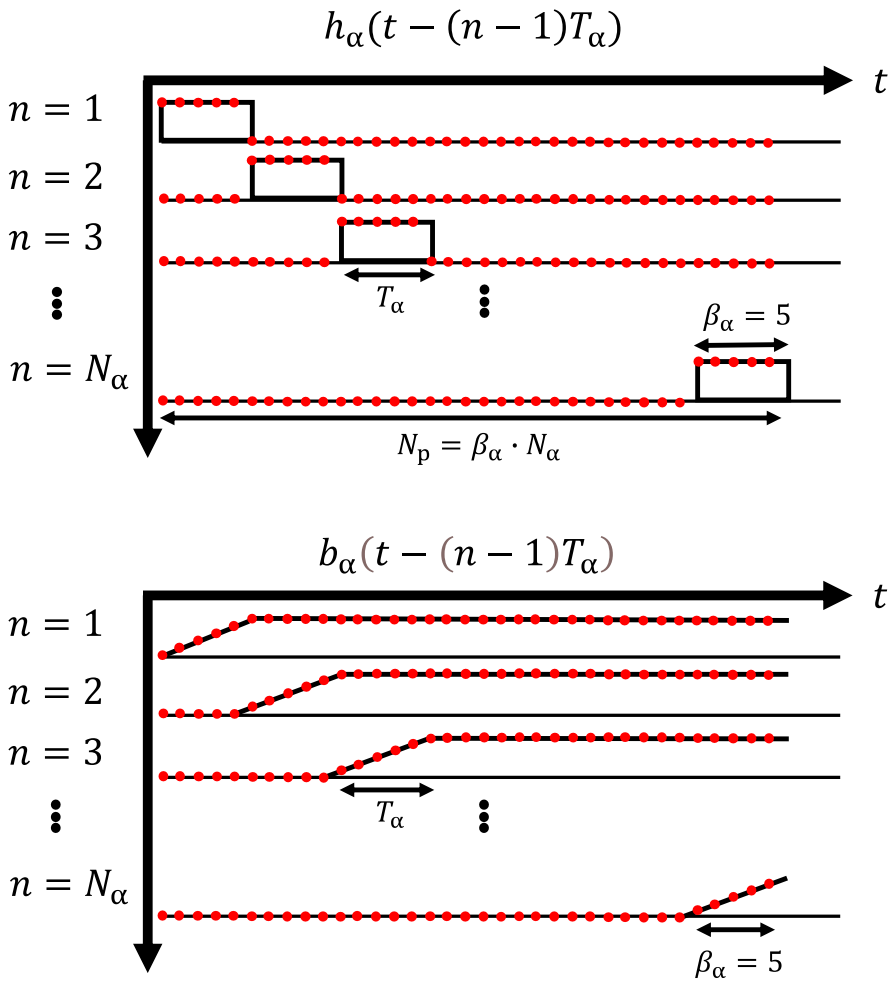

Figure 40: Relationship between the frequency shaping filter $h_\alpha(\tau-(n-1)T_\alpha)$ and the phase shaping filter $b_\alpha(t-(n-1)T_\alpha)$, where $h_\alpha(t)=\frac{1}{T_\alpha}\text{rect}(\frac{t-T_\alpha/2}{T_\alpha})$ and $b_\alpha(t)=\int_0^t h_\alpha(\tau)\,d\tau$.

When the baseband waveform $s_\alpha(t)$ is uniformly sampled at intervals $=(n/\beta_\alpha)T_\alpha$, the waveform model is defined by (1.113). The truncated convolution matrix $\mathbf{B}$ of size $N_p\times N_\alpha$ contains time-shifted versions of the phase shaping filter $\mathbf{b}_\alpha$. The instantaneous frequencies in $\boldsymbol{\alpha}=[\alpha_1\quad\alpha_2\quad\cdots\quad\alpha_{N_\alpha}]^T$ of size $N_\alpha\times 1$ determine the waveform properties. The upsampling factor β_α describes the factor of phase interpolated samples $N_p=\beta_\alpha N_\alpha$ imprinted by the phase shaping filter $\mathbf{b}$ between sample intervals nT_α.

$$\mathbf{s}_\alpha=e^{\mathbf{B}\boldsymbol{\alpha}} \tag{1.113}$$

When the frequency shaping filter $h_\alpha(\tau)$ is selected as the rectangular function $h_\alpha(t) = \frac{1}{T_\alpha}\text{rect}(\frac{\tau - T_\alpha/2}{T_\alpha})$ the resulting phase shaping filter $b_\alpha(t) = \int_0^t h_\alpha(\tau)\, d\tau$ becomes the ramp-and-hold function, which behaves similar to linear phase interpolation. The upsampling factor $\beta_\alpha = N_\text{p}/N_\alpha$ effectively limits the largest phase transition between adjacent waveform samples. Consequently, the upsampling factor β_α and the 6-dB oversampling ratio $\kappa_{6\text{dB}}$ are approximately equivalent $\kappa_{6\text{dB}} = f_\text{s}^{\text{DAC}}/B_{6\text{dB}} \approx \beta_\alpha$ as shown in Figure 42. The inherent spectral containment of PCFM waveforms minimizes distortion caused during sample-and-hold DAC reconstruction.

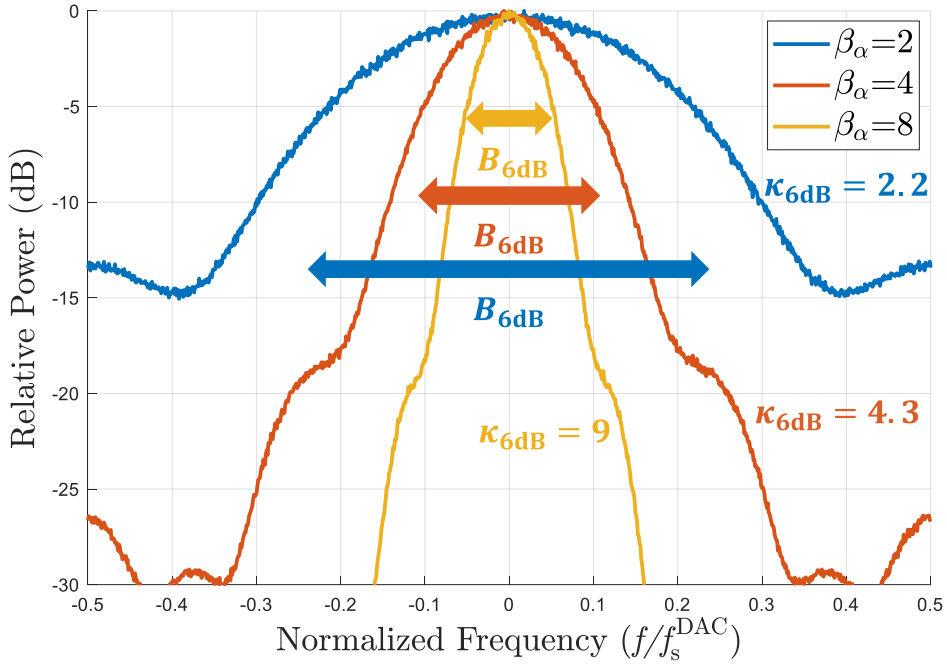

Figure 41: Mean power spectrum of $P = 1000$ unoptimized PCFM waveforms for upsampling factors $\beta_\alpha = 2, 4, 8$. The 6-dB oversampling ratio $\kappa_{6\text{dB}}$ is approximately equal to the upsampling factor β_α. The instantaneous frequency values are drawn from a uniform distribution $\alpha_n \in [-\pi, \pi]$.

Figure 42 illustrates unoptimized PCFM waveform characteristics, where the instantaneous frequency values are drawn from a uniform distribution $\alpha_n \in [-\pi, \pi]$ to generate $P = 10$ waveforms. The unoptimized PCFM waveforms exhibit innate spectral containment via the upsampling factor β_α for virtually no computational cost, yielding compact instantaneous frequencies while maintaining constant amplitude temporal envelopes. Optimization can improve the degree of spectral containment or reduce autocorrelation sidelobes [123-132].

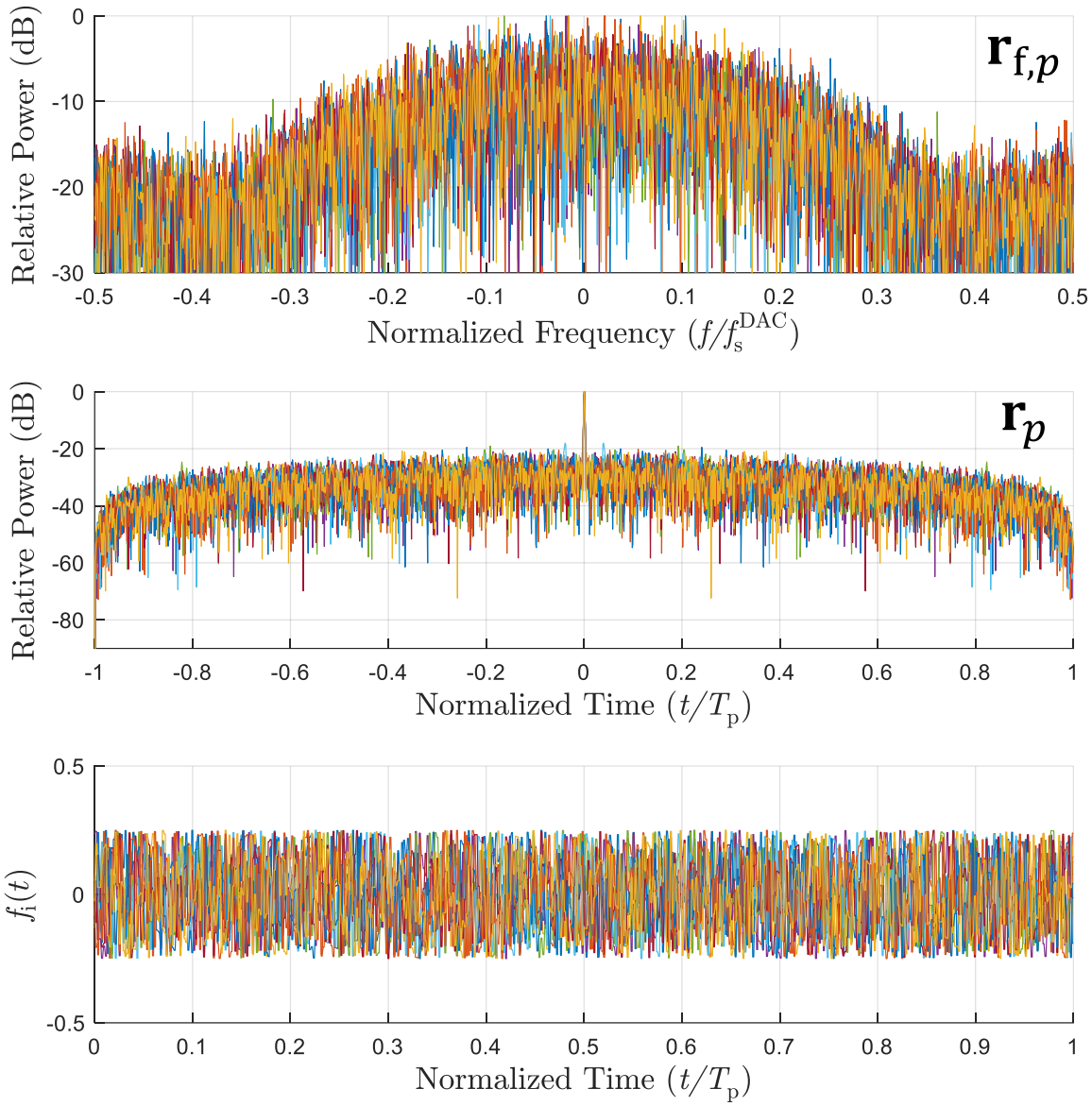

Figure 42: Various unoptimized PCFM waveforms (top) power spectra, (middle) autocorrelations, and (bottom) instantaneous frequencies over time for $B_{3\mathrm{dB}}T_\mathrm{p} \approx 500$, for $P = 10$ waveforms and factor $\beta_\alpha = 2$.

1.4.2.7. RANGE AMBIGUITIES AND PULSE ECLIPSING

Consider a waveform set transmitted in a uniform pulsed manner. Upon transmitting a given pulse $s_p(t)$, the received returns are range unambiguous if the electromagnetic scattering arrives at time delays that are non-overlapping with the returns from other pulse transmissions $s_{\tilde{p}}(t)$. In contrast, the received returns are range ambiguous if the scattering from pulse $s_p(t)$ temporally overlaps with the scattering from other pulses $s_{\tilde{p}}(t)$. Pulse eclipsing occurs when the scattered returns temporally overlap with the pulse transmission, wherein the receiver is switched off, thus concealing a portion of the scattered return. Due to the propagation power drop-off, the scattered signal from $s_p(t)$ is assumed negligible relative to the noise floor over sufficient distance. These scenarios are illustrated in Figure 43.

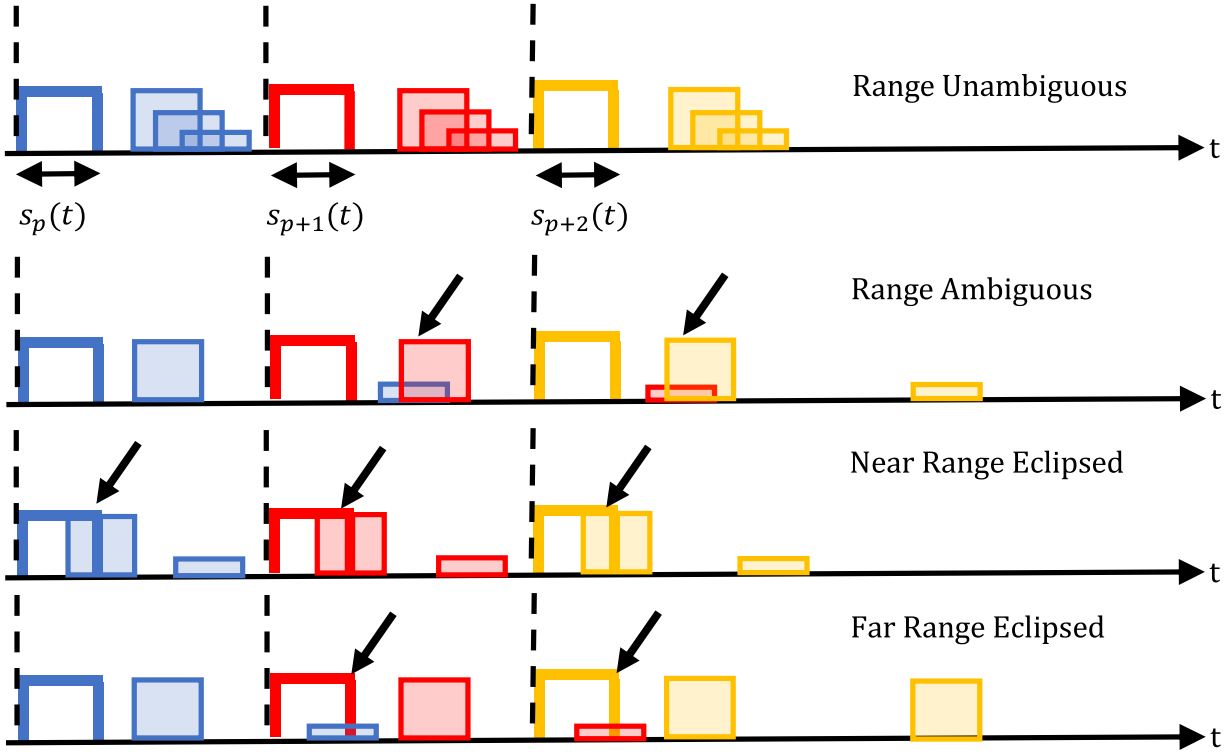

Figure 43: Range Unambiguous, Ambiguous, and Eclipsed Returns.

1.4.2.8. SIGNAL-TO-NOISE RATIO, PULSE COMPRESSION GAIN & COHERENT INTEGRATION

The impact of pulse compression and slow time processing on signal-to-noise ratio (SNR) is considered in the presence of additive white Gaussian noise (AWGN), represented by the random process $v(t)$. Consider the receive signal model $y(t) = s(t) + v(t)$. The pulse compression estimate becomes

$$\hat{\gamma}(t) = w(t) \star y(t) = w(t) \star s(t) + w(t) \star v(t) \, .$$

(1.114)

The noise $v(t)$ is spectrally filtered by $w(t)$, preserving a Gaussian distribution after the linear transformation [61]. The deterministic filter $w(t)$ and the random process $v(t)$ are uncorrelated in the expectation, such that $E\{|w(t) \star v(t)|^2\} = \|w(t)\|_2^2 \, \mathrm{E}\{|v(t)|^2\}$. The pulse compression gain G_{pc} and filter mismatch loss σ_{mml} determine the peak power of the pulse compression estimate $\hat{\gamma}(t)$. The pulse compressed SNR is

$$\mathrm{SNR}_{\mathrm{pc}} = \frac{\max\{|w(t) \star s(t)|^2\}}{E\{|w(t) \star v(t)|^2\}} = \frac{(\sigma_{\mathrm{mml}} G_{\mathrm{pc}}) \mathcal{P}_s}{\|w(t)\|_2^2 \, \mathrm{E}\{|v(t)|^2\}} = \frac{(\sigma_{\mathrm{mml}} G_{\mathrm{pc}}) \left(\frac{1}{T} \int_0^T |s(t)|^2 dt \right)}{\|w(t)\|_2^2 \lim\limits_{T \to \infty} \left\{ \frac{1}{T} \int_0^T |v(t)|^2 dt \right\}} = \left(\frac{\sigma_{\mathrm{mml}} G_{\mathrm{pc}}}{\|w(t)\|_2^2} \right) \mathrm{SNR}_{\mathrm{init}} \, .$$

(1.115)

Further SNR improvement to improve estimation accuracy is achieved by coherent integration across slow time pulse returns. Coherent integration requires that the radar transmitter and receiver are phase coherent. Assume that the given signal $s(t)$ is pulsed for P uniform pulse repetition intervals (PRI). Furthermore, assume scatterers are stationary to temporarily ignore Doppler effects. The range profile estimate $\hat{\gamma}_p(t)$ is formed by correlating the filter $w(t)$ and the p^{th} received signal $y_p(t)$. Coherent integration is expressed as

$$\hat{\gamma}_p(t) = w(t) \star y_p(t) = w(t) \star s(t) + w(t) \star v_p(t)$$

$$\hat{\gamma}_{\mathrm{int}}(t) = \sum_{\forall p} \hat{\gamma}_p(t) = \sum_{\forall p} \Big(w(t) \star s(t) + w(t) \star v_p(t) \Big) = P\big(w(t) \star s(t)\big) + \sum_{\forall p} w(t) \star v_p(t)$$

(1.116)

The noise signal $v_p(t)$ captured during the p^{th} received signal $y_p(t)$ is assumed independent and identically distributed, relative to noise signals $v_{\tilde{p}}(t)$ captured during other pulse repetition intervals. The expected noise power after coherent integration is then expressed as

$$E\left\{\left|\sum_{\forall p} w(t) \star v_p(t)\right|^2\right\} = E\left\{\left(\sum_{\forall p} w(t) \star v_p(t)\right)\left(\sum_{\forall p} w(t) \star v_p(t)\right)^*\right\} = P\,\|w(t)\|_2^2\,\sigma_{\mathrm{v}}^2\,.$$

(1.117)

The pulse compressed, coherently integrated SNR becomes

$$SNR_{\mathrm{int}} = \frac{\max\left\{\left|P\left(w(t) \star s(t)\right)\right|^2\right\}}{E\left\{\left|\sum_{\forall p} w(t) \star v_p(t)\right|^2\right\}} = \frac{P^2 \cdot (\sigma_{\mathrm{mml}} G_{\mathrm{pc}})\mathcal{P}_{\mathrm{s}}}{P \cdot \|w(t)\|_2^2\,\mathrm{E}\{|v(t)|^2\}} = P \cdot \mathrm{SNR}_{\mathrm{pc}} = P\left(\frac{\sigma_{\mathrm{mml}} G_{\mathrm{pc}}}{\|w(t)\|_2^2}\right)\mathrm{SNR}_{\mathrm{init}}\,.$$

(1.118)

The coherent integration across P pulse compressed LFM waveforms with AWGN present is shown in Figure 44.

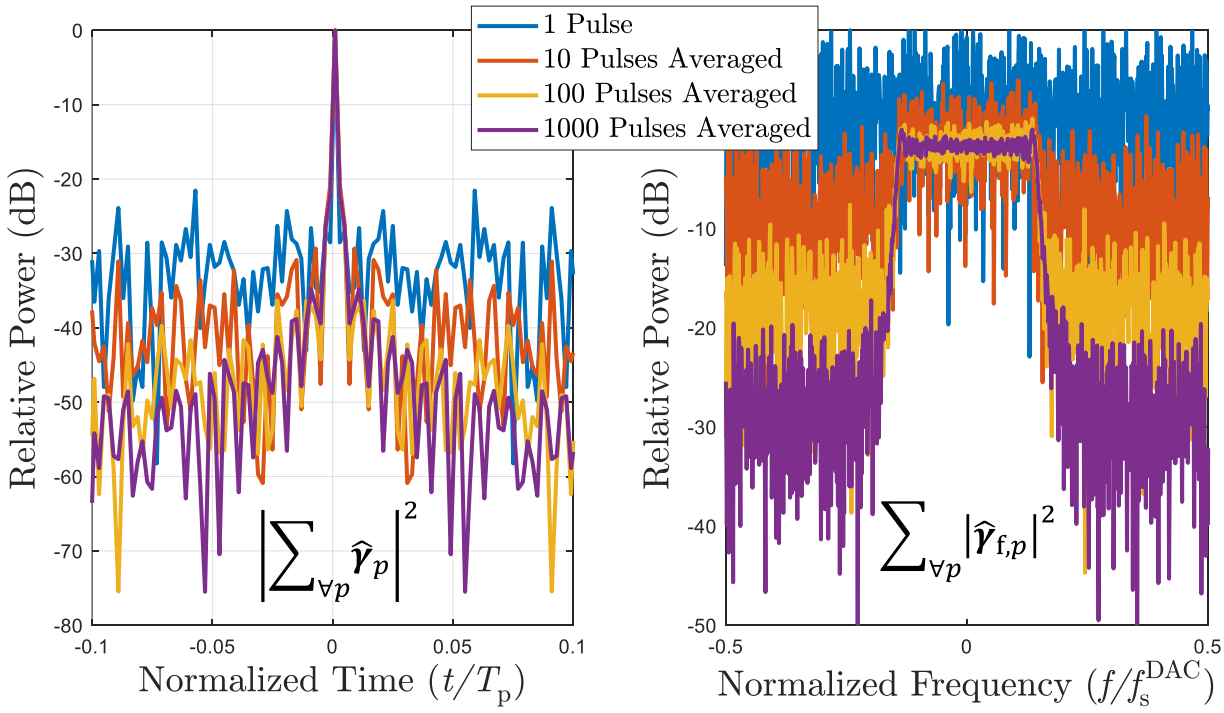

Figure 44: Coherent integration across P pulse compressed, identical LFM chirp waveforms with AWGN present.

1.4.2.9. COHERENT INTEGRATION RANGE SIDELOBE REDUCTION FOR NON-REPEATING WAVEFORMS, RANGE SIDELOBE MODULATION (RSM)

Nonrepeating waveforms, when optimized with unique initializations, tend towards different local minima within an objective function. For instance, the angle modulated waveform denoted PRO-FM are shaped to a desired power spectrum template, however, each PRO-FM waveform exhibits unique instantaneous frequency structures. Assume that the unique signals $s_p(t)$ are pulsed for P uniform PRIs. Furthermore, assume scatterers are stationary to temporarily ignore Doppler effects. Recall the ideal receive signal model $y_p^{\text{ideal}}(t) = s_p(t)$, here indicating the p^{th} received signal $y_p(t)$ from the p^{th} unique transmission $s_p(t)$. The ideal pulse compression estimate becomes

$$\hat{\gamma}_p(t) = w_p(t) \star y_p(t) = w_p(t) \star s_p(t) = c_p(t) \, .$$

(1.119)

The range profile estimate $\hat{\gamma}_p(t)$ is formed by correlating the p^{th} filter $w(t)$ and received signal $y_p(t)$, which under ideal conditions forms the p^{th} cross correlation function $c_p(t)$. Coherent integration is then expressed as

$$\begin{aligned} \hat{\gamma}_p(t) &= w_p(t) \star y_p(t) = w_p(t) \star s_p(t) \\ \hat{\gamma}_{\text{int}}(t) &= \sum_{\forall p} \hat{\gamma}_p(t) = \sum_{\forall p} w_p(t) \star s_p(t) = \sum_{\forall p} c_p(t) \end{aligned}$$

(1.120)

Importantly, note that the coherently averaged cross-correlation $\sum_{\forall p} c_p(t)$ and mean cross-power spectrum $\sum_{\forall p} c_p(f)$ are Fourier transform pairs, proven by operation linearity as

$$\sum\nolimits_{\forall p} c_p(t) = \sum\nolimits_{\forall p} \mathcal{F}^{-1}\{c_p(f)\} = \mathcal{F}^{-1}\left\{\sum\nolimits_{\forall p} c_p(f)\right\} \, .$$

(1.121)

When the filter $w_p(t)$ is selected as the p^{th} matched filter, the statement is extended to the Fourier relationship between the coherently averaged autocorrelation $\sum_{\forall p} r_p(t)$ and mean power spectrum $\sum_{\forall p} r_p(f)$.

$$\sum_{\forall p} r_p(t) = \sum_{\forall p} \mathcal{F}^{-1}\{r_p(f)\} = \mathcal{F}^{-1}\left\{\sum_{\forall p} r_p(f)\right\} .$$

(1.122)

The pulse compressed sidelobes of unique nonrepeating waveforms exhibit noise-like characteristics, with approximately complex Gaussian distributions due to the central limit theorem, as detailed in [134]. The correlation mainlobe remains coherent while the sidelobes decohere, which inherently reduces the coherently averaged pulse compression estimate sidelobe levels. The coherent sidelobe reduction applied to uniquely optimized PRO-FM waveforms when no AWGN is present is illustrated in Figure 45.

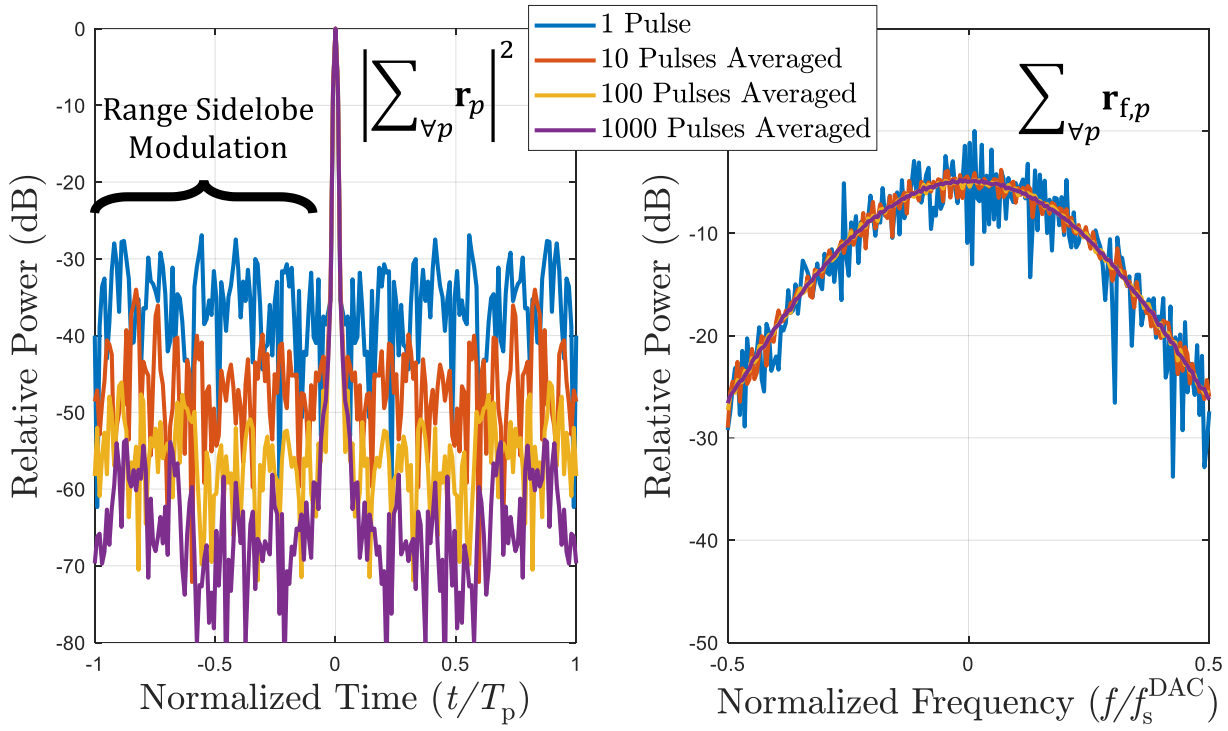

Figure 45: Sidelobe reduction from coherently integrating non-identical PROFM autocorrelations, with no AWGN.

Note that coherent sidelobe reduction of nonrepeating waveforms does not improve SNR, but rather reduces the pulse compression estimate sidelobe levels for improved detection of small scatterers. Range sidelobes fluctuations occur with increasing integration, due to the randomness of the correlation sidelobes. The correlation sidelobe phenomena of nonrepeating waveforms is called range sidelobe modulation (RSM).

1.4.3. DOPPLER FREQUENCY

The Doppler effect occurs when scatterers are moving throughout the illuminated scene, which distorts the scattered electromagnetic wavefront. The Doppler effect is dependent on the scatterer velocity relative to the speed of light c and the operating wavelength $\lambda(t)$. Here, the fundamental physics describing the Doppler effect are examined with respect to the fast time and slow time radar dimensions.

1.4.3.1. THE DOPPLER EFFECT

The Doppler effect is a distortion of electromagnetic wave time-frequency characteristics when moving scatterers are present in the observed scene, as explained by the theory of relativity [77]. The Doppler effect impacts the perceived time and frequency characteristics of the reflected pulse. When scatterers travel radially towards or away from the monostatic radar with constant velocity v_{r}, the reflected pulse is distorted temporally as

$$T_{\mathrm{p}}' = \left(\frac{c - v_{\mathrm{r}}}{c + v_{\mathrm{r}}}\right) T_{\mathrm{p}} = \frac{T_{\mathrm{p}}}{\psi}$$

(1.123)

The instantaneous frequency $f_{\mathrm{i}}(t) = f_{\mathrm{c}} + \frac{1}{2\pi}\frac{d\phi(t)}{dt}$ of the frequency modulated electromagnetic wave becomes inversely distorted as

$$f_{\mathrm{i}}'(t) = \left(\frac{c + v_{\mathrm{r}}}{c - v_{\mathrm{r}}}\right) f_{\mathrm{i}}(t) = \psi f_{\mathrm{i}}(t)$$

(1.124)

The Doppler distortion imposed by a moving scatterer is approximated by geometric expansion when $v_{\mathrm{r}} \ll c$ as

$$T_{\mathrm{p}}' = \left(\frac{c - v_{\mathrm{r}}}{c + v_{\mathrm{r}}}\right) T_{\mathrm{p}} \quad \approx \left(1 - \frac{2v_r}{c}\right) T_{\mathrm{p}}$$

$$f_{\mathrm{i}}'(t) = \left(\frac{c + v_{\mathrm{r}}}{c - v_{\mathrm{r}}}\right) f_{\mathrm{i}}(t) \approx \left(1 + \frac{2v_{\mathrm{r}}}{c}\right) f_{\mathrm{i}}(t) = f_{\mathrm{i}}(t) + \frac{2v_{\mathrm{r}}}{\lambda(t)} = f_{\mathrm{i}}(t) + f_{\mathrm{d}}(t)$$

(1.125)

The narrowband assumption imposes that the expected Doppler response $f_{\mathrm{d}}(t)$ from the scatterer with velocity v_{r} is invariant over time. The Doppler frequency is expressed as

$$f_{\mathrm{d}}(t) = f_{\mathrm{i}}'(t) - f_{\mathrm{i}}(t) = \left(\frac{2v_{\mathrm{r}}}{c}\right) f_{\mathrm{i}}(t) \qquad \text{(Wideband)}$$

$$f_{\mathrm{d}} \approx f_{\mathrm{i}}' - f_{\mathrm{c}} = \left(\frac{2v_{\mathrm{r}}}{c}\right) f_{\mathrm{c}} \qquad \text{(Narrowband)}$$

(1.126)

When a single scatterer traveling with radial velocity v_{r} imposes the Doppler effect, the passband receive signal under the narrowband assumption is modeled as

$$\begin{aligned} y_{\mathrm{pb}}(t) &= \gamma s_{\mathrm{pb}}\left(\psi \cdot \left(t - \frac{2R}{c + v_{\mathrm{r}}}\right)\right) = \gamma s_{\mathrm{pb}}\left(\psi t - \frac{2R}{c - v_{\mathrm{r}}}\right) \\ &= \gamma\, Re\left\{s_{\mathrm{bb}}\left(\psi t - \frac{2R}{c - v_{\mathrm{r}}}\right) e^{j2\pi f_{\mathrm{c}}\left(\psi t - \frac{2R}{c - v_{\mathrm{r}}}\right)}\right\} \\ &= \gamma\, Re\left\{s_{\mathrm{bb}}\left(\psi t - \frac{2R}{c - v_{\mathrm{r}}}\right) e^{j2\pi f_{\mathrm{c}}\psi t} e^{-j4\pi f_{\mathrm{c}}\left(\frac{R}{c - v_{\mathrm{r}}}\right)}\right\}. \end{aligned}$$

(1.127)

When the scatterer velocity is considerably less than the speed of light $v_{\mathrm{r}} \ll c$, the passband receive model under the narrowband assumption is approximated as

$$y_{\mathrm{pb}}(t) \approx \gamma\, Re\left\{s_{\mathrm{bb}}\left(\left(1 + \frac{2v_{\mathrm{r}}}{c}\right) t - \frac{2R}{c - v_{\mathrm{r}}}\right) e^{j2\pi(f_{\mathrm{c}} + f_{\mathrm{d}})t} e^{-j4\pi f_{\mathrm{c}}\left(\frac{R}{c - v_r}\right)}\right\}.$$

(1.128)

With sufficiently small velocity v_{r} the passband signal is further reduced to

$$y_{\mathrm{pb}}(t) \approx \gamma\, Re\left\{s_{\mathrm{bb}}\left(t - \frac{2R}{c}\right) e^{j2\pi(f_{\mathrm{c}} + f_{\mathrm{d}})t} e^{-j4\pi f_{\mathrm{c}}\left(\frac{R}{c}\right)}\right\}.$$

(1.129)

Subsuming miscellaneous terms into γ, the passband model is simplified to

$$y_{\mathrm{pb}}(t) \approx \gamma\, Re\left\{s_{\mathrm{bb}}\left(t-\frac{2R}{c}\right)e^{j2\pi(f_{\mathrm{c}}+f_{\mathrm{d}})t}\right\}$$

$$= \gamma s_{\mathrm{pb}}\left(t-\frac{2R}{c}\right)e^{j2\pi f_{\mathrm{d}}t}\,.$$

(1.130)

The baseband receive signal representation is similarly represented as

$$y_{\mathrm{bb}}(t) = \gamma s_{\mathrm{pb}}(t-\tau)e^{j2\pi f_{\mathrm{d}}t}e^{-j2\pi f_{\mathrm{c}}t}$$

$$= \gamma s_{\mathrm{bb}}(t-\tau)e^{j2\pi f_{\mathrm{c}}(t-\tau)}e^{j2\pi f_{\mathrm{d}}t}e^{-j2\pi f_{\mathrm{c}}t}$$

$$= \gamma\, s_{\mathrm{bb}}(t-\tau)e^{-j2\pi f_{\mathrm{c}}\tau}e^{j2\pi f_{\mathrm{d}}t} = \gamma\, s_{\mathrm{bb}}\left(t-\frac{2R}{c}\right)e^{-j\left(\frac{4\pi R}{\lambda_{\mathrm{c}}}\right)}e^{j2\pi f_{\mathrm{d}}t}$$

(1.131)

Assume a single point target is present in the scene where $\gamma(t)e^{-j2\pi f_{\mathrm{c}}t} = \gamma\delta(t-\tau)$. The ideal Doppler-shifted receive signal is expressed as

$$y_{\mathrm{ideal}}(t) = \gamma\, s\left(t-\frac{2R}{c}\right)e^{j2\pi f_{\mathrm{d}}t} = \left(s(t) * \gamma\delta\left(t-\frac{2R}{c}\right)\right)e^{j2\pi f_{\mathrm{d}}t}$$

(1.132)

1.4.3.2. THE AMBIGUITY FUNCTION

When moving targets are present in the illuminated scene, the reflected signal is frequency shifted due to the Doppler effect. When the received signal from a single pulse is Doppler-shifted by frequency f_{d}, but the pulse compression filter is tuned assuming the scattered return has no Doppler shift ($f_{\mathrm{d}} = 0$), the pulse compression estimate varies with the degree of Doppler shift f_{d}. Consider the pulse compression filter $w(t)$ applied to the ideal Doppler-shifted signal $y_{\mathrm{ideal}}(t)$.

$$\hat{y}(t) = \int_{-\infty}^{\infty} w^*(\tau - t)\, y_{\text{ideal}}(\tau)\, d\tau = \int_{-\infty}^{\infty} w^*(\tau - t) s\left(\tau - \frac{2R}{c}\right) e^{j2\pi f_{\text{d}}\left(\tau - \frac{2R}{c}\right)} d\tau$$

(1.133)

The narrowband (or Woodward's) ambiguity function defined in (1.134) is constructed from matched filter estimates of the ideal Doppler-shifted baseband or passband signal $y_{\text{ideal}}(t)$ assuming no range delay, swept over every possible Doppler shift f_{d}.

$$\chi(t, f_{\text{d}}) = \int_{-\infty}^{\infty} w_{\text{mf}}^*(\tau - t)\, y_{\text{ideal}}(\tau)\, d\tau = \frac{1}{\|s(t)\|_2^2} \int_{-\infty}^{\infty} s^*(\tau - t)(s(\tau)\, e^{j2\pi f_{\text{d}}\tau})\, d\tau$$

(1.134)

The ambiguity function of an LFM waveform and a PROFM waveform are shown in Figure 46. The LFM waveform is called Doppler tolerant because a strong matched filter response exists across all Doppler frequencies. The PROFM waveforms are called Doppler selective (or Doppler intolerant) because the matched filter response rapidly drops off at significant Doppler shifts. Ambiguity function waveform metrics are discussed further in [135].

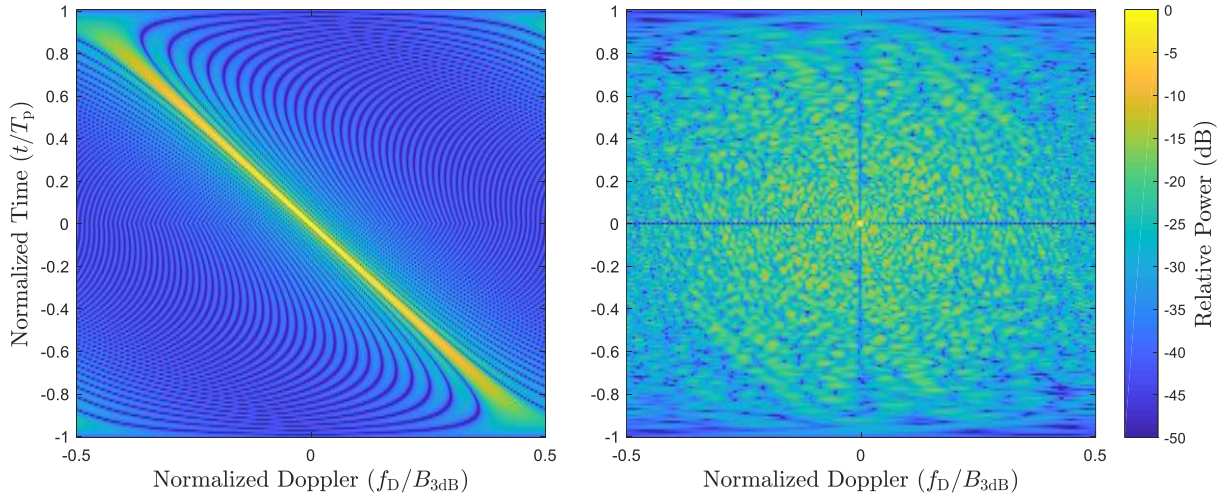

Figure 46: Ambiguity function $|\chi(t, f_{\text{d}})|^2$ of an up-chirped LFM waveform (left) and a single PROFM waveform (right), with time-bandwidth product $B_{\text{3dB}}T_{\text{p}} = 100$.

1.4.3.3. RANGE-DOPPLER PROCESSING, THE POINT SPREAD FUNCTION

Fast time-Doppler and slow time-Doppler are distinct only with respect to the examined time scale. Fast time-Doppler refers to Doppler shifts induced within a single pulse, elicited by high velocity scatterers. Slow time-Doppler refers to Doppler shifts induced across multiple pulses, elicited by low velocity scatterers. Consider the pulse train $s_{\text{train}}(t)$ formed by the p^{th} of P pulses $s_p(t)$, which are uniformly spaced by the PRI duration $T_{\text{PRI}} \gg T_{\text{p}}$.

$$s_{\text{train}}(t) = \sum_{p=0}^{P-1} s_p(t - pT_{\text{PRI}})$$

(1.135)

The ideal baseband or passband scatterer response from the pulse train is then

$$y_{\text{ideal}}(t) = \left(\sum_{p=0}^{P-1} s_p\left(t - pT_{\text{PRI}} - \frac{2R}{c}\right)\right) e^{j2\pi f_{\text{d}} t}.$$

(1.136)

The p^{th} pulse compression filter $w_p(t)$ is applied to the listening interval of the p^{th} pulse repetition interval to form the range estimate $\hat{\gamma}_p(t)$.

$$\hat{\gamma}_p(t) = \int_{pT_{\text{PRI}}}^{(p+1)T_{\text{PRI}}} w_p^*(\tau - t)\, s_p\left(\tau - pT_{\text{PRI}} - \frac{2R}{c}\right) e^{j2\pi f_{\text{d}}\tau}\, d\tau$$

(1.137)

The set of range estimates over the entire coherent processing interval (CPI) becomes

$$\hat{\gamma}(t) = \sum_{p=0}^{P-1} \int_{pT_{\text{PRI}}}^{(p+1)T_{\text{PRI}}} w_p^*(\tau - t)\, s_p\left(\tau - pT_{\text{PRI}} - \frac{2R}{c}\right) e^{j2\pi f_{\text{d}}\tau}\, d\tau$$

(1.138)

The stop-and-hop assumption imposes that the fast time-Doppler shift is negligible within the scattered pulse duration. The scatterer is assumed to have constant velocity over the entire CPI, and to not traverse a significant distance within the CPI. The Doppler shift is uniformly sampled every pT_{PRI} seconds at delay bin $2R/c$. For slow moving scatterers $f_{\mathrm{d}} \ll 1/T_{\mathrm{p}}$, the introduced error is negligible.

$$\begin{aligned}
\hat{\gamma}\left(t+\frac{2R}{c}\right) &= \sum_{p=0}^{P-1}\left(\int_{pT_{\mathrm{PRI}}}^{(p+1)T_{\mathrm{PRI}}} w_p^*\left(\tau-\left(t+\frac{2R}{c}\right)\right) s_p\left(\tau-pT_{\mathrm{PRI}}-\frac{2R}{c}\right) e^{j2\pi f_{\mathrm{d}}\cdot(pT_{\mathrm{PRI}})}\, d\tau\right) \\
&= \sum_{p=0}^{P-1}\left(\int_{pT_{\mathrm{PRI}}}^{(p+1)T_{\mathrm{PRI}}} w_p^*\left(\tau-t-\frac{2R}{c}\right) s_p\left(\tau-pT_{\mathrm{PRI}}-\frac{2R}{c}\right) d\tau\right) e^{j2\pi f_{\mathrm{d}}\cdot(pT_{\mathrm{PRI}})} \\
&= \sum_{p=0}^{P-1} c_p\left(t-pT_{\mathrm{pri}}\right) e^{j2\pi\left(\frac{f_{\mathrm{d}}}{f_{\mathrm{PRF}}}\right)p} \\
&= \sum_{p=0}^{P-1} c_p(t-pT_{\mathrm{pri}}) e^{j2\pi\varpi p}
\end{aligned}$$

(1.139)

The pulse compression estimate of the ideal Doppler shifted return becomes the time-delayed cross-correlation responses, phase shifted by the slow time Doppler phasor $e^{j2\pi\varpi p}$ under the stop-and-hop assumption. The Doppler response of the scatterer is sampled every pT_{pri} seconds, which is considered sampling across pulses (or slow time) with pulse repetition frequency f_{PRF}. The sampling bounds of the uniform slow time-Doppler dimension are determined by the Nyquist theorem as

$$\begin{aligned}
f_{\mathrm{PRF}} &\geq 2f_{\mathrm{d}} = 2\left(\frac{2v_{\mathrm{r}}}{c}\right) f_{\mathrm{c}} \\
\rightarrow\ v_{\mathrm{r}} &\leq \pm\frac{1}{4}\left(\frac{c}{f_{\mathrm{c}}}\right) f_{\mathrm{PRF}} = \pm\frac{\lambda_{\mathrm{c}} f_{\mathrm{PRF}}}{4}\ .
\end{aligned}$$

(1.140)

The slow time-Doppler phase response of the scattering scene is "sampled" across P pulses. The received fast time response $\mathbf{y}_p$ from the p^{th} transmit pulse is modeled under the stop-and-hop assumption with AWGN as

$$\mathbf{y}_p = \sum_{\forall \varpi} \mathbf{S}_p \boldsymbol{\gamma}(\varpi) e^{j2\pi\varpi p} + \mathbf{v}$$

(1.141)

where $\boldsymbol{\gamma}(\varpi)$ is the scattering range profile corresponding to the normalized Doppler shift ϖ, $\mathbf{S}_p$ is the convolution matrix of the p^{th} pulse, and $\mathbf{v}$ is noise. The slow time-Doppler phase progression (or steering vector) $\mathbf{u}(\varpi)$ for the normalized Doppler-shift ϖ is expressed as

$$\mathbf{u}(\varpi) = [e^{j2\pi\varpi(0)} \quad \dots \quad e^{j2\pi\varpi(P-1)}]^T$$

(1.142)

Pulse compression is applied to the p^{th} receive vector to form the range estimate $\hat{\boldsymbol{\gamma}}_p$ wherein moving scatterers having Doppler-shift ϖ may be present at the ℓ^{th} range bin. $\mathbf{W}_p$ is the convolution matrix of the p^{th} pulse compression filter $\mathbf{w}_p$.

$$\hat{\boldsymbol{\gamma}}_p = \mathbf{w}_p \star \mathbf{y}_p = \mathbf{W}_p^H \mathbf{y}_p = \mathbf{W}_p^H \left(\sum_{\forall \varpi} \mathbf{S}_p \boldsymbol{\gamma}(\varpi) e^{j2\pi\varpi p} + \mathbf{v} \right) = \mathbf{W}_p^H \left(\sum_{\forall \varpi} \mathbf{S}_p \boldsymbol{\gamma}(\varpi) e^{j2\pi\varpi p} \right) + \mathbf{W}_p^H \mathbf{v}$$

(1.143)

Each range estimate from the p^{th} PRI is stacked horizontally to form the fast/slow time matrix $\hat{\boldsymbol{\Upsilon}} = [\hat{\boldsymbol{\gamma}}_0 \quad \cdots \quad \hat{\boldsymbol{\gamma}}_{P-1}]$.

To determine the Doppler content in the pulse compressed data matrix $\hat{\boldsymbol{\Upsilon}}$, the Doppler filter bank $\mathbf{U} = [\mathbf{u}^*(\varpi_0) \quad \cdots \quad \mathbf{u}^*(\varpi_{P-1})]$ hypothesizes various normalized slow-time Doppler shifts ϖ that are uniformly spaced over the set $\varpi \in [-0.5, 0.5)$. The Doppler filter bank $\mathbf{U}$ correlates the data matrix $\hat{\boldsymbol{\Upsilon}}$ with each possible Doppler steering vector $\mathbf{u}^*(\varpi)$, applied along the slow time dimension as

$$\hat{\boldsymbol{\Upsilon}}_{\text{d}} = \hat{\boldsymbol{\Upsilon}} \mathbf{U}$$

(1.144)

Noting that the pulse repetition intervals p and hypothesized Doppler shifts ϖ are each uniformly sampled, the Doppler filter bank now takes the form of a DFT matrix $\overline{\mathbf{A}}$ with dimension $P \times P$ (which can be efficiently implemented with an FFT). Consequently, (1.144) may be rewritten as

$$\widehat{\mathbf{Y}}_{\mathrm{d}} = \widehat{\mathbf{Y}}\overline{\mathbf{A}}$$

(1.145)

Now, assume a single point scatterer is present with no range delay and no Doppler shift. The set of P waveform/filter cross-correlation functions $\mathbf{c}_p$ are concatenated to form the matrix $\mathbf{C} = [\mathbf{c}_0 \quad \mathbf{c}_1 \quad \cdots \quad \mathbf{c}_{P-1}]$. The DFT applied to the cross-correlation fast time dimension of $\mathbf{C}$ forms the set of waveform cross-power spectra $\mathbf{C}_{\mathrm{f}}$.

$$\mathbf{C}_{\mathrm{f}} = \overline{\mathbf{A}}_1\mathbf{C}$$

$$\mathbf{C} = \left(\frac{1}{N_{\mathrm{c}}}\right)\overline{\mathbf{A}}_1^H\mathbf{C}_{\mathrm{f}}$$

(1.146)

The DFT applied to the slow time dimension of $\mathbf{C}$ forms the point spread function $\mho$.

$$\mho = \mathbf{C}\overline{\mathbf{A}}_2 = \left(\frac{1}{N_{\mathrm{c}}}\right)\overline{\mathbf{A}}_1^H\mathbf{C}_{\mathrm{f}}\overline{\mathbf{A}}_2$$

(1.147)

For the case of matched filter pulse compression, the point spread function (PSF) may be expressed more specifically.

$$\mho = \left(\frac{1}{\sum_{\forall p}\left\|\mathbf{s}_{\mathrm{p}}\right\|_2^2}\right)\mathbf{R}\overline{\mathbf{A}}_2 = \left(\frac{1}{N_{\mathrm{r}}\sum_{\forall p}\left\|\mathbf{s}_{\mathrm{p}}\right\|_2^2}\right)\overline{\mathbf{A}}_1^H\mathbf{R}_{\mathrm{f}}\overline{\mathbf{A}}_2$$

(1.148)

The PSF may be determined in a vectorized form by applying the Kronecker product identity [69].

$$\mathrm{vec}(\mho) = \mathrm{vec}(\overline{\mathbf{A}}_1^H\mathbf{R}_{\mathrm{f}}\overline{\mathbf{A}}_{\mathbf{2}}) = (\overline{\mathbf{A}}_2^T \otimes \mathbf{A}_1^H)\mathrm{vec}(\mathbf{R}_{\mathrm{f}})$$

(1.149)

The PSF of a repeated LFM waveform set and a non-repeated PRO-FM waveform set is shown in Figure 47. The range sidelobe modulation (RSM) observed for non-repeating waveforms is visible across slow time-Doppler. The SNR and sidelobe decoherence benefits of coherent integration apply in the slow time-Doppler dimension.

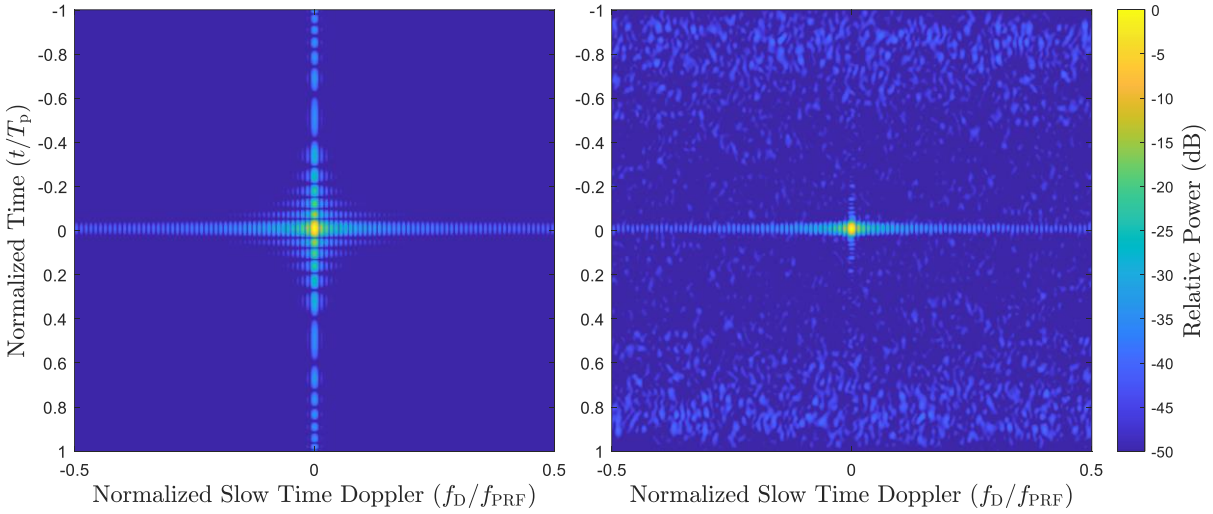

Figure 47: Comparison of point spread functions $\mho$ for LFM waveforms (left) and PROFM waveforms (right) for $P = 100$ pulse repetition intervals.

2. CHAPTER II: COGNITIVE RADAR AND SPECTRUM SHARING

The RF spectrum is becoming congested due to the proliferation of wireless devices, wideband 5G communications, and the internet of things [1, 3]. As a result of RF spectrum auctioning, radar users are becoming secondary users in frequency bands that they previously had sole ownership of. Various methods now exist to contend with operation of radar and communications users operating within the same RF bands, including dual-function radar communications (DFRC) [33], cognitive (or fully adaptive) radar [136-138], and spectrum management by time-frequency scheduling. Spectrum sharing technology offers the opportunity for radar to dynamically access the spectrum and mitigate mutual interference [2]. The cognitive perception-action cycle (PAC) involves sensing the environment, deciding upon an appropriate action, and subsequent system adaptation.

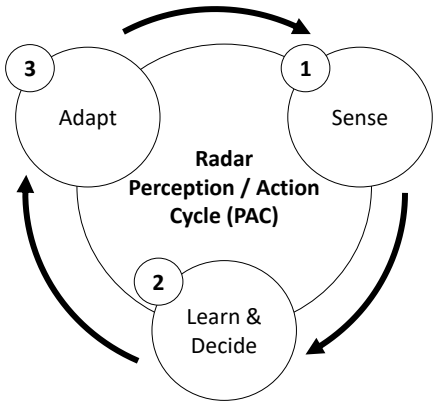

Figure 48: Perception-action cycle (PAC) concept for radar [136].

The PAC is considered for radar waveform adaptation to the observed RF interference environment, with intent to perform pulse-Doppler radar for moving target indication (MTI). The RF bands of interest are assumed narrowband. Spectrum sensing and transmit waveform frequency notching is a form of cognitive radar that seeks to reduce mutual interference with other spectrum users in a cohabitated band. The cognitive sense-and-notch emission strategy is experimentally demonstrated as an effective way to reduce interference caused to other in-band users. The physical radar emission is based on a random FM waveform structure possessing attributes that are inherently robust to range sidelobes. One or more spectral nulls are reactively incorporated into the radar waveform to occupy as much available bandwidth possible within a band-of-interest.

Recent work examined the sense-and-avoid (SAA) cognitive approach [139, 140], which gleans information from spectrum measurements of potential interferers and modifies the waveform center frequency and bandwidth to occupy the largest available contiguous band. The sense-and-notch (SAN) cognitive approach likewise employs spectrum measurements to identify interferers, however, the waveform incorporates spectral nulls collocated with the RF interferers to realize wider bandwidths and maximize spectrum occupancy (e.g. [141-152]). The efficacy of adapting waveform spectral notches dynamically in reaction to interference is explored, with the ultimate goal of achieving real-time sense-and-notch mutual interference mitigation.

The "learn and decide" stage of the PAC is performed with the fast spectral sensing (FSS) algorithm [153, 154], which quickly determines the occupied frequency band locations from the "sensed" receive data. Waveform spectral nulls must coincide with the identified interference regions to diminish mutual interference. Based on the perceived interference bands, the frequency notch locations are "adaptively" incorporated into the random FM waveform design [150-152]. The random FM (RFM) waveform class exhibits pseudo-random phase while maintaining an FM temporal structure, subsuming both the angle modulation and PCFM waveform subclasses. Orthogonal frequency division multiplexing (OFDM) is a communication system design concept applied in long-term evolution (LTE) networks. Due to the modern prevalence of 5G LTE networks, OFDM-structured waveforms such as quadrature amplitude modulation (QAM) are considered as the primary observed interference source. Decision latency is vitally important because the RF interference (RFI) environment may change instantaneously. Figure 49 illustrates experimental measurements of RFM waveforms designed in response to OFDM interference.

The emulation and analysis performed here is unique compared to previously explored forms of mutual interference mitigation. For foliage penetration (FOPEN) radar, spectral notches were incorporated into an LFM waveform to avoid interfering with local communications bands, although the spectral notch was stationary for the entire coherent processing interval and did not require real-time reaction [28]. Interference avoidance was investigated for stepped frequency radar; however, the tones did not exhibit fast time-frequency bandwidths [80]. Of course, dynamic interference requires dynamic radar waveform design.

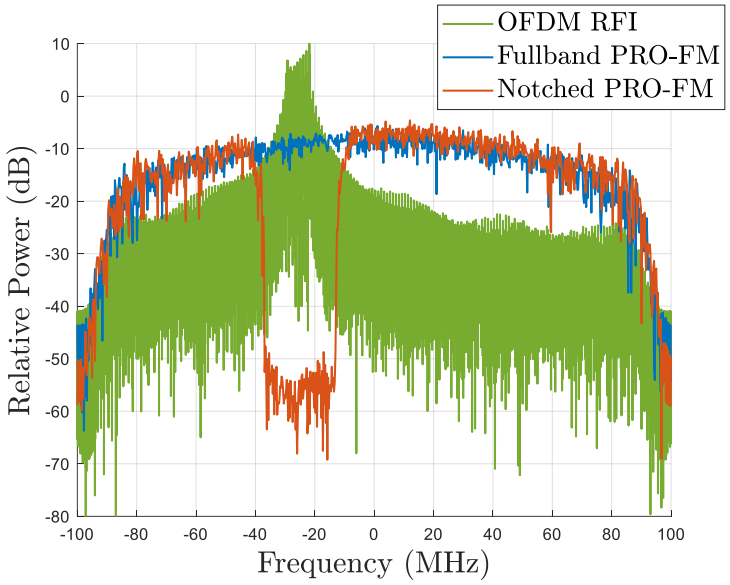

Figure 49: Experimental measurements of PRO-FM waveforms, designed with or without a spectral null collocated with observed OFDM interference.

2.1. SPECTRALLY NOTCHED RADAR WAVEFORM DESIGN

Recall the pseudo-random optimized FM (PRO-FM) algorithm, which produces spectrally shaped angle modulated radar waveform. The p^{th} of P PRO-FM waveforms is initialized with phase chips drawn from the uniform distribution $\phi_n \in [-\pi, \pi]$ to form the signal $\mathbf{s}_{0,p}$. The PRO-FM algorithm performs the k^{th} of K alternating iterations

$$\dot{\mathbf{s}}_p^{(k+1)} = \tilde{\mathbf{A}}^H\left\{\mathbf{d}_\mathrm{f}^{1/2} \odot \exp\left(j\angle\tilde{\mathbf{A}}\mathbf{s}_p^{(k)}\right)\right\}$$

$$\mathbf{s}_p^{(k+1)} = \mathbf{u} \odot \exp\left(j\angle\dot{\mathbf{s}}_p^{(k+1)}\right) \tag{2.1}$$

where $\tilde{\mathbf{A}}$ is the $M \times N$ truncated DFT matrix with $M \geq 2N-1$, $\tilde{\mathbf{A}}^H$ is the $N \times M$ truncated IDFT matrix, $\mathbf{d}_\mathrm{f}$ is the $M \times 1$ desired PSD, $\mathbf{u}$ is the $N \times 1$ desired amplitude envelope, and $\angle(\cdot)$ extracts the argument phase. Spectral nulls may be incorporated into the desired PSD $\mathbf{d}_\mathrm{f}$ over the set of frequency indices to null Λ by enforcing

$$d_{\mathrm{f},m} = 0 \quad \text{for } m \in \Lambda\,. \tag{2.2}$$

Inclusion of rectangular notches in the spectrum has been shown [148] to induce degraded range sidelobe roll-off in the autocorrelation. However, inclusion of a taper in the spectral region surrounding the notches via

$$d_{\mathrm{f},m} = \begin{cases} h_{\mathrm{L},m} & \text{for } m \in \Lambda_{\mathrm{L}} \\ 0 & \text{for } m \in \Lambda \\ h_{\mathrm{U},m} & \text{for } m \in \Lambda_{\mathrm{U}} \end{cases}$$

(2.3)

has been demonstrated to be an effective solution [149]. The frequency intevals Λ_{L} and Λ_{U} indicate the lower and upper frequency regions adjacent to the notch, to which are applied the tapers $h_{\mathrm{L},m}$ and $h_{\mathrm{U},m}$, respectively. A gradual transition between a notch and its local power spectrum is attained by forcing each tapered region to be continuous with its surrounding power spectrum. The shape of the taper regions can be arbitrary, but it has been observed that the Tukey taper well-compensates for the sidelobe degradation [149].

PRO-FM waveforms can achieve spectral notch depths of ~ 20 dB relative to the peak spectral power with sufficient iterations K. Waveform spectrum nulling algorithms [155-159] have been experimentally demonstrated to deepen spectral notches, while simultaneously maintaining a constant temporal amplitude. If deeper spectral notches are desired, the reiterative uniform weight optimization (RUWO) technique [156, 157] has been shown to attain appreciably deeper notches when applied after the optimization process above. The final signal vector $\mathbf{s}_p^{(K)}$ from (2.1) is used to initialize the RUWO algorithm. The RUWO algorithm performs the the q^{th} of Q iterations to deepen the waveform spectral notches. In the RUWO formulation, the frequency null intervals Λ are denoted by the M_Λ discretized frequency values f_{m}, such that the $N_{\mathrm{p}} \times M_\Lambda$ matrix $\mathbf{B}_\Lambda$ comprised of frequency steering vectors is formed as

$$\mathbf{B}_\Lambda = \begin{bmatrix} 1 & 1 & \cdots & 1 \\ e^{j2\pi f_0} & e^{j2\pi f_1} & \dots & e^{j2\pi (f_{M_\Lambda - 1})} \\ \vdots & \vdots & \ddots & \vdots \\ e^{j2\pi f_0 (N_{\mathrm{p}}-1)} & e^{j2\pi f_1 (N_{\mathrm{p}}-1)} & \dots & e^{j2\pi \left(f_{M_\Lambda - 1}\right)(N_{\mathrm{p}}-1)} \end{bmatrix}$$

(2.4)

An $N_\mathrm{p} \times N_\mathrm{p}$ structured matrix is subsequently obtained by

$$\mathbf{W}_\Lambda = \mathbf{B}_\Lambda \mathbf{B}_\Lambda{}^H + \Delta \mathbf{I} \tag{2.5}$$

where $\mathbf{I}$ is an $N_\mathrm{p} \times N_\mathrm{p}$ identity matrix and Δ is a diagonal loading term. The RUWO algorithm is performed for Q iterations to deepen the spectral notch obtained via the PRO-FM process.

$$\mathbf{s}_p^{(q)} = \exp\left(j \angle \mathbf{W}_\Lambda^{-1} \mathbf{s}_p^{(q-1)}\right) \tag{2.6}$$

The mean power spectrum and coherently averaged autocorrelations of $P = 2500$ full-band waveforms and $P = 2500$ spectrally notched waveforms are illustrated in Figure 50, where $K = 200$ PRO-FM iterations and $Q = 100$ RUWO iterations are applied.

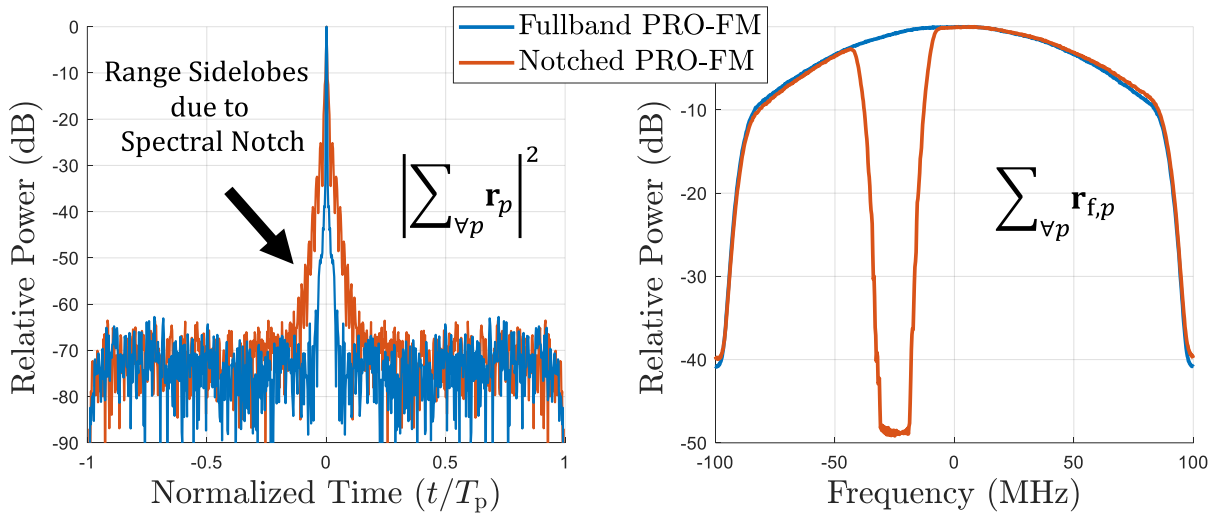

Figure 50: The coherently averaged waveform autocorrelations $\sum_{p=1}^{P} \mathbf{r}_p$ and mean waveform power spectra $\sum_{p=1}^{P} \mathbf{r}_{\mathrm{f},p}$ for 2500 full-band PROFM and 2500 spectrally notched PROFM waveforms, transmitted on an arbitrary waveform generator and received on a real-time spectrum analyzer. Here $K = 200$ PRO-FM iterations and $Q = 100$ RUWO iterations are applied.

2.2. EXPERIMENTAL EMULATION

The interference spectrum of OFDM experimental loopback measurements is determined by FSS to inform the null locations of frequency notched PROFM waveforms, which are subsequently transmitted in a separate free-space radar measurement. The synthetic combination of the closed-loop and free-space collections is examined to evaluate the impact to the radar performance. It is demonstrated that reactive spectral notching provides a significant signal to interference plus noise ratio (SINR) enhancement for moving target indication (MTI) via pulse-Doppler processing. The SINR improvement is degraded when an adaptation latency occurs between observance of interference and updating spectral notch locations within the radar waveform.

2.2.1. FAST SPECTRUM SENSING (FSS) ALGORITHM

The fast spectrum sensing (FSS) algorithm is a rapid band aggregation method that identifies the locations and widths of spectral regions requiring nulling for interference mitigation with other users. Here the FSS algorithm is used to identify the locations and widths of spectral regions that require notching in an efficient manner by reducing the number of frequency bins needed to analyze the spectrum. Frequency bins (ϑ) undergo a spectrum power threshold to produce alternating groups of low and high power "meso-bands (Ψ)" [182]. The meso-bands are then merged according to a minimum meso-bandwidth requirement $B_{\min}$ to form the final merged sub-bands (Φ) where notches are needed.

For the given discrete observed spectrum $\Theta = \{\vartheta_1 \dots \vartheta_M\}$ with frequency discretization Δf between samples, the FSS approach operates by first applying threshold T_{f} to label frequency samples as occupied or unoccupied. Define the set of $Q \leq M$ intermediate meso-bands as $\Psi = \{\Psi_1 \dots \Psi_Q\}$, where meso-band q contains $\Psi_q = \{\vartheta_{\acute{S}(q)}, \dots, \vartheta_{\acute{E}(q)}\}$, for $\acute{S}(q)$ and $\acute{E}(q)$ the start and end frequency indices composing a contiguous band of occupied or unoccupied bands. A low-power meso-band requires that $\vartheta_m \leq T_f$ while a high-power meso-band has $\vartheta_m > T_f$ for all $m \in \{\acute{S}(q), \dots, \acute{E}(q)\}$.

Meso-bands are merged according to rules governing the minimum allowable meso-bandwidth $B_{\min}$ (corresponding to a discrete length $L_{\min} = \lceil B_{\min}/\Delta f \rceil$) so the radar spectrum does not become too fragmented, as there is a need for a gradual transition into each notch to constrain the range sidelobe levels [149]. A low-power meso-band is merged with a high-power meso-band when $\acute{L}(q) = \left(\acute{E}(q) - \acute{S}(q) + 1\right) < L_{min}$ is satisfied. Define the set of $\mathcal{R} \leq Q \leq M$ merged meso-bands as $\Phi = \{\Phi_1, \ldots, \Phi_{\mathcal{R}}\}$, where merged meso-band r contains $\Phi_r = \{\Psi_{S(r)}, \ldots, \Psi_{E(r)}\}$, for $S(r)$ and $E(r)$ the start and end frequency indices composing a contiguous band. The number of samples in each Φ_r band is $L(r) = E(r) - S(r) + 1$. The length of each merged meso-band Φ_r defines its bandwidth

$$B(r) = L(r)\Delta f \tag{2.7}$$

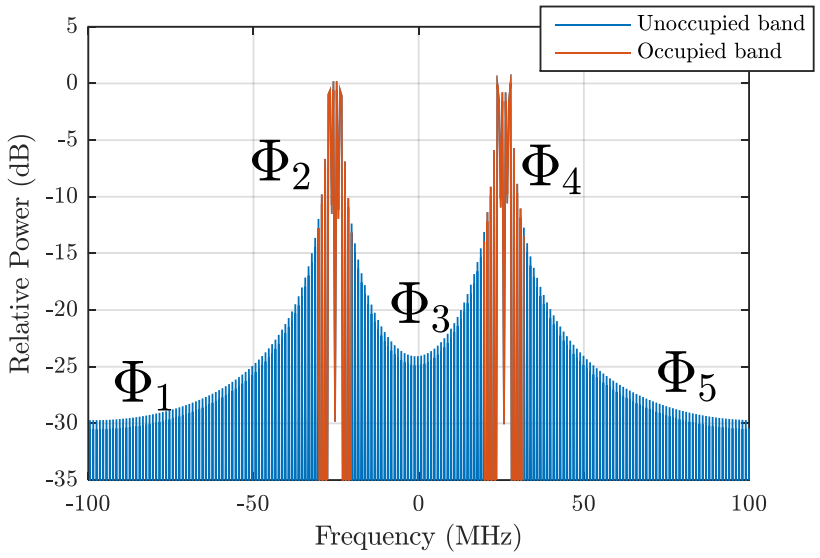

Figure 51: FSS-determined sub-bands for two OFDM signals, where $\{\Phi_1, \Phi_3, \Phi_5\}$ represent unoccupied sub-bands and $\{\Phi_2, \Phi_4\}$ represent occupied sub-bands.

2.2.2. COGNITIVE RADAR EMULATION

Consider the situation in which OFDM interference is cohabitating the bandwidth occupied by the radar. To simplify analysis, a stationary monostatic radar performing moving target indication (MTI) is considered, for which the range-Doppler response can be accurately modeled by the point spread function. The performance of the radar is evaluated experimentally when in the presence of the communications RFI and with/without the use of cognitive spectral notching. To isolate the impact of the spectral notch and the presence of the interference separately, the communication signal measurement and the free-space radar measurement are collected separately and then combined synthetically. Notch-free, full-band waveforms are included to provide a performance baseline.

To fully characterize the interaction of sense-and-notch cognitive radar with the in-band interference, different interference arrangements are generated and the FSS algorithm is applied on a per-pulse basis to identify the occupied RFI bands. Each pulsed radar waveform is then designed to notch the regions of occupied spectrum. The waveforms are transmitted to collect free-space measurements of moving vehicles. The loopback measurements of interference and the free-space radar measurements are then combined synthetically in Matlab™ to determine how well notching mitigates the interference. The radar measurements are also evaluated individually (without interference included) to assess the trade-off notching imposes.

Three RFI scenarios are considered here:

- Case 1: the RFI is stationary in frequency over the CPI.
- Case 2: the RFI hops to a random center frequency every four PRIs and the radar waveform adapts without latency.
- Case 3: the RFI hops to a random center frequency every four PRIs and the radar waveform adapts with a latency of T_{PRI}.

The OFDM interference is modeled either as a single band consisting of eight adjacent subcarriers comprising a single contiguous bandwidth of 10 MHz, or two disjoint bands consisting of four adjacent subcarriers comprising separate contiguous bandwidths of 5 MHz. Each subcarrier is modulated by a random stream of quadrature amplitude modulated (QAM) symbols from a 4-QAM constellation at a symbol rate of 1 MHz. Example power spectra for both RFI models are shown in Figure 52. The width of the observed notches arises because FSS identified the OFDM spectral roll-off as an occupied region. The sharp roll-off of the measured spectrum is caused by the limited analysis bandwidth (160 MHz) of the real-time spectrum analyzer. Note that the OFDM signals are not spectrally well-contained, which means that leakage interference will occur despite the waveform spectral notches. If the interference possessed better spectral containment the leakage degradation would largely be avoided.

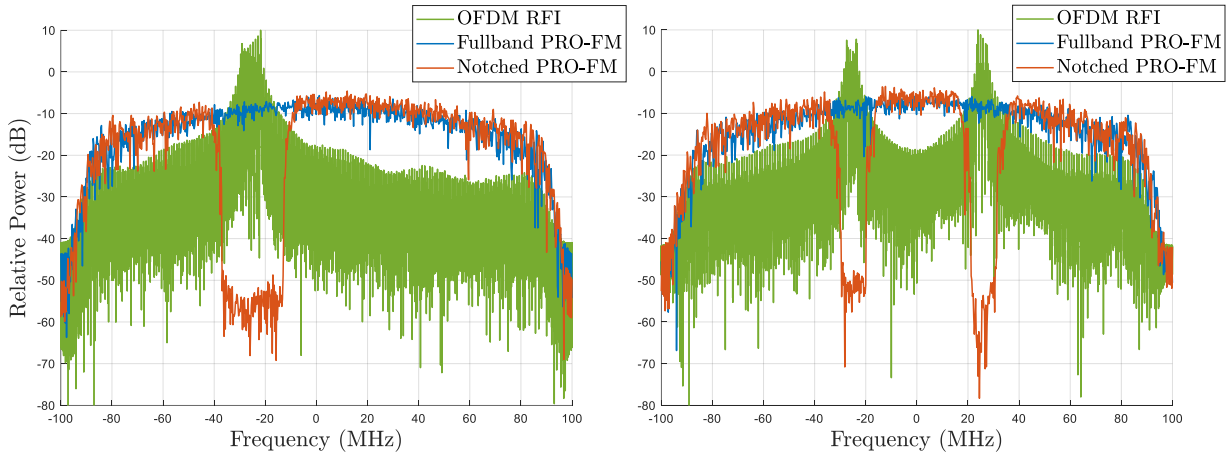

Figure 52: Example power spectra of measured OFDM interference, spectrally notched PROFM (adapted using FSS), and full-band PROFM waveforms. The RF interference either has a single contiguous bandwidth of 10 MHz (left) or two disjoint bands comprising separate contiguous bandwidths of 5 MHz (right).

The experimental timing diagrams for each case are illustrated in Figure 53 and Figure 54. Note that the full-band PROFM waveform and the notched PROFM waveform are interleaved such that both illuminate the same moving target scene for comparison. Note that in instances where the disjoint RFI bands hop near one another, FSS may combine the identified meso-bands into a single sub-band for subsequent notching.

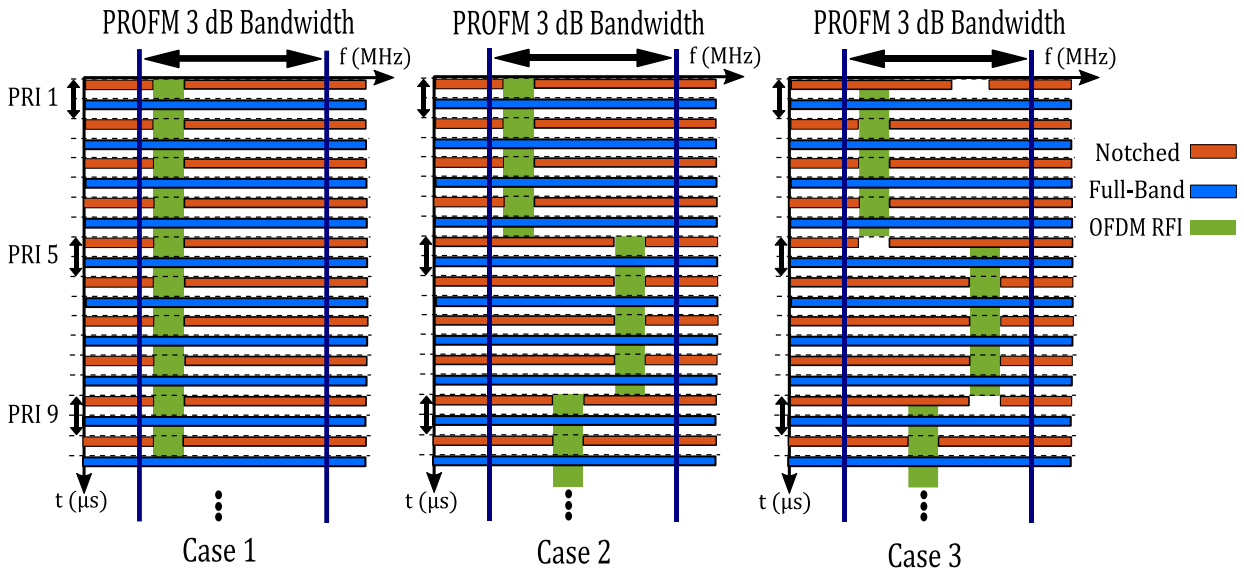

Figure 53: Experimental timing diagram for the single contiguous RFI band scenario: Case 1 - the interference and the radar notch is stationary; Case 2 - the radar adapts new notches instantly when the interference location changes (no latency); Case 3 - the radar adapts new notches with a delay T_{PRI} when the interference location changes.

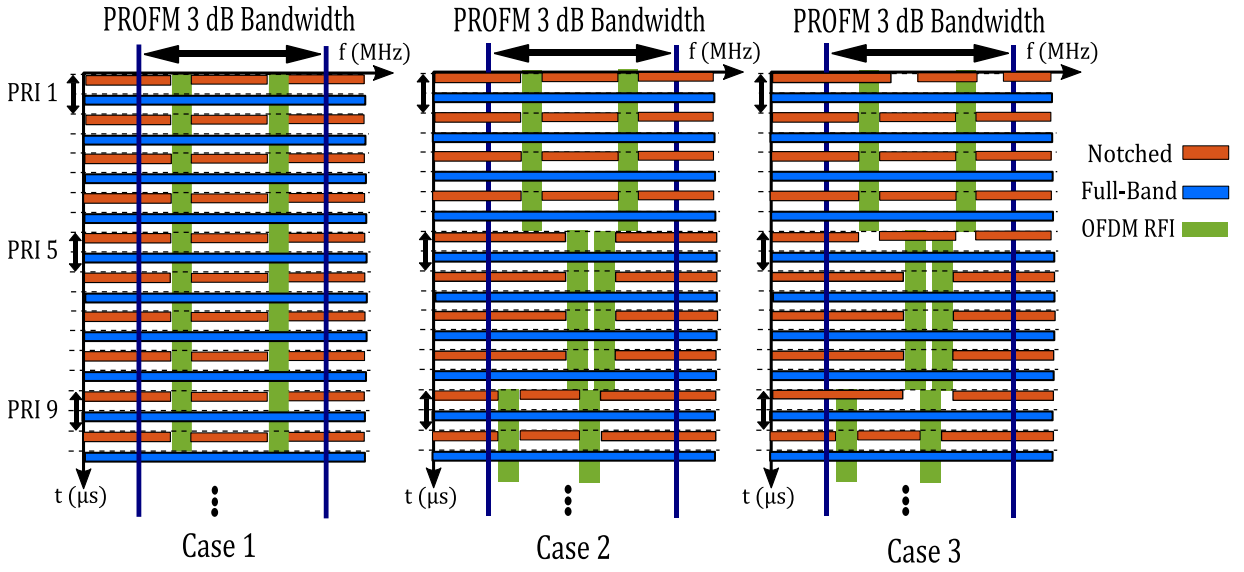

Figure 54: Experimental timing diagram for the two disjoint contiguous RFI bands scanario. Case 1 - the interference and the radar notches are stationary; Case 2 - the radar adapts new notches instantly when the interference location changes (no latency); Case 3 - the radar adapts new notches with delay T_{PRI} when the interference location changes.

To facilitate the synthetic combination of communication and radar data, the OFDM signal is generated in Matlab™ and the FSS algorithm is applied to the communication signal on a per-PRI basis to identify the occupied RFI band using a minimum continuous-band grouping $B_{\min}$ requirement of either 8 MHz for a single contiguous band, or 4 MHz for two disjoint contiguous bands. For all cases, the FSS algorithm is used to identify the spectrum users with a power threshold T_{f} set to be 15 dB below the average peak power of the OFDM subcarriers. The results obtained from FSS are used to adapt the notched PROFM waveforms according to the latency incurred. Each OFDM signal is captured in a loopback configuration using RF test equipment consisting of a Tektronix arbitrary waveform generator and a Rohde & Schwarz real-time spectrum analyzer. The set of notched PROFM waveforms dictated by FSS were then transmitted (using the test setup in Figure 55) from the roof of Nichols Hall on the KU campus to illuminate the intersection of 23rd St. and Iowa St. in Lawrence, KS. These open-air measurements were combined synthetically with the loopback-measured communication signals to assess overall performance. The baseband waveforms are transferred to passband via digital upsampling, interpolation, and upconversion.

For each case a total of 5000 interleaved pulses were transmitted, with 2500 each for full-band and frequency notched PROFM. Accounting for the interleaving, the PRI is defined as the time interval between each pair of pulses and is set to $T_{\mathrm{PRI}} = 40\ \mu\mathrm{s}$. Each pulse has a duration of $T_{\mathrm{p}} = 2\ \mu\mathrm{s}$ and bandwidth $B_{3\mathrm{dB}} = 100\ \mathrm{MHz}$. Both sets of radar waveforms have individual time-bandwidth products $T_{\mathrm{p}}B_{3\mathrm{dB}} = 200$. The total CPI for each waveform set is $T_{\mathrm{CPI}} = 100\ \mathrm{ms}$. The OFDM signals and radar emissions were each generated at a center frequency of 3.55 GHz and the resulting I/Q data was captured at a sample rate of $f_s = 200\ \mathrm{MHz}$ for loopback and open-air measurements, respectively. For radar receive processing, pulse compression matched filtering is performed using loopback captured versions of the emitted waveforms (also at $f_s = 200\ \mathrm{MHz}$ sampling rate) to account for hardware imperfections. Since there was no platform motion, clutter cancellation was performed by a simple projection of the zero-Doppler response and a Taylor taper was applied across Doppler. Platform motion effects such as angle-Doppler coupling of clutter and changing RFI spatial direction need not be addressed here.

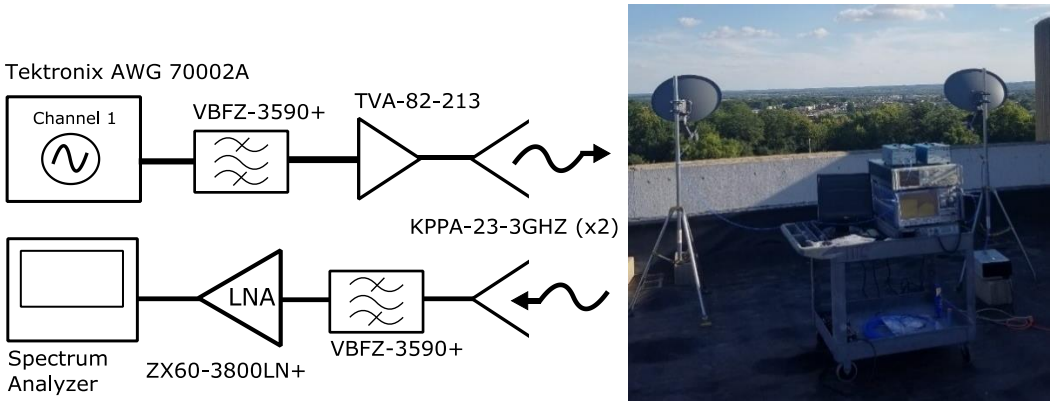

Figure 55: Open-air hardware setup.

2.2.3. CASE 1: STATIONARY INTERFERENCE

As a baseline, Figure 56 shows the measured range-Doppler response after clutter cancellation for the full-band PROFM waveform, prior to synthetic RFI injection. Multiple automobiles were traversing the intersection, which are clearly visible here as moving targets. Note that different traffic patterns are observed for the single-notch and multi-notch transmission, though the same intersection is probed. It is useful to compare the full-band result against the notched PROFM radar measurement without the inclusion of RFI, as depicted in Figure 57. A spreading in range is observed due to the presence of the stationary notch that degrades the range sidelobe levels.

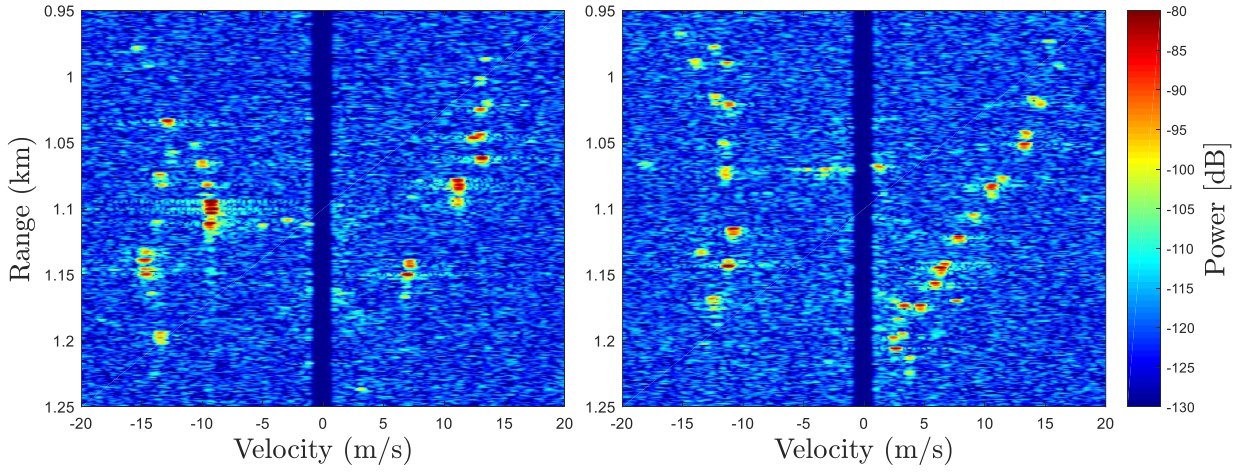

Figure 56: Range-Doppler plot of full-band PRO-FM with no injected RFI, intended as the baseline comparison, for the single-notch data collect (left) and multi-notch data collect (right). Case 1.

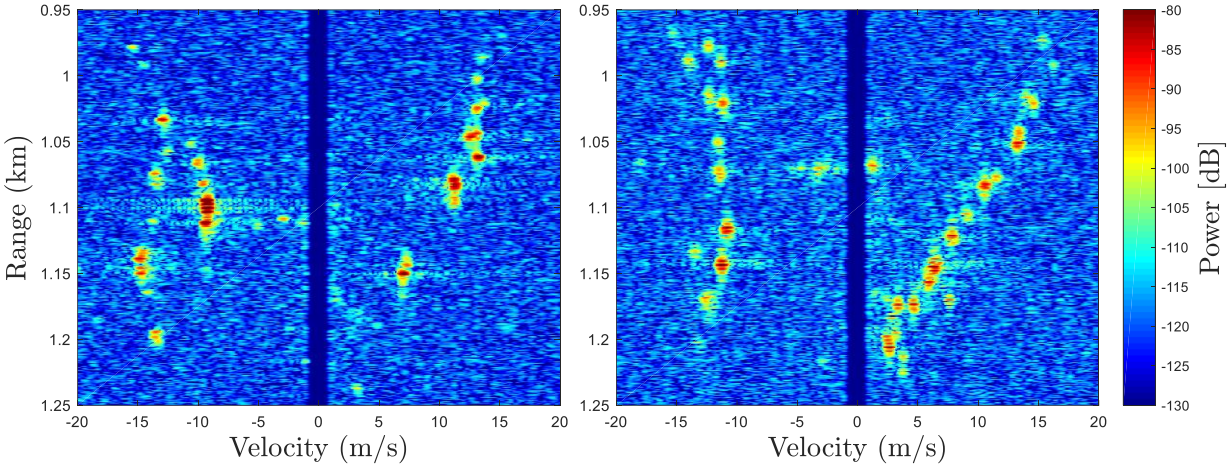

Figure 57: Range-Doppler plot of notched PRO-FM with no injected RFI, possessing a stationary spectral notch, for the single notch data collect (left) and multi-notch data collect (right). Case 1.

The OFDM RFI measured in loopback is power-scaled and then synthetically combined with the free-space test measurements. It is assumed that the measured clutter power is sufficiently greater than the noise power for the latter to be neglected. The "received" unprocessed signal to interference ratio (SIR) is defined as the average power of the received radar backscatter signal (excluding direct path) divided by the average power of the OFDM interference, within the time interval that the backscatter was received. Figure 58 and Figure 59 show the range-Doppler plots for the full-band and notched PRO-FM when RFI is injected that is 20 dB greater than the radar receive echoes (i.e. a received SIR of −20 dB). The notched waveforms experience some degradation due to an increased background response, caused by interference leakage. In contrast, the full-band waveforms are greatly affected by the interference, so much so that the moving targets are essentially obscured beyond recognition. Qualitatively, the baseline case for full-band PROFM when interference is injected shown in Figure 58 will be the same regardless of the interference hopping pattern and therefore will not be shown redundantly.

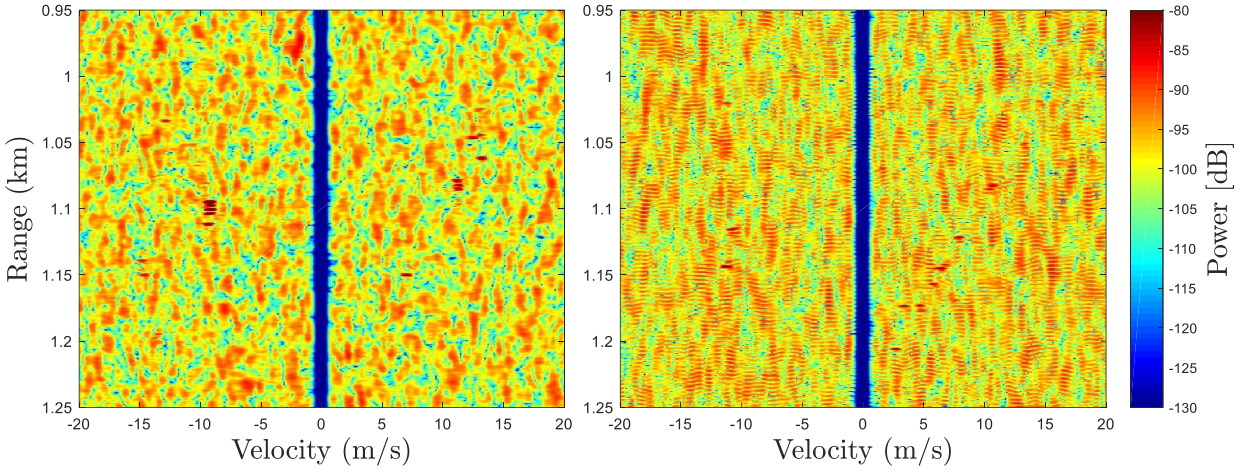

Figure 58: Range-Doppler plot of full-band PROFM with injected stationary RFI of received SIR = −20 dB, for the single notch data collect (left) and multi-notch data collect (right). Case 1.

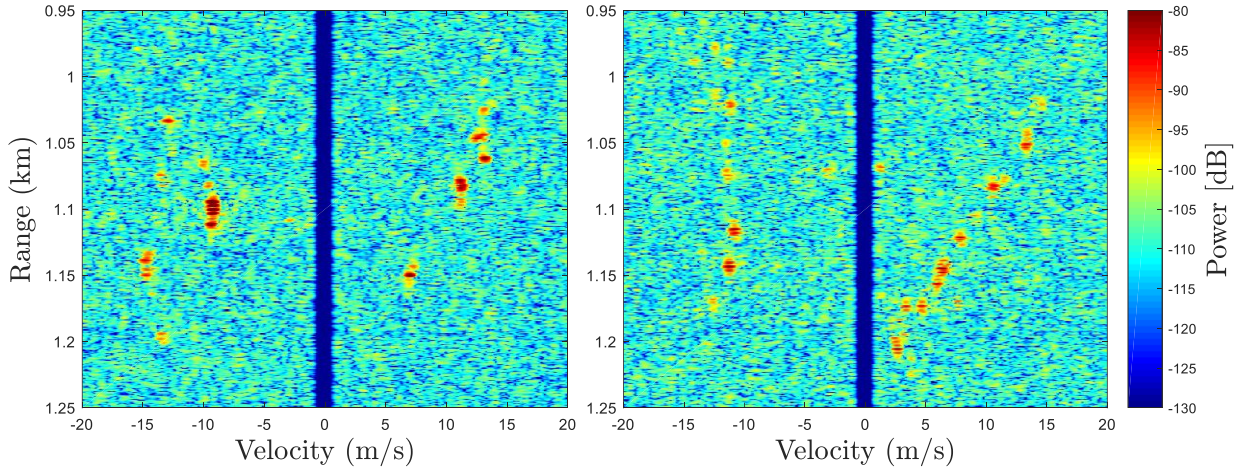

Figure 59: Range-Doppler plot of notched PROFM with injected stationary RFI of received SIR = −20 dB, for the single notch data collect (left) and multi-notch data collect (right). Case 1.

A useful metric to assess the impact of interference that is facilitated by this synthetic combination, along with the individual impact of hopping notches, is

$$\bar{\Delta} = \frac{I_{\text{meas}}}{I_{\text{baseline}}} \tag{2.8}$$

where I_{meas} is the average power measured for each scenario in the range/Doppler regions that do not contain discernible targets or the clutter notch. The value I_{baseline} is then the particular value of I_{meas} for the full-band, no RFI scenario (e.g. Figure 56). Consequently, the metric in (2.8) represents the change in the background response induced by RFI or spectral notches that would impact downstream CFAR (constant false alarm rate) detection. Table 2 shows that, compared to the full-band scenario, the stationary notch of Case 1 incurs around 1 dB of degradation in terms of an increased noise floor when no RFI is present. When RFI is present the full-band waveforms realize a 23 dB sensitivity degradation, while the notched waveforms only suffer 11 dB, a net difference of 12 dB.

Table 2: Impact of interference and notching for Case 1, when a single RFI or two disjoint RFI bands are present.

	I_{meas}, single	$\bar{\Delta}$, single	I_{meas}, multi	$\bar{\Delta}$, multi
Full-band, no RFI (baseline)	−120.3 dB	--	−119.8 dB	--
Notched, no RFI	−119.5 dB	+0.8 dB	−118.7 dB	+1.1 dB
Full-band, with RFI	−96.8 dB	+23.5 dB	−96.1 dB	+23.7 dB
Notched, with RFI	−109.0 dB	+11.3 dB	−108.2 dB	+11.6 dB

2.2.4. CASE 2: HOPPED INTERFERENCE, NO LATENCY

The hopped interference and notched waveforms in this case follow the timing arrangement when there is no adaptation latency between the interference changing (every four PRIs) and when the notch location adjusts in response. Figure 60 and Figure 61 show the full-band and notched PRO-FM responses when the RFI is not present.

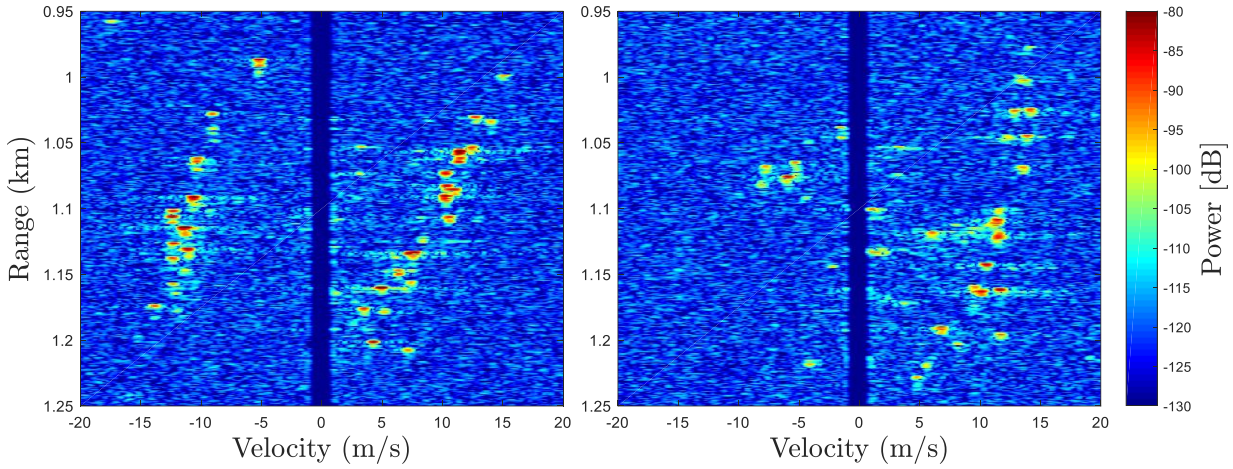

Figure 60: Range-Doppler plot of full-band PRO-FM with no injected RFI, intended as the baseline comparison, for the single notch data collect (left) and multi-notch data collect (right). Case 2.

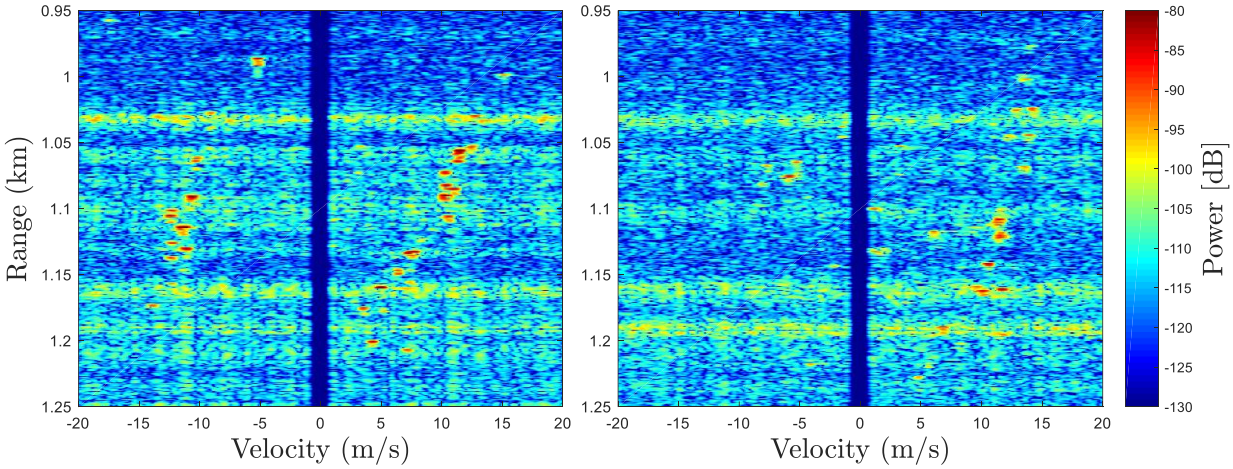

Figure 61: Range-Doppler plot of notched PRO-FM with no injected RFI, possessing a spectral notch hopped every four PRIs, for the single notch data collect (left) and multi-notch data collect (right). Case 2.

Moving the frequency notch location during the CPI introduces a Doppler smearing effect, due to innately varying range sidelobe modulation from pulse-to-pulse. When the hopped RFI is present, again with a received SIR of −20 dB, the notched PROFM responses in Figure 62 is realized. Per Table 3, it is interesting to observe that the hopping notch (without RFI) yields a nearly 7 dB increase in the noise floor, which is actually uncanceled clutter sidelobes distributed across range and Doppler. When frequency hopping RFI is present, again with a received SIR of −20 dB, the full-band response (not shown) experiences the same 23 dB degradation as before. In contrast, the MTI performance of the notched waveforms realizes $\bar{\Delta}$ = 12 dB, only 1 dB worse than the stationary RFI case.

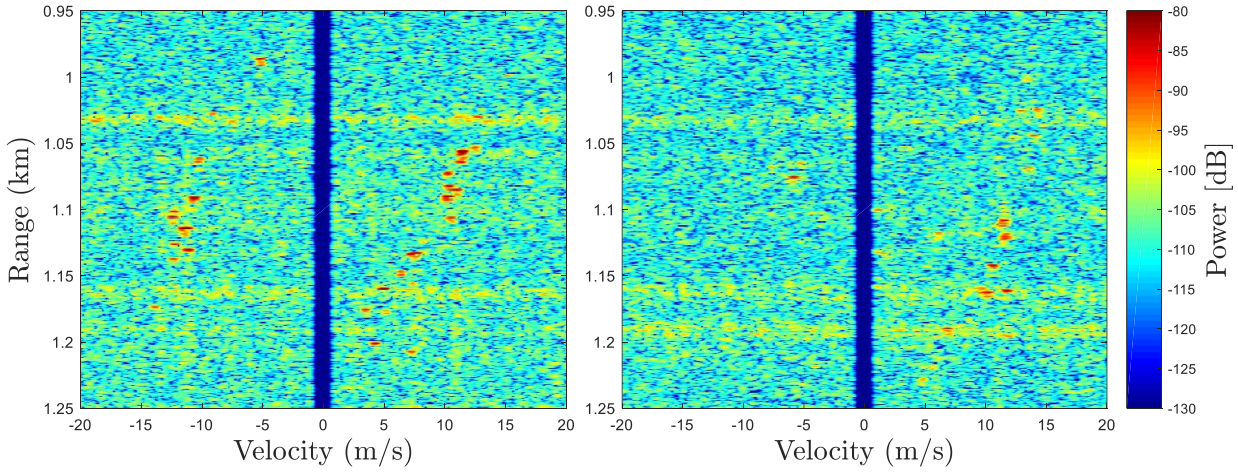

Figure 62: Range-Doppler plot of notched PROFM with injected frequency hopping RFI of received SIR = −20 dB, reacting with no adaptation latency, for the single notch data collect (left) and multi-notch data collect (right). Case 2.

Table 3: Impact of interference and notching for Case 2, when a single RFI or two disjoint RFI bands are present.

	I_{meas}, single	$\bar{\Delta}$, single	I_{meas}, multi	$\bar{\Delta}$, multi
Full-band, no RFI (baseline)	−120.8 dB	--	−120.3 dB	--
Notched, no RFI	−113.8 dB	+7 dB	−113.4 dB	+6.9 dB
Full-band, with RFI	−97.0 dB	+23.8 dB	−96.7 dB	+23.6 dB
Notched, with RFI	−108.1 dB	+12.7 dB	−108.4 dB	+11.9 dB

2.2.5. CASE 3: HOPPED INTERFERENCE, 1 PRI LATENCY

The scenario is examined where there is a latency of duration T_{PRI} before the location of the spectral notch can be determined and the waveform is adapted. The fullband and notched PROFM range-Doppler maps prior to RFI injection are depicted in Figure 63 and Figure 64, respectively, and are qualitatively the same as seen in Case 2.

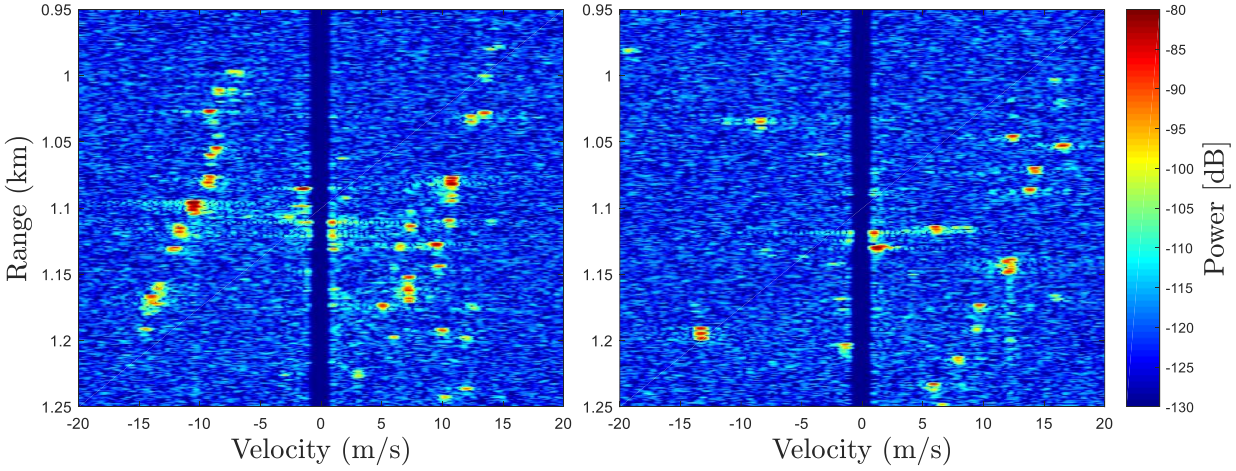

Figure 63: Range-Doppler plot of full-band PRO-FM with no injected RFI, intended as the baseline comparison, for the single notch data collect (left) and multi-notch data collect (right). Case 3.

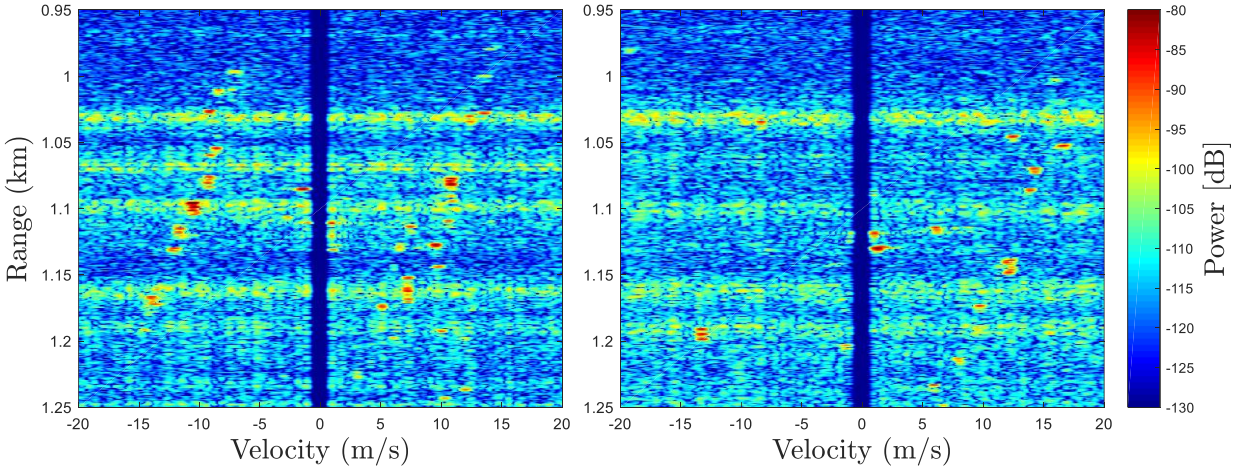

Figure 64: Range-Doppler plot of notched PRO-FM with no injected RFI, possessing a spectral notch hopped every four PRIs, for the single notch data collect (left) and multi-notch data collect (right). Case 3.

Upon adding interference, Figure 65 depicts the notched PROFM responses with adaptation latency effects. Due to the perception-action cycle latency, the notched case now experiences about $\bar{\Delta}= 18$ dB because 1 PRI out of every 4 pulses is corrupted by interference. This result emphasizes the importance of adapting the waveform to changing RFI as quickly as possible.

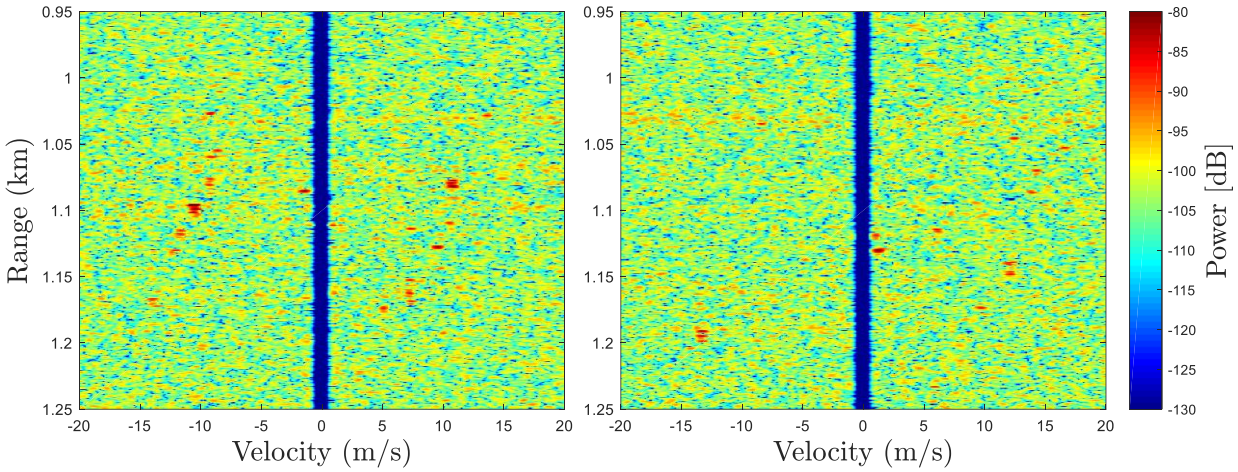

Figure 65: Range-Doppler plot of full-band PROFM with injected frequency hopping RFI of received SIR = −20 dB, reacting with adaptation latency T_{PRI}, for the single notch data collect (left) and multi-notch data collect (right). Case 3.

Table 4: Impact of interference and notching for Case 3, when a single RFI or two disjoint RFI bands are present.

	I_{meas}, single	$\bar{\Delta}$, single	I_{meas}, multi	$\bar{\Delta}$, multi
Full-band, no RFI (baseline)	−120.9 dB	--	−120.6 dB	--
Notched, no RFI	−113.9 dB	+7.0 dB	−113.6 dB	+7.0 dB
Full-band, with RFI	−97.2 dB	+23.7 dB	−97.0 dB	+23.6 dB
Notched, with RFI	−102.3 dB	+18.6 dB	−102.3 dB	+18.3 dB

2.2.6. CONCLUSIONS

It has been experimentally demonstrated using the synthetic combination of open-air radar measurements and loopback measurements of OFDM communication interference that cognitive spectrum sensing and notching can provide proactive interference mitigation. Compared to stationary interference, when frequency hopping of the interference occurs during the radar CPI, a range sidelobe modulation (RSM) induced Doppler response is observed. Latency to adjust the notch location(s) will further degrade the output SINR. Practical factors contribute to the efficacy of this approach, such as Doppler smearing caused by notch hopping to address changing RFI. The matched filter response of spectrally notched waveforms provides significant RFI suppression.

2.3. CLUTTER RANGE SIDELOBE MODULATION COMPENSATION

Cognitive spectral notching of FM noise waveforms on transmit is shown to be an effective means to mitigate in-band interference. However, to contend with dynamic interference, the transmit notch may be required to move during the CPI, which introduces a nonstationarity effect across slow time that results in increased RSM after slow time-Doppler processing and cancellation. The degradation is linked to a distortion of the delay/Doppler point spread function. The least square optimal mismatched filtering (LS-MMF) can partially mitigate this degradation while maintaining the necessary spectral notch for interference mitigation [160].

An approach to compensate for the nonstationarity is proposed that borrows the missing portion of the clutter frequency response (due to notching) from another pulsed response (having a notch in a different location) [161]. By using this borrowed response to fill in the notched clutter, subsequent clutter cancellation minimizes the RSM residue effect. It is shown using measured data that the combination of the clutter filling approach with notched LS-MMFs realizes clutter cancellation performance on par with full-band waveforms that do not possess notches.

To that end, an ad hoc approach denoted as devoid clutter capture and filling (DeCCaF) is proposed whereby the clutter frequency response from a different pulse is bandpass filtered (BPF) commensurate with the notch location in the present pulse, and then subsequently added to the clutter response for the present pulse. Measured data collected using waveforms having moving spectral notches is used to assess the efficacy of this approach. For application to cognitive RFI avoidance, each unique LS-MMF must also contain spectral notches that align with the given notched waveform. Care must be taken so that the inverse nature of the LS-MMF does not invert the desired spectral notch, but instead preserves sufficient notch depth for interference suppression on receive.

2.3.1. DEVOID CLUTTER CAPTURE AND FILLING

Moving spectral notches during the CPI (due to dynamic RFI) hinders clutter cancellation because the changing notch locations introduce significant deviations from the mean power spectrum of the waveform set, inflicting time-varying RSM structure. Modest variation of the spectral density already occurs for notch-free RFM waveforms, though the application of LS-MMFs has been found to compensate to a sufficient degree [72]. The presence of moving notches requires more substantial steps to homogenize the individual spectral densities across the CPI.

Consider a set of P random FM waveforms denoted $s_p(t)$ that possess the same general power spectrum aside from a) modest variation due to their random nature and b) spectral notch locations that may change on a pulse-to-pulse basis. For ease of explanation, the case in which only a single notch is present for each pulse is considered, though the proposed compensation approach can be applied to the case of multiple notches. The received response after transmitting this sequence of waveforms can be expressed as

$$y_p(t) = s_p(t) * \gamma_p(t) + v_p(t) \tag{2.9}$$

where $*$ is the convolution operation, $\gamma_p(t)$ is the impulse response of the environment during the p^{th} PRI, and $v_p(t)$ is additive noise. One can generally expect the stationary ($f_{\mathrm{d}} \approx 0$) clutter component of $\gamma_p(t)$ to be essentially unchanged over the CPI. Pulse compression of (2.9) is then performed via

$$\hat{\gamma}_p(t) = w_p(t) \star y_p(t) \tag{2.10}$$

for $w_p(t)$ the matched filter or LS-MMF of the p^{th} waveform. Normally, Doppler processing and clutter cancellation would then be performed across the set of P responses from (2.10). However, when frequency hopping waveform spectral notches are present during the CPI, an RSM effect causing residual clutter sidelobes is observed.

Consider the same experimentally measured data collected from a stationary platform observing moving vehicles leaving/entering an intersection in Lawrence, KS. The residual clutter response due to RSM, which takes the form of the large streaks across Doppler, is caused by the slow time nonstationarity introduced by moving the spectral notches. The DeCCaF approach seeks to compensate for this residual clutter effect via an ad hoc "clutter filling" solution. While the notion of estimation/interpolation of static spectral notches are used for wideband radar applications to compensate/enhance image quality (e.g. [163, 164]), the distinction here is that the intent is to mitigate clutter residuals by reducing range-Doppler sidelobes and better facilitate clutter cancellation.

If the p^{th} waveform contains a spectral notch at a given location, a similar spectral portion of the clutter is borrowed from the response generated by a different waveform that does not have a notch in that same location. Denoting the index of that other waveform as $\tilde{p}$ and $w_p(t)$ as a bandpass filter (BPF) whose passband aligns with the notch location of the p^{th} waveform, the borrowed clutter component is

$$\hat{\gamma}_{p,\tilde{p}}^{\text{filt}}(t) = w_p(t) * \hat{\gamma}_{\tilde{p}}(t) \tag{2.11}$$

Thus, the DeCCaF response is obtained by simply combining the original response with the borrowed clutter via

$$\tilde{\gamma}_p(t) = \hat{\gamma}_{\text{p}}(t) + \hat{\gamma}_{p,\tilde{p}}^{\text{filt}}(t) \tag{2.12}$$

Subsequent Doppler processing and clutter cancellation is then performed on the spectrally homogenized estimate. As an illustration of the concept, Figure 66 depicts the closed-loop measured spectra for a full-band waveform, a notched waveform, and the BPF version of the full-band waveform corresponding to spectral notch location. These full-band and notched RFM waveforms were obtained from completely independent initializations and optimization processes, and thus the only thing they have in common is the same general spectrum shape. While the DeCCaF combination of the notched and BPF waveforms would not yield a spectrum that is identical to that of the full-band waveform, the resulting shape is rather close. Further, since convolution is a linear operation, consideration of Figure 66 in the context of (2.9) and (2.12) implies that this approach should do well to recapture the missing clutter component as long as the clutter phenomenology is sufficiently stationary.

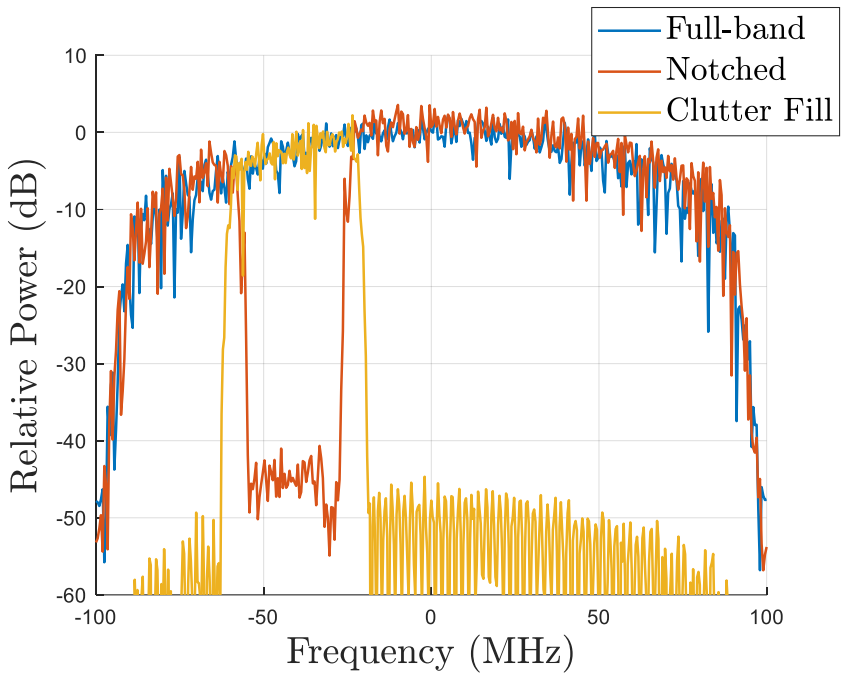

Figure 66: Loopback measured spectra for a full-band waveform, a notched waveform, and a BPF version of the full-band waveform

To establish a baseline for achievable performance using this clutter borrowing/filling approach, two sets of unique RFM waveforms were transmitted in an open-air setting with an interleaved arrangement (see Figure 67). Both sets were generated according to the PROFM scheme. One set contains 2500 full-band waveforms that are all independently initialized and optimized. The other set likewise contains 2500 independent waveforms, which contain a spectral notch moving to a new random location within the 3-dB bandwidth after every fourth pulse. This waveform arrangement is clearly not suitable for actual cognitive interference avoidance due to the presence of the interleaved full-band waveform but is used here to provide a controlled experiment regarding the utility of borrowed clutter responses. Consequently, two different cases are considered in extension of section 2.2, both illuminating the same intersection of 23rd and Iowa.

- Case 4: RFM waveforms with moving notches where DeCCaF is applied using interleaved full-band responses to performing clutter filling
- Case 5: The full-band responses are disregarded and the borrowed clutter responses are taken from other notched waveform responses.

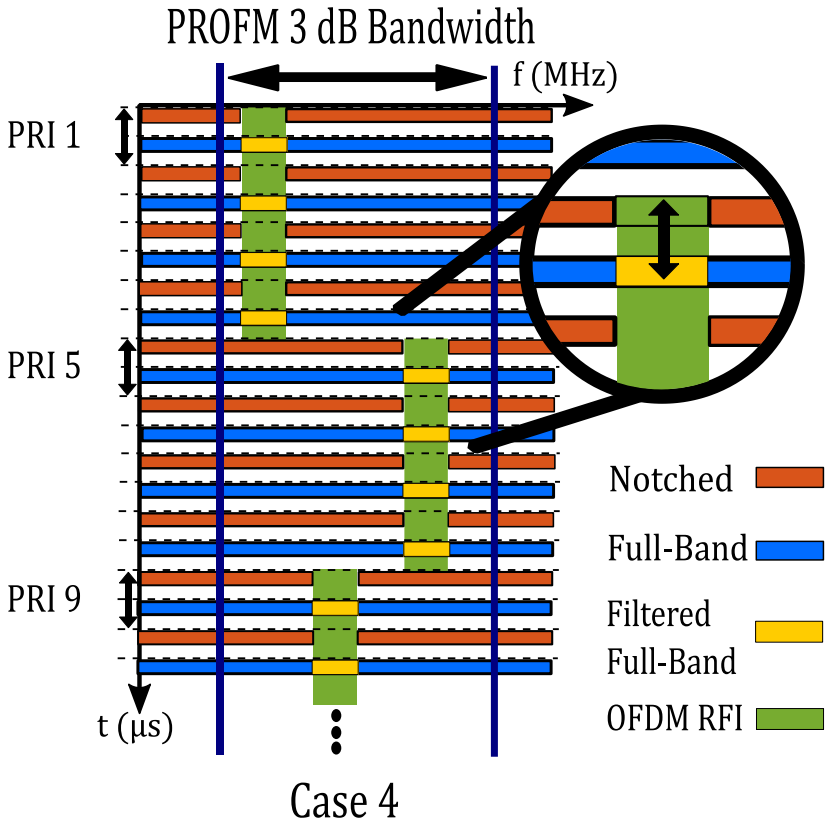

Figure 67: Timing diagram of the waveform arrangement used for experimental evaluation of DeCCaF. Full-band and notched waveforms are interleaved, with the borrowed clutter taken from an adjacent full-band response

The last of these represents the operating arrangement one would expect in practice. Both the matched filter (MF) and the least squares mismatched filter (LS-MMF) are applied for each case. It is important to note that, while the primary purpose of this manner of cognitive operation is to mitigate mutual RFI between the radar and other in-band spectrum users, the following results contain the associated spectral notches but not the RFI itself. The degradation from RFI was shown to be significantly reduced in section 2.2, which is especially true when the RFI possesses good spectral containment. Consequently, the RSM limitation imposed by the moving spectral notches (which provide the mutual RFI suppression) is considered here. The LS-MMF was constructed with a length that is 3× that of the MF length ($N_{\mathrm{w}} = 3N_{\mathrm{p}}$) and with sufficient diagonal loading to avoid notch inversion and minimize mismatch loss. Beamspoiling is not applied in the LS-MMF formulation, as it was found to degrade the spectral homogenization across range estimates and thus sustain the clutter range-Doppler sidelobes.

Figure 68 show the matched filtered full-band PRO-FM responses when the RFI is not present for baseline comparison, repeated from Case 2. Figure 69 illustrates the degradation that arises for the MF and LS-MMF when notched PRO-FM waveforms are employed and the notch locations move dynamically during the CPI. The streaks observed in Figure 69 are clutter sidelobes that could not be cancelled due to the nonstationarity induced by changing notch locations. The use of notched LS-MMFs provides some compensation for this effect.

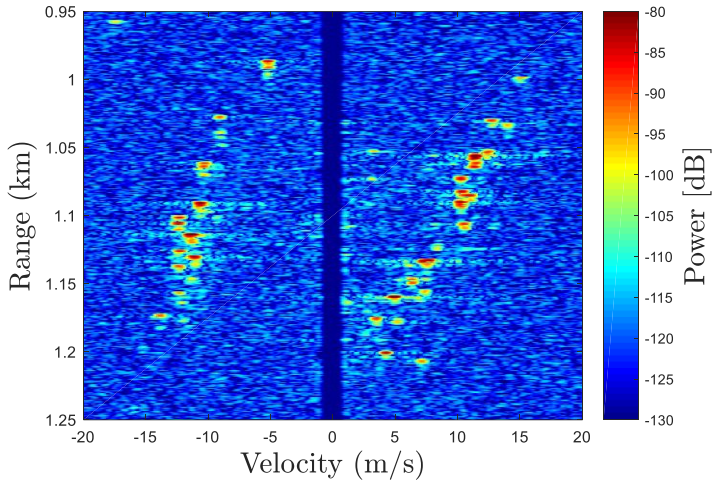

Figure 68: Range-Doppler plot of full-band PRO-FM with no injected RFI, intended as the baseline comparison, applying the matched filter to the single notch data collect. Repeated from Case 2.

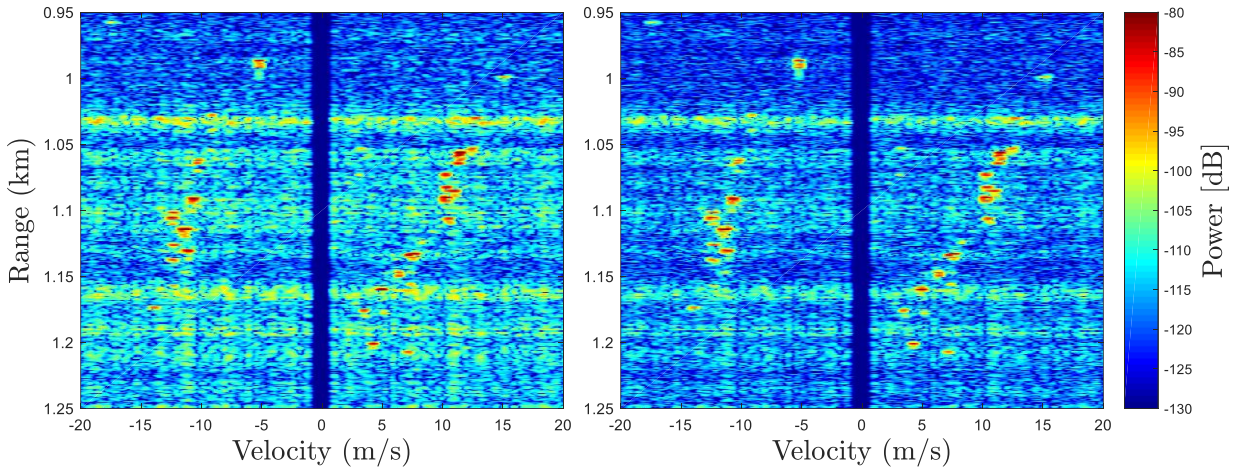

Figure 69: Measured range-Doppler response from 2500 PRO-FM waveforms with dynamic spectral notches, applying the matched filter (left) and least squares mismatched filter (right), for the single notch data collect.

2.3.2. CASE 4: HOPPED INTERFERENCE, NO LATENCY, CLUTTER FILLING BY TEMPORALLY ADJACENT FULL-BAND WAVEFORMS

Figure 70 shows the MF and notched LS-MMF range-Doppler responses for the same set of notched waveforms when DeCCaF is applied using the borrowed clutter estimate elicited by the adjacent full-band waveforms. Recall the metric for interference impact $\bar{\Delta}$, where I_{meas} is the average power measured for each scenario in the range/Doppler regions that do not contain discernible targets or the clutter notch. The value I_{baseline} is then the particular value of I_{meas} for the full-band, no RFI scenario (e.g. Figure 68). Without application of DeCCaF, the matched filter estimate is degraded by $\bar{\Delta}= 7.0$ dB and the mismatched filter estimate is degraded by $\bar{\Delta}= 3.8$ dB, demonstrating a slight improvement. The addition of DeCCaF before Doppler processing improves the background floor, where the matched filter estimate is degraded by $\bar{\Delta}= 2.7$ dB, demonstrating an improvement of 4.3 dB of the uncompensated counterpart. Applying DeCCaF in addition to the LS-MMF achieve $\bar{\Delta}= 0.8$ dB, which is near the level achieved by the baseline. In other words, this combination of approaches seems to have come rather close to completely compensating for degradation imposed by spectral notches that address dynamic RFI.

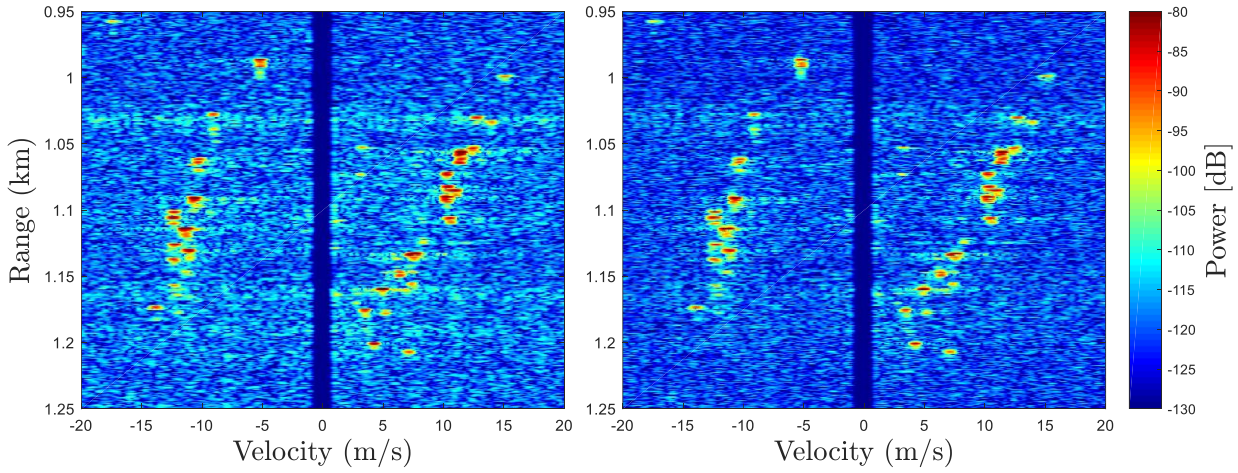

Figure 70: Measured range-Doppler response from 2500 PRO-FM waveforms with dynamic spectral notches, applying interleaved & spectrally-filtered full-band responses for clutter filling via the matched filter & DeCCaF (left) or the mismatched filter & DeCCaF (right).

Table 5: Impact of notching, MF or LS-MMF estimation, and DeCCaF using temporally adjacent full-band estimates, for Case 4, when a single RFI band is present.

	I_{meas}, single	$\overline{\Delta}$, single
Full-band, no RFI, MF (baseline)	−120.8 dB	--
Notched, no RFI, MMF	−117.0 dB	+3.8 dB
Notched, no RFI, MF	−113.8 dB	+7.0 dB
Notched, no RFI, DeCCaF, MMF	−120.0 dB	+0.8 dB
Notched, no RFI, DeCCaF, MF	−118.1 dB	+2.7 dB

2.3.3. CASE 5: HOPPED INTERFERENCE, NO LATENCY, CLUTTER FILLING BY TEMPORALLY ADJACENT NOTCHED WAVEFORMS

Having established the performance enhancement of DeCCaF when the borrowed clutter responses are taken from the separate (interleaved) set of full-band waveforms, now consider the impact of borrowing clutter from other notched pulses within the same CPI. The BPF clutter is borrowed from the temporally nearest notched waveform that has a non-overlapping notch location relative to the pulse under consideration, as shown in Figure 71. The resulting DeCCaF response therefore involves the re-use of clutter and noise from elsewhere in the CPI, as opposed to the statistically independent instantiations considered in the previous interleaved case, which would likely not be realistic. Some degradation in the degree of residual clutter compensation is expected.

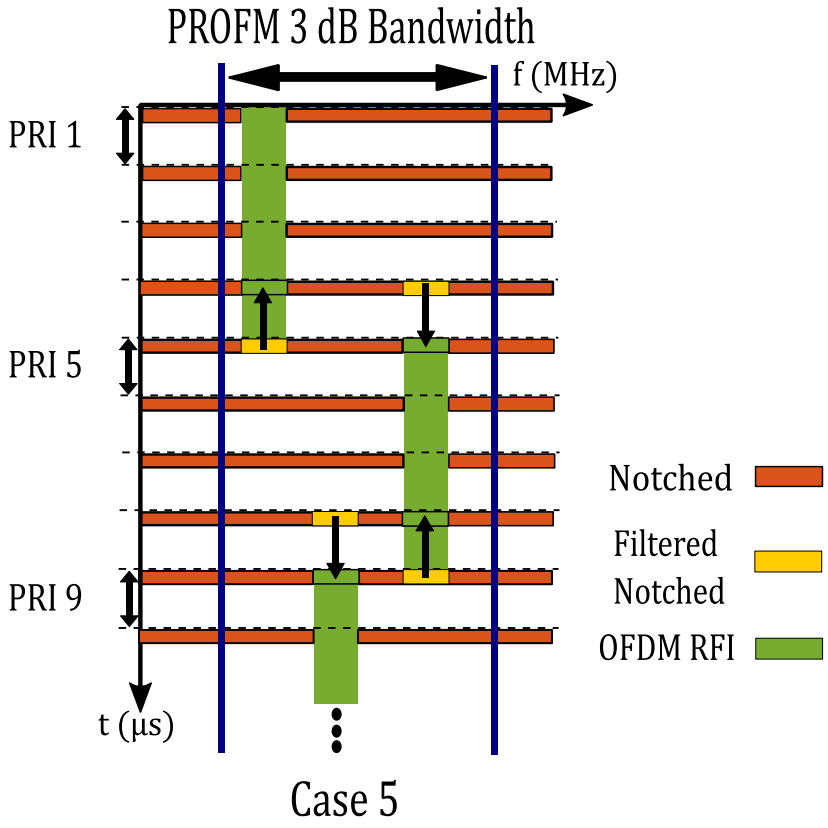

Figure 71: Timing diagram of the waveform arrangement used to evaluate the operationally useful form of DeCCaF. The borrowed clutter is taken from temporally adjacent, spectrally non-overlapping notched responses.

Figure 72 shows the MF and MMF range-Doppler responses for this arrangement. Compared to Figure 70, the residual clutter floor is slightly increased, though the overall performance improvement relative to Figure 69 without DeCCaF is still quite clear. The addition of DeCCaF before Doppler processing improves the background floor, where the matched filter estimate is degraded by $\bar{\Delta}= 4.4\ \mathrm{dB}$, demonstrating an improvement of 2.6 dB of the uncompensated counterpart. Applying DeCCaF in addition to the LS-MMF achieve $\bar{\Delta}= 1.7\ \mathrm{dB}$, which is still near the level achieved by the baseline.

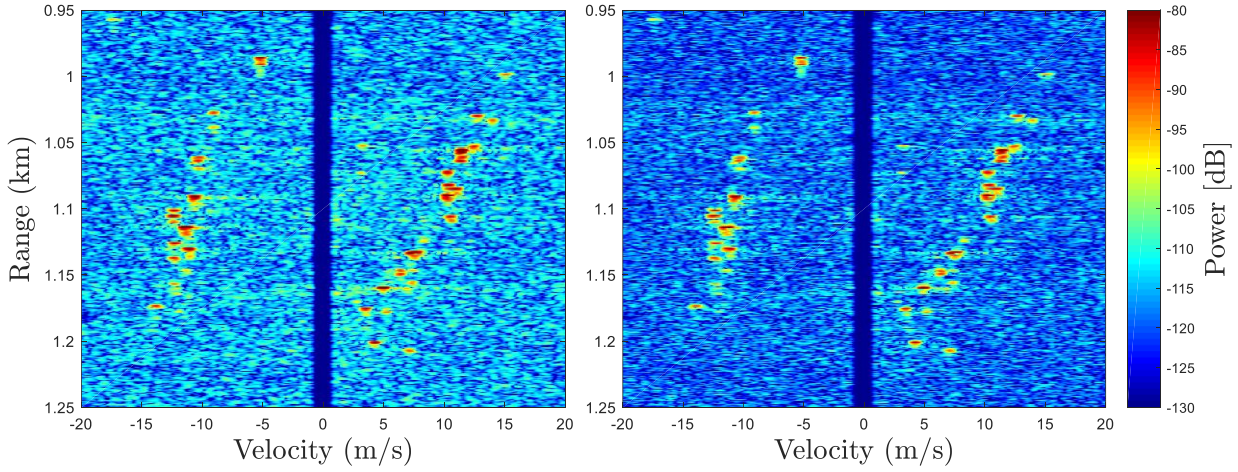

Figure 72: Measured range-Doppler response from 2500 PRO-FM waveforms with moving spectral notches, applying adjacent spectrally-filtered notched waveform responses for clutter filling via the matched filter & DeCCaF (left) or the mismatched filter & DeCCaF (right).

Table 6: Impact of notching, MF or LS-MMF estimation, and DeCCaF using temporally adjacent notched estimate, for Case 5, when a single RFI band is present.

	I_{meas}, single	$\overline{\Delta}$, single
Full-band, no RFI, MF (baseline)	−120.8 dB	+0.9 dB
Notched, no RFI, MMF	−117.0 dB	+3.8 dB
Notched, no RFI, MF	−113.8 dB	+7.0 dB
Notched, no RFI, DeCCaF, MMF	−119.1 dB	+1.7 dB
Notched, no RFI, DeCCaF, MF	−116.4 dB	+4.4 dB

For a different perspective on how DeCCaF is compensating for notch-induced clutter modulation, the mean PSD of the MF range estimate across the CPI in slow-time are examined. The PSD having moving notches exhibits a noticeable deviation from the PSD when full-band waveforms are used, as shown in Figure 73. However, refilling the missing clutter response via DeCCaF returns the mean PSD closely to the full-band case. Figure 74 shows the PSDs of the MF range estimates, indexed over the p^{th} pulse of the CPI, before and after applying DeCCaF.

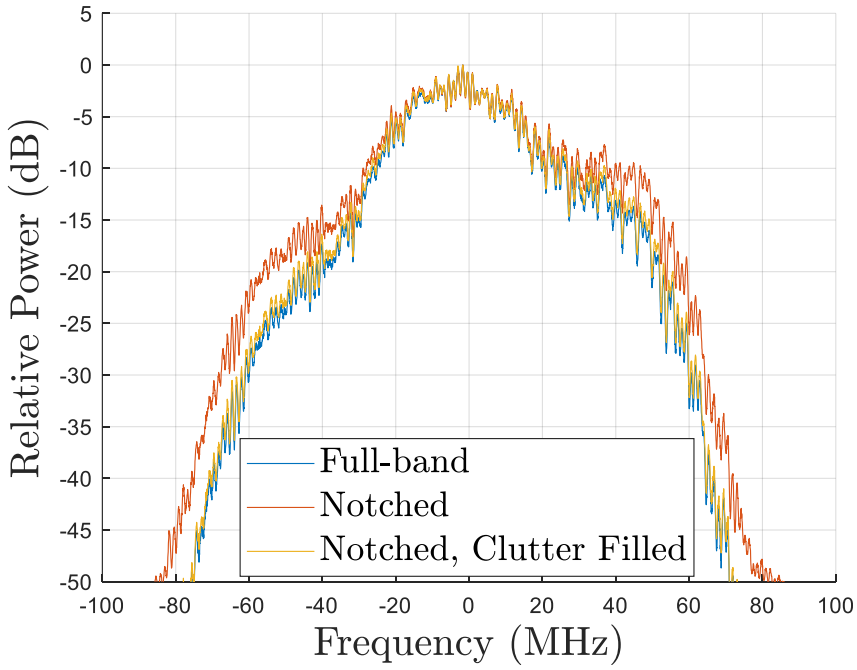

Figure 73: Mean power spectra of the matched filtered range profile estimate $\sum_{\forall p}\left|\hat{\gamma}_p(f)\right|^2$ over the given CPI for Case 1 (full-band) and Case 2 (notched without clutter filling). The mean compensated range profile estimate $\sum_{\forall p}\left|\tilde{\gamma}_p(f)\right|^2$ after applying DeCCaF for Case 5 (notched, clutter filling with other notched responses) is quite similar the full-band response.

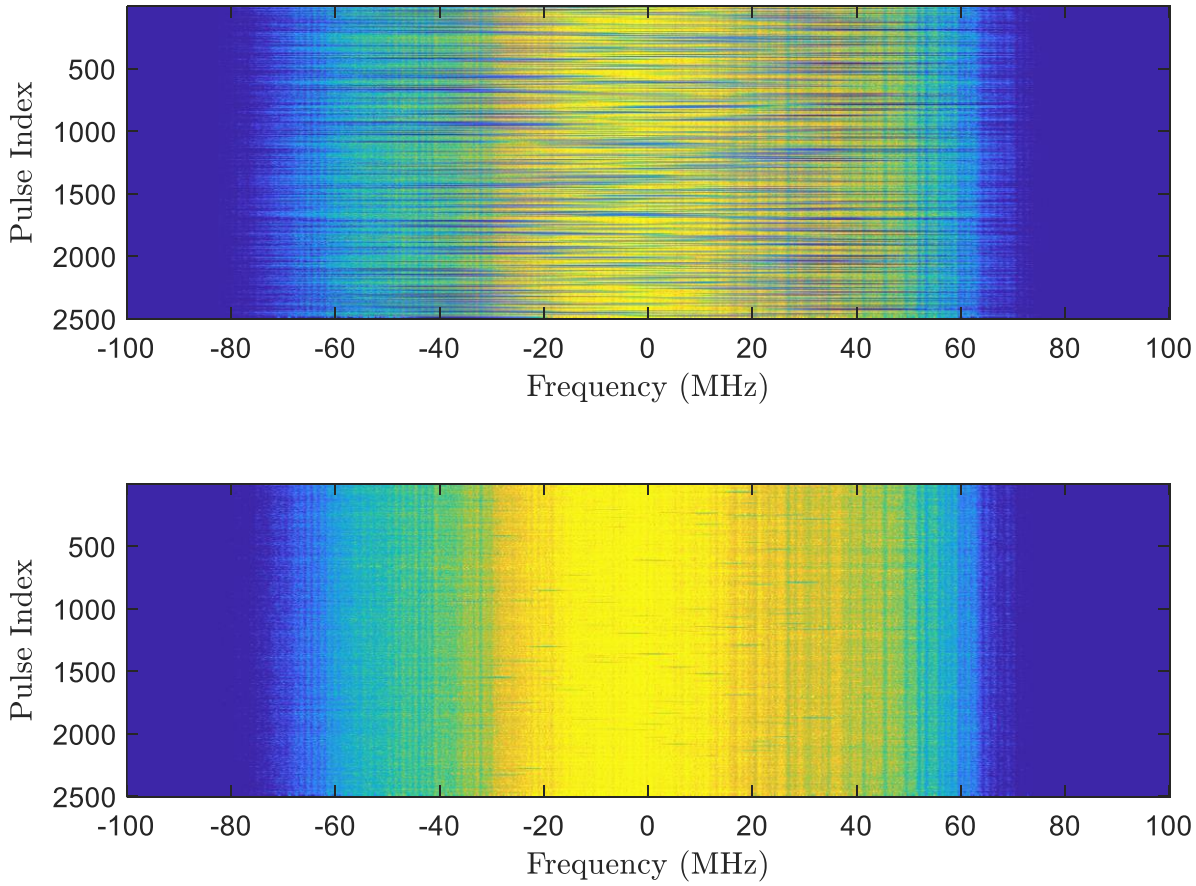

Figure 74: Power spectra of the matched filtered range profile estimate $\left|\hat{\gamma}_p(f)\right|^2$ for the p^{th} pulse before applying DeCCaf (top) and the compensated range profile estimates $\left|\tilde{\gamma}_p(f)\right|^2$ after applying DeCCaF (bottom)

2.3.4. CONCLUSIONS

An ad hoc approach denoted as devoid clutter capture and filling (DeCCaF) has been proposed and demonstrated on measured data as a means to address the nonstationarity that arises when spectral notches must move during the CPI to mitigate interference with dynamic RFI. When DeCCaF is combined with appropriately notched optimal mismatched filtering the result is nearly indistinguishable from the case in which no spectral notches are employed.

2.4. NOTCHED POWER SPECTRA FOR OPTIMAL SIDELOBE REDUCTION

Designing radar waveforms with notched spectral regions can mitigate mutual interference with other proximate RF users. However, this capability comes at the cost of degraded range-Doppler sidelobe performance. To evaluate the limitations of correlation-based processing in the range dimension, the null-constrained power spectral density that globally minimizes correlation sidelobe levels is determined for comparison with waveform and pulse compression filter design methods. Existence of the least-squares global optimum indicates a fundamental dynamic range limitation for notched power spectra (notwithstanding further receive compensation such as DeCCaF or range resolution spoiling). By extension, the limitations of combined pulse compression and slow time-Doppler processing are assessed by determining the null-constrained set of power spectral densities that globally minimizes the range-Doppler sidelobes indicated by the point spread function (PSF).

Section 2.1 examined spectrally notched random FM (RFM) waveform design where ad-hoc tapering was incorporated into the null shape as a heuristic means of reducing range sidelobes. Here, waveforms designed according to the optimal null-constrained spectral template are demonstrated to have improved sidelobe performance after pulse compression and slow-time processing. Further, because these waveforms are designed according to the least squares optimal spectral template, application of the least squares mismatched filter provides additional sidelobe reduction (toward the global limit) with minimal mismatch loss.

2.4.1. GLOBAL MINIMUM POWER SPECTRUM FOR RANGE SIDELOBE REDUCTION

To gain insight about the behavior of spectrally notched power spectra when attempting to minimize correlation sidelobes, it is interesting to first examine solutions to a well-posed (less constrained) objective statement. The waveform power spectral density (PSD) $\mathbf{r}_f$ and autocorrelation $\mathbf{r}$ are a Fourier transform pair; therefore, waveforms designed to conform to a desired PSD template $\mathbf{d}_f$ can be directly optimized for both autocorrelation and spectral properties. Moreover, doing so while constraining spectral null locations provides global minimum boundaries for waveform/filter spectral notches due to convexity.

Consider the optimization problem to design the desired PSD template $\mathbf{d}_{\mathrm{f}}$, which can be written as

$$\begin{aligned} \min_{\mathbf{d}_{\mathrm{f}}} \ & \|\mathbf{e} - \overline{\mathbf{A}}^{H}\mathbf{d}_{\mathrm{f}}\|_2^2 \\ \text{s.t.} \ & d_{\mathrm{f},m} \le \varepsilon_m \quad \text{for } m \in \Lambda \\ & 0 \le d_{\mathrm{f},m} \quad \text{for } m = 0,1,\ldots M_{\mathrm{d}} - 1 \end{aligned} \tag{2.13}$$

where $\mathbf{d}_{\mathrm{f}}$ is the $M_{\mathrm{d}} \times 1$ discretized PSD template with $d_{\mathrm{f},m}$ as the m^{th} element, $\overline{\mathbf{A}}^{H}$ is an $M_{\mathrm{d}} \times M_{\mathrm{d}}$ shifted inverse discrete Fourier transform (IDFT) matrix, $\mathbf{e}$ is the ideal impulse autocorrelation response, $(\cdot)^*$ denotes complex conjugation, $\|\cdot\|_2$ is the 2-norm operator, and ε_m is the constrained maximum value for the associated $d_{\mathrm{f},m}$ and for m in the subset Λ (i.e. null constraints). Each element of $\mathbf{d}_{\mathrm{f}}$ must be non-negative by definition of the PSD. The objective function in (2.13) therefore determines $\mathbf{d}_{\mathrm{f}}$ such that the corresponding autocorrelation (via IDFT) has a minimized integrated sidelobe level (ISL), subject to spectral null constraints.

The problem formulation in (2.13) is a hybrid of non-negative LS and boxed LS, each being convex and having unique global solutions if $\overline{\mathbf{A}}^{H}$ has full column rank (true for the DFT matrix) [165]. Different degrees of beamspoiling [71] can be achieved by replacing $\bar{L}$ rows of $\overline{\mathbf{A}}^{H}$ (corresponding to autocorrelation mainlobe roll-off) with zeros, thus permitting different mainlobe widths and achievable sidelobe levels. The resulting beam-spoiled matrix still maintains full column rank; therefore, (2.13) is convex and yields the globally optimal solution $\hat{\mathbf{d}}_{\mathrm{f}}$.

For convenience, (2.13) is solved using the Matlab™ fmincon optimization toolkit [166]. The resulting optimal PSD templates for minimizing ISL, and their associated autocorrelation structures with various degrees of beamspoiling, are shown in Figure 75. The spectral window length is chosen to be $M_{\mathrm{d}} = 200$ samples. Notches are imposed at the band edges for containment, and an additional notch is imposed off-center from normalized frequencies -0.2 to -0.1. For all illustrated cases, each notch occupies 10% of the band with an enforced relative depth of 40 dB. The autocorrelation mainlobe resolution is defined by the ratio (%) of beamspoiled rows in $\overline{\mathbf{A}}^{H}$ relative to the total spectral window length M_{d}.

A notable characteristic of the power spectra in Figure 75 is that the larger primary band (between digital frequencies −0.1 and +0.4) maintains a majority of the power, with the smaller supplementary band (between digital frequencies −0.4 and −0.2) used to improve resolution. In fact, for the 6% beamspoiling case, the supplementary band is hardly occupied, implying that a sense-and-avoid [140] approach may be suitable depending on the desired resolution and sidelobe levels. Prior findings [150] that spectral notching near the band center degrades the achievable range sidelobe level is also confirmed in Figure 76. Compared to traditional windowing methods [167], the least squares optimal spectral templates are rather custom-designed via (2.13) to include spectral notches based on a prior spectrum-sensing process.

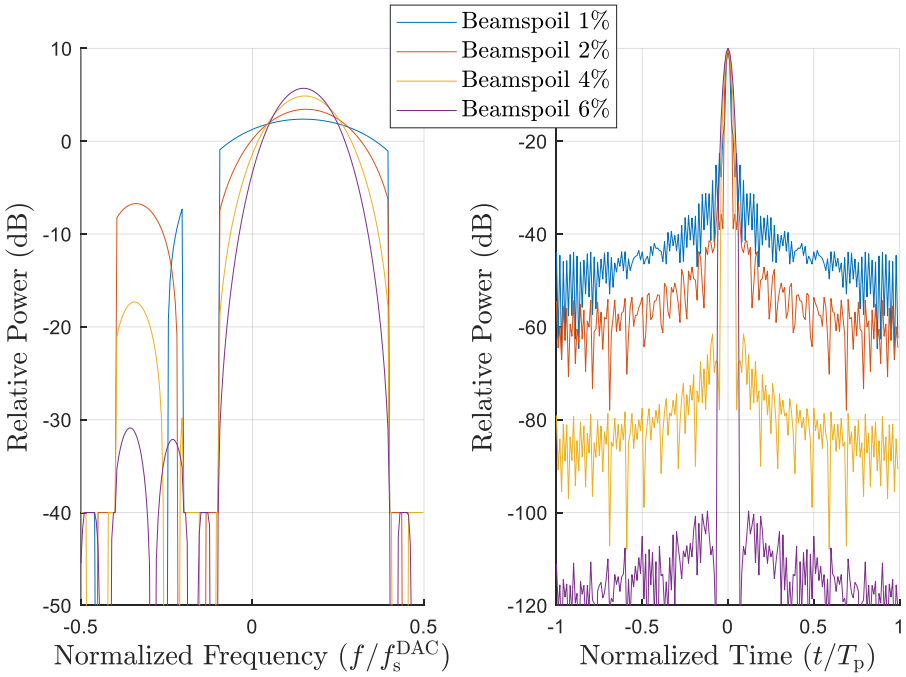

Figure 75: Optimum desired power spectrum templates $\hat{\mathbf{d}}_{\mathrm{f}}$ and autocorrelation responses $\hat{\mathbf{d}}$ with minimized autocorrelation ISL according to (2.13), for 40 dB spectral null and varied beamspoiling ratios of 1%, 2%, 4%, 6% relative to total window length

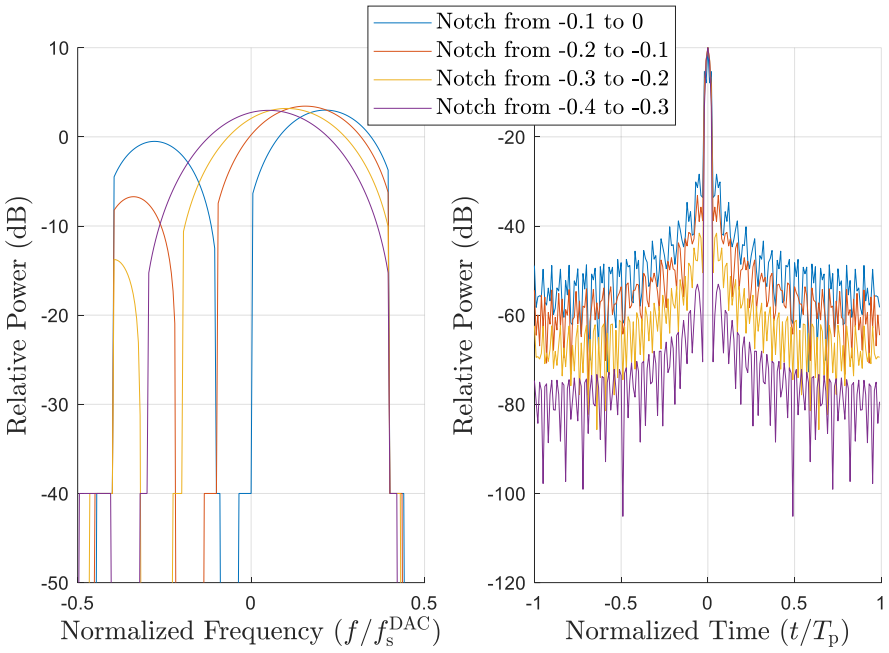

Figure 76: Optimum desired power spectrum templates $\hat{\mathbf{d}}_{\mathrm{f}}$ and autocorrelation responses $\hat{\mathbf{d}}$ with minimized autocorrelation ISL according to (2.13), for 40 dB spectral nulls (at different locations) and beamspoiling ratio of 2% relative to total window length.

The cost function in (2.13) can be readily generalized to a $\mathcal{p}$-norm framework

$$\begin{aligned} \min_{\mathbf{d}_{\mathrm{f}}} \ & \|\mathbf{e} - \overline{\mathbf{A}}^{H}\mathbf{d}_{\mathrm{f}}\|_{\mathcal{p}}^{\mathcal{p}} \\ \text{s.t.} \ & d_{\mathrm{f},m} \le \varepsilon_m \quad \text{for } m \in \Lambda \\ & 0 \le d_{\mathrm{f},m} \quad \text{for } m = 0,1,\dots M_{\mathrm{r}} - 1 \end{aligned}$$

(2.14)

with sufficiently large $\mathcal{p}$ well-approximating the peak sidelobe level (PSL) metric. The $\mathcal{p}$ -norm version still maintains convexity, so therefore global optimality is likewise preserved. The gradient of (2.14) is

$$\underline{\nabla}_{\mathbf{r}_{\mathrm{f}}} \|\mathbf{e} - \overline{\mathbf{A}}^{H}\mathbf{d}_{\mathrm{f}}\|_{\mathcal{p}}^{\mathcal{p}} = -\mathcal{p}\, Re\{\overline{\mathbf{A}}(|\mathbf{e} - \overline{\mathbf{A}}^{H}\mathbf{d}_{\mathrm{f}}|^{\mathcal{p}-2} \odot (\mathbf{e} - \overline{\mathbf{A}}^{H}\mathbf{d}_{\mathrm{f}}))\}$$

(2.15)

where $Re\{\cdot\}$ extracts the real part of the argument.

For example, the resulting optimal PSD templates $\hat{\mathbf{d}}_{\mathrm{f}}$ and their corresponding autocorrelations $\hat{\mathbf{d}}$ for various degrees of beamspoiling are shown in Figure 77 for $\mathscr{p} = 8$. The same constraints are enforced as in Figure 75 for the ISL case. Interestingly, these PSDs exhibit ridged structures at low resolutions. Similar to the ISL case, as the degree of beamspoiling is increased (relaxing autocorrelation mainlobe width) the sidelobe floor is correspondingly reduced. This interplay between sidelobe level and mainlobe resolution is a fundamental trade-space for this design. A given degree of beamspoiling is necessary to achieve a desired dynamic range (i.e. sidelobe level); though increasing the beamspoiling factor does reduce 3-dB bandwidth and therefore degrades mainlobe resolution.

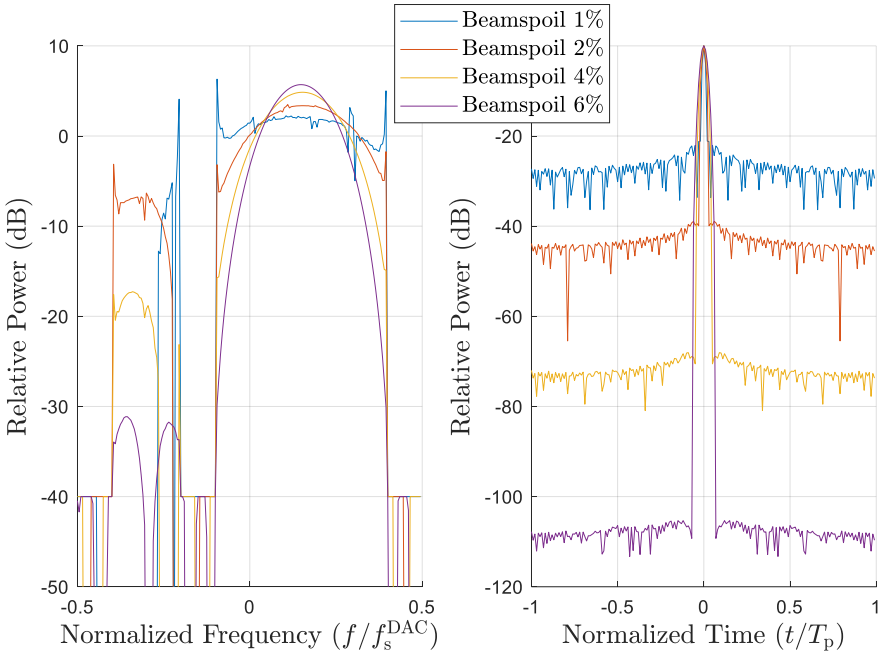

Figure 77: Optimum desired power spectrum templates $\hat{\mathbf{d}}_{\mathrm{f}}$ and autocorrelation responses $\hat{\mathbf{d}}$ with minimized autocorrelation PSL ($\mathscr{p} = 8$) according to (2.14), for 40 dB spectral null and varied beamspoiling ratios of 1%, 2%, 4%, 6% relative to total window.

2.4.2. GLOBAL MINIMUM POWER SPECTRUM FOR RANGE-DOPPLER SIDELOBE REDUCTION

While the global minimum template for range sidelobe reduction provides insight regarding the per-pulse limitation of correlation-based processing (i.e. assuming $f_{\mathrm{d}} = 0$) for arbitrary notch depths and locations, consideration must be taken regarding range-Doppler sidelobes resulting from a non-stationary spectral notch. Recall from (1.149) that the range-Doppler point spread function may be expressed (excluding normalizations) as

$$\mho = \overline{\mathbf{A}}_1^H \mathbf{R}_{\mathrm{f}} \overline{\mathbf{A}}_{\mathbf{2}} \tag{2.16}$$

The ideal range-Doppler point spread function is the two-dimensional impulse function $\mathbf{E}$ having a mainlobe peak and no range-Doppler sidelobes. The set of waveform PSDs $\mathbf{R}_{\mathrm{f}}$ and the point spread function $\mho$ are a two-dimensional Fourier transform pair; therefore, waveforms designed to conform to the desired PSD template set $\mathbf{D}_{\mathrm{f}} = [\mathbf{d}_{\mathrm{f},0} \quad \mathbf{d}_{\mathrm{f},2} \quad \cdots \quad \mathbf{d}_{\mathrm{f},P-1}]$ can be directly optimized for both range-Doppler and spectral properties. Moreover, doing so while constraining spectral null locations provides global minimum boundaries for waveform/filter spectral notches due to convexity. Of course, knowledge of future notch locations would require precise knowledge of future interference spectral patterns which is rarely had, and the range-Doppler optimum is intended here for analytical purposes. Consider the optimization problem to design the PSD template set $\mathbf{D}_{\mathrm{f}}$ written as

$$\begin{aligned} \min_{\mathbf{D}_{\mathrm{f}}} \ & \|\mathrm{vec}(\mathbf{E}) - \mathrm{vec}(\overline{\mathbf{A}}_1^H \mathbf{D}_{\mathrm{f}} \overline{\mathbf{A}}_{\mathbf{2}})\|_{\mathscr{p}}^{\mathscr{p}} = \|\mathrm{vec}(\mathbf{E}) - (\overline{\mathbf{A}}_2^T \otimes \mathbf{A}_1^H)\mathrm{vec}(\mathbf{D}_{\mathrm{f}})\|_{\mathscr{p}}^{\mathscr{p}} \\ \text{s.t.} \ & d_{\mathrm{f},m,p} \le \varepsilon_{m,p} \quad \text{for } m,p \in \Lambda \\ & 0 \le d_{\mathrm{f},m,p} \qquad \text{for } m = 0,1,\dots M_{\mathrm{d}} - 1;\ p = 0,1,\dots,P-1 \end{aligned} \tag{2.17}$$

where $\mathbf{D}_{\mathrm{f}}$ is the $M_{\mathrm{d}} \times P$ discretized PSD template set with $d_{\mathrm{f},m,p}$ as the m^{th} element of the p^{th} spectral template, $\overline{\mathbf{A}}_1^H$ is an $M_{\mathrm{d}} \times M_{\mathrm{d}}$ shifted IDFT matrix, $\overline{\mathbf{A}}_2$ is an $P \times P$ shifted DFT matrix, $\mathbf{E}$ is the ideal impulse point spread function, and $\varepsilon_{m,p}$ is the constrained maximum value for the associated $d_{\mathrm{f},m,p}$ and for m in the subset Λ (i.e. null constraints). Each element of $\mathbf{D}_{\mathrm{f}}$ must be non-negative by definition of the PSD.

The objective function in (2.17) therefore determines $\mathbf{D}_{\mathrm{f}}$ such that the corresponding point spread function has minimized integrated sidelobe levels (ISL) or peak sidelobe levels (PSL) inside the constrained range-Doppler region, subject to spectral null constraints. Different degrees of range beamspoiling or Doppler beamspoiling [71] can be achieved by replacing $\bar{L}$ rows of $\overline{\mathbf{A}}_1^H$ (spanning the autocorrelation mainlobe roll-off) or $\bar{P}$ columns of $\overline{\mathbf{A}}_2$ (spanning to the Doppler mainlobe roll-off) with zeros, thus permitting different mainlobe widths and achievable sidelobe levels. The resulting beam-spoiled matrix $(\overline{\mathbf{A}}_2^T \otimes \mathbf{A}_1^H)$ maintains full column rank; therefore, (2.17) is convex and yields the globally optimal solution $\widehat{\mathbf{D}}_{\mathrm{f}}$.

The objective function must include an appended set of linear constraints to ensure that the total power in each PSD is uniform across all pulses. Linear constraints maintain objective function convexity, under the condition that the constraints are not disjoint [168]. The constraints are appended as

$$\begin{aligned} \min_{\mathbf{D}_{\mathrm{f}}} \ & \|\mathrm{vec}(\mathbf{E}) - \mathrm{vec}(\overline{\mathbf{A}}_1^H \mathbf{D}_{\mathrm{f}} \overline{\mathbf{A}}_2)\|_p^p = \|\mathrm{vec}(\mathbf{E}) - (\overline{\mathbf{A}}_2^T \otimes \mathbf{A}_1^H)\mathrm{vec}(\mathbf{D}_{\mathrm{f}})\|_p^p \\ \text{s.t.} \ & d_{\mathrm{f},m,p} \le \varepsilon_{m,p} \quad \text{for } m,p \in \Lambda \\ & 0 \le d_{\mathrm{f},m,p} \qquad \text{for } m = 0,1,\dots M_{\mathrm{d}} - 1;\ p = 0,1,\dots P-1 \\ & \mathbf{1}^T \mathbf{d}_{\mathrm{f},p} = 1 \qquad \text{for } p = 0,1,\dots P-1 \end{aligned} \tag{2.18}$$

Because the optimization is extended to a two-dimensional problem space, the spectral notch constraints become time-varying and numerous possible variants would result in different global minima. Here, three representative notch patterns are demonstrated, and the corresponding PSDs and PSFs after optimizing point spread function ISL are illustrated. The spectral window length is chosen to be $M_{\mathrm{d}} = 200$ samples and the pulse number is selected as $P = 50$. Note that the number of optimizable parameters becomes $M_{\mathrm{d}} \cdot P$, thus signifying a rapidly growing computational cost as variable size increases. Notches are imposed at the band edges for containment. For all illustrated cases, each notch occupies 10% of the band with an enforced relative depth of 40 dB. The range mainlobe resolution is defined by the ratio (%) of beamspoiled rows in $\overline{\mathbf{A}}_1^H$ relative to the total spectral window length M_{d}. The Doppler mainlobe resolution is defined by the ratio (%) of beamspoiled columns in $\overline{\mathbf{A}}_2$ relative to the total number of pulses P.

Consider a stationary spectral notch from normalized frequency -0.2 to -0.1 over the CPI duration, optimized when $\wp = 2$, enforcing the 2% range beamspoiling ratio and 4% Doppler beamspoiling ratio. The resulting optimal PSD templates that minimize point spread function ISL according to (2.18), and the corresponding PSF, are shown in Figure 78. The power spectrum set $\widehat{\mathbf{D}}_{\mathrm{f}}$ remains mostly unchanged across pulses, with minor deviations present, which indicates that maintaining a homogenous spectrum across slow time minimizes range-Doppler sidelobes. For comparison, the same interference pattern is used to optimize autocorrelation ISL on a per-pulse basis via (2.14), illustrated in Figure 79. When the RF interference is stationary, only minor differences are observed between the PSF-optimized and autocorrelation-optimized solution.

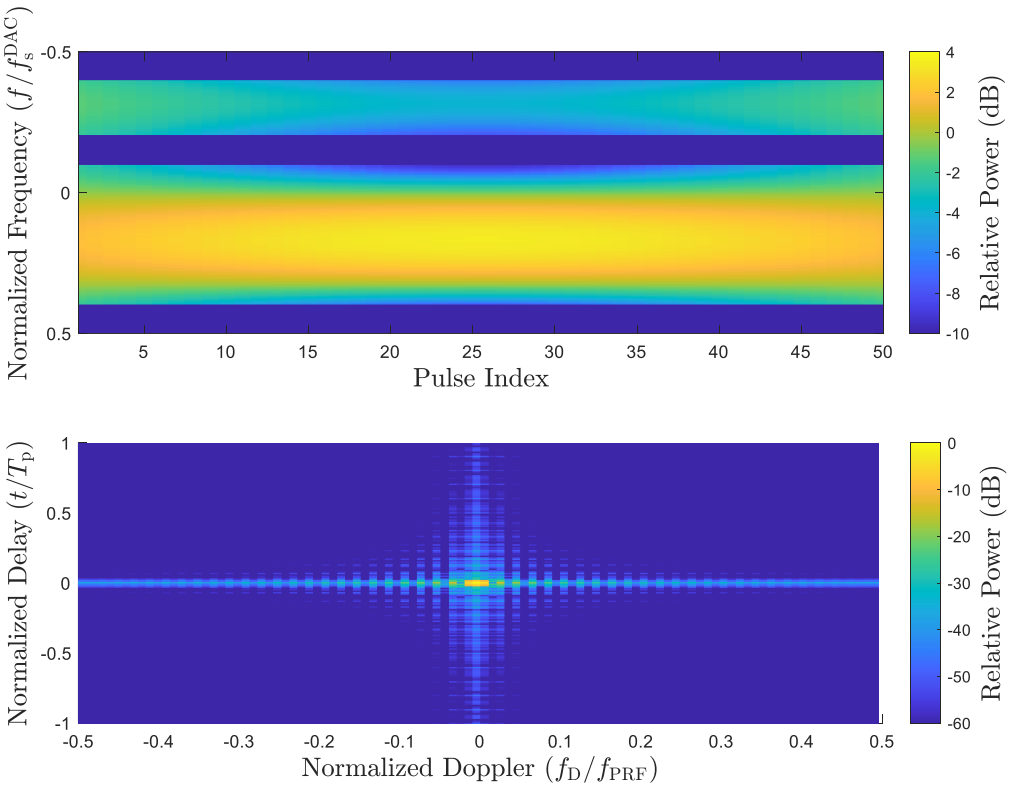

Figure 78: Optimum desired power spectrum template set $\widehat{\mathbf{D}}_{\mathrm{f}}$ and point spread function responses $\mathfrak{V}$ with minimized point spread function ISL $(\wp = 2)$ according to (2.18), for 40 dB spectral nulls and enforcing the 2% range beamspoiling ratio relative to the window length M_{d} and 4% Doppler beamspoiling ratio relative to the number of pulses P. The spectral notches are stationary across all pulses.

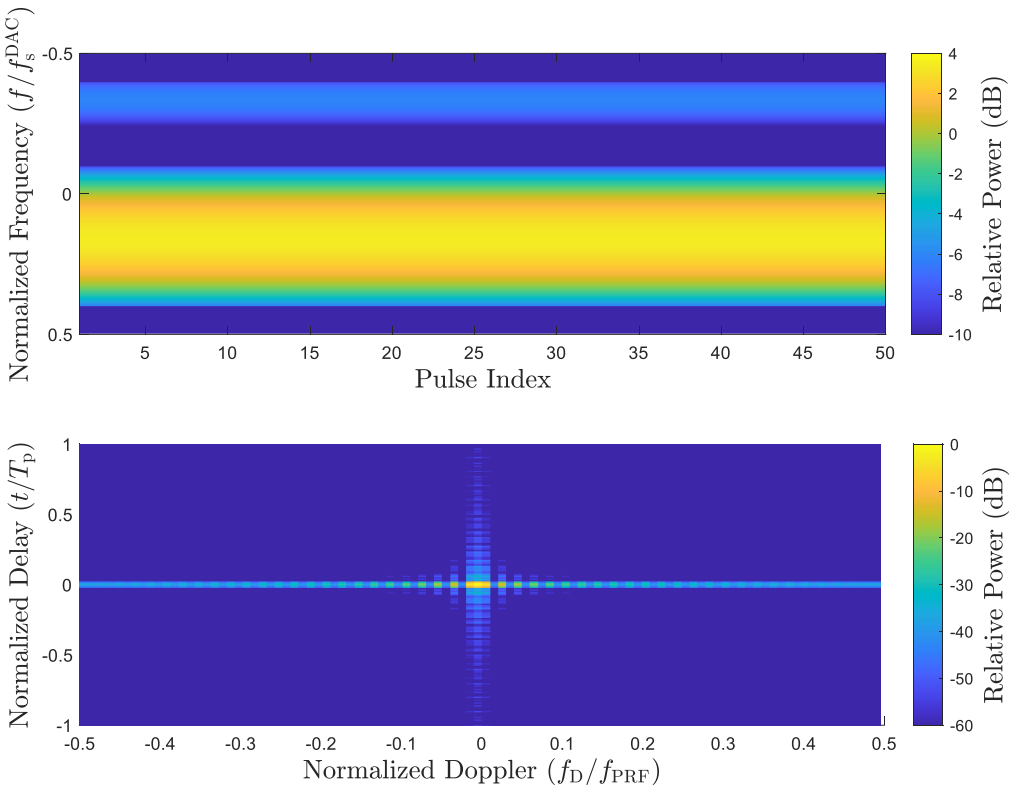

Figure 79: Desired power spectrum set $\mathbf{D}_{\mathrm{f}}$ and point spread function responses $\mathfrak{V}$ with minimized autocorrelation ISL ($\mathscr{p} = 2$) determined on a per-pulse basis according to (2.14), for 40 dB spectral nulls and enforcing the 2% range beamspoiling ratio relative to the window length M_{d}. The spectral notches are stationary across all pulses.

Now consider when the spectral notch deviates by small steps throughout the CPI duration. The resulting optimal set of PSDs that minimizes point spread function ISL, and the corresponding PSF, are shown in Figure 80. The power spectrum set $\widehat{\mathbf{D}}_{\mathrm{f}}$ allocates power across slow time pulses in spectral regions having the fewest total notches, further revealing that maintaining a homogenous spectrum across slow time minimizes range-Doppler sidelobes. Interestingly, the reduction in point spread function ISL causes power to smear, forming a background pedestal in the PSF. In contrast, the same interference pattern is used to optimize autocorrelation sidelobes on a per-pulse basis via (2.14), illustrated in Figure 81. Because the impact of slow time spectrum deviation is not considered in the per-pulse autocorrelation optimization, range-Doppler sidelobes appear in a concentrated band neighboring the zero-range cut. However, the sidelobe power outside of banded region is significantly reduced, posing an interesting performance tradeoff regarding the expected sparsity of the ensuing range-Doppler sidelobes.

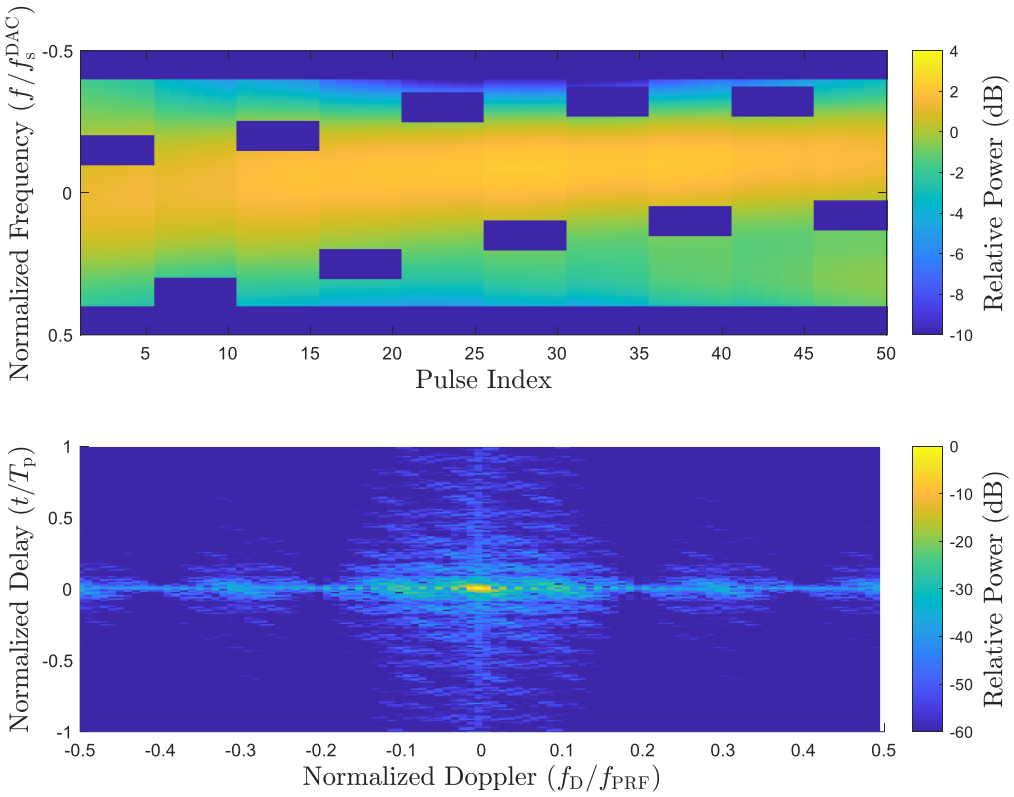

Figure 80: Optimum desired power spectrum template set $\widehat{\mathbf{D}}_{\mathrm{f}}$ and point spread function responses $\mathfrak{V}$ with minimized point spread function ISL $(\mathscr{p} = 2)$ according to (2.18), for 40 dB spectral nulls and enforcing the 2% range beamspoiling ratio relative to the window length M_{d} and 4% Doppler beamspoiling ratio relative to the number of pulses P. The spectral notches drift slowly across pulses in a semi-deterministic pattern.

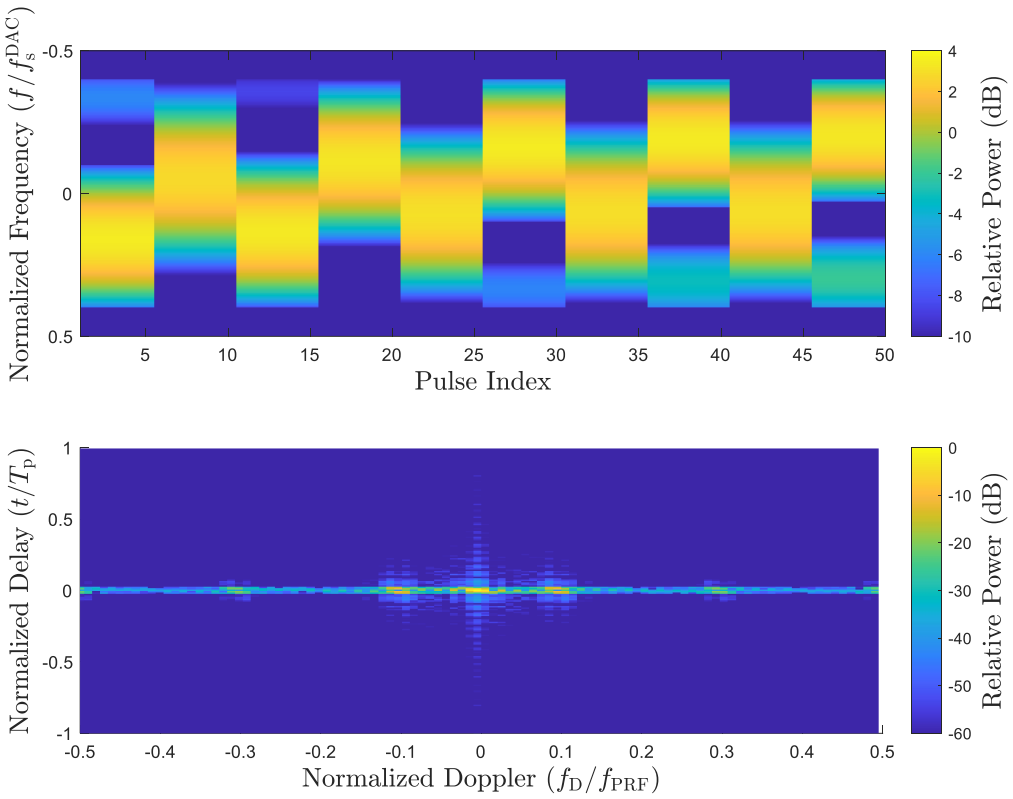

Figure 81: Desired power spectrum set $\mathbf{D}_{\mathrm{f}}$ and point spread function responses $\mathfrak{V}$ with minimized autocorrelation ISL ($\mathscr{p} = 2$) determined on a per-pulse basis according to (2.14), for 40 dB spectral nulls and enforcing the 2% range beamspoiling ratio relative to the window length M_{d}. The spectral notches drift slowly across pulses in a semi-deterministic pattern. RSM appears in the zero-range cut due to slow time spectral deviations.

The spectral notch is now made to deviate randomly throughout the CPI duration. The resulting optimal PSDs that minimize point spread function ISL, and the corresponding PSF, are shown in Figure 82. An important takeaway is that, regardless of the notch locations across pulses, the PSF-optimal power spectrum set $\widehat{\mathbf{D}}_{\mathrm{f}}$ always allocates power over the entire available bandwidth. Rather, regions exhibiting multiple spectral notches across slow time are distributed less (though non-zero) power to minimize range-Doppler sidelobes, verifying the necessity for the sense-and-notch paradigm. Once more, the resulting PSF exhibits a background pedestal. In contrast, the same interference pattern is used to optimize autocorrelation sidelobes on a per-pulse basis via (2.14), illustrated in Figure 83. Significant range-Doppler sidelobes appear within a concentrated band neighboring the zero-range cut.

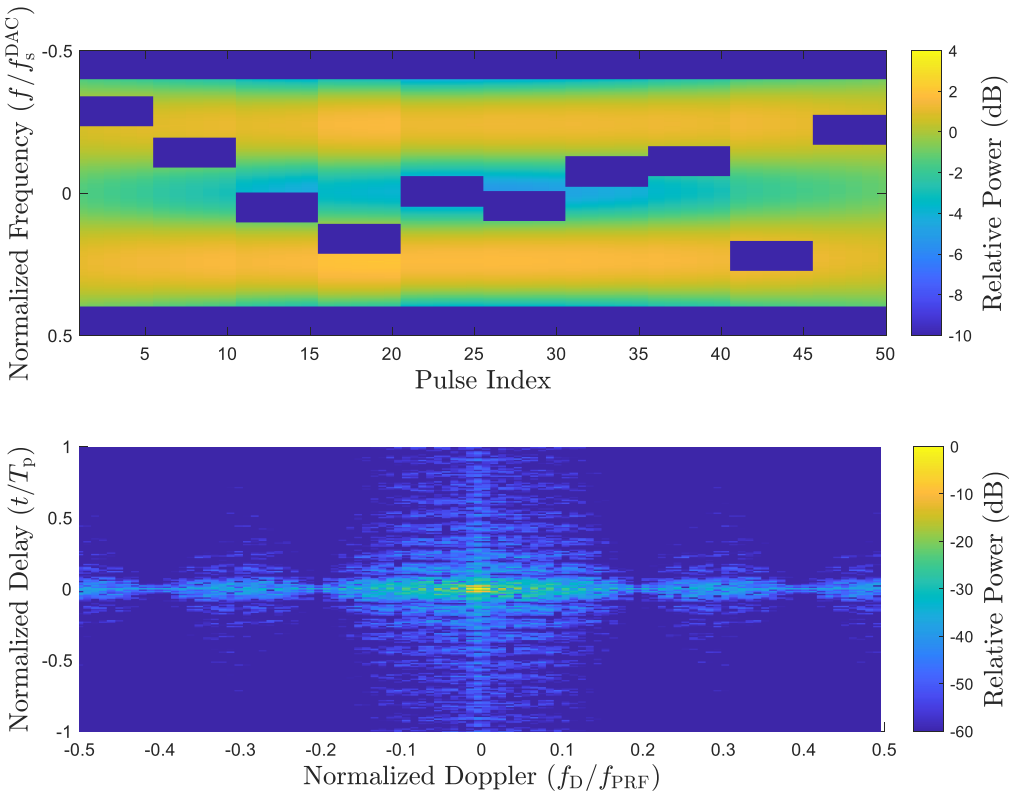

Figure 82: Optimum desired power spectrum template set $\widehat{\mathbf{D}}_\mathrm{f}$ and point spread function responses $\mathfrak{V}$ with minimized point spread function ISL $(\wp = 2)$ according to (2.18), for 40 dB spectral nulls and enforcing the 2% range beamspoiling ratio relative to the window length M_d and 4% Doppler beamspoiling ratio relative to the number of pulses P. The spectral notch randomly hops within the radar operational band over the CPI. Interestingly, the optimal power spectrum templates exhibit a bimodal distribution.

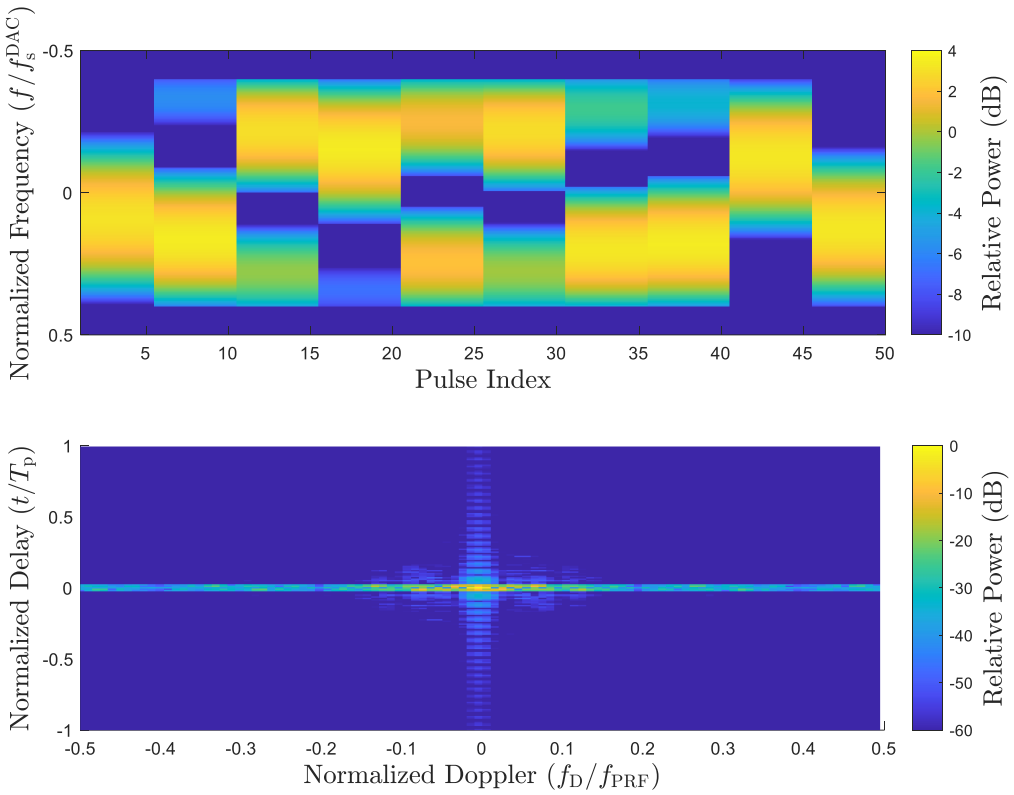

Figure 83: Desired power spectrum set $\mathbf{D}_{\mathrm{f}}$ and point spread function responses $\mathfrak{V}$ with minimized autocorrelation ISL ($\mathscr{p} = 2$) determined on a per-pulse basis according to (2.14), for 40 dB spectral nulls and enforcing the 2% range beamspoiling ratio relative to the window length M_{d}. The spectral notch randomly hops within the radar operational band over the CPI.

2.4.3. APPLICATION OF OPTIMAL TEMPLATE FOR SPECTRAL SHAPING

Achieving real-time reactivity on a practical time scale can make optimal solutions impractical, though the evaluation of optimality (for a given metric [36]) is still beneficial to determine bounds on performance. Specifically, in [149] a heuristic method was introduced that mitigates correlation sidelobes arising from waveform spectral nulls. That method attempted to reduce sidelobes by spectral shaping with templates having tapered spectral null borders, which thereby softened sharp transitions, within the context of PRO-FM waveforms. While PRO-FM does involve optimization (via alternating time/frequency projections) the computational cost is low and therefore realizable in real-time. However, the heuristic approach in [149] does not guarantee optimality.

Here, PRO-FM is likewise used, but in conjunction with the optimal least squares (LS) null-constrained power spectrum that minimizes autocorrelation sidelobe levels (based on matched filtering). The sidelobe level is then further reduced using LS mismatched filtering that was previously shown to be effective while maintaining spectral notches [160]. Since both the waveforms and mismatched filters are shaped according to the LS optimal power spectrum, their combination improves sidelobe performance with only rather modest mismatch loss.

We compare the PRO-FM waveform spectra using two different desired templates $\mathbf{d}_{\mathrm{f}}$, both intended to reduce autocorrelation sidelobes in the context of spectral nulls. The desired templates are selected to be the ISL-optimal PSD template determined via (2.14) and the ad hoc tapered template determined via (2.2) and (2.3), where the latter was shown to be an effective (though suboptimal) solution. For this comparison, both templates have the same nulled region(s) defined by Λ, with the range-optimal template based on the constrained LS framework and the ad hoc template adhering to a notched Gaussian shape (same as [149]). After PRO-FM optimization, the nulls of either spectrum may not achieve an acceptable depth; therefore, subsequent application of the zero-order reconstruction of waveforms (ZOROW) algorithm [159] reinforces spectral notching while maintaining constant amplitude. The ZOROW algorithm operates on the phase values of the converged PRO-FM waveform, then minimizing spectral power in designated null Λ regions. See Section 2.5 for additional details.

Consider the case where $P = 1000$ waveforms are generated by sequentially applying the PRO-FM and ZOROW algorithms to adhere with the optimal PSD template and the ad hoc template from [149]. The PRO-FM and ZOROW algorithms were implemented for $K = 200$ and $Q = 1000$ iterations, respectively, to ensure full convergence. The number of waveform parameters $N_{\mathrm{p}} = 200$ is held constant. The spectrum template size is set to $M_{\mathrm{d}} = 4N_{\mathrm{p}} - 1$. Spectral nulls for both templates are placed at both band edges and at a single off-center location, with each null occupying a normalized spectral width of $0.1f_{\mathrm{s}}$ (so $0.3f_{\mathrm{s}}$ in total).

For the ad hoc spectral template, $\mathbf{d}_{\mathrm{f}}$ has a Gaussian shape with normalized 3-dB bandwidth $B = 0.5f_s$, which imposes low range sidelobes before spectral notches are inserted. The additional tapering of sharp nulls takes the form of a raised-cosine function spanning $f_{\mathrm{s}}/16$ at each null transition (one at each band edge and one either side of the off-center null, totaling four and spanning $0.25f_s$).

The resulting mean power spectrum and averaged autocorrelation responses over all 1000 waveforms for the ad-hoc case are shown in Figure 84. The optimum PSD template (with beamspoiling ratio of 2%) is included for reference. While the ad hoc spectral template is clearly different from the optimal template (top panel), it does provide a reasonable approximation, with the resulting mean waveform PSD yielding a good match to the heuristic design. The coherently averaged (CA) autocorrelation computed over the waveform set (bottom panel) demonstrates the expected incoherent sidelobe averaging reduction [41] due to the non-repeating nature of RFM waveforms. While approaching the optimum, the ad hoc autocorrelation response does experience some mainlobe broadening and “shoulder” lobes.

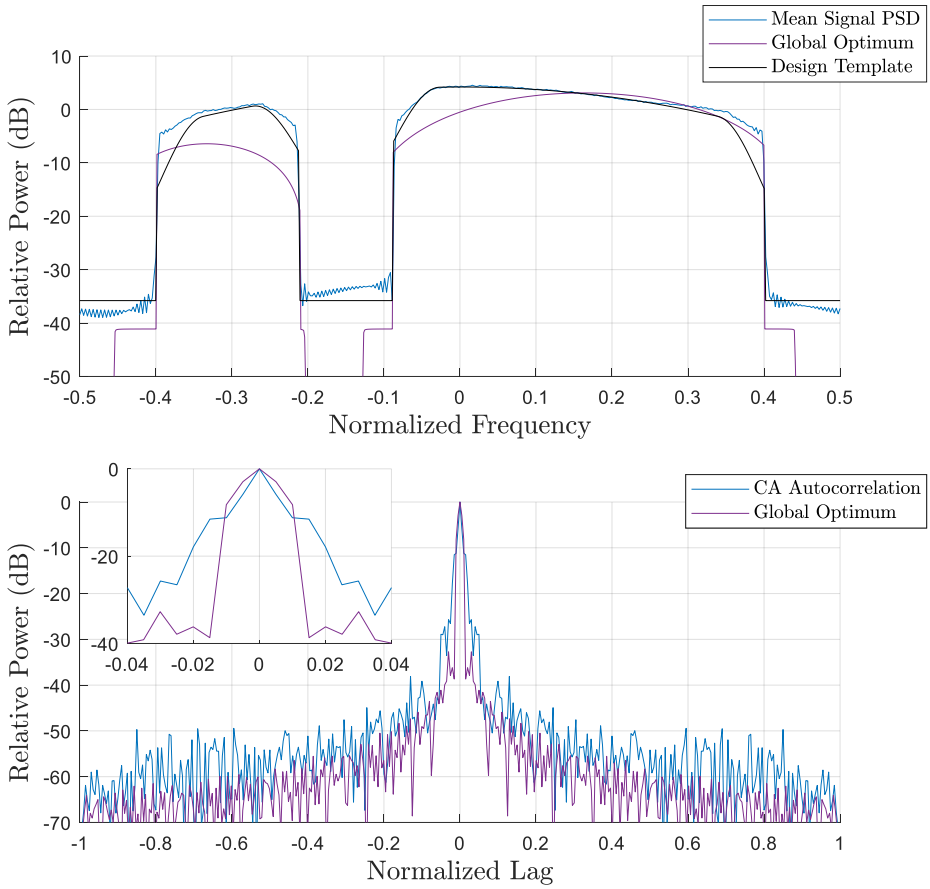

Figure 84: Notched PRO-FM mean PSD $\sum_{\forall p} \mathbf{r}_{\mathrm{f},p}$ and coherently averaged autocorrelation $\sum_{\forall p} \mathbf{r}_p$ from applying an ad-hoc tapered [149] spectral template determined via (2.2) and (2.3). The optimum template $\hat{\mathbf{d}}_{\mathrm{f}}$ determined according to (2.14) is included for comparison.

Now consider waveform design using the autocorrelation-optimal template as shown in Figure 85, which is based on the 2-norm version from (2.14). Clearly the mean PSD across the waveform set is closer to optimality than in the ad hoc case, and likewise for the ensuing CA autocorrelation. Of course, some deviation is also observed because perfect time-limited waveform spectrum shaping is not possible. Consequently, shoulder lobes are noticeably lower, yet are still present. However, the mainlobe broadening is essentially avoided. The sidelobe response is modestly lower than in the ad hoc case, though neither reach the optimal sidelobe roll-off.

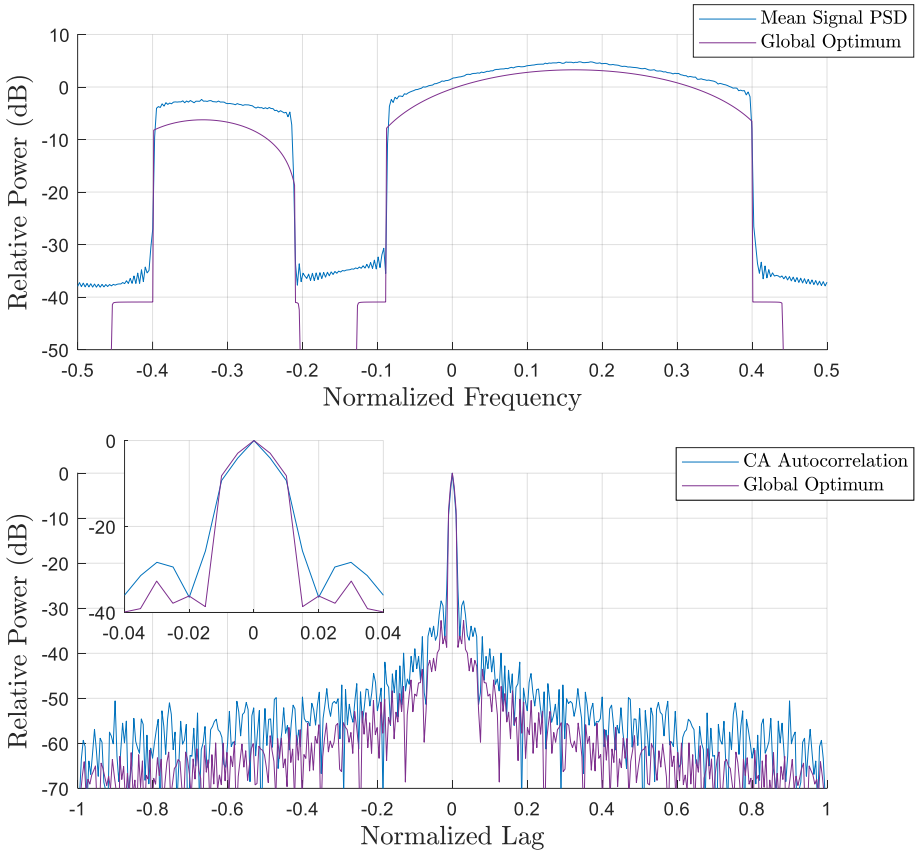

Figure 85: Notched PRO-FM mean PSD $\sum_{\forall p} \mathbf{r}_{\mathrm{f},p}$ and coherently averaged autocorrelation $\sum_{\forall p} \mathbf{r}_p$ from applying the least-squares optimal spectral template that minimizes autocorrelation ISL determined via (2.14). The optimum template $\hat{\mathbf{d}}_{\mathrm{f}}$ determined according to (2.14) is included for comparison.

Because the optimum spectral template is based on LS in a 2-norm sense, it is logical to apply the LS mismatched filter (LS-MMF) to these same waveform sets. Here the desired correlation response in the LS-MMF formulation is the IDFT of the globally optimum desired spectrum $\hat{\mathbf{d}} = \overline{\mathbf{A}}^H \hat{\mathbf{d}}_{\mathrm{f}}$. The optimal power spectrum $\hat{\mathbf{d}}_{\mathrm{f}}$ has length $M_{\mathrm{d}} = 4N_{\mathrm{p}} - 1$ and the LS-MMF has length $N_{\mathrm{w}} = 3N_{\mathrm{p}}$, such that $M_{\mathrm{d}} = N_{\mathrm{p}} + N_{\mathrm{w}} - 1$. The diagonal loading term Δ is set to 1% of the maximum eigenvalue of $\mathbf{S}^H\mathbf{S}$ to bias the LS-MMF towards the matched filter, reducing spectral notch degradation [160].

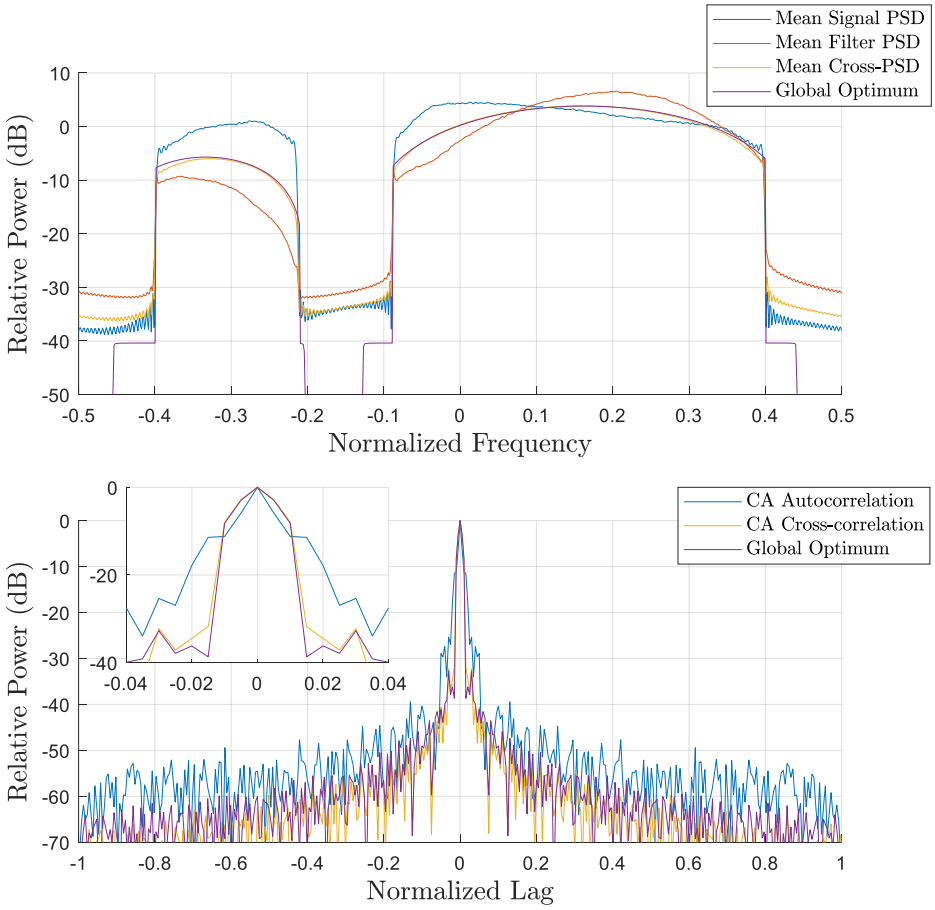

Figure 86: Notched PRO-FM mean PSD $\sum_{\forall p} \mathbf{r}_{\mathrm{f},p}$ and coherently averaged autocorrelation $\sum_{\forall p} \mathbf{r}_p$ from applying an ad-hoc tapered [149] spectral template determined via (2.2) and (2.3). The coherently averaged LS-MMF cross-correlations $\sum_{\forall p} \mathbf{c}_p$ are shown along with their mean cross-power spectrum $\sum_{\forall p} \mathbf{c}_{\mathrm{f},p}$. The optimum template $\hat{\mathbf{d}}_{\mathrm{f}}$ is included for comparison. The mean signal and filter PSDs are complementary, forming the desired cross-PSD.

For the ad hoc case, Figure 86 depicts the mean signal and filter PSDs, their mean cross-PSD, and the optimum PSD template. The LS-MMF elicits an average mismatch loss of 2.59 dB, but the signal/filter combination also almost perfectly overlaps with the optimal response. Consequently, the sidelobes likewise reach nearly to the optimum level. The LS-MMF also mitigates the notch degradation observed in [160]. Figure 87 then shows the optimal template case, where we see the filter and cross-PSDs now align well with the optimal PSD and the mismatch loss is now 1.37 dB, a 1.22 dB improvement over the ad hoc case. Of course, mismatch loss for both could be reduced by increasing the diagonal loading Δ, though doing so will increase deviation from the optimal sidelobe level.

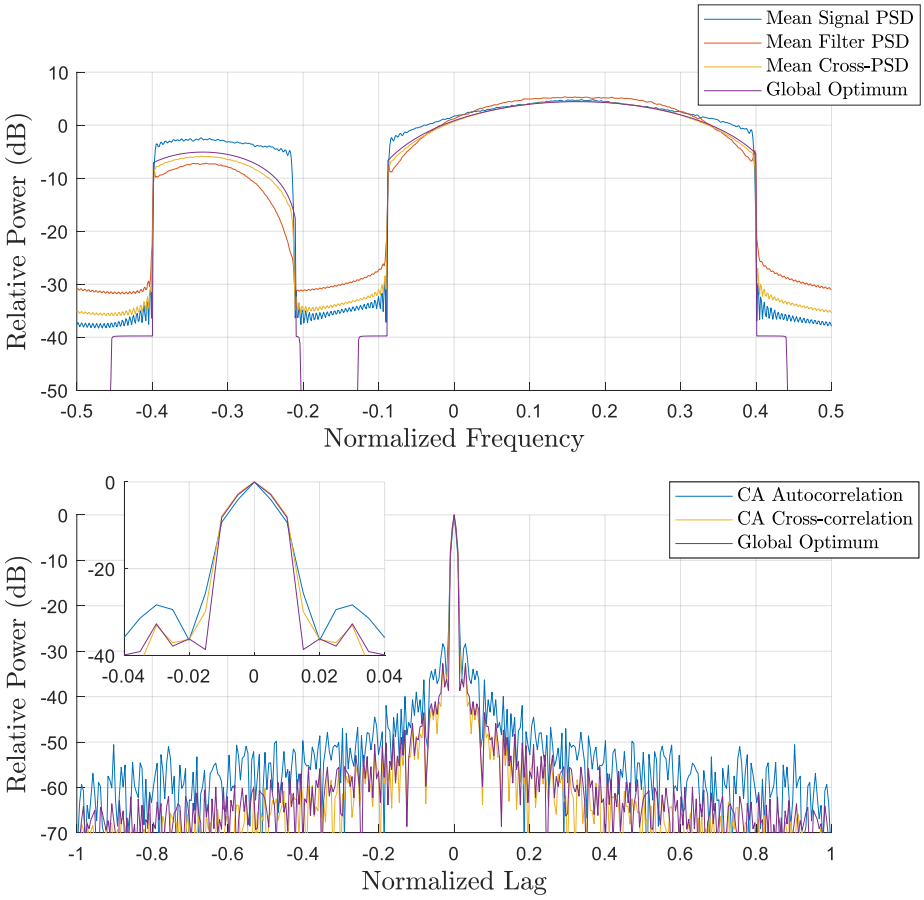

Figure 87: Notched PRO-FM mean PSD $\sum_{\forall p} \mathbf{r}_{\mathrm{f},p}$ and coherently averaged autocorrelation $\sum_{\forall p} \mathbf{r}_p$ from applying the LS optimal spectral template determined via (2.14). The coherently averaged LS-MMF cross-correlations $\sum_{\forall p} \mathbf{c}_p$ are shown along with their mean cross-power spectrum $\sum_{\forall p} \mathbf{c}_{\mathrm{f},p}$. The optimum template $\hat{\mathbf{d}}_{\mathrm{f}}$ is included for comparison. The mean signal and filter PSDs are near the global optimum, with the cross-PSD in close agreeance.

2.4.4. CONCLUSIONS

The globally optimum power spectrum for correlation sidelobe reduction and for range-Doppler sidelobe reduction is determined when portions of the spectrum are null constrained. By designing waveforms so that their spectrum closely matches the optimum, their attendant sidelobes likewise approach the optimum level. Application of the least-squares mismatched filter then closes much of the remaining sidelobe difference with mismatch loss in trade. Importantly, it is found that a previous ad hoc approach involving simple tapering of notch edges achieves near-optimal performance with a computational cost that is low enough for real-time implementation.

2.5. REAL TIME IMPLEMENTATION OF SENSE-AND-NOTCH RADAR (EARLY DEVELOPMENT)

With the reality of increasing radio frequency (RF) spectral congestion, radar systems capable of dynamic spectrum sharing are needed. Recent work has demonstrated a real-time cognitive capability on a software defined radio (SDR) by generating pulse-agile LFM chirps that vary their center frequency and bandwidth to avoid dynamic interference on a per-pulse basis. Separately, spectral notching of random FM waveforms was developed and experimentally evaluated as another means with which to mitigate emulated interference, though real-time operation had not yet been demonstrated.

Here the operational framework of the former is combined with the waveform agility of the latter to facilitate real-time generation of notched, random FM waveforms as part of an integrated cognitive SDR architecture. The early development of the sense-and-notch radar supported pulse repetition frequencies up to 2.2 kHz for on-the-fly waveform synthesis, could incorporate multiple spectral notches per waveform, and achieve notch depths of 25 dB relative to peak power (with greater depth possible given greater computational resources). Performance examples are illustrated along with implementation decisions and design trade-offs [169].

Cognitive radar, also known as fully adaptive radar, is generally understood to refer to systems that in some sense learn and subsequently respond to attributes of their operational environment [11, 170]. Due to increasing spectral congestion and competition [1], an important topic of research is the use of cognition in a spectrum sharing context [171] to modify the radar's physical emission structure according to sensed RF interference (RFI) in the band of interest. Essentially, these efforts are working to develop "good spectral neighbor" capabilities for the radar by mitigating the mutual interference to/from other spectrum users.

A separate, yet related, research direction has focused on the radar utilization of emerging software-defined radio (SDR) platforms (e.g. [172, 173]) due to their cost-effectiveness, scalability, and the prospect of rapid prototyping. Specifically, a growing body of work is devoted to the application of SDRs to realize real-time cognitive radar capabilities (e.g. [140, 174-176]). For example, it was recently shown that by utilizing a rapid band-aggregation method [154] to monitor RFI and select appropriate usable subbands, subsequent LFM waveforms could be generated via direct digital synthesis (DDS) on an Ettus x310 SDR to avoid interferers in real-time [140].

The purpose of this paper is to demonstrate how another cognitive radar capability for spectrum sharing can likewise be deployed for real-time mutual interference mitigation. Where the approach in [140] involves a sense-and-avoid (SAA) strategy, this other approach [152] employs a sense-and-notch (SAN) strategy that leverages spectrally-shaped, random FM waveforms to place in-band spectral notches on a per-waveform basis in response to dynamic RFI. Based on emulated (i.e. not real-time) RFI it was previously experimentally shown using test equipment that spectral notches having better than 50 dB in depth (relative to the peak spectrum power) can be achieved for these physically realizable waveforms [152].

It was noted in [174] that a key enabler to realizing spectral notching that is responsive on a per-pulse timescale is implementation of waveform generation on the field-programmable gate array (FPGA) of the SDR. When in-band RFI is dynamically changing during the radar's coherent processing interval (CPI), these SAA or SAN capabilities must likewise perform at the rate of the pulse repetition frequency (PRF). Consequently, here the SAN method [151-154], which also leverages aspects of the SAA deployment from [140], is implemented on the FPGA of an Ettus x310 SDR and demonstrated for real-time operation.

In [152] it was experimentally demonstrated, albeit not yet at real-time, that random FM waveforms possessing deep spectral notches could be physically realized according to the available in-band spectrum determined using the fast spectrum sensing (FSS) method of [153]. It has been observed that changing the radar emission structure during the CPI in response to dynamic RFI does introduce a significant clutter modulation effect [152]. That said, a variety of recent receive processing methods have been developed and experimentally demonstrated to compensate for this effect with varying efficacy [160, 161, 177, 178].

2.5.1. COGNITIVE SPECTRAL NOTCHING ON SOFTWARE-DEFINED RADAR

Implementation of the SAN capability on an SDR platform is accomplished by sequentially applying two random FM waveform generation methods. First, the PRO-FM approach is employed to produce a transmitter-suitable waveform that possesses a desirable overall power spectrum shape (Gaussian is useful for this purpose) and containing spectral notches based on the RFI determination from FSS. However, because PRO-FM generally cannot achieve very significant notch depths by itself (20 dB at best), further notch suppression is required. In [152] it was shown that the reiterative uniform weighted optimization (RUWO) method [156] could accomplish this task, though the attendant computation cost is rather high. Then in [158] the analytical spectrum notching (ASpeN) approach was developed and experimentally demonstrated using a high-fidelity arbitrary waveform generator (AWG) to achieve notch depths better than 50 dB. Most recently, ASpeN has been modified for use on the more modest digital-to-analog conversion (DAC) rates, and thus lower fidelity, available in SDRs. The resulting zero-order reconstruction optimization of waveforms (ZOROW) method [159] accounts for much, though not all, of the distortion arising from this lower fidelity, which is particularly important when attempting to form spectral notches.

The notched waveform generation approach implemented on the SDR's FPGA is summarized as follows. Recall the pseudo-random optimized FM (PRO-FM) algorithm, which produces spectrally shaped angle modulated radar waveform. The p^{th} of P PRO-FM waveforms is initialized with phase chips drawn from the uniform distribution $\phi_n \in [-\pi, \pi]$ to form the signal $\mathbf{s}_{0,p}$. The PRO-FM algorithm performs the k^{th} of K alternating iterations

$$\dot{\mathbf{s}}_p^{(k+1)} = \widetilde{\mathbf{A}}^H\left\{\mathbf{d}_\mathrm{f}^{1/2} \odot \exp\left(j\angle\widetilde{\mathbf{A}}\mathbf{s}_p^{(k)}\right)\right\}$$
$$\mathbf{s}_p^{(k+1)} = \mathbf{u} \odot \exp\left(j\angle\dot{\mathbf{s}}_p^{(k+1)}\right) \tag{2.19}$$

where $\widetilde{\mathbf{A}}$ is the $M \times N$ truncated DFT matrix with $M \geq 2N-1$, $\widetilde{\mathbf{A}}^H$ is the $N \times M$ truncated IDFT matrix, $\mathbf{d}_\mathrm{f}$ is the $M \times 1$ desired PSD, $\mathbf{u}$ is the $N \times 1$ desired amplitude envelope, and $\angle(\cdot)$ extracts the argument phase. Spectral nulls may be incorporated into the desired PSD $\mathbf{d}_\mathrm{f}$ over the set of frequency indices to null Λ by enforcing

$$d_{\mathrm{f},m} = 0 \quad \text{for } m \in \Lambda\,.$$

(2.20)

The desired PSD $\mathbf{d}_{\mathrm{f}}$ is not otherwise reshaped, due to considerations of increasing computational cost for real-time implementation. Imposing the null constraint in (2.20) via the alternating projections of (2.19) can produce spectral notches with depths up to 20 dB. Moreover, this process can require hundreds of iterations that would generally preclude real-time operation. Therefore, in this implementation notched PRO-FM via (2.19) and (2.20) is used to roughly shape the entire waveform spectrum, including the formation of shallow notches, and then ZOROW [159] is applied to complete the notching process. It has been found that at least initiating notch formation with PRO-FM facilitates faster convergence for subsequent ZOROW application, which is likewise iterative.

The ZOROW formulation operates on the version of the discretized waveform at the $k = K$ terminal PRO-FM iteration, which we shall denote as

$$\mathbf{s}_p = e^{j\boldsymbol{\phi}_p}$$

$$\boldsymbol{\phi}_p = \begin{bmatrix} \phi_{1,p} & \phi_{2,p} & \cdots & \phi_{N_{\mathrm{p}},p} \end{bmatrix}^T$$

(2.21)

This signal representation conforms to the zero-order hold model employed by the SDR DAC, in which the DAC input sample is held constant for T_{s} seconds. The resulting analog signal is then fed through a reconstruction filter to suppress the repeated images outside the fundamental frequency interval of $[-f_{\mathrm{s}}/2\,, +f_{\mathrm{s}}/2]$. It was shown in [158] that perfect Nyquist reconstruction can be realized for a pulsed (i.e. time-limited) signal given sufficient sampling of the analytical spectrum. For the ZOROW waveform representation [159], this sampled analytical spectrum has the form

$$S_p\big(f_m, \boldsymbol{\phi}_p\big) = \frac{\sin(\pi f_m T_s)}{\pi f_m} \sum_{n=1}^{N} \exp\Big(-j\big(2\pi f_m (n - .5) T_s + \phi_{n,p}\big)\Big)$$

(2.22)

where $f_m = m\Delta f$ for integer m on the interval $-\infty < m < \infty$ as long as $\Delta f \leq 1/(2T)$. Noting that (2.22) takes the form of a discrete Fourier transform (DFT) with an imposed $\mathrm{sinc}(\cdot)$ envelope, it can be calculated efficiently using a fast Fourier transform (FFT). The ZOROW formulation [159] then employs the cost function

$$J = \min_{\boldsymbol{\phi}} \sum_{m \in \Lambda} \left| S_p\left(f_m, \boldsymbol{\phi}_p\right) \right|^2$$

(2.23)

where the summation corresponds to the frequency interval(s) Λ for which notching is required. The gradient of (2.23) with respect to $\boldsymbol{\phi}_p$ is then determined for use in gradient-descent optimization as

$$\boldsymbol{\phi}_p^{(q+1)} = \boldsymbol{\phi}_p^{(q)} + \mu_q \tilde{\mathbf{g}}_p^{(q)}$$

(2.24)

where μ_q is the step-size based on a simple back-tracking technique [179] and

$$\tilde{\mathbf{g}}_p^{(q)} = \begin{cases} -\mathbf{g}_0 & \text{when } q = 0 \\ \mathbf{g}_p^{(q)} + \rho \tilde{\mathbf{g}}_p^{(q-1)} & \text{otherwise} \end{cases}$$

(2.25)

is the search direction at the q^{th} iteration. Here $0 < \rho < 1$ dictates the type of gradient-descent being used and it can be shown that (2.25) can be efficiently computed via

$$\mathbf{g}_p^{(q)} = 2\, Im\left\{ \tilde{\mathbf{A}}^H \left(\left(\tilde{\mathbf{A}} \mathbf{s}_p^{(q)} \right) \odot \mathbf{w}_{\mathrm{sinc}} \right) \odot \mathbf{s}_p^{*(q)} \right\}$$

(2.26)

Here $Im\{\cdot\}$ extracts the imaginary part of the argument, $\tilde{\mathbf{A}}^H$ is the $M \times N$ truncated inverse DFT matrix, $(\cdot)^*$ denotes complex conjugation, $\mathbf{s}_p^{(q)}$ is the discrete signal vector from (2.21) at the q^{th} iteration of ZOROW, and $\mathbf{w}_{\mathrm{sinc}}$ is the length M vector representing the $\mathrm{sinc}(\cdot)$ envelope in (2.22) with the unnotched portions replaced by zeros. With the gradient expressed in this manner it can be efficiently computed using FFTs [13, 180].

The gradient-descent implementation in [158, 159] relies on a "heavy ball" framework [181] with a backtracking technique [179] to select the step-size. However, backtracking involves determination of cost function values that can be inefficient to compute on an FPGA. That said, it has been observed for this formulation that the use of standard steepest descent ($\rho = 0$) combined with backtracking via a simple line-search method tends to converge quickly to a constant step-size value. Thus μ_q is set to 1 for this FPGA implementation, which has been found to be less than the smallest optimized step-size obtained by backtracking.

As an example, Figure 88 illustrates the mean power spectra of $Q = 1000$ random FM waveforms containing a central spectral notch location spanning 10% of the band. These waveforms were generated using only $K = 2$ PRO-FM iterations and either $Q = 6$ or 1000 ZOROW iterations. Significant notch depth can clearly be achieved via $Q = 1000$ iterations, though the $Q = 6$ case is applied for FPGA implementation. Figure 89 compares this particular implementation in terms of convergence over 1000 iterations to other gradient-descent approaches [182] when a spectral notch is placed in the center of the spectrum. While the heavy ball scheme (yellow trace) is the best overall after 1000 iterations, this simple approach involving straightforward steepest descent (SD) without backtracking yields the best performance after the first 100 iterations. Since real-time operation limits the number of feasible iterations, this streamlined approach is clearly an attractive solution.

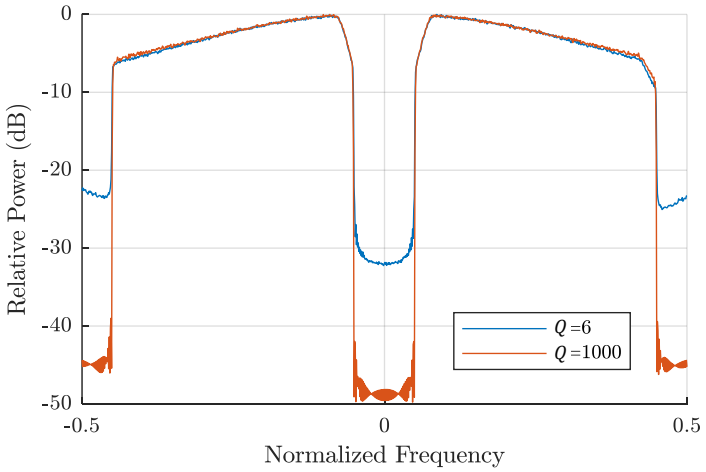

Figure 88: Mean power spectra of PRO-FM / ZOROW waveform sets for a central notch location spanning 10% of the band after $K = 2$ PRO-FM iterations and $Q = 6$ and 1000 ZOROW iterations. Per [159], notches are also placed at the band edges to facilitate spectral containment prior to DAC reconstruction.

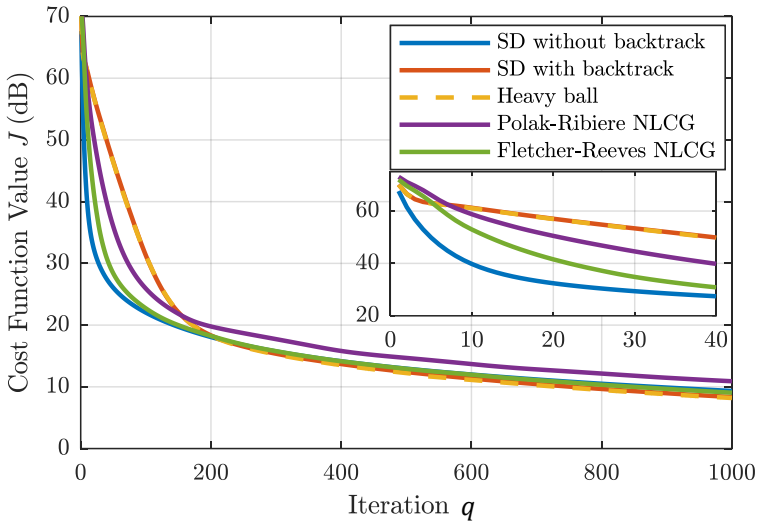

Figure 89: Comparison of cost-function (2.23) minimization for various gradient-descent methods

2.5.2. IMPLEMENTATION CONSIDERATIONS

A block diagram of the SDR cognitive radar architecture during early development is shown in Figure 90. The RF environment is sensed at the receive port of the SDR, where the signal is frequency down-converted and quantized into in-phase & quadrature channels at 100 MSamples/s, processed by a high throughput FFT performed on the FPGA, and then continuously streamed to the host computer. Here FSS [154] is performed on the host computer to identify the spectral locations of RFI within the 100 MHz band during the radar listening periods. The identified RFI spectral locations are returned to the SDR, where the PRO-FM / ZOROW notched waveform generation process is performed.

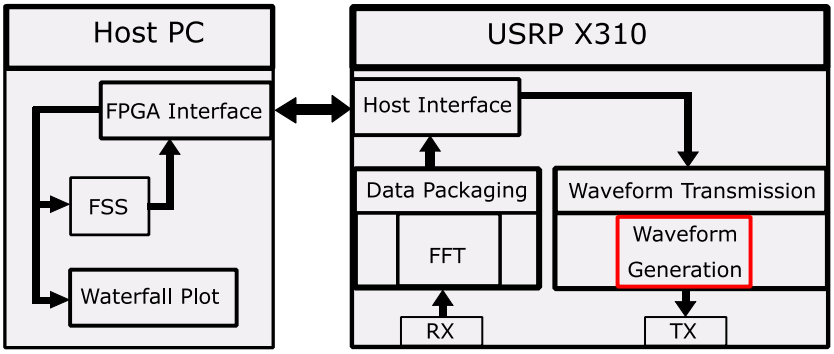

Figure 90: Cognitive radar architecture on the SDR during early development. See [140] for further details.

The maximum time T_{PRI} required to generate each waveform establishes the minimum feasible pulse repetition interval (PRI) and thus the maximum PRF for cognitive operation. However, a latency also exists between the observance of changes in the RFI and when FSS responds with the appropriate notch locations, which currently establishes the minimum adaptation interval T_{adapt}. Consequently, while a new waveform is generated on a per-PRI basis, the notch locations for each waveform are currently updated by FSS at a rate of once every $\mathcal{R}$ PRIs (depending on the PRF employed). Figure 91 exemplifies a timing diagram of the SDR operation where the RFI changes every 4 PRIs, but the radar adaptation latency is $\mathcal{R} = 3$ PRIs.

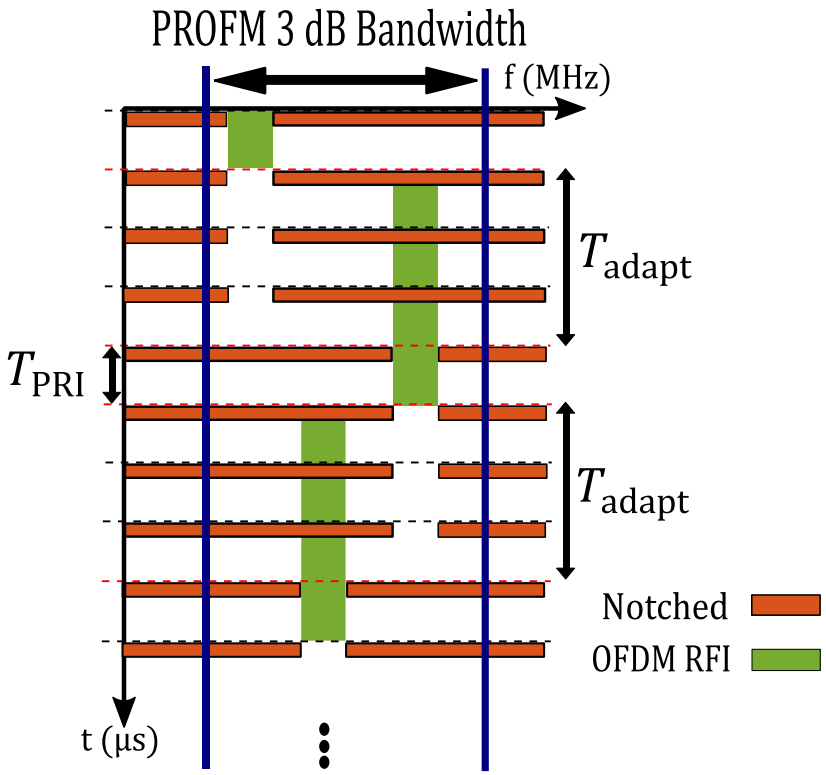

Figure 91: Timing diagram of SAN cognitive radar adjusting a spectral notch location to coincide with dynamic RFI, where $T_{\mathrm{adapt}} = 3T_{\mathrm{PRI}}$ for this example.

The FPGA code architecture was developed such that board resources are conservatively utilized, timing constraints imposed by the PRI ($< 1\text{ms}$ desired) are met, and notch depths in the waveform are maximized under these conditions. As such, $K = 2$ iterations of PRO-FM was deemed sufficient to impose a preliminary spectral shape followed by $Q = 6$ iterations of ZOROW, thereby realizing ~25 dB of notch depth relative to peak power. As illustrated in Figure 88, greater notch depth could be achieved on the SDR, though doing so would alter the response time trade-space. With this parameterization, the SDR supports cognitive spectral notching at a PRF up to 2.2 kHz, a minimum adaptation interval of $T_{\text{adapt}} = 3\text{ms}$, and can incorporate multiple spectral notches per waveform. Thus, the adaptation rate $\mathcal{R}$ is 7 PRIs at the highest PRF supported during early development. All FPGA processing, including the implementations of PRO-FM and ZOROW for notched waveform generation, is performed using FFTs, inverse FFTs, multiplies, and additions in a burst streaming format compatible with a commercial off-the-shelf (COTS) SDR. The final FPGA resource utilization was at ~30%, thereby providing the possibility for additional upgrades.

2.5.3. EVALUATION OF REAL-TIME OPERATION

To characterize the behavior of the real-time cognitive SAN architecture on the SDR, various RFI patterns were generated and resulting performance assessed. The SDR operates at a center frequency of 2 GHz and measures complex baseband data after receive analog down-conversion based on a 100 MHz sample clock. The SAN implementation has an adaptation interval of $\mathcal{R} = 7$ PRIs, a pulse duration of $T_{\text{p}} = 2.56\mu\text{s}$, and PRI duration of $T_{\text{PRI}} = 450.6\mu\text{s}$. The RFI test cases include

- Case 1: Three swept-frequency tones with 15 ms or 5 ms dwell times
- Case 2: Three independent 5 MHz bands of OFDM subcarriers randomly hopping with dwell times of 15 ms
- Case 3: One contiguous 40 MHz band of OFDM subcarriers randomly hopping with a dwell time of 15 ms

An independent arbitrary waveform generator (AWG) is used to generate the RFI scenarios that are combined with the radar transmissions in closed loop for subsequent cognitive radar performance testing.

Figure 92 shows a spectral capture of three independent frequency tones (Case 1) as well as a corresponding notched random FM waveform generated by the SDR. Figure 93 shows a waterfall spectrogram (frequency content versus time) when the RFI dwell time is 15 ms. With a response time of $T_{\text{adapt}} = 3\text{ms}$ the SAN cognitive radar is able to respond relatively quickly and form multiple notches that coincide with the sensed RFI.

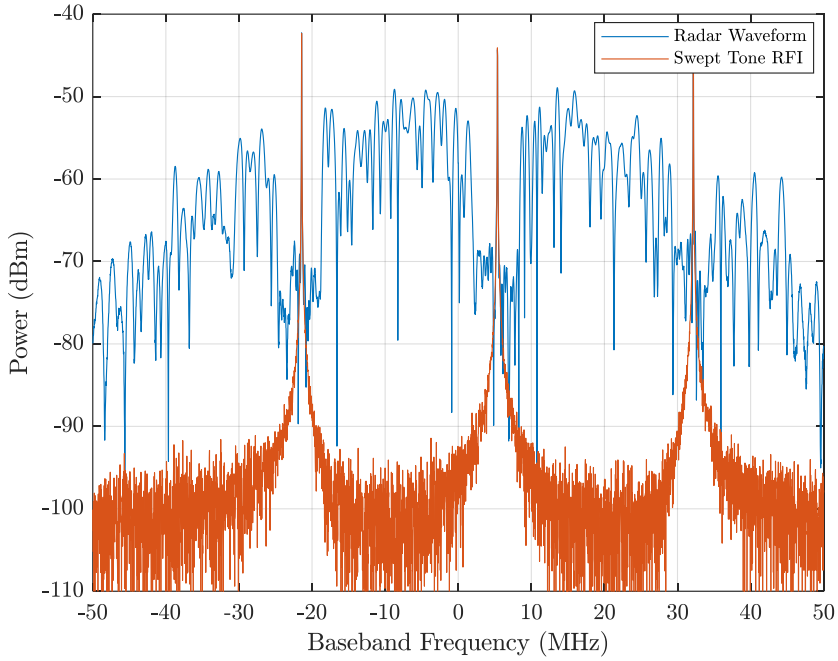

Figure 92: (Case 1) Spectrum capture showing three tonal interferers (red) and the SAN radar spectrum (blue) with collocated notches.

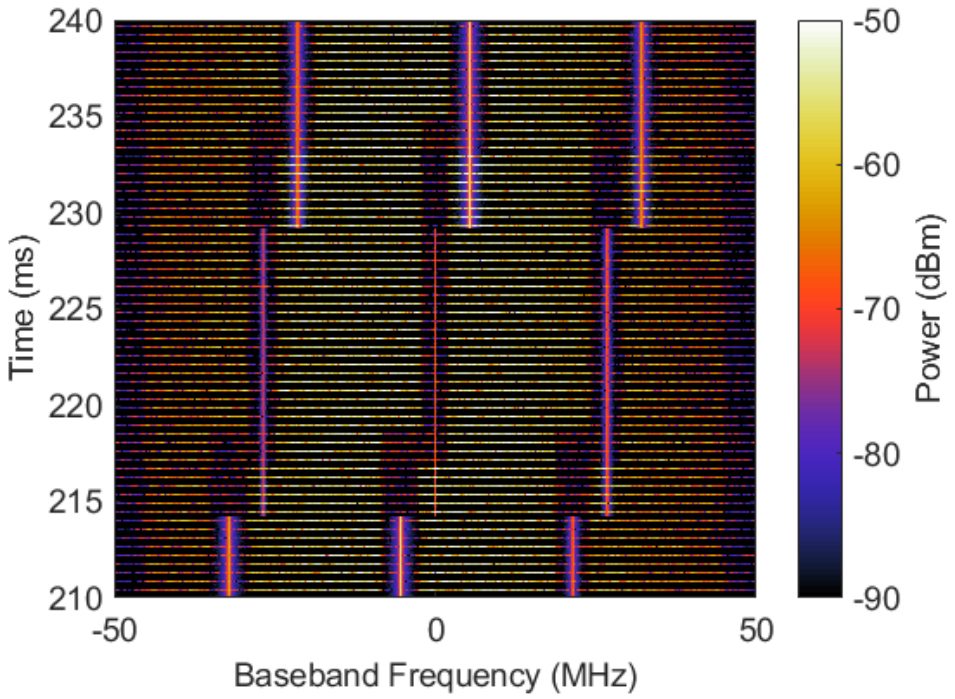

Figure 93: (Case 1a) Waterfall spectrogram versus time for RFI comprised of three stepped tones (vertical pink bars) and the SAN radar spectrum (horizontal yellow lines) with notches. The RFI changes every 15 ms.

For the same case, when the dwell time of the three swept tones is commensurate with the adaptation speed of this SAN implementation, notching alignment accuracy is observed to degrade rather significantly, as in Figure 94. For this reason, ongoing work investigated how adaptation latency can be further reduced. For environments in which the RFI exhibits observable patterns, prediction was explored as means to anticipate where notching is likely to be required so that corresponding waveform generation can be initiated earlier [183]. The concept of meta-cognition has been investigated to examine when operational cognitive schemes may function optimally [184-186].

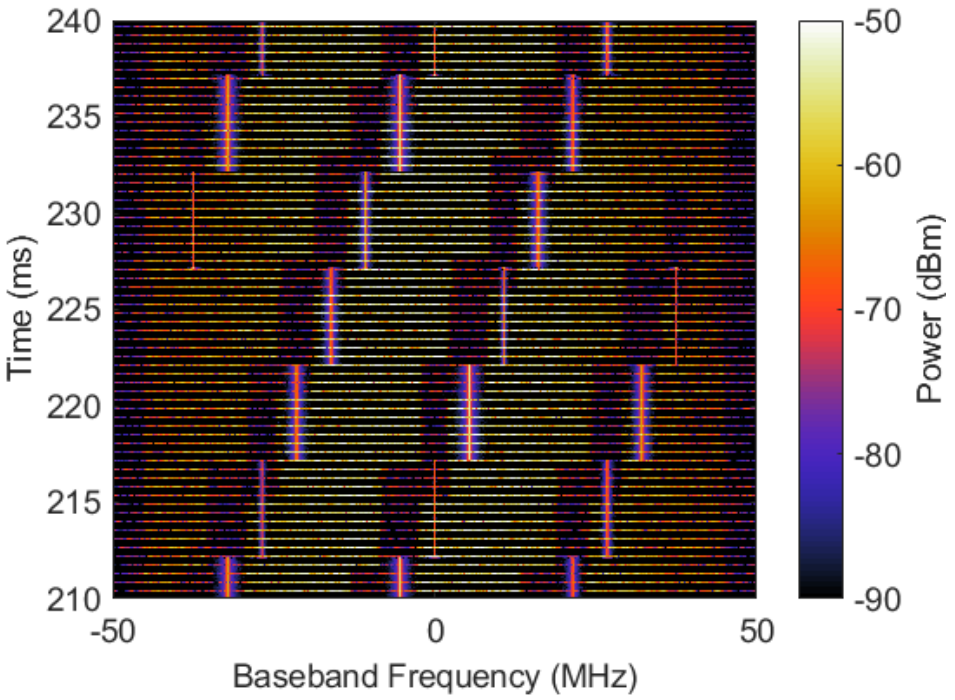

Figure 94: (Case 1b) Waterfall spectrogram versus PRI time for RFI comprised of three stepped tones (vertical pink bars) and the SAN radar spectrum (horizontal yellow lines) with notches. The RFI changes every 5 ms.

Figure 95 shows a scenario in which the RFI consists of three 5 MHz bands comprised of OFDM subcarriers (Case 2) that change spectral locations randomly every 15 ms. The same 7-PRI latency is again observed, with the notch widths and locations adjusting according to the observed RFI. For randomly changing RFI, presuming no discernible pattern is available, this manner of reactive mode is more appropriate than a predictive mode like [183]. Moreover, while the persistent RFI around −33 MHz is a random occurrence in these results, such an outcome could occur more frequently in practice if the RFI is likewise employing some form of dynamic spectrum access. Specifically, the two systems could potentially achieve a steady-state condition in which it is more beneficial from a mutual signal-to-interference-plus-noise (SINR) perspective for both the radar and the other user to maintain the same spectral disposition. Of course, this manner of "locked in" behavior may not require spectral maneuver freedom.

Finally, Figure 96 shows the cognitive SAN radar adapting to a single 40 MHz band of OFDM subcarriers (Case 3) that changes spectral locations randomly every 15 ms. The 7-PRI adaptation latency is once again observed. However, this result highlights the fact that, while transmit spectral notching generally permits more overall bandwidth to be preserved and is more robust to clutter modulation relative to a sense-and-avoid (SAA) mode [140, 152], the SAA may still be preferred in some instances. Specifically, the time interval from 210 to 223 ms in Figure 96 illustrates that SAN provides access to both sides of the remaining bandwidth. However, when significant RFI content is present in an off-center portion of the available band (223 to 240 ms and beyond in Figure 96) the SAA approach would realize essentially the same spectral content as SAN at a lower computational cost, which would translate into lower response latency.

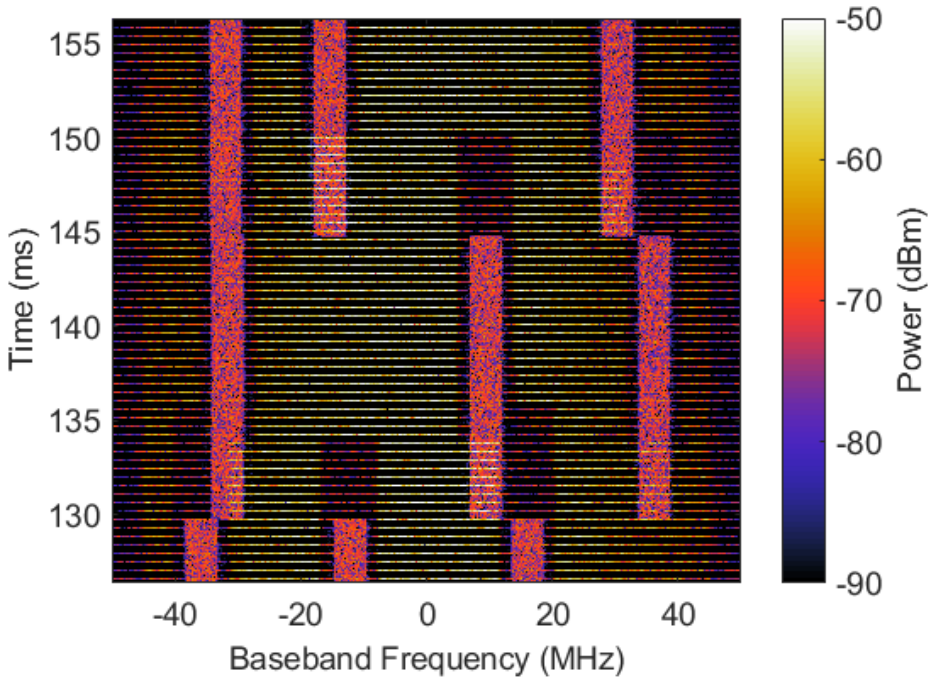

Figure 95: (Case 2) Waterfall spectrogram versus PRI time for RFI comprised of three 5 MHz bands of OFDM subcarriers (vertical pink bars) and the SAN radar spectrum (horizontal yellow lines) with notches. The RFI changes every 15 ms.

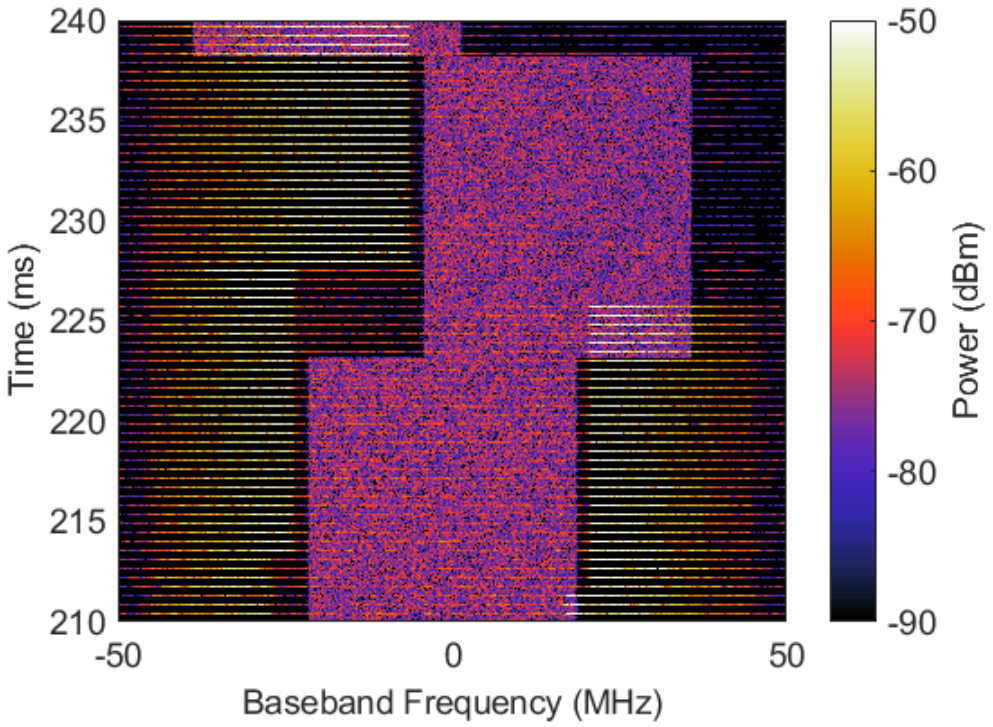

Figure 96: (Case 3) Waterfall spectrogram versus PRI time for RFI comprised of one 40 MHz band of OFDM subcarriers (vertical pink bar) and the SAN radar spectrum (horizontal yellow lines) with notches. The RFI changes every 15 ms.

2.5.4. CONCLUSIONS

A sense-and-notch (SAN) cognitive radar approach involving the use of spectrally notched, random FM waveforms has been implemented and demonstrated for real-time operation on a COTS SDR. The waveform generation process only requires simple FPGA resource blocks including FFTs, multiplications, and additions. The early development SDR architecture supported PRFs up to 2.2 kHz, can incorporate multiple spectral notches per waveform, and achieves notch depths of 25 dB relative to peak power. This capability for operational radar modes such as moving target indication (MTI) in the presence of dynamic RFI is evaluated next. To improve the adaptation latency, the FSS algorithms is offloaded from the host computer to the FPGA.

2.6. REAL TIME IMPLEMENTATION OF SENSE-AND-NOTCH RADAR (LATE DEVELOPMENT)

Here we demonstrate the final cognitive evaluation step in which the sense-and-notch SDRadar operates in real-time in an open-air setting, performing moving target indication (MTI) processing (except for clutter cancellation) in the presence of a dynamically hopping interferer. This implementation is shown to support pulse repetition frequencies (PRFs) up to 4.4 kHz, meaning new interference-responsive waveforms can be produced at that rate, while achieving a transmit notch depth of 25 dB relative to peak power (greater depth is possible with additional computational resources).

This work represents the culmination of a multi-year effort to achieve a real-time sense-and-notch radar capability that can contend with highly dynamic spectrum users. It consequently involves the intersection of practical waveform design, a novel method for efficient spectral notch generation, RF systems engineering for physical deployment, field-programmable gate array (FPGA) implementation for real-time processing, and assessment of a performance vs. computation trade-space.

Specifically, the FPGA of an Ettus x310 SDR was used to implement this SDRadar capability, consisting of the fast spectrum sensing (FSS) [154] algorithm to quickly assess the portions of the band occupied by other users on a per-pulse basis, followed by incorporation of corresponding spectral notches within a nonrepeating RFM waveform and the subsequent open-air transmission. Aspects of this approach were previously assessed in [152] using open-air measurements, though notched waveform generation was not yet real-time, and in [169] at real-time speeds, though not yet in an open-air setting. Here these attributes are combined to realize full sense-and-notch functionality in real-time for an MTI application.

2.6.1. REDUCING THE ADAPTATION LATENCY

The stages within this sense-and-notch method are outlined in Table 7, which also includes the latency of each stage when implemented on the FPGA of the SDR. The first stage is clearly the spectrum sensing process, which uses the FSS algorithm from [154] that quickly identifies and aggregates a "good enough" partitioning of the operating band into appropriately sized subbands, which either do or do not contain a meaningful amount of RFI. The spectral locations and widths of the RFI-occupied subbands, collected in Λ, then inform where spectral notching is necessary.

Table 7: Sense-and-notch stages with latencies

Algorithm	**Latency**
Fast Spectral Sensing (FSS)	120 μs
Pseudo-Random Optimized FM (PRO-FM)	28 μs / iteration
Zero-Order Reconstruction Optimization of Waveforms (ZOROW)	28 μs / iteration

A block diagram of the SDRadar cognitive radar architecture is shown in Figure 97. The RF environment is sensed at the receive port of the SDRadar, where the signal is frequency down-converted and quantized into in-phase & quadrature channels at 100 MSamples/s, processed by a high-throughput FFT performed on the FPGA, and then continuously streamed to the host computer. Relative to [169], in which the latency of FSS on the host PC was $T_{\mathrm{FSS}} = 3.1\mathrm{ms}$ and therefore served as the bottleneck in RFI identification, it has now been integrated onto the FPGA to operate in 120 μs, a 25× reduction.

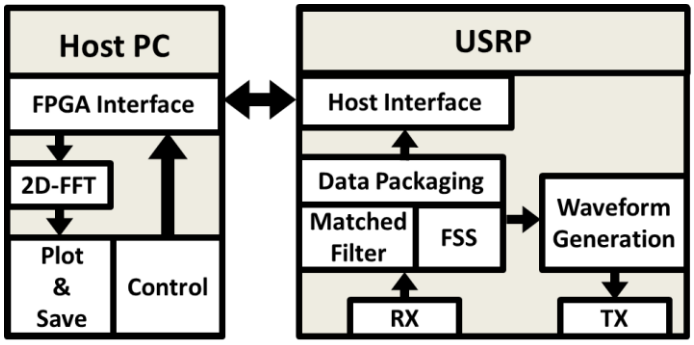

Figure 97: Cognitive radar architecture on the SDRadar

The overall adaptation time T_{adapt} dictates how quickly the overall implementation can identify available spectrum and synthesize waveforms in reaction to environmental changes. It can be expressed as

$$T_{\text{adapt}} = T_{\text{FSS}} + T_{\text{PRO}} + T_{\text{ZOROW}}$$
$$= 120 + 28K + 28L \ \mu\text{s} \tag{2.27}$$

where the lower line captures the currently achievable process times as implemented on the x310 FPGA, for K and Q the respective number of iterations for PRO-FM and ZOROW. Here $K = 2$ and $Q = 6$ iterations are used, still realizing 25dB spectral notches relative to peak power. Consequently, the adaptation delay is $T_{\text{adapt}} = 344\ \mu\text{s}$.

In [169], a PRF of 2.22 kHz ($T_{\text{PRI}} = 550.6\ \mu\text{s}$) was used. Software modification in the FPGA since then to operate the clock at twice the rate (from 100 to now 200 MHz), permits PRF values up to 4.4 kHz ($T_{\text{PRI}} = 225.3\mu\text{s}$). Therefore, while the implementation in [169] incurred a 7-pulse latency ($T_{\text{adapt}} = 3.1\text{ms}$) at the lower PRF, the new instantiation could either update with no latency at the 2.22 kHz PRF or with a 1-pulse latency at the 4.44 kHz PRF. Here the latter is examined, meaning that as the rate of RFI hopping increases there will be a growing number of pulses in which the RFI and notch locations are mismatched (i.e. “collisions”). The reason for choosing this arrangement is because, in reality, there would be a degree of randomness that would almost certainly lead to some percentage of pulses with collisions. If further latency is acceptable, based on an expectation of little/no RFI hopping, then deeper notches are also achievable via additional ZOROW iterations. Moreover, as SDR and RF-SoC technology progresses, these limits will become less restrictive.

2.6.2. REAL-TIME COGNITIVE SENSE-AND-NOTCH MOVING TARGET INDICATION

In [152] an open-air MTI test was performed based on prior observation and determination of notched waveforms, i.e. not reacting in real-time. Here the test is repeated using the SDRadar, along with the procedure outlined above, to generate new notched waveforms in real-time as the RFI moves around in frequency. As before, this open-air test took place on the roof of Nichols Hall on the University of Kansas campus, observing the intersection of 23rd and Iowa streets roughly 1.1 km away. Figure 98 provides a block diagram of test setup components, while Figure 99 and Figure 100 respectively show photos of the SDRadar (using separate transmit/receive antennas) and the location of the nearby RFI source.

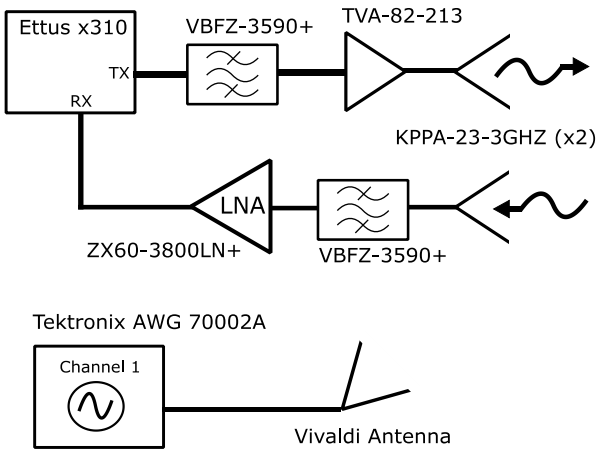

Figure 98: Test setup overview, with sense-and-notch radar (top) and dynamic interferer (bottom)

Figure 99: Open-air test setup: Ettus x310 SDRadar (white oval) and illuminated traffic intersection (green oval)

Figure 100: Open-air test setup: interference source (red oval)

The SDRadar operates at 3.5 GHz and measures complex baseband data after receive down-conversion based on a 100 MHz sample clock. The pulse duration is $T_{\mathrm{p}} = 2.56\mu\mathrm{s}$, which corresponds to a duty cycle of about 1.2 percent at the 4.44 kHz PRF. Each CPI comprises $P = 1000$ unique pulsed waveforms. The RFI source is produced by a Tektronix AWG connected to a quad-ridge horn antenna, which transmits a single contiguous signal comprised of OFDM subcarriers having a 10 MHz bandwidth that randomly hops in frequency over the operating band at time intervals of T_{RFI} , which corresponds to a hopping rate of $f_{\mathrm{RFI}} = 1/T_{\mathrm{RFI}}$. In addition to a stationary RFI case, interference dwell times of $T_{\mathrm{RFI}} = 50\ \mathrm{ms}, 10\ \mathrm{ms}$ and $0.6\ \mathrm{ms}$ are considered, which correspond to $f_{\mathrm{RFI}} = 20\ \mathrm{Hz}, 100\ \mathrm{Hz}$ and $1.66\ \mathrm{kHz}$. A full-band RFM waveform case with no interference present is included for comparison. For $T_{\mathrm{PRI}} = 225.3\mu\mathrm{s}$, these cases amount to hopping of roughly 5, 23, and 375 times during the CPI (the RFI and SDRadar are not synchronized so the precise number could vary). While only a single hopping RFI source is considered here, no change is needed to realize an arbitrary number of RFI sources/notches. Of course, further degradation is expected due to less available bandwidth for the radar to operate. Moreover, because the focus here is to demonstrate real-time notched waveform design/generation, clutter cancellation has not yet been incorporated.

To establish a baseline case, Figure 101 illustrates the range/ Doppler response for a CPI of full-band PRO-FM waveforms when no interference is present. Movers are clearly detectable against the background. However, once the RFI is turned on (Figure 102), the movers are no longer visible. When sense-and-notch operation is engaged for this stationary RFI case, movers once again become visible (Figure 103). While arguably not necessary in this case, each notched waveform in the CPI is produced according to real-time sensing of RFI on a per-pulse basis. Comparison of the background responses in Figure 101 and Figure 103 shows an increase of a few dB for the latter, which is due to notch depth being limited to 25 dB here as a trade-off for real-time responsiveness.

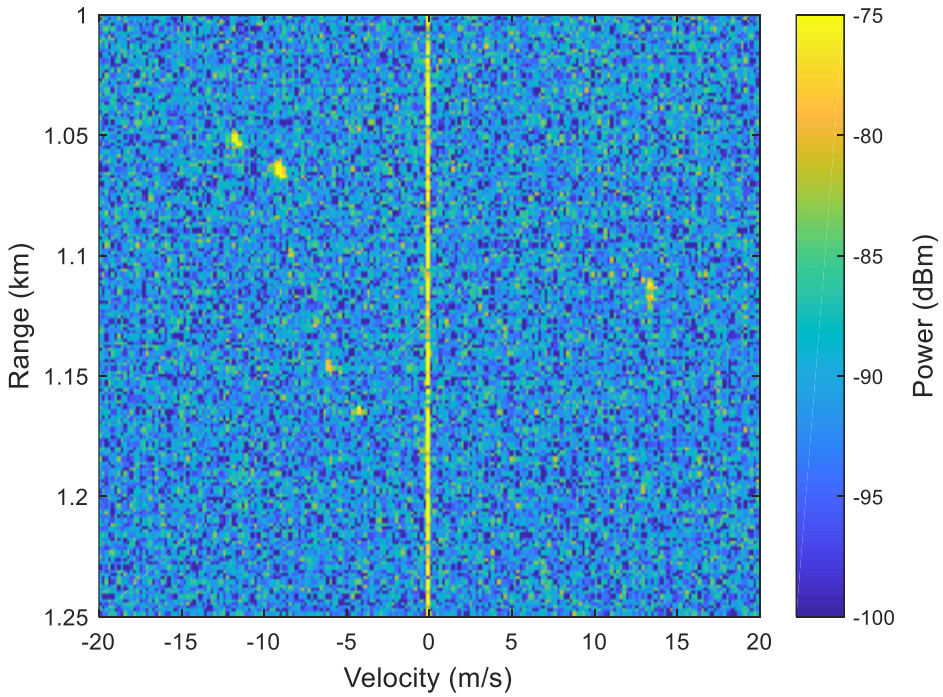

Figure 101: Range-Doppler plot of full-band PRO-FM without RFI, intended as the baseline comparison. All radar operations are performed in real-time via the SDRadar.

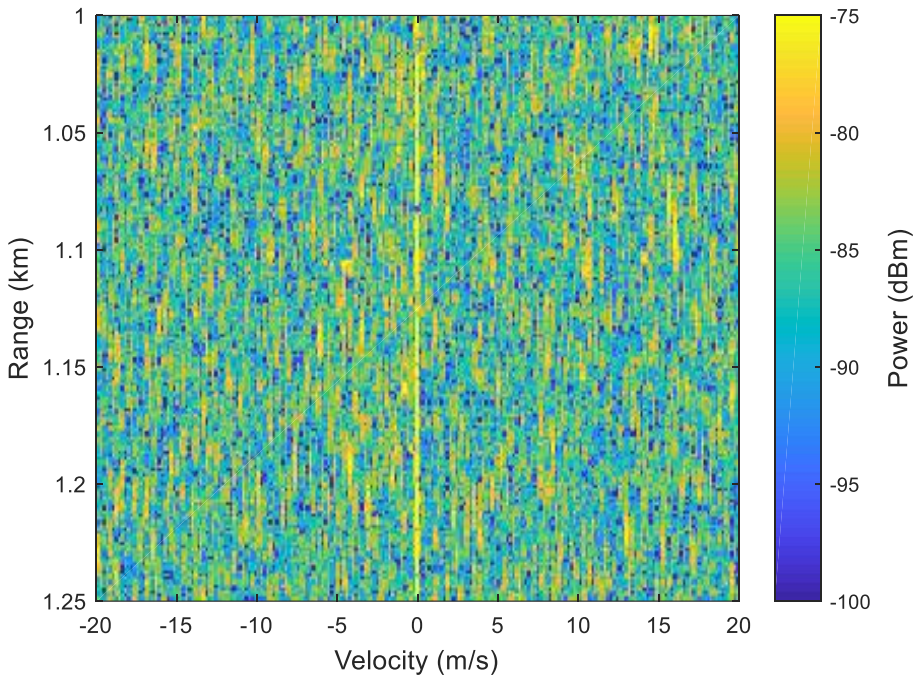

Figure 102: Range-Doppler plot of full-band PRO-FM with stationary RFI, intended as the baseline comparison. All radar operations are performed in real-time via the SDRadar.

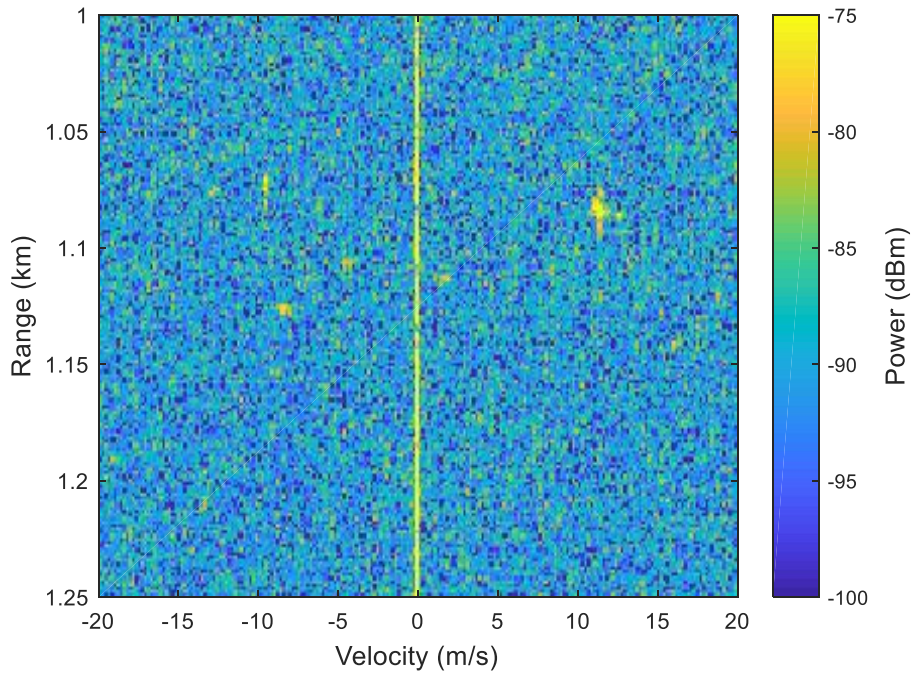

Figure 103: Range-Doppler plot for sense-and-notch PRO-FM with stationary RFI. All radar operations are performed in real-time via the SDRadar.

The RFI is now allowed to change dynamically at different rates, as illustrated in Figure 104 through Figure 106. It is observed that hopping every 50 ms in Figure 104 is qualitatively the same as Figure 103 because the RFI hopping rate is slow enough that additional clutter modulation induced by dynamic notching remains below the background response from RFI leakage. As the hopping rate increases to occurring every 10 ms in Figure 105, clutter modulation begins to arise that can mask movers if not properly compensated. However, the many movers are still visible. Finally, when the hopping increases again to changing every 0.6 ms, Figure 106 shows that clutter modulation has now grown to mask the movers. Moreover, with the PRI interval of $T_{\mathrm{PRI}} = 225.3\mu\mathrm{s}$ relative to the RFI hopping every $T_{\mathrm{RFI}} = 600\mu\mathrm{s}$, the number of latency-induced collisions grows significant. In short, there is a need for further reduction of the adaptation latency T_{adapt} if RFI becomes more dynamic.

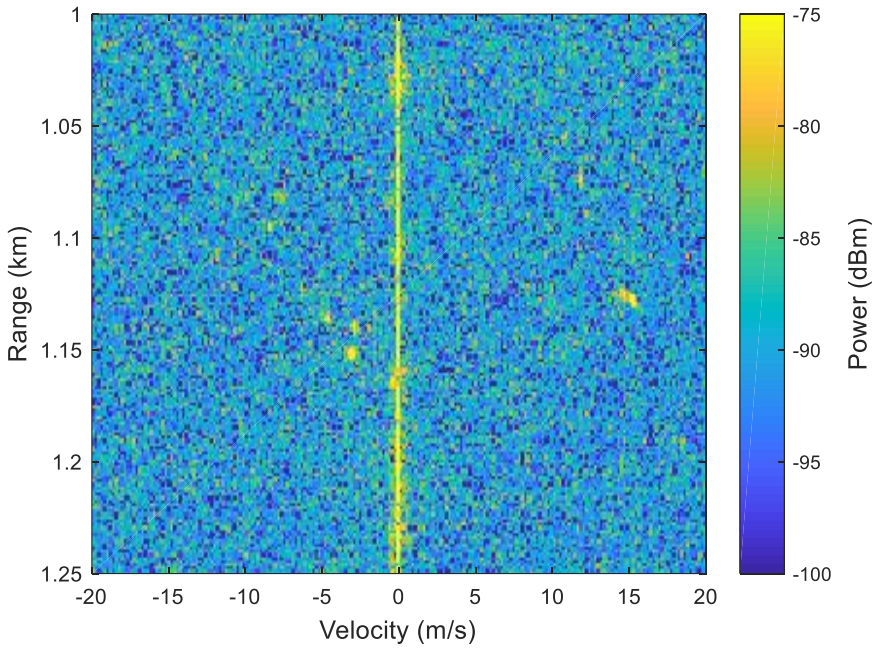

Figure 104: Range-Doppler plot for sense-and-notch PRO-FM with RFI hopping every 50ms. All radar operations are performed in real-time via the SDRadar.

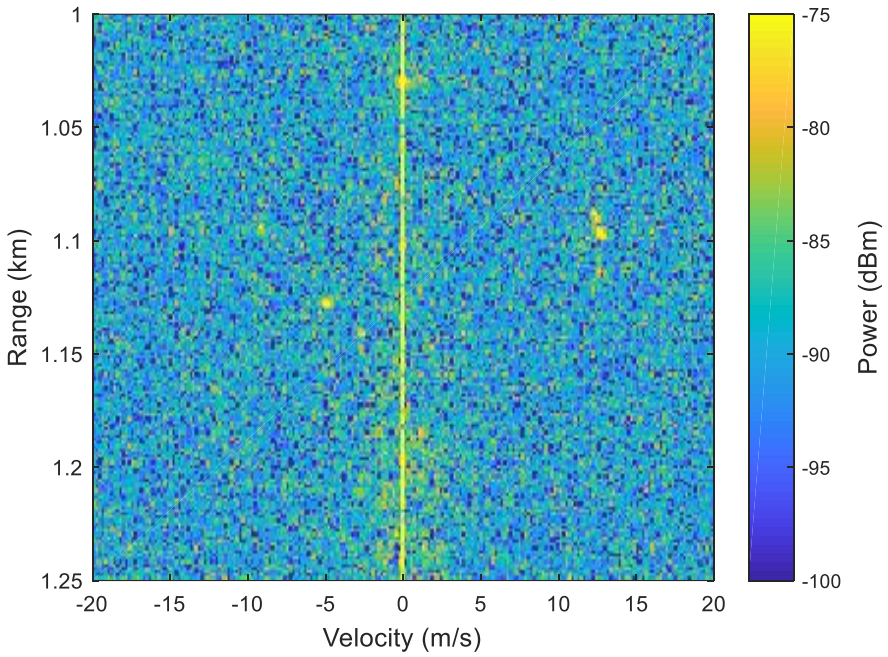

Figure 105: Range-Doppler plot for sense-and-notch PRO-FM with RFI hopping every 10ms. All radar operations are performed in real-time via the SDRadar.

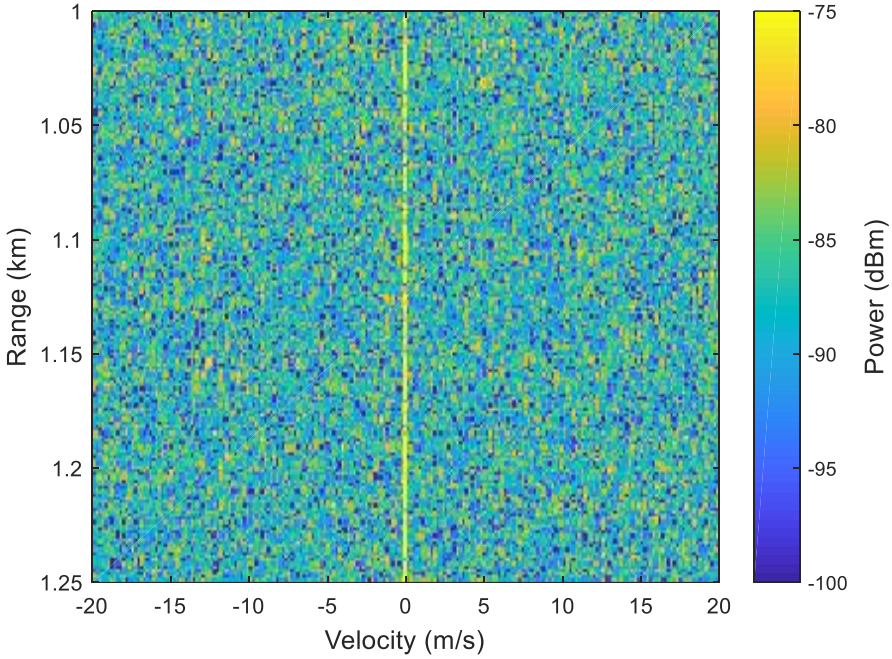

Figure 106: Range-Doppler plot for sense-and-notch PRO-FM with RFI hopping every 0.6ms. All radar operations are performed in real-time via the SDRadar.

2.6.3. CONCLUSIONS

A real-time open-air experimental demonstration of a cognitive sense-and-notch radar capability has been shown to have practical feasibility. This approach addresses the limiting factors of physical generation of on-the-fly notched waveform design, hardware fidelity effects, and acceptable latency for response time. Of course, the increasing complexity of the RF environment, including a multiplicity of distributed and dynamic spectrum users, will continue to drive the need for faster responses of higher quality (in this context, deeper) notches. As required adaptation rates are driven faster by greater congestion, techniques to mitigate clutter modulation effects also become critical.

2.7. FINAL REMARKS

With the available spectrum becoming increasingly congested, spectrum sharing is inevitable. From the radar perspective, significant fundamental challenges must be addressed to be a “good spectral neighbor” while simultaneously achieving sufficient scatterer detection performance. Foremost, the radar adaptation latency is the major driving factor towards mitigating interference between the radar and other spectral users. If an LTE signal is frequency hopping within an operational band, the radar may be required to spectrally null the transmission in a time-varying pattern within a coherent processing interval, which creates fundamental dynamic range limitations when applying standard range-Doppler processing. Additional post-processing methods (such as DeCCaF) are critical to achieve sense-and-notch radar performance requiring large dynamic ranges over extended processing intervals.

The global bounds have been determined for both range sidelobe and range-Doppler sidelobe minimization when waveform/filter spectral notches are present in the CPI. Designing waveforms to the global optimum power spectrum template, followed by subsequent least squares mismatched filtering, was shown to achieve the global optimum bound after coherent integration with modest mismatch loss. However, for real-time implementation, sub-optimal solutions are required to meet timing requirements and rapidly react to the presence of RF users. The sense-and-notch radar prototype implementation presented demonstrates the capability to achieve real-time interference avoidance for spectrum sharing applications using commercial-of-the-shelf (COTS) hardware. Spectral coexistence is quite feasible.

3. REFERENCES

1. H. Griffiths, L. Cohen, S. Watts, E. Mokole, C. Baker, M. Wicks, S. Blunt, “Radar spectrum engineering and management: technical and regulatory issues,” Proc. IEEE, vol. 103, no. 1, pp. 85-102, Jan. 2015.
2. J.M. Peha, “Sharing spectrum through spectrum policy reform and cognitive radio,” Proc. IEEE, vol. 97, no. 4, pp. 708-719, Apr. 2009.
3. M. Labib, V. Marojevic, A.F. Martone, J.H. Reed, A.I. Zaghloul, “Coexistence between communications and radar systems – a survey,” to appear in Radio Science Bulletin.
4. S.Z. Gurbuz, H.D. Griffiths, A. Charlish, M. Rangaswamy, M.S. Greco, K. Bell, "An overview of cognitive radar: past, present, and future," IEEE Aerospace & Electronic Systems Mag., vol. 34, no. 12, pp. 6-18, Dec. 2019.
5. M. López-Benítez, “Sensing-based spectrum awareness in cognitive radio: challenges and open research problems,” Intl. Symp. Communication Systems, Networks & DSP, Manchester, UK, July 2014.
6. https://www.defense.gov/News/News-Stories/Article/Article/3165774/ spectrum-sharing-is-way-ahead-to-maintain-economic-dominance-defense-official-s/
7. M. Greenspan, "Potential pitfalls of cognitive radars," IEEE Radar Conf., Cincinnati, OH, May 2014.
8. A.E. Mitchell, J.L. Garry, A.J. Duly, G.E. Smith, K.L. Bell, M. Rangaswamy, “Fully adaptive radar for variable resolution imaging,” IEEE Trans. Geoscience & Remote Sensing, vol. 57, no. 12, pp. 9810-9819, Dec. 2019.
9. A. Aubry, V. Carotenuto, A. DeMaio, A. Farina, L. Pallotta, “Optimization theory-based radar waveform design for spectrally dense environments,” IEEE Aerospace & Electronic Systems Mag., vol. 31, no. 12, pp. 14-25, Dec. 2016.
10. A. Aubry, V. Carotenuto, A. DeMaio, A. Farina, A. Izzo, R.S.L. Moriello, “Assessing power amplifier impairments and digital predistortion on radar waveforms for spectral coexistence,” IEEE Trans. Aerospace & Electronic Systems, vol. 58, no. 1, pp. 635-650, Feb. 2022.
11. J. Guerci, Cognitive Radar: The Knowledge-Aided Fully Adaptive Approach, 2nd ed., Artech House, 2020.
12. P. Stinco, M.S. Greco, F. Gini, “Spectrum sensing and sharing for cognitive radars,” IET Radar, Sonar & Navigation, vol. 10, no. 3, pp. 595-602, Feb. 2016.

13. B. O'Donnell, J.M. Baden, "Fast gradient descent for multi-objective waveform design," IEEE Radar Conf., Philadelphia, PA, May 2016.
14. S.W. Frost and B. Rigling, "Sidelobe predictions for spectrally-disjoint radar waveforms," IEEE Radar Conf., Atlanta, GA, May 2012.
15. G. Mazzaro, A. Martone and D. McNamara, "Detection of RF Electronics by Multitone Harmonic Radar," in *IEEE Transactions on Aerospace and Electronic Systems*, vol. 50, no. 1, pp. 477-490, January 2014.
16. M. Skolnik, "Introduction to radar systems". New York, Auckland. McGraw-Hill, 1962.
17. U. Nickel, "Overview of generalized monopulse estimation," in *IEEE Aerospace and Electronic Systems Magazine*, vol. 21, no. 6, pp. 27-56, June 2006.
18. S. Sherman, D. Barton, "Monopulse Principles and Techniques", Artech House 2nd edition, 2011.
19. V. Chen, "The Micro-doppler Effect in Radar", Artech House 2nd edition, 2019.
20. I. Cumming, F. Wong, "Digital Processing of Synthetic Aperture Radar Data" Artech House. 2005.
21. W. Carrara, R. Goodman, R. Majewski, "Spotlight Synthetic Aperture Radar", Artech House. 1995.
22. S. Blunt, A. Shackelford and K. Gerlach, "Single pulse imaging," *2006 International Waveform Diversity & Design Conference*, 2006.
23. M. Amin and F. Ahmad, "Through-the-Wall Radar Imaging: Theory and Applications," *Academic Press Library in Signal Processing*, Volume 2, 2014, pp. 857-909.
24. M. Amin, "Through-the-Wall Radar Imaging", CRC Press. 1st edition. 2010.
25. K. Ward, S. Watts, R. Tough, "Sea Clutter: Scattering, the K Distribution, and Radar Performance". The Institution of Engineering and Technology, 2nd Edition, 2013.
26. L. Rosenberg, S. Watts, "Radar Sea Clutter: Modelling and Target Detection", *IET Radar, Sonar and Navigation*, Scitech Publishing, 2022.
27. G. Fabrizio, "High Frequency Over the Horizon Radar", McGraw Hill, 1st Edition, 2013.
28. M. Davis, "Foliage penetration radar: Detection and Characterization of Objects under Trees". Scitech Publishing, 2011.
29. M. Skolnik, "Radar Handbook", McGraw Hill, 3rd Edition, 2008.

30. P. McCormick, “Design and Optimization of Physical Waveform-Diverse and Spatially-Diverse Radar Emissions”. University of Kansas. Doctoral Dissertation.
31. J. Li, P. Stoica, “MIMO Radar Signal Processing”, Wiley, 1st Edition, 2008.
32. G. Zook, P. McCormick and S. Blunt, "Fixational eye movement radar: Random spatial modulation," *2018 IEEE Radar Conference*, 2018, pp. 0827-0832.
33. B. Ravenscroft, P. McCormick, S. Blunt, E. Perrins and J. Metcalf, "A power-efficient formulation of tandem-hopped radar & communications," *2018 IEEE Radar Conference*, 2018.
34. P. McCormick, B. Ravenscroft, S. Blunt, A. Duly, J. Metcalf, “Simultaneous Radar and Communication Emissions from a Common Aperture, Part II: Experimentation,” *2017 IEEE Radar Conference*, 2017.
35. P. McCormick, C. Sahin, S. Blunt, J. Metcalf, “FMCW Implementation of Phase-Attached Radar-Communications (PARC),” *2019 IEEE Radar Conference*, 2019.
36. A. Mitchell, G. Smith, K. Bell, A. Duly and M. Rangaswamy, "Fully adaptive radar cost function design," *2018 IEEE Radar Conference*, 2018.
37. T. Kramer and S. Blunt, "Time-Frequency Analysis of Spectrally-Notched Random FM Waveforms," *2020 IEEE International Radar Conference*, 2020, pp. 163-168
38. F. Hlawatsch and G. Boudreaux-Bartels, "Linear and quadratic time-frequency signal representations," in *IEEE Signal Processing Magazine*, vol. 9, no. 2, pp. 21-67, April 1992
39. L. Almeida, "The fractional Fourier transform and time-frequency representations," in *IEEE Transactions on Signal Processing*, vol. 42, no. 11, pp. 3084-3091, Nov. 1994
40. R. Tancrell and M. Holland, "Acoustic surface wave filters," in *Proceedings of the IEEE*, vol. 59, no. 3, pp. 393-409, March 1971
41. S. Blunt and E. Mokole, "Overview of radar waveform diversity," in *IEEE Aerospace and Electronic Systems Magazine*, vol. 31, no. 11, pp. 2-42, November 2016
42. J. Proakis, D. Manolakis, “Digital signal processing: principles, algorithms, and applications”, Macmillan.
43. S. Blunt, L. Harnett, B. Ravenscroft, R. Chang, P. McCormick, “Implications of Diversified Doppler for Random PRI Radar,” accepted to *IEEE Trans. Aerospace & Electronic Systems*.

44. B. Boashash, “Time-Frequency Signal Analysis and Processing”, 2016.
45. J. Buckwalter, “Power Amplifiers,” University of California Santa Barbara, 2016. Lecture Slides. https://web.ece.ucsb.edu/Faculty/rodwell/Classes/ece218c/notes/
46. D. Morgan, Z. Ma, J. Kim, M. Zierdt and J. Pastalan, "A Generalized Memory Polynomial Model for Digital Predistortion of RF Power Amplifiers," in *IEEE Transactions on Signal Processing*, vol. 54, no. 10, pp. 3852-3860, Oct. 2006.
47. M. Isaksson, D. Wisell and D. Ronnow, "A comparative analysis of behavioral models for RF power amplifiers," in *IEEE Transactions on Microwave Theory and Techniques*, vol. 54, no. 1, pp. 348-359, Jan. 2006.
48. J. Owen, S. Blunt, K. Gallagher, P. McCormick, C. Allen, K. Sherbondy, “Nonlinear Radar via Intermodulation of FM Noise Waveform Pairs”, *2018 IEEE Radar Conference*, 2018.
49. E. Ward and B. Mulgrew, “Baseband Equivalent Volterra Series for Modelling Cross-channel Nonlinear Distortion,” *2019 IEEE Radar Conference, 2019.*
50. A. Tehrani, H. Cao, S. Afsardoost, T. Eriksson, M. Isaksson and C. Fager, "A Comparative Analysis of the Complexity/Accuracy Tradeoff in Power Amplifier Behavioral Models," in *IEEE Transactions on Microwave Theory and Techniques*, vol. 58, no. 6, pp. 1510-1520, June 2010.
51. Matlab Documentation, “System Identification Toolbox”, The Mathworks Inc. 2022. https://www.mathworks.com/help/ident/
52. M. Herndon and M. Yeary, "Real-Time FPGA-based Digital Predistortion for Improved Amplifier Performance in Next Generation Phased Arrays," *2022 IEEE Radar Conference*, 2022.
53. D. Lee, R. Cheung, W. Luk and J. Villasenor, "Hardware Implementation Trade-Offs of Polynomial Approximations and Interpolations," in *IEEE Transactions on Computers*, vol. 57, no. 5, pp. 686-701, May 2008
54. R. Lyons, “Sum of Two Cosines”. 2011.

55. J. Metcalf, S. Flandermeyer, C. Mohr, A. Kordik, P. McCormick and C. Sahin, "Characterizing the Impact of IQ Imbalance and DC Bias on Pulse-Agile Radar Processing," *2020 IEEE International Radar Conference*, 2020.
56. D. Frizelle, “Transmit LO Leakage (LOL)- An issue of zero-IF that isn’t making people laugh out loud”. AnalogDialogue. Vol. 51, July 2017.
57. D. Pozar, “Microwave Engineering”, Wiley, 4th Edition, 2011.
58. F. Harris, “Multirate Signal Processing for Communications”, Wiley, 1st Edition, 2004.
59. D. Turek, “Design of Efficient Interpolation Filters for Integer Upsampling”, Massachusetts Institute of Technology. Master’s Thesis.
60. W. Gautschi, “Numerical Analysis”, Birkhauser, 2nd Edition, 2012.
61. K. Shanmugan, A. Breipohl, “Random Signals: Detection, Estimation and Data Analysis”
62. C. Balanis, “Antenna Theory Analysis and Design”, 4th ed.
63. J. Jackson, “Classical Electrodynamics”, 3rd ed.
64. M. Roberts, “Signals and Systems : Analysis Using Transform Methods and Matlab”, 2nd ed.
65. D. Long, F. Ulaby, “Microwave Radar and Radiometric Remote Sensing” 2014.
66. Van Trees, “Detection, Estimation, and Modulation Theory, Part 1”.
67. J. Klauder, A. Price, S. Darlington and W. Albersheim, "The theory and design of chirp radars," in *The Bell System Technical Journal*, vol. 39, no. 4, pp. 745-808, July 1960
68. T. Moon and C. Wynn, “Mathematical methods and algorithms for signal processing”. Pearson, 2000.
69. K. Petersen and M. Pedersen, “The Matrix Cookbook”. November 2012.
70. S. Haykin, “Adaptive Filter Theory”. 5th ed.
71. D. Henke, P. McCormick, S. Blunt and T. Higgins, "Practical aspects of optimal mismatch filtering and adaptive pulse compression for FM waveforms," *2015 IEEE Radar Conference*, 2015.
72. J. Jakabosky, S. Blunt, B. Himed, “Spectral-Shape Optimized FM Noise Radar for Pulse Agility”, *2016 IEEE Radar Conference*, 2016.

73. M. Heintzelman, J. Owen, S. Blunt, B. Maio, E. Steinbach, “Practical Considerations for Optimal Mismatched Filtering of Nonrepeating Waveforms,” *2023 IEEE Radar Conference*, 2023.
74. S. Blunt and K. Gerlach, "Joint adaptive pulse compression to enable multistatic radar," *2004 International Waveform Diversity & Design Conference*, 2004.
75. C. Jones, L. Harnett, C. Mohr, S. Blunt and C. Allen, "Structure-Based Adaptive Radar Processing for Joint Clutter Cancellation and Moving Target Estimation," *2020 IEEE International Radar Conference*, 2020.
76. E. Hornberger, S. Blunt and T. Higgins, "Partially constrained adaptive beamforming for super-resolution at Low SNR," *2015 IEEE 6th International Workshop on Computational Advances in Multi-Sensor Adaptive Processing*, 2015, pp. 129-132
77. W. Holm, M. Richards, J. Scheer, “Principles of Modern Radar, Basic Principles”. 2010.
78. S. Blunt et al., "Principles and Applications of Random FM Radar Waveform Design," in *IEEE Aerospace and Electronic Systems Magazine*, vol. 35, no. 10, pp. 20-28, 1 Oct. 2020
79. N. Levanon, E. Mozeson, “Radar Signals”. 2004.
80. B. Phelan, “Theory, Design, Analysis, and Implementation of a Spectrally Agile Frequency-Incrementing Reconfigurable (SAFIRE) Forward Looking Ground Penetrating Radar”. PhD Dissertation. June 2016.
81. L. Nguyen, “Signal and Image Processing Algorithms for the U.S. Army Research Laboratory Ultra-wideband (UWB) Synchronous Impulse Reconstruction (SIRE) Radar”, ARL Report. April 2009.
82. A. Doerry, “Generating nonlinear FM chirp waveforms for radar”. Sandia Report. September 2006.
83. H. Milczarek, C. Leśnik and A. Kawalec, "Doppler-tolerant NLFM Radar Signal Synthesis Method," *2020 IEEE Radar Conference*, 2020.
84. C. Cook, J. Paolillo, “A Pulse Compression Predistortion function for efficient sidelobe reduction in a high-power radar”, *Proceedings of IEEE*, 1964, 52, pp. 377-389.
85. H. Griffiths, L. Vinagre, “Design of low-sidelobe pulse compression waveforms”, *Electronic Letters*, June 1994, Vol. 30, No. 12., pp. 1004-1005.
86. E. De Witte and H. D. Griffiths: “Improved ultra-low range sidelobe pulse compression waveform design”, *Electronics Letters*, 2004, pp. 1448-1450.

87. E. De Witte and H. D. Griffiths, "Improved waveforms for satellite-borne precipitation radar," *2006 International Waveform Diversity & Design Conference*, 2006

88. Vizitiu, I., “Some Aspects of Sidelobe Reduction in Pulse Compression Radars Using NLFM Signal Processing,” *Progress in Electromagnetics Research C,* Vol. 47, 119-129, 2014.

89. J. Song, Y. Gao, and D. Gao, “Analysis and detection of S-shaped NLFM signal based on instantaneous frequency,” *J. Commun.*, vol. 10, no. 12, Dec. 2015.

90. W. Yue and Y. Zhang, "A novel nonlinear frequency modulation waveform design aimed at side-lobe reduction," *2014 IEEE International Conference on Signal Processing, Communications and Computing*, 2014.

91. C. Gao, K. Teh and A. Liu, "Frequency diversity waveform with NLFM signals," *2015 10th International Conference on Information, Communications and Signal Processing*, 2015.

92. F. Gran and J. A. Jensen, “P2F-6 Designing Non-Linear Frequency Modulated Signals for Medical Ultrasound Imaging,” *2006 IEEE Ultrasonics Symposium*, 2006.

93. S. Alphonse, G. Williamson, Evaluation of a class of NLFM radar signals. *EURASIP J. Adv. Signal Process*. 2019.

94. T. Collins, P. Atkins, “Nonlinear frequency modulation chirps for active sonar”. *Radar, Sonar and Navigation*, *IEE Proceedings*. 2000.

95. R. Milleit, "A Matched-Filter Pulse-Compression System Using a Nonlinear FM Waveform," in *IEEE Transactions on Aerospace and Electronic Systems*, vol. AES-6, no. 1, pp. 73-78, Jan. 1970.

96. C. Cook, "A class of nonlinear FM pulse compression signals," in *Proceedings of the IEEE*, vol. 52, no. 11, pp. 1369-1371, Nov. 1964.

97. I. Gladkova, "Design of frequency modulated waveforms via the Zak transform," in *IEEE Transactions on Aerospace and Electronic Systems*, vol. 40, no. 1, pp. 355-359, Jan. 2004

98. A. Rihaczek, "Doppler-tolerant signal waveforms," in *Proceedings of the IEEE*, vol. 54, no. 6, pp. 849-857, June 1966.

99. A. Balleri, A. Farina. “Ambiguity function and accuracy of the hyperbolic chirp: Comparison with the linear chirp”. *IET Radar, Sonar & Navigation*. 2016.

100. S. Alphonse, G. Williamson, “Novel Radar Signal Models Using Nonlinear Frequency Modulation.”

101. R. Ghavamirad, M. Sebt, “Sidelobe Level Reduction in ACF of NLFM Waveform”. 2018.

102. Pan Yichun, Peng Shirui, Yang Kefeng and Dong Wenfeng, "Optimization design of NLFM signal and its pulse compression simulation," *IEEE International Radar Conference, 2005.*, 2005, pp. 383-386.

103. I. C. Vizitiu, F. Enache and F. Popescu, "Sidelobe reduction in pulse-compression radar using the stationary phase technique: An extended comparative study," *2014 International Conference on Optimization of Electrical and Electronic Equipment*, 2014, pp. 898-901

104. Q. Xie, H. Zeng, Z. Mo and W. Li, "A Two-Step Optimization Framework for Low Sidelobe NLFM Waveform Using Fourier Series," in *IEEE Geoscience and Remote Sensing Letters*, vol. 19, pp. 1-5, 2022.

105. F. Argenti and L. Facheris, "Radar Pulse Compression Methods Based on Nonlinear and Quadratic Optimization," in *IEEE Transactions on Geoscience and Remote Sensing*, vol. 59, no. 5, pp. 3904-3916, May 2021.

106. J. M. Kurdzo, B. L. Cheong, R. D. Palmer and G. Zhang, "Optimized NLFM pulse compression waveforms for high-sensitivity radar observations," *2014 International Radar Conference*, 2014.

107. D. A. Hague, "Nonlinear frequency modulation using fourier sine series," *2018 IEEE Radar Conference*, 2018.

108. W. Wang et al., "First Demonstration of Airborne SAR With Nonlinear FM Chirp Waveforms," in *IEEE Geoscience and Remote Sensing Letters*, vol. 13, no. 2, pp. 247-251, Feb. 2016

109. J. Saeedi, K. Faez, "Synthetic aperture radar imaging using nonlinear frequency modulation signal," in *IEEE Transactions on Aerospace and Electronic Systems*, vol. 52, no. 1, pp. 99-110, Feb. 2016.

110. G. Jin et al., "Mitigating Range Ambiguities With Advanced Nonlinear Frequency Modulation Waveform," in *IEEE Geoscience and Remote Sensing Letters*, vol. 16, no. 8, pp. 1230-1234, Aug. 2019.

111. G. Jin et al., "An Advanced Nonlinear Frequency Modulation Waveform for Radar Imaging With Low Sidelobe," in *IEEE Transations on Geoscience and Remote Sensing*, vol. 57, no. 8, pp. 6155-6168, Aug. 2019.

112. E. Fowle, "The Design of FM Pulse Compression Signals," *IEEE Transactions of Information Theory.* 1964.

113. D. Rabideau, "Nonlinear synthetic wideband waveforms," *Proceedings of the 2002 IEEE Radar Conference*, 2002.

114. S. Prager, D. Hawkins and M. Moghaddam, "Arbitrary Nonlinear FM Waveform Construction and Ultra-Wideband Synthesis," *2020 IEEE International Geoscience and Remote Sensing Symposium*, 2020.

115. J. Kurdzo, J. Cho, B. Cheong and R. Palmer, "A Neural Network Approach for Waveform Generation and Selection with Multi-Mission Radar," *2019 IEEE Radar Conference*, 2019.

116. L. Jackson, S. Kay and N. Vankayalapati, "Iterative Method for Nonlinear FM Synthesis of Radar Signals," in *IEEE Transactions on Aerospace and Electronic Systems*, vol. 46, no. 2, pp. 910-917, April 2010.

117. J. Roberts, "Angle Modulation: The theory of system assessment," *IEE Telecommunications Series*. 1977.

118. C. A. Mohr, S. Blunt, "FM Noise Waveforms Optimized According to a Temporal Template Error (TTE) Metric," *2019 IEEE Radar Conference*, 2019.

119. C. A. Mohr, S. Blunt, "Design and Generation of Stochastically Defined, Pulsed FM Noise Waveforms," *2019 International Radar Conference*, 2019.

120. J. Jakabosky, S. Blunt and B. Himed, "Spectral-shape optimized FM noise radar for pulse agility," *2016 IEEE Radar Conference*, 2016.

121. M. Heintzelman, T. Kramer, S. Blunt, "Experimental Evaluation of Super-Gaussian-Shaped Random FM Waveforms," *2022 IEEE Radar Conference*, 2022.

122. T. Kramer, "Time-Frequency Analysis of Waveform Diverse Designs", University of Kansas. Master's Thesis.

123. Blunt, et. al, "Polyphase-Coded FM (PCFM) Radar Waveforms, Part I: Implementation," *IEEE Transactions on Aerospace and Electronic Systems*.

124. Blunt, et. al, “Polyphase-Coded FM (PCFM) Radar Waveforms, Part II: Optimization,” *IEEE Transactions on Aerospace and Electronic Systems*.

125. J. Jakabosky, P. McCormick, S. Blunt, “Implementation & Design of Physical Radar Waveform Diversity,” *IEEE Aerospace and Electronic Systems Magazine*, vol. 31, no. 12, pp. 26-33, December 2016.

126. J. Jakabosky, S. Blunt, B. Himed, “Optimization of “over-coded” radar waveforms”, *2014 IEEE Radar Conference*, Cincinnati, OH, 2014.

127. L. Ryan, J. Jakabosky, S. Blunt, C. Allen, L. Cohen, “Optimizing polyphase-coded FM waveforms within a LINC transmit architecture,” *2014 IEEE Radar Conference*, Cincinnati, OH, 2014.

128. P. McCormick, S. Blunt, “Nonlinear conjugate gradient optimization of polyphase-coded FM radar waveforms,” *2017 IEEE Radar Conference*, Seattle, WA, 2017.

129. C. Mohr, P. McCormick, C. Topliff, S. Blunt, M. Baden, “Gradient-Based Optimization of PCFM Radar Waveforms,” *IEEE Transactions on Aerospace and Electronic Systems*, vol. 57, no. 2, pp. 935-956.

130. C. Mohr, P. McCormick, S. Blunt, “Optimized Complementary Waveform Subsets within an FM Noise Radar CPI,” *2018 IEEE Radar Conference*, Oklahoma City, OK, 2018.

131. C. Mohr, P. McCormick, S. Blunt, C. Mott, “Spectrally-efficient FM noise radar waveforms optimized in the logarithmic domain,” 2018 IEEE Radar Conference, Oklahoma City, OK, 2018.

132. C. Mohr, “Design and Evaluation of Stochastic Processes as Physical Radar Waveforms”, PhD Dissertation.

133. B. Evans, J. Moon, “Time Invariance for an Integrator”, The University of Texas Austin, Jan. 2023.

134. M. Heintzelman, D. Herr, S. Blunt, C. Mohr, C. Sahin, A. Kordik, “Separability Analysis of Random Radar Waveforms”, in preparation for Transactions on Radar Systems (TRS). 2023.

135. J. Quirk, R. Chang, J. Owen, S. Blunt, P. McCormick, “A Simple yet Effective Metric for Assessing Doppler Tolerance,” in IEEE Transactions on Radar Systems. 2023.

136. S. Haykin, “Cognitive radar: a way of the future,” IEEE Signal Processing Mag., vol. 23, no. 1, pp. 30-40, Jan. 2006.

137. A.F. Martone, “Cognitive radar demystified,” URSI Bulletin, no. 350, pp. 10-22, Sept. 2014.

138. K.L. Bell, C.J. Baker, G.E. Smith, J.T. Johnson, M. Rangaswamy, “Cognitive radar framework for target detection and tracking,” IEEE J. Selected Topics Signal Processing, vol. 9, no. 8, pp. 1427-1439, Dec. 2015.

139. B.H. Kirk, K.A. Gallagher, J.W. Owen, R.M. Narayanan, A.F. Martone, K.D. Sherbondy, “Cognitive software defined radar for time-varying RFI avoidance,” submitted to IEEE Radar Conf., Oklahoma City, OK, Apr. 2018.

140. B.H. Kirk, R.M. Narayanan, K.A. Gallagher, A.F. Martone, K.D. Sherbondy, "Avoidance of time-varying radio frequency interference with software-defined cognitive radar," IEEE Trans. Aerospace & Electronic Systems, vol. 55, no. 3, pp. 1090-1107, June 2019.

141. M.J. Lindenfeld, “Sparse frequency transmit-and-receive waveform design,” IEEE Trans. Aerospace & Electronic Systems, vol. 40, no. 3, pp. 851-861, July 2004.

142. K. Gerlach, M.R. Frey, M.J. Steiner, A. Shackelford, “Spectral nulling on transmit via nonlinear FM radar waveforms,” IEEE Trans. Aerospace & Electronic Systems, vol. 47, no. 2, pp. 1507-1515, Apr. 2011.

143. I.W. Selesnick and S.U. Pillai, “Chirp-like transmit waveforms with multiple frequency-notches,” IEEE Radar Conf., Kansas City, MO, May 2011.

144. C. Nunn, L.R. Moyer, “Spectrally-compliant waveforms for wideband radar,” Aerospace & Electronic Systems Mag., vol. 27, no. 8, pp. 11-15, August 2012.

145. L.K. Patton, B.D. Rigling. "Phase retrieval for radar waveform optimization," IEEE Trans. Aerospace & Electronic Systems, vol. 48, no. 4, pp. 3287-3302, October 2012.

146. L.K. Patton, C.A. Bryant, B. Himed, “Radar-centric design of waveforms with disjoint spectral support,” IEEE Radar Conf., Atlanta, GA, May 2012.

147. A. Aubry, A. De Maio, Y. Huang, M. Piezzo, A. Farina, “A new radar waveform design algorithm with improved feasibility for spectral coexistence,” IEEE Trans. Aerospace & Electronic Systems, vol. 51, no. 2, pp. 1029-1038, Apr. 2015.

148. J. Jakabosky, S.D. Blunt, A. Martone, "Incorporating hopped spectral gaps into nonrecurrent nonlinear FMCW radar emissions," IEEE CAMSAP Workshop, Cancun, Mexico, Dec. 2015.

149. J. Jakabosky, B. Ravenscroft, S. Blunt and A. Martone, "Gapped spectrum shaping for tandem-hopped radar/communications & cognitive sensing," *2016 IEEE Radar Conference*, 2016.

150. B. Ravenscroft, S.D. Blunt, C. Allen, A. Martone, K. Sherbondy, "Analysis of spectral notching in FM noise radar using measured interference," IET Intl. Radar Conf., Belfast, UK, Oct. 2017.

151. J. W. Owen et al., "Experimental demonstration of cognitive spectrum sensing & notching for radar," *2018 IEEE Radar Conference*, 2018, pp. 0957-0962.

152. B. Ravenscroft, J. Owen, J. Jakabosky, S.D. Blunt, A.F. Martone, K.D. Sherbondy, "Experimental demonstration and analysis of cognitive spectrum sensing and notching for radar," *IET Radar, Sonar & Navigation*, vol. 12, no. 12, pp. 1466-1475, Dec. 2018.

153. A. Martone, K. Ranney, "Fast technique for wideband spectrum sensing," IEEE Antennas & Propagation Intl. Symp., Memphis, TN, July 2014.

154. A. Martone, K. Ranney, K. Sherbondy, K. Gallagher, S. Blunt, "Spectrum allocation for non-cooperative radar coexistence," to appear in IEEE Trans. Aerospace & Electronic Systems.

155. M. Cook, T. Higgins, A. Shackelford, "Thinned spectrum radar waveforms," Intl. Waveform Diversity & Design Conf., Niagara Falls, ON, Canada, Aug. 2010.

156. T. Higgins, T. Webster, A. Shackelford. "Mitigating interference via spatial and spectral nulling," IET Radar, Sonar & Navigation, vol.8, no.2, pp.84-93, Feb. 2014.

157. T. Webster, T. Higgins, A. Shackelford, J. Jakabosky and P. McCormick, "Phase-only adaptive spatial transmit nulling," *2015 IEEE Radar Conference*, 2015, pp. 0931-0936.

158. C. Mohr, S. Blunt, "Analytical Spectrum Representation for Physical Waveform Optimization Requiring Extreme Fidelity". *2019 IEEE Radar Conference*. 2019.

159. C. Mohr, J. W. Owen, S. Blunt and C. Allen, "Zero-Order Reconstruction Optimization of Waveforms (ZOROW) for Modest *DAC Rates," 2020 IEEE International Radar Conference, Washington, DC, USA, 2020*

160. B. Ravenscroft, J. Owen, S. Blunt, A. Martone, K. Sherbondy, "Optimal Mismatch Filtering to Address Clutter Spread from Intra-CPI Variation of Spectral Notches," *2019 IEEE Radar Conference*, Boston, MA. 2019.

161. J. Owen, B. Ravenscroft, S. Blunt, “Devoid Clutter Capture and Filling (DeCCaF) to Compensate for Intra-CPI Spectral Notch Variation”, 2019 SEE International Radar Conference, Toulon, FR. 2019.

162. C. Sahin, J. Metcalf, S. Blunt, "Filter design to address range sidelobe modulation in transmit-encoded radar-embedded communications," IEEE Radar Conf., Seattle, WA, May 2017.

163. K.M. Cuomo, J.E. Piou, J.T. Mayhan, “Ultrawide-band coherent processing,” IEEE Trans. Antennas & Propagation, vol. 47, no. 6, pp. 1094-1107, June 1999.

164. J. Salzman, D. Akamine, R. Lefevre, J.C. Kirk, “Interrupted synthetic aperture radar (SAR),” IEEE Aerospace & Electronic Systems Magazine, vol. 17, no. 5, pp. 33-39, May 2002.

165. J. Mead, R. Renaut, “Least squares problems with inequality constraints as quadratic constraints,” Linear Algebra & its Applications, vol. 432, no. 8, pp. 1936-1949, Apr. 2010.

166. Matlab Documentation, “Optimization Toolbox”, The Mathworks Inc. 2022. https://www.mathworks.com/help/optim/ug/fmincon.html

167. A.W. Doerry, “Catalog of window taper functions for sidelobe control,” Sandia Technical Report SAND2017-4042, Apr. 2017.

168. S. Boyd, L. Vanderberghe, “Convex Optimization”, 1st Ed, Cambridge University Press, March 2004.

169. J. W. Owen, C. A. Mohr, B. H. Kirk, S. D. Blunt, A. F. Martone and K. D. Sherbondy, "Demonstration of Real-time Cognitive Radar using Spectrally-Notched Random FM Waveforms," 2020 IEEE International Radar Conference, Washington, DC, USA, 2020

170. A. Farina, A. De Maio, S. Haykin, The Impact of Cognition on Radar Technology, SciTech Publishing, 2017.

171. S.D. Blunt, E.S. Perrins, Radar & Communication Spectrum Sharing, SciTech Publishing, 2018.

172. B.L. Cheong, R. Palmer, Y. Zhang, M. Yeary, T.-Y. Yu, "A software-defined radar platform for waveform design," IEEE Radar Conf., Atlanta, GA, May 2012.

173. K. El-Darymli, N. Hansen, B. Dawe, E.W. Gill, W. Huang, "Design and implementation of a high-frequency software-defined radar for coastal ocean applications," IEEE Aerospace & Electronic Systems Mag., vol. 33, no. 3, pp. 14-21, Mar. 2018.

174. J.M. Christiansen, G.E. Smith, K.E. Olsen, "USRP based cognitive radar testbed," IEEE Radar Conf., Seattle, WA, May 2017.

175. J.M. Christiansen, K.E. Olsen, G.E. Smith, "Fully adaptive radar for track update-interval control," IEEE Radar Conf., Oklahoma City, OK, Apr. 2018.

176. J.M. Christiansen, G.E. Smith, "Parameter selection in a fully adaptive tracking radar," Intl. Radar Conf., Toulon, France, Sept. 2019.

177. B.H. Kirk, A.F. Martone, K.D. Sherbondy, R.M. Narayanan, "Mitigation of target distortion in pulse-agile sensors via Richardson-Lucy deconvolution," Electronics Letters, vol. 55, no. 23, pp. 1249-1252, Nov. 2019.

178. B. Ravenscroft, J.W. Owen, B.H. Kirk, S.D. Blunt, A.F. Martone, K.D. Sherbondy, R.M. Narayanan, "Experimental assessment of joint range-Doppler processing to address clutter modulation from dynamic radar spectrum sharing," IEEE Intl. Radar Conf., Washington, DC, Apr. 2020.

179. J. Nocedal, S. Wright, "Numerical Optimization", Springer Science & Business Media, 2006.

180. D. Zhao, Y. Wei, Y. Liu, "Spectrum optimization via FFT-based conjugate gradient method for unimodular sequence design," Signal Processing, vol. 142, pp. 354-365, Jan. 2018.

181. E. Ghadimi, R. Feyzmahdavian, M. Johansson, "Global convergence of the heavy-ball method for convex optimization," European Control Conf., Linz, Austria, July 2015

182. W.W. Hager, H. Zhang, "A survey of nonlinear conjugate gradient methods," Pacific Journal of Optimization, vol. 2, no. 1, pp. 35-58, Dec. 2005.

183. J. Kovariskiy, J.W. Owen, R.M. Narayanan, S.D. Blunt, A.F. Martone, K.D. Sherbondy, "Spectral prediction and notching of RF emitters for cognitive radar coexistence," IEEE Intl. Radar Conf., Washington, DC, Apr. 2020.

184. A.F. Martone, K.D. Sherbondy, J.A. Kovarskiy, B.H. Kirk, C.E. Thornton, J.W. Owen, B. Ravenscroft, A. Egbert, A. Goad, A. Dockendorf, M. Buehrer, R.M. Narayanan, S.D. Blunt, C. Baylis, "Metacognition for Radar Coexistence," 2020 IEEE International Radar Conference, Washington, DC, 27-30 Apr. 2020.

185. A.F. Martone, J.A. Kovarskiy, C.E. Thornton, B.H. Kirk, J.W. Owen. B. Ravenscroft, A. Egbert, A. Goad, R.M. Buehrer, R.M. Narayanan, S.D. Blunt, C. Baylis, K.D. Sherbondy, “Closing the Loop on Cognitive Radar for Spectrum Sharing,” IEEE Aerospace & Electronic Systems Magazine, vol. 36, no. 9, pp. 44-55, Sept. 2021.

186. A.F. Martone, K.D. Sherbondy, J.A. Kovarskiy, B.H. Kirk, J.W. Owen, B. Ravenscroft, A. Egbert, A. Goad, A. Dockendorf, C.E. Thornton, R.M. Buehrer, R.M. Narayanan, S. Blunt, C. Baylis, "Practical Aspects of Cognitive Radar," IEEE Radar Conference, Florence, Italy, 21-25 Sept. 2020.

187. J.W. Owen, G.B. Ravenscroft, S.D. Blunt, "Devoid Clutter Capture and Filling (DeCCaF) to Compensate for Intra-CPI Spectral Notch Variation," US Patent Application #62/903,618, filed on Sept. 20, 2019.

188. J. Owen, C. Mohr, S.D. Blunt, and K. Gallagher, "Nonlinear Radar via Intermodulation of Jointly Optimized FM Noise Waveform Pairs," IEEE Radar Conference, Boston, MA, 22-26 Apr. 2019.

4. APPENDIX

4.1. TABLE OF NONLINEAR FM WAVEFORMS

The desired starting and stopping frequencies are f_1 and f_2, the center frequency is $f_c = \frac{f_2 - f_1}{2} + f_1$, the approximate swept bandwidth is $B = f_2 - f_1$, and the pulse width is T_p. The arbitrary factors are in the ranges of $c_1 \in (0,1)$, $c_2 \in \left(0, \frac{\pi}{2}\right)$, $c_3 \in (0, \infty)$, $c_4 \in (1, \infty)$, $c_5 \in (1,2]$.

For the piecewise defined functions, $-0.5 < f_1 < f_1' < 0 < f_2' < f_2 < 0.5$ are intermediate frequencies such that $B_2 = f_2 - f_2'$, $B_1 = f_2' - f_1'$, and $B_0 = f_1' - f_1$.

Table 8: Nonlinear FM Waveform Equations

$s_{\mathrm{LFM}}(t) = e^{j2\pi\left(f_1 t + 0.5\left(\frac{B}{T_\mathrm{p}}\right)t^2\right)}$	$t \in (0, T_\mathrm{p})$	[79]
$s_{\mathrm{price}}(t) = e^{j2\pi\left(f_\mathrm{c}\left(t+\frac{T_\mathrm{p}}{2}\right)+\int_0^t f_\mathrm{i}(t)dt\right)}$ $f_\mathrm{i}(t) = \left(t/T_\mathrm{p}\right)\left(B + B_1 \frac{1}{\sqrt{1 - 4c_1\left(t/T_\mathrm{p}\right)^2}}\right)$	$t \in \left(-\frac{T_\mathrm{p}}{2}, \frac{T_\mathrm{p}}{2}\right)$	[79]
$s_{\mathrm{cosh}}(t) = e^{j2\pi\left(f_\mathrm{c}\left(t+\frac{T_\mathrm{p}}{2}\right)+\frac{c_1 c_3}{2\pi}\cosh\left(\frac{(t/T_\mathrm{p})}{c_3}\right)+\frac{(1-c_1)(t/T_\mathrm{p})^2}{\sqrt{c_4 - 4(t/T_\mathrm{p})^2}}\right)}$	$t \in (-\frac{T_\mathrm{p}}{2}, \frac{T_\mathrm{p}}{2})$	[83]
$s_{\mathrm{pw}}(t) = e^{j2\pi(f_\mathrm{c} t + \phi(t))}$ $\phi(t) = \begin{cases} f_1 t + \frac{B_0}{T_1}\left(\frac{t^2}{2}\right) & 0 \le t \le T_1 \\ f_1' t + \frac{B_1}{T_2 - T_1}\left(\frac{t^2}{2} - T_1 t\right) & T_1 \le t \le T_2 \\ f_2' t + \frac{B_2}{T_\mathrm{p} - T_2}\left(\frac{t^2}{2} - T_2 t\right) & T_2 \le t \le T_\mathrm{p} \end{cases}$	$t \in (0, T_\mathrm{p})$ $T_1 = T_\mathrm{p} - T_2$ $f_1' = -f_2'$	[84, 85]

$$s_{\text{ddfc}}(t) = e^{j2\pi\left(f_c\left(t+\frac{T_\text{p}}{2}\right)+\int_0^t f_\text{i}(t)dt\right)}$$ $$f_\text{i}(t) = \begin{cases} \left(\frac{B_1}{T_2-T_1}\right)t - \left(\frac{2T_\text{edge}(f_1-\Delta f)f_1'}{2(B_0+\Delta f)t+(B_0+\Delta f)T_\text{p}-2T_\text{edge}f_1'}+f_1'\right) & -\frac{T_\text{p}}{2} \le t \le T_1 \\ \left(\frac{B_1}{T_2-T_1}\right)t & T_1 < t < T_2 \\ \left(\frac{B_1}{T_2-T_1}\right)t + \left(\frac{2T_\text{edge}(f_2+\Delta f)f_2'}{-2(B_2+\Delta f)t+(B_2+\Delta f)T_\text{p}+2T_\text{edge}f_2'}-f_2'\right) & T_2 \le t \le \frac{T_\text{p}}{2} \end{cases}$$ $$\Delta f = \frac{f_1'(2T_\text{edge})}{T_2-T_1} = \frac{-f_2'(2T_\text{edge})}{T_2-T_1} \qquad T_\text{edge} = \frac{T_\text{p}}{2} - T_2$$	$t \in \left(-\frac{T_\text{p}}{2}, \frac{T_\text{p}}{2}\right)$ $T_1 = -T_2$ $f_1' = -f_2'$ $T_1 < 0$ $T_2 > 0$ $f_2 > \lvert\Delta f\rvert$	[86, 87]
$$s_{\text{viz}-1}(t) = e^{j2\pi\left(f_c\left(t+\frac{T_\text{p}}{2}\right)+\int_0^t f_\text{i}(t)dt\right)}$$ $$f_\text{i}(t) = \begin{cases} f_1' + \frac{2}{\pi}B_0 \operatorname{asin}\left(\frac{t-T_1}{T_1}\right) & 0 \le t \le T_1 \\ \left(\frac{B_1}{T_2-T_1}\right)\left(t-\frac{T_\text{p}}{2}\right) & T_1 < t < T_2 \\ f_2' + \frac{2}{\pi}B_2 \operatorname{asin}\left(\frac{t-T_2}{T_\text{p}-T_2}\right) & T_2 \le t \le T_\text{p} \end{cases}$$	$t \in (0, T_\text{p})$ $T_1 = T_\text{p} - T_2$ $f_1' = -f_2{}'$ $0 < T_1 < 0.5$ $0.5 < T_2 < T_\text{p}$	[88]
$$s_{\text{viz}-2}(t) = e^{j2\pi\left(f_c\left(t+\frac{T_\text{p}}{2}\right)+\int_0^t f_\text{i}(t)dt\right)}$$ $$f_\text{i}(t) = \begin{cases} f_1' - B_0 + B_0\left(\frac{t}{T_1}\right)^{c_1} & 0 \le t \le T_1 \\ \left(\frac{B_1}{T_2-T_1}\right)\left(t-\frac{T_\text{p}}{2}\right) & T_1 < t < T_2 \\ f_2' + B_2 - B_2\left(\frac{T_\text{p}-t}{T_\text{p}-T_2}\right)^{c_1} & T_2 \le t \le T_\text{p} \end{cases}$$	$t \in (0, T_\text{p})$ $T_1 = T_\text{p} - T_2$ $f_1' = -f_2{}'$ $0 < T_1 < 0.5$ $0.5 < T_2 < T_\text{p}$	[88]
$$s_{\tan}(t) = e^{j2\pi\left(f_\text{c}\left(t+\frac{T_\text{p}}{2}\right)+B\left(\frac{\ln\lvert\sec(2c_2(t/T_\text{p}))\rvert}{4c_2\tan(c_2)}\right)\right)}$$	$t \in \left(-\frac{T_\text{p}}{2}, \frac{T_\text{p}}{2}\right)$	[89, 90]
$$s_{\sec}(t) = e^{j2\pi\left(f_\text{c}\left(t+\frac{T_\text{p}}{2}\right)+\frac{c_3 B\sec\left(2\operatorname{atan}\left(\frac{\pi}{2c_3}\right)(t/T_\text{p})\right)}{2\pi\operatorname{atan}\left(\frac{\pi}{2c_3}\right)\sec\left(\operatorname{atan}\left(\frac{\pi}{2c_3}\right)\right)}\right)}$$	$t \in \left(-\frac{T_\text{p}}{2}, \frac{T_\text{p}}{2}\right)$	[91]

$s_{\text{opfs}}(t) = e^{j2\pi\left(f_c\left(t+\frac{T_p}{2}\right)+\int_0^t f_i(t)dt\right)}$ $f_i(t) = c_3 B \sum_{n=1}^{N} K_n \left(\frac{2t}{T_p}\right)^{N-n}$	$t \in \left(-\frac{T_p}{2}, \frac{T_p}{2}\right)$	[92, 93]
$s_{\text{ate}}(t) = e^{j2\pi\left(f_c\left(t+\frac{T_p}{2}\right)+\int_0^t f_i(t)dt\right)}$ $f_i(t) = \begin{cases} \frac{B}{2}\left(\frac{2\left(t+\frac{T_p}{2}\right)}{T_p}\right)^{c_5-1} - \frac{B}{2} & -T_p/2 \le t < 0 \\ \frac{B}{2} - \frac{B}{2}\left(\frac{2\left(\frac{T_p}{2}-t\right)}{T_p}\right)^{c_5-1} & 0 \le t \le T_p/2 \end{cases}$	$t \in \left(-\frac{T_p}{2}, \frac{T_p}{2}\right)$	[92]
$s_{\text{tan2}}(t) = e^{j2\pi\left(f_c\left(t+\frac{T_p}{2}\right)+\int_0^t f_i(t)dt\right)}$ $f_i(t) = \frac{B}{2}\left(\frac{c_1 \tan\left(\frac{2c_2 t}{T_p}\right)}{\tan(c_2)} + \frac{2(1-c_1)t}{T_p}\right)$	$t \in \left(-\frac{T_p}{2}, \frac{T_p}{2}\right)$	[94]
$s_{\text{millet}}(t) = e^{j2\pi\left(f_c\left(t+\frac{T_p}{2}\right)+\int_0^t f_i(t)dt\right)}$ $-T_p\left[\frac{f_i}{B} + \frac{1}{2\pi}\left(\frac{1-c_1}{1+c_1}\right)\sin\left(\frac{2\pi f_i}{B}\right)\right] - t = 0$ (Use nonlinear solver)	$t \in \left(-\frac{T_p}{2}, \frac{T_p}{2}\right)$	[95, 96]
$s_{\text{cook}}(t) = e^{j2\pi\left(f_c\left(t+\frac{T_p}{2}\right)+\int_0^t f_i(t)dt\right)}$ $-T_p\left[\frac{f_i}{B} + \frac{1}{2\pi}\sin\left(\frac{2\pi f_i}{B}\right)\right] - t = 0$ (Use nonlinear solver) $-T_p\left[\frac{f_i}{B} + \frac{1}{2\pi}\sin\left(\frac{2\pi f_i}{B}\right) + \frac{2}{3\pi}\cos\left(\frac{\pi f_i}{B}\right)^3 \sin\left(\frac{\pi f_i}{B}\right)\right] - t = 0$	$t \in \left(-\frac{T_p}{2}, \frac{T_p}{2}\right)$	[96]

$s_{\text{poly}}(t) = e^{j\,2\pi\left(f_c t+\left(c_3-\left((c_3)^{c_4}-\left(c_3\frac{2t}{T_p}\right)^{c_4}\right)^{\frac{1}{c_4}}\right)\right)}$	$t \in \left(-\frac{T_p}{2}, \frac{T_p}{2}\right)$	[97]
$s_{\text{HFM}}(t) = e^{j2\pi\left(f_c t+\frac{f_1 f_2}{f_1-f_2}\cdot \ln\left(1+\frac{(f_1-f_2)}{f_2}\left(\frac{t}{T_p}\right)\right)\right)}$	$t \in (0, T_p)$ $f_1 > 0$ $f_2 > 0$	[98, 99]
$s_{\text{TEFM}}(t) = e^{j2\pi\left(f_c t+\int_0^t f_i(t)dt\right)}$ $f_i(t) = f_1 + B\left(\frac{t}{T_p}\right)^{c_4-1}$	$t \in (0, T_p)$	[100]
$s_{\text{SEFM}}(t) = e^{j2\pi\left(f_c t+\int_0^t f_i(t)dt\right)}$ $f_i(t) = f_1 + B\sin^{c_3}\left(\frac{t}{T_p}\left(\frac{\pi}{2}\right)\right)$	$t \in (0, T_p)$	[100]